PERMANENT MAGNET BRUSHLESS DC MOTOR DRIVES AND CONTROLS


SHOUT
SHARE
IT

PERMANENT MAGNET BRUSHLESS DC MOTOR DRIVES AND CONTROLS

Chang-liang Xia
Tianjin University, P.R. China

WILEY
John Wiley & Sons Singapore Pte. Ltd.

This edition first published 2012
© 2012 Science Press. All rights reserved.

Published by John Wiley & Sons Singapore Pte. Ltd., 1 Fusionopolis Walk, #07-01 Solaris South Tower, Singapore 138628, under exclusive license by Science Press in all media and all languages throughout the world excluding Mainland China and excluding Simplified and Traditional Chinese languages.

For details of our global editorial offices, for customer services and for information about how to apply for permission to reuse the copyright material in this book please see our website at www.wiley.com.

All Rights Reserved. No part of this publication may be reproduced, stored in a retrieval system or transmitted, in any form or by any means, electronic, mechanical, photocopying, recording, scanning, or otherwise, except as expressly permitted by law, without either the prior written permission of the Publisher, or authorization through payment of the appropriate photocopy fee to the Copyright Clearance Center. Requests for permission should be addressed to the Publisher, John Wiley & Sons Singapore Pte. Ltd., 1 Fusionopolis Walk, #07-01 Solaris South Tower, Singapore 138628, tel: 65-66438000, fax: 65-66438008, email: enquiry@wiley.com.

Wiley also publishes its books in a variety of electronic formats. Some content that appears in print may not be available in electronic books.

Designations used by companies to distinguish their products are often claimed as trademarks. All brand names and product names used in this book are trade names, service marks, trademarks or registered trademarks of their respective owners. The Publisher is not associated with any product or vendor mentioned in this book. This publication is designed to provide accurate and authoritative information in regard to the subject matter covered. It is sold on the understanding that the Publisher is not engaged in rendering professional services. If professional advice or other expert assistance is required, the services of a competent professional should be sought.

MATLAB® is a trademark of The MathWorks, Inc. and is used with permission. The MathWorks does not warrant the accuracy of the text or exercises in this book. This book's use or discussion of MATLAB® software or related products does not constitute endorsement or sponsorship by The MathWorks of a particular pedagogical approach or particular use of the MATLAB® software.

Library of Congress Cataloging-in-Publication Data

Xia, Chang-liang.
Permanent magnet brushless DC motor drives and controls / Chang-liang Xia.
p. cm.
Includes bibliographical references and index.
ISBN 978-1-118-18833-0 (cloth)
1. Electric motors, Direct current. 2. Permanent magnet motors. 3. Electric motors, Brushless. I. Title.
TK2681.X53 2012
621.46–dc23

2012000619

Set in 10/12 pt Times by Thomson Digital, Noida, India

Contents

About the Author **xi**
Preface **xiii**
List of Nomenclature **xv**

1 Introduction **1**
1.1 History of BLDC Motors 1
1.2 Applications for BLDC Motors 3
1.2.1 Automotive BLDC Motor 4
1.2.2 BLDC Motor in Aerospace 5
1.2.3 BLDC Motor in Household Appliances 6
1.2.4 BLDC Motor in Office Automation 7
1.2.5 BLDC Motor in Other Industries 8
1.3 Advances in BLDC Motor Drives 8
1.3.1 Position-Sensorless Control 9
1.3.2 Torque-Ripple Reduction 10
1.3.3 Hardware Implementation 12
1.4 Future of BLDC Motor Drives 15
1.4.1 Impacts of Power Electronics and Microprocessors on BLDC Motor 15
1.4.2 Permanent Magnet and Design Considerations 17
1.4.3 New Types of BLDC Motor 18
1.4.4 Applications of Advanced Control Strategies 20
1.5 Other Kinds of PM Motors 20
Questions 21
References 21

2 Mathematical Model and Characteristics Analysis of the BLDC Motor **25**
2.1 Structure and Drive Modes 25
2.1.1 Basic Structure 25
2.1.2 General Design Method 28
2.1.3 Drive Modes 28
2.2 Mathematical Model 33

2.2.1 Differential Equations 33
2.2.2 Transfer Functions 40
2.2.3 State-Space Equations 45
2.3 Characteristics Analysis 47
2.3.1 Starting Characteristics 47
2.3.2 Steady-State Operation 48
2.3.3 Dynamic Characteristics 52
2.3.4 Load Matching 56
2.3.5 Commutation Transients 58
Questions 62
References 62

3 Simulation for BLDC Motor Drives 63
3.1 S-Function Simulation 63
3.2 Graphical Simulation 69
3.2.1 Simulation of Double Closed-Loop Speed-Control System 72
3.2.2 Advanced Conduction of Phase Current for BLDC Motor Control 76
Questions 82
References 82

4 Speed Control for BLDC Motor Drives 83
4.1 Introduction 83
4.1.1 PID Control Principle 83
4.1.2 Antiwindup Controller 86
4.1.3 Intelligent Controller 88
4.1.4 Representations of Uncertainty 89
4.2 Advanced Speed Control for BLDC Motor Drives 90
4.2.1 Fuzzy Control 90
4.2.2 Neural-Network Control 94
4.2.3 Genetic Algorithm Optimization Control 102
4.2.4 Sliding-Mode Variable Structure Control 107
4.2.5 Grey Control 113
4.2.6 Other Intelligent Control Strategies 117
4.3 Influences of Machine Parameters on Dynamic Response and Speed Range 119
4.3.1 Armature Resistance 119
4.3.2 Armature Inductance 120
4.3.3 Rotor Inertia 122
4.4 Practical Issues on Implementation 123
4.4.1 Type of Power Switches and Circuit Forms 123
4.4.2 Detection of Rotor Position 123
4.4.3 Braking Circuit and Protection Circuit 123
4.4.4 Antidisturbance Measures of Software and Hardware 124
Questions 124
References 124

5 Analysis and Reduction of Torque Ripple 127
5.1 Cogging Torque-Ripple-Minimization Techniques Analysis 127
5.1.1 Skewing Slots and Magnets 129
5.1.2 Embedding Magnetic Slot Wedges 130
5.1.3 Auxiliary Slots and Teeth 130
5.1.4 Fractional Number of Slots Per Pole 130
5.2 Torque-Ripple Reduction with Time-Sharing Commutation Strategy 131
5.2.1 Time-Sharing Commutation Strategy 131
5.2.2 Analysis of Time-Sharing Commutation Strategy 140
5.2.3 Optimal Time-Sharing Commutation 144
5.3 Torque-Ripple Reduction with Active Disturbance Rejection Control 146
5.3.1 Principles of ADRC 146
5.3.2 ADRC Controller Design 147
5.3.3 Experimental Results 150
5.4 Torque-Ripple Reduction with BP Neutral Network 152
5.4.1 BP Neural Network 152
5.4.2 Self-Tuning Regulator 155
5.4.3 Experimental Results 155
5.5 Motor Optimization and Torque-Ripple Minimization with Fuzzy Niche Genetic Algorithm 157
5.5.1 Platform-Width Calculation of Back-EMF Waveform 158
5.5.2 Fuzzy Niche Genetic Algorithm 161
5.5.3 Optimization Design of BLDC Motors 163
Questions 165
References 165

6 Sensorless Control for BLDC Motor Drives 167
6.1 Principle of Sensorless Position Detection 167
6.1.1 Back-EMF-Based Method 168
6.1.2 Flux-Linkage-Based Method 178
6.1.3 Inductance-Based Method 179
6.1.4 Intelligence-Based Method 180
6.2 Sensorless Control Strategy 181
6.2.1 Sensorless Control Based on Disturbance Observer 181
6.2.2 Sensorless Control Based on a Kalman Filter 187
6.2.3 Sensorless Control Based on Sliding-Mode Observer 191
6.2.4 Position-Sensorless Control Using Wavelet Neural Network (WNN) 196
6.3 Starting Process for Sensorless Control 200
6.3.1 Determination of Initial Rotor Position at Standstill 200
6.3.2 Starting Methods for Sensorless Control 201
Questions 206
References 206

7 Realization of BLDC Motor Drives 209
7.1 Main Circuit 209
7.2 Driving Circuit 212

7.2.1 MOSFET Driving Circuit 212
7.2.2 IGBT Driving Circuit 215
7.2.3 Intelligent Power Module (IPM) 215
7.3 Rotor-Position Sensor Circuit 216
7.4 Microprocessor Control Circuit 218
7.4.1 Introduction 218
7.4.2 MCU Control Circuit 220
7.4.3 DSP Control Circuit 223
7.5 Protecting Circuit 224
7.5.1 Overvoltage Protection 224
7.5.2 Overcurrent Protection 229
7.5.3 Logic Protection 229
7.5.4 Other Protection Circuits 230
7.6 Sensorless Control Circuits 232
7.6.1 Voltage Detection 232
7.6.2 Filtering and Phase Shifting 234
7.6.3 Current Detection 236
7.7 ASIC for BLDC Motor Drives 238
7.7.1 MC33033 238
7.7.2 TB6537P 240
7.8 Software Design 246
7.8.1 BLDC Motor Driving with Position Sensor 246
7.8.2 BLDC Motor Driving Without Position Sensor 247
7.8.3 Reliability 248
7.9 EMC Design 250
7.9.1 EMC Design of High-Voltage Part 250
7.9.2 EMC Design of Low-Voltage Part 251
Questions 253
References 253

8 Applications of BLDC Motor Drives 255
8.1 Elevator-Door Control System 255
8.1.1 Introduction 255
8.1.2 Hardware Design 259
8.1.3 Software Design 261
8.2 Elevator Traction Machine System 265
8.2.1 Introduction 265
8.2.2 Characteristics of a BLDC Motor Gearless Elevator Traction Machine 266
8.2.3 The Technical Requirements of the Elevator Traction Machine 267
8.2.4 Hardware Design 268
8.2.5 Software Design 269
8.3 Inverter Air Conditioner 270
8.3.1 Control Function of Indoor Controller 271
8.3.2 Control Function of Outdoor Controller 271

8.4 Electric Vehicles 272
8.4.1 Pure Electric Vehicles 272
8.4.2 Hybrid Electric Vehicles 273
8.5 Electric Bicycles 274
8.6 Others 275
8.6.1 The Applications in the Fan and Pump 275
8.6.2 The Application in the Washing Machine 276
8.6.3 The Application in Medical Instrumentation 277
Questions 277
References 277

Index **279**

About the Author



Chang-liang Xia was born in Tianjin, China, in 1968. He received his B.S. degree from Tianjin University, China, in 1990, and his M.S. and Ph.D. degrees from Zhejiang University, China, in 1993 and 1995 respectively, all in electrical engineering.

He is currently a Professor in the School of Electrical Engineering and Automation, Tianjin University. In 2008, he became "Yangtze Fund Scholar" Distinguished Professor and is currently supported by the National Science Fund for Distinguished Young Scholars.

His research interests include wind power generation system and intelligent control, motor control and power electronics, novel electric machine and intelligent control, and electrical energy saving control technology. He has published more than 180 papers in these areas. In addition, he has presided over more than 40 scientific research projects as the prime principal of the project. As the first inventor, he holds 13 authorized national invention patents of P. R. C.

In 2011, Prof. Xia was awarded the Second Prize of National Science and Technology Advancement (Rank First) for his work "Study and Application of High-efficiency Machine System Optimal Design under Complicated Constrains." He was also awarded the First Prize of Science and Technology Advancement from Tianjin Province (Rank First) twice, in 2005 and 2008, respectively. In addition, he has awarded the First Prize of Science and Technology Advancement from the National Ministry of Education (Rank First) in 2009.

Prof. Xia is a member of China Electrotechnical Society (CES). He is an editorial member of Transactions of China Electrotechnical Society, and the Advanced Technology of Electrical Engineering and Energy as well. He is also a deputy committee director in Electric Control System and Equipment Committee of CES, Electrical Automation Committee of Chinese Association of Automation, and Sub-committee on Electrical Machinery and Electrical Appliances of the China Machinery Industry Federation. In addition, he is the Vice Chairman of the Tianjin Society of Electrical Engineering.

Preface

In the past five years, the permanent magnet brushless motor market has grown much faster than the other small-motor markets. Thus, it is essential for electrical and electromechanical researchers to stay up-to-date on the latest developments in modern electrical motors and drives, including their control, simulation and hardware implementation.

I have been engaged in the design, modeling, control and application of BLDC motors for more than 15 years. In this field, I have published more than 50 papers in refereed journals and conferences. I have also been an instructor for 6 PhD students and 15 Master's students who have been researching on this subject. This book is an integration of many achievements from the corresponding projects supported by the National Natural Science Foundation of China, Ministry of Education of P. R. C, and the Tianjin Municipal Science and Technology Commission.

Thus, this book is an academic book based on the above research work of the BLDC motor drives over more than a decade. It includes many advances on the control of BLDC motor drives, such as intelligent control, sensorless control, torque ripple reduction, hardware implementation, and so on. Some materials of this book have been used in Tianjin University for the Masters course – "Electrical Motor Drives and Power Electronics" since 2002. In 2009, most of these materials were published in a Chinese book by Science Press, which was entitled *Brushless DC Motor Control Systems*. It has been used as a textbook for the graduate course – "Intelligent Control of Electrical Machines" in Tianjin University since 2009.

In this English edition, new materials have been added to cover the rapid advances of BDLC motor drives. Thus the book is rewritten and organized as follows:

Chapter 1 provides an introduction to the history, current situation and development prospects of BLDC motor drives and control.

Chapter 2 presents the basic principles and the mathematical models of BLDC motors. The related mechanical properties, regulation characteristics and commutation transient process are investigated.

Chapter 3 is devoted to the modeling and control of BLDC motors based on MATLAB. Practical examples are given and analyzed.

Chapter 4 focuses on the analysis of the most important issues related to the speed-control system of BLDC motors, such as the classic double-loop speed-control system, various speed control methods based on modern intelligent algorithms, the influences of the motor internal parameters on system performances, and so on.

One of the most important research directions of BLDC motors, that is the analysis and suppression of torque ripple, is investigated in Chapter 5. The causes and types of torque

ripple are analyzed. The cogging torque ripple and its minimization methods are studied. Further, torque ripple reduction approaches based on ADRC, BP neural networks and fuzzy genetic algorithms are presented, respectively.

Sensorless control, another research focus of BLDC motor control systems, is considered in Chapter 6. Based on modern control theory and intelligent algorithm, various types of position-detection methods of BLDC motor and a variety of control methods without position sensors are studied. In addition, different means for motor starting and ways to widen the speed range are proposed.

The software/hardware design approaches and related key technologies for the MCU- and DSP-based BLDC motor control systems are addressed in Chapter 7.

Chapter 8 describes the particular applications of the BLDC motors in elevator doors, elevator traction machines, inverter air conditioners, electric vehicles, electric bicycles, etc.

In addition, questions are supplied at the end of each chapter to facilitate class discussions and as home assignments. Supplementary PowerPoint slides and simulation materials for studying and teaching are provided too. Readers can download them from the book's website (www.wiley.com/go/xia/dcmotor).

In future, permanent-magnet BLDC motor will be used in more applications, especially in those that require a high level of accuracy and performance. Also, key technologies such as sensorless control and torque ripple reduction will be more mature. Thus, this book will allow people who are engaged in the control of BLDC motor drives to gain more knowledge about the principles, simulation and hardware implementation of BLDC motor drives and controls. I hope it will also be useful for other electrical engineers and students who are related to this topic. Some special issues, such as sensorless control, intelligent control, torque ripple reduction and hardware implementation will be valuable for the control of other motors. New progress in power electronics, control theory, and MCU will propel further development of the BLDC motor drives and controls.

This book is intended to be used as a reference book for related technicians in the field of design and control for BLDC motor drives, and a textbook for undergraduates and post-graduates who have learned the following courses: electrical machines, automatic control, motor control, MCU & DSP, and so on.

Over the years, the help and support from Associate Prof. Hong-wei Fang, Associate Prof. Wei Chen, Dr. Qiang Geng, Dr. Yan Yan, Dr. Peng Song and Dr. Ying-fa Wang of Tianjin University have contributed greatly to the success of this book.

Finally, I must also thank my wife Tingna Shi and my son Yuxuan Xia for their love and understanding, without which this task could not have been brought to fruition.

Chang-liang Xia

List of Nomenclature

A	real-time value of torque subsystem during its operation; the electrical load
B	magnetic flux density
B_δ	magnetic load
$B(\theta)$	radial flux density in air gap of PM rotor, which is in trapezoidal distribution along θ
B_m	maximum value of PM density distribution in air gap
B_v	viscous friction coefficient
b_t	stator tooth width
C_i	center vector of Gaussian function at the ith hidden layer unit
$\boldsymbol{C}_j$	center of the jth hidden layer unit that is the closest to the input sample
D_1	diameter of armature; stator outer diameter
D_1, D_2, ……, D_6	diodes
D_{i1}	stator inner diameter
d_l	wire diameter of the winding
E	phase back-EMF
E_0	gradient of the sloping part for back-EMF
e_A, e_B and e_C	phase back-EMF of phase A, phase B, and phase C, respectively
e_c	rate of change for motor speed error e
e_i	output error of the ith network
e_L	line back-EMF
e_max	largest positive error value in basic domain
e_sr	stable error
e_x	phase back-EMF, in which subscript x denote phase A, B and C
e_y	output of the fuzzy controller
$e_{\psi x}$	phase-induced EMF
f	frequency of the back-EMF; fitness of the mutation individuals
f_avg	average fitness for per generation population
$f_\mathrm{A}(\theta)$, $f_\mathrm{B}(\theta)$, $f_\mathrm{C}(\theta)$	waveform coefficient of back-EMF
f_i	fitness of ith individual
f_max	maximum population fitness
f'	larger fitness in two crossover individuals
f_st	starting commutation frequency

f_{xt}	resonator frequency
g	feedback gain coefficient
H_A, H_B, H_C	output signals of Hall position sensors
H	conjugate and transpose symbol
h_m	alnico thickness
I	current amplitude
$\boldsymbol{I}$	phase current matrix
i	steady phase current; detected armature current
i_x	phase current, in which subscript x denote phase A, B and C
i^*	reference current
J	moment of inertia
K	gain constant of the integrator; sliding gain
K_D	differential coefficient
K_I	integral coefficient
K_P	proportional gain
K_{e10}, K_{ec0}, K_{u0}	base values
K_1, K_2, K_3	fine-tuning parameters (all are non-negative)
K_T	torque coefficient
k_e	coefficient of line back-EMF, $k_e = 2p\psi_m = 4pNSB_m$
K_{e1}, K_{ec}	quantization factors
K_{e1}	error quantization factor
K_{ec}	error change quantization factor
K_u	scaling factor
L	inductance; length
L_0	nominal inductance
L_1	stator iron core length
L_A	self inductance of phase A
L_{af}	armature effective length
L_a	equivalent line inductance of winding, $L_a = 2(L - M)$
L'	equivalent phase inductance of winding, $L' = L - M$
M	population size; mutual inductance of phase winding
M_{AB}, M_{AC}, M_{BC}	phase mutual inductance
M_p	system maximum overshoot
$\boldsymbol{M}$	controllability matrix
N	number of winding turns
N_a	peripheral speed
N_r	sampling frequency
n	motor or rotor speed; numbers
n_N	rated speed
n^*	reference speed
P_0	no-load loss, including the core loss and mechanical friction loss
P_2	output power ($P_2 = T_L\Omega$)
P_C	copper loss
P_{Cu}	armature copper loss ($P_{Cu} = r_a I^2$)
P_T	loss of bridge power switches ($P_T = \Delta UI$)
P_{si}	selected probability of the ith individual

P_c	crossover probability
P_e	electromagnetic power ($P_e = k_e \Omega I$)
P_m	mutation probability
P_N	rated power
p	number of conductors in series per phase; number of pole pairs
q	number of slots per phase and per pole
$Q_1, Q_2, \ldots\ldots, Q_6$	instant of phase commutation
R_x	phase resistance, in which subscript x denote phase A, B and C
R_0	stator nominal resistor
$\boldsymbol{R}$	phase winding resistance matrix
r_a	line resistance of winding, $r_a = 2R$
s	switching function
S	product of rotor radius and the effective length of conductors
$S_1, S_2, \ldots\ldots, S_6$	conduction signals
$T_1, T_2, \ldots\ldots, T_6$	power switches
T_0	no-load torque corresponding to no-load loss ($T_0 = P_0/\Omega$)
T_c	cogging torque
T_D	differential time constant
T_e	electromagnetic torque
T_I	integral time constant
T_L	load torque
T_N	rated torque
T_r	rising time of the system response
T_{st}	starting torque
$T(k)$	the kth commutation instant
$\hat{T}_e$	tracking value of electromagnetic torque
T_{b0}	starting friction torque
t_e	time constant
t_s	adjusting time
$\boldsymbol{U}$	phase voltage matrix
U_d	DC bus voltage; DC voltage of the inverter bridge
U_N	neutral to ground voltage of the three phase windings
U_{out}	output voltage of the integrator
u_{sum}	sum of three-phase voltages
U_{th}	threshold
$\triangle U$	voltage drop of the power switches of the bridge inverter
u	number of existed hidden layer unit
u_{AG}, u_{BG}, u_{CG}	phase to ground voltages
u_{AB}, u_{BC}, u_{CA}	line voltages
u_x	phase voltage, in which subscript x denote phase A, B and C
$u(t_0)$	step function
V	electric voltage
V_{CE}	forward voltage of the power switch
V_D	forward voltage of the diode
W_m	energy of air gap electromagnetic filed
w_{ij}	weight between network layers

X_i	N-dimensional input
y_1	polar distance
y_i	network output; actual output of the ith neuron
Z	slots of the armature core
$Z(k)$	moment of the kth zero crossing point
α	momentum factor; learning rate; leading conducting angle
α_p	pole arc coefficient
α_{sk}	skewed slot coefficient
β_{01}, β_{02}	coefficients of observer
γ	learning rate
ξ	damping ratio of the second-order system
ε	unmodeled dynamics
η	efficiency of the motor
λ	coefficient of leakage permeance
λ	forgetting factor ($0 \leq \lambda \leq 1$)
θ	relative angular displacement between rotor and stator; rotor position angle
θ_B	air-gap flux density; platform width of air-gap flux density waveform
θ_E	electric angle at the decreasing moment of the line back-EMF
θ_e	platform width of overall back-EMF
θ^*	electric angle at the crossing point of the line back-EMF
σ_i	normalized constants of the ith hidden layer unit
δ	air gap; local gradient for weight correction of ith neuron
Λ_A	permeance of self-inductance of flux in phase A
Λ_{AB}	permeance of mutual inductance flux between phase A and phase B
ω	electrical angular speed of motor; electricity angle of motor
ω_k	weighting coefficient from the hidden layer to the output layer
ω_n	natural frequency of the second-order system
ω^*	rotate speed reference signal
$\hat{\omega}$	estimated signal
Ω	mechanical angular speed of the motor
Ω_r	reference mechanical angular speed
φ	output function
$\boldsymbol{\Psi}$	matrix of flux linkage
ψ_{f0}	nominal flux
ψ_m	magnetic flux linkage of each phase; maximum value of PM flux linkage of each winding, $\psi_m = 2NSB_m$
$\psi_{pm}(\theta)$	PM flux linkage
ψ_{rotor}	flux of rotor permanent magnet
ψ_{sum}	total flux of each phase
$\Delta_a(s)$	additive perturbation
$\Delta_i(s)$	input multiplicative perturbation
$\Delta_o(s)$	output multiplicative perturbation

1

Introduction

Two typical definitions about the brushless DC motor (BLDC motor, BLDCM) have been presented by scholars. Some of them considered that only the trapezoid-wave/square-wave brushless motors could be called BLDC motors, and sine-wave brushless motors should be called permanent magnet synchronous motors (PMSM) [1,2]. However, other scholars thought that all the motors above should be considered as BLDC motor [3]. ANSI/IEEE Standard 100-1984 has just defined "Brushless Rotary Machinery" [4]. Moreover, in NEMA Standard MG7-1987, a BLDC motor is defined as a type of self-synchronous rotary motor controlled by electronic commutation, where the rotor is a permanent magnet with rotor-position sensors [5], and the related commutation circuit could be either independent or integrated to the motor. So far, there has not been a unified standard about the classification or definition of the BLDC motor. By using the former definition, a BLDC motor is considered in this book as the trapezoid/square wave motor with the starting characteristics of series excitation DC motors and the speed-regulation characteristics of shunt excitation DC motors. It has advantages like simple structure, high efficiency and large torque, etc. Hence, it is widely used in national defense, aerospace, robotics, industrial process control, precision machine tools, automotive electronics, household appliances and office automation. The development history of BLDC motor, its application fields, research status and the development tendency of related technology are presented in this chapter.

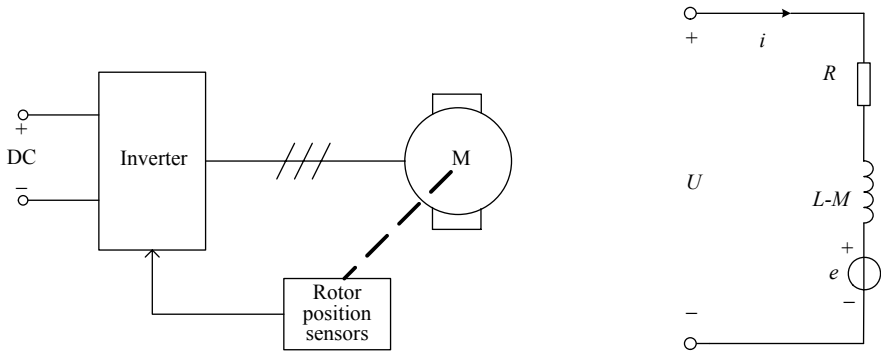
1.1 History of BLDC Motors

In the modern society, electricity is the most popular secondary energy source. The application of motors has spread to all kinds of fields in national economy and our daily life as the main mechanic-electronic energy-conversion device for more than a century. In order to adapt to different practical applications, various types of motors, from several milliwatts to millions of kilowatts, including synchronous motors, induction motors, DC motors, switched reluctance motors and so on, emerge as the times require. Although the synchronous motor has advantages of large torque, hard mechanical characteristic, high precision and efficiency, it has difficulties in speed regulation, which limits the range of its application. An induction motor has the advantages of simple structure, easy fabrication, reliable work and low price, but it is uneconomical to regulate the speed smoothly over a wide range and it is not easy to start up.

Permanent Magnet Brushless DC Motor Drives and Controls, First Edition. Chang-liang Xia.
© 2012 Science Press. Published 2012 by John Wiley & Sons Singapore Pte. Ltd.

Also, it is necessary to absorb the lagging field current from the power system resulting in the decrease of grid power factor. Moreover, its mechanical characteristic is soft and the power factor is small. Without windings or a permanent magnet on its rotor, a switched reluctance motor has a simple structure and low price. It can produce high torque at low speed. However, the noise and torque ripples limit its popularization and applications. DC motors are still widely used in electric power drive systems that have demands for start up and speed regulation, such as electric traction, rolling mill and hoisting equipment, because this type of motors have high efficiency and good speed-regulation performance. Nowadays, DC motors of small capacity are still widely used in automation and control systems. But in traditional DC motors, mechanical commutation is implemented by using brushes, which will result in problems like mechanical friction that would shorten the lifetime, and create noise, electric sparks, and radio interference, etc. In this condition, considering the disadvantages of high production cost and inconvenient maintenance [6–10], the range of applications in particular areas has been limited. Therefore, applications of small and medium size are in urgent need of novel high-performance motors.

The BLDC motor is developed on the basis of brushed DC motors. The modern machine theory was established when Faraday discovered the electromagnetism induction phenomenon in 1831. The first DC motor was born in the 1840s. Confined by the development of power electronic devices and permanent magnet materials, BLDC motor was designed successfully until more than one century later. In 1915, an American, Langmuir, invented the mercury rectifier to control grid electrode and made the DC/AC converter. Contraposing the disadvantages of traditional motors, in the 1930s, some scholars started developing brushless motors in which electronic commutation was implemented, which made preparations for the BLDC motor. However, at that time, power electronic devices were still in the early stage of development, scholars could not find an appropriate commutation device. This type of motor, with less reliable work and low efficiency, was only used in the lab instead of being popularized. In 1955, Harrison and Rye made the first patent claim for a thyristor commutator circuit to take the place of mechanical commutation equipment. This is exactly the rudiment of the BLDC motor [11]. The principles of operation are as follows, when the rotor rotates, periodic electromotive force (EMF) is induced in the signal winding, which leads to the conduction of related thyristors. Hence, power windings feed by turns to achieve commutation. However, the problems are, first, when the rotor stops rotating, induced EMF cannot be produced in the signal windings and the thyristor is not biased, so the power winding cannot feed the current and this type of brushless motor has no starting torque. Furthermore, power consumption is large because the gradient of the electric potential's sloping part is small. To overcome these problems, researchers introduced the commutators with centrifugal plant or put an accessory steel magnet to ensure the motor started reliably. But the former solution is more complex, while the latter needs an additional starting pulse. After that, by numerous experiments and practices, the electronic commutation brushless motor was developed with the help of Hall elements in 1962, which inaugurated a new era in productionization of BLDC motors. In the 1970s, a magnet sensing diode, whose sensitivity is almost thousands of times greater than that of the Hall element, was used successfully for the control of BLDC motor. Later, as the electrical and electronics industry was developing, a large number of high-performance power semiconductors and permanent magnet materials like samarium cobalt and NdFeB emerged, which established a solid ground for widespread use of BLDC motors.



(a) Topology (b) Equivalent circuit

Figure 1.1 Topology and equivalent circuit of BLDC motor.

In 1978, the Indramat branch of Mannesmann Corporation of the Federal Republic of Germany officially launched the MAC brushless DC motor and its drive system on Trade Shows in Hanover, which indicates that the BLDC motor had entered into the practical stage. Since then, worldwide further research has proceeded. Trapezoid-wave/square-wave and sine-wave BLDC motors were developed successively. The sine-wave brushless DC motor is the so-called permanent magnet synchronous motor. Generally, it has the same topology shown in Figure 1.1(a) as that of trapezoid-wave/square-wave brushless DC motors. It can be considered as a PMSM where rotor-position detection is used to control the commutation in order to ensure self-synchronization operation without starting windings. Meantime, these two kinds of motors have the same equivalent circuit as shown Figure 1.1(b), in which *L–M* is the equivalent inductance of each phase. With the development of permanent magnet materials, microelectronics, power electronics, detection techniques, automation and control technology, especially the power-switched devices like insulated gate bipolar transistor (IGBT), integrated gate-commutated thyristor (IGCT) and so on, the BLDC motors in which electronic commutation is used are growing towards the intelligent, high-frequency and integrated directions.

In the late 1990s, computer techniques and control theories developed rapidly. Microprocessors such as microcontroller units (MCU), digital signal processors (DSP), field programmable gate arrays (FPGA), complex programmable logic devices (CPLD) made unprecedented development, while a qualitative leap was taken in instruction speed and storage space, which further promoted the evolution of BLDC motor. Moreover, a series of control strategies and methods, such as sliding-mode variable structure control, neural-network control, fuzzy control, active disturbance rejection control (ADRC), adaptive control and so on [6,12–20], are constantly used in BLDC motor drive systems. These methods can improve the performance of BLDC motor drive systems on torque-ripple minimization, dynamic and steady-state speed response and system antidisturbance ability to some extent, as well as enlarge the application range and enrich the control theory.

1.2 Applications for BLDC Motors

In recent years, small and medium size motor industries are developing rapidly. About these industries, incomplete statistics of proceeds and volume of sales in China during 2004–2008

Table 1.1 Sales of small and medium electric motor during 2004–2008

Year	2004	2005	2006	2007	2008
Volume of sales (10 k kW)	7847	9702	10950	13009.5	13336
Product revenue (10 k RMB)	1 560 933	2 182 281	2 686 147	3 299 004	3 675 679

are shown in Table 1.1 [21]. In particular, the BLDC motor has achieved a brilliant expansion in automotive, aerospace and household equipment industries, because it has the advantages of high efficiency, long lifetime, low noise and good speed–torque characteristics. Some representative application situations are described as follows.

1.2.1 Automotive BLDC Motor

Automobiles, as a convenient and efficient vehicle, are very close to our daily life. In developed countries, it has a high automobile popularization rate. In China, the automobile industry had been conducted as a pillar industry in industrial policies that was established during the Ninth Five-Year Plan period. In 2007, domestic production was 8 million. There are usually dozens or even hundreds of motors inside an automobile. As the automobile is developing towards energy-saving and environmentally friendly, high-efficiency permanent magnet motors including BLDC motors have a bright future. Some frequently-used performance indexes of motors that are used to drive the electric vehicles are shown in Table 1.2. It can be seen from Table 1.2 that the BLDC motor, which is included in permanent magnet motors, has a good technical superiority [22].

Table 1.2 Comparison between motors used in electric vehicles

Motor type / Performance index	DC motor	Induction motor	PM motor	Switched reluctance motor
Power density	Low	Intermediate	High	Very high
Peak efficiency (%)	<90	90–95	95–97	<90
Load efficiency (%)	80–87	90–92	85–97	78–86
Controllability	Simple	Complex	Hard for field-weakening	Complex
Reliability	Normal	Good	Excellent	Good
Heat dissipation	Bad	Bad	Good	Good
Size & weight	Big, Heavy	Normal, Normal	Small, Light	Small, Light
High-speed performance	Poor	Excellent	Good	Excellent
Construction	Slightly worse	Better	Slightly better	Excellent
Cost of motor ($/kW)	10	8–10	10–15	6–10
Cost of controller	Low	High	High	Normal
Combination property	Slightly worse	Normal	Excellent	Better

Besides the hardcore of automotive drives, motors can be used on the drives of air conditioners, wiper blades, air bags, electric doors and power seats. Automotive air conditioning is one of the most important accessory products on an automobile, and its performance will change the passengers' comfort directly. Also, it will influence their impression and evaluation about the entire automobile in an indirect way. The motor drive used in automotive air conditioners is often operating with constant load, so it has lower requirements regarding the dynamic response of the system. A motor and its control system have a direct relationship with the performance of automotive air conditioners. Certain key aspects of BLDC motor drives used in automotive air conditioners, has been studied in [23,24]. Similar to the techniques of household air conditioners, air-conditioner compressor driven by a BLDC motor is developing towards more energy-efficient and comfortable directions. As the techniques of power electronics, automation control and computer science are developing, BLDC motor speed-regulation techniques become mature gradually with higher quality and lower price. Therefore, BLDC motors will get a wider range of application, and be a mainstream in speed-regulation techniques.

It is necessary to note that the usage and installation of position sensors would increase the cost of motor drives and affect the reliability and lifetime of the control system. Moreover, automobiles usually have strict restrictions for the volume of the motor. However, sensors are usually installed inside the motors, which will increase the volume. Consequently, the sensorless control strategy will be an important development direction of automotive BLDC motor drive systems.

1.2.2 BLDC Motor in Aerospace

Air-driven and hydraulic-type transmission devices are being replaced by motor-drive equipments, which is a tendency in the aerospace industry. Due to its particular application, in aerospace industry, motors are required to be small size with simple structure. The special structure and position-sensorless control method of BLDC motors make it possible for them to be widely used in aerospace industry. In this condition, the BLDC motor is often operating with variable load, which requests good high-speed regulation and dynamic response, for instance, the application of gyroscopes and robotic arms. It is controlled by using semiclosed or closed-loop speed feedback, where advanced control algorithms are usually implemented in the corresponding systems.

In aerospace, some BLDC motors, such as motors used in high-speed centrifugal pumps and high-speed cameras, could reach the speed of tens of thousands of rev/min or more. Hence, it is necessary to consider the requirements and solutions of mechanical and electrical performance when it operates at high speed. For instance, the bearing problem of a high-velocity rotating motor can be solved by implementing an active magnetic bearing or bearingless design. Moreover, there are significant differences in voltage levels and frequency between universal power and those in aerospace. Therefore, special requirements for rectifier circuits and frequency-conversion drive circuits should be taken into account in BLDC motor control systems, where soft-switching technology can be introduced to minimize the noise and loss during high-frequency switching to improve the properties of the system. Meanwhile, to meet the needs of high reliability, some special means, such as trapping techniques, redundancy techniques and so on, are adopted to prevent software sinking into dead circulation or getting other problems.

1.2.3 BLDC Motor in Household Appliances

Recently, motor drives used in household appliances have increased about 30 per cent every year worldwide. These modern electric appliances are developing towards energy-saving, low-noise, intelligent and high-reliability directions. With the improvement of the living standard of the people and the increasing attention on energy saving and emission reduction from the government, BLDC motors are chosen as the drive motor of household appliances increasingly.

In China, durable consumer goods, air conditioning and refrigerators, whose production has ranked top in recent years throughout the world, have been popularized in cities. Both electric appliances have compressor motors that are usually induction motors. Usually, they have low efficiency and a small power factor and these disadvantages may be overcome by using frequency-conversion technology. Compared with induction motors, BLDC motors have the following advantages: (1) high efficiency; (2) the speed is not limited by power frequency, hence the rated speed can be designed higher, which is beneficial to increasing the capacity and decreasing the size; (3) the power factor is higher, by which the capacity required of the inverter is reduced.

So, if the BLDC motor is implemented in the compressor, it will improve the properties of the compressor significantly and meet the requirements of energy saving and environment protection in modern society. Nowadays, 90 per cent of the induction motors used to drive the compressors have been replaced by BLDC motors in Japan.

Because the compressor motors are sealed, whether in the condition of high or low temperature, position sensors of BLDC motors will influence the reliability of the compressors. The position sensor takes the space inside the compressor, and the signal wires may have an unfavorable influence. Therefore, position-sensorless control is preferable for BLDC motors of the compressor. To reduce the cost and improve the stability of the control system for frequency air conditioning compressors, current commutation signals are acquired by using the back-EMF-based method with a DSP and module IR2316. It achieves the position-sensorless control of BLDC motor for frequency compressor systems, with a motor efficiency of 86 per cent [25]. In addition, position-sensorless control is achieved by implementing the brushless linear DC motor to drive the compressor directly [26]. The transmission mechanism of the eccentric wheel is removed in this system, which is convenient for the design and installation of the compressor. This system, which is suitable for long-stroke linear motion system, is beneficial to reducing the size and the transmission loss, and improving the efficiency.

BLDC motors are also used as the spindle motor drive in VCD, DVD and CD players. Disk-type coreless BLDC motors, which are cheap and usually used in this type of application, have been produced on a large scale. According to different requirements for torque, disk-type BLDC motors as shown in Figure 1.2, can be classified as single-stator type and double-stator type, which is suitable for high-torque drive applications. A product of a DVD/CD player driven by BLDC motor is shown in Figure 1.3.

Moreover, the structure of multipole and external rotors, which is a mature technology, is used in BLDC motors of electric bicycles. BLDC motors used in electric bicycles based on nanotechnology have been designed by a British Company, OLEXI-NANO. Due to its features of high efficiency, low temperature rise, high comfort level and stability, and so on, the comprehensive properties of the electric bicycles are improved. In some areas of household appliances such as vacuum cleaners, agitators, hair dryers, cameras, electric fans and so on, BLDC motors have gradually taken the place of current popular motors that include DC

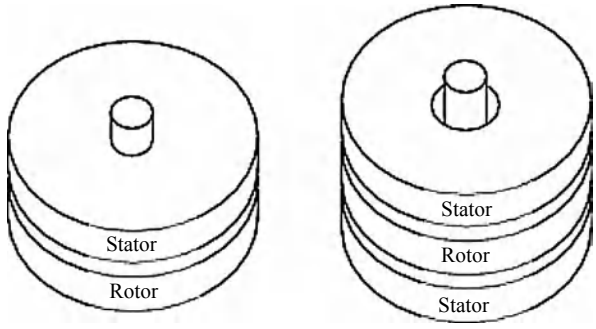


Figure 1.2 Structure of disk-type BLDC motor.

motors, single-phase induction motors and variable-voltage variable-frequency (VVVF) drive induction motors. BLDC motors cannot only overcome some disadvantages of traditional household motors but also reduce the energy loss, which brings a more comfortable lifestyle and properly realizes sustainable energy utilization for people.

1.2.4 BLDC Motor in Office Automation

Most motors used in office automation and computer peripheral equipments are BLDC motors, which is a combination of advanced technology and modern microelectronics. The adoption of the high-performance BLDC motor servosystem improves the quality and increases the value of the products. For example, the BLDC motor used on the main shaft of the hard-disk drives can rotate at high speed with the magnetic disk. The magnetic head, which achieves the executive function for the data on the disk, takes a suspension motion over the surface of the disk about 0.1–0.3 μm to increase the read-write speed. BLDC motors can also be the spindle motor for optical disc and floppy disc drives, and in that case, the BLDC motor has



Figure 1.3 Application of DVD/CD players.

the advantages of low noise, low temperature and high temperature tolerance and it can withstand shock and vibration to a certain extent, which improves the stability of the system. Cooling fans driving motors for computers are usually required to have characteristics such as low noise, compact construction, long lifetime and high speed. Hence, the BLDC motor used in this area adopts an external rotor on which the magnetic steel pieces are usually made of bonded NdFeB. In the area of digital cameras, the BLDC motor has also been widely used. For instance, the Japanese companies Toshiba and Sanyo have both produced the products of BLDC motor drive cameras with the corresponding integrated drive chips TA8479F and LB8632V respectively. With a long history, laser printers driven by BLDC motors are a promising technology and have strong market competitiveness. Its speed can be controlled accurately from thousands of rev/min to tens of thousands of rev/min [27]. Moreover, BLDC motors have good applications in duplicators, facsimiles, recorders, LD video disk players, paper shredders and other office equipments.

1.2.5 BLDC Motor in Other Industries

A BLDC motor control system is an electromechanical integration product that combines the advantages of brushed DC motor and AC asynchronous motor control systems. As the performances of power electronic device and rare-earth permanent magnetic materials are improving and the price is reducing, BLDC motor drive systems, which have increasing applications in industry, has been a main developing direction in the industrial motor drives. Considering performance and cost of the product, famous international motor manufacturers have carried out much research and development. Nowadays, BLDC motors occupy a great portion in civil and military robots and manipulators, where there is a trend that they will take the place of stepping motors and traditional DC servomotors driving robots. High-power BLDC motors also have a good application prospect in some certain occasions, such as low speed, adverse circumstances or where good speed regulation performance is required. For example, in the applications of gearless elevator traction motor drives, pumped storage, transmission of rolling mills, they have the advantages of fast dynamic speed response, small tracking error and static difference ratio, and wide range of speed regulation. Besides the above, practical applications of BLDC motors consist of medical equipments, textile machinery, printing machinery, digital control machine tools, etc.

1.3 Advances in BLDC Motor Drives

Currently, general BLDC motor control is relatively mature and China has developed a specification GJB1863 for it. Research of BLDC motors in developed countries is roughly the same as that in China, whereas the United State and Japan have more advanced manufacturing and control technology. In particular, Japan is more prominent in civil aspects, while the United States is more advanced in the military arena. The current researches mainly focus in the following areas: (1) Develop position-sensorless control technology to improve system reliability and further reduce the motor size and weight. (2) Investigate methods of torque-ripple reduction for BLDC motors, from motor design and control aspects, to improve the servoprecision and expand the scope of application. (3) Design reliable, compact and versatile integrated BLDC motor controllers.

1.3.1 Position-Sensorless Control

The rotor position is directly detected by a position sensor in the traditional method of BLDC motor-position detection, which is called the direct position-detection method. Voltage or current signals of the motor, which are easily acquired, are processed with certain algorithms to get the rotor position signals in the position-sensorless control method, which is also called the indirect rotor-position-detection method. This concept started from the position estimation method by using capacitor shifting, which was proposed by Mieslinger in 1966 [28]. The commonly used indirect rotor-position-detection methods are shown in Figure 1.4.

The back-EMF-based method has a simple principle that is convenient to achieve and is widely used. By using the computer, position-sensorless control was processed in 1985 by Iizuka *et al*. [29] who made comprehensive analysis of software and hardware design for the method, which improved the BLDC motor control to a new level.

During the end of the 1980s to the early 1990s, indirect detection methods of rotor position developed in a diversified trend. Lin *et al*. [30] presented a rotor-position-detection method by using phase current in 1989, considering the principle that if the phase current and the stator flux have the same phase, the rotor position of BLDC motor can be accurately reflected by the change of phase current. In 1990, scholar Ogasawara [31] proposed the inverter switching state estimation method, an ingenious method, which is shown in Figure 1.6 as the freewheeling diode-based method. The basic principle of this method is still the back-EMF-based method, but the EMF is considered from the perspective of current, which is a novel and clever design. Matsui *et al*. [32] presented a detection method for rotor position based on transient current and voltage equations. People began to understand the nature of BLDC motor rotor position variation since the methods were presented in [31,32]. The stator flux-based estimation detection method was proposed in 1994 by Ertugrul *et al*. [33]. In this method, the flux of each stator winding is calculated by the phase voltage and the line current, in order to get the rotor position signal from the flux [33]. Although the computation complexity is higher, the error of this method is less and the range of speed regulation is wider. This method, which is an ideal testing method and has been applied to production, is not only suitable for BLDC motors, but also for PMSM. In the same period, the rotor-position-detection method using a state estimator and a Kalman filter was proposed [34]. Since this method requires a lot of calculations and was limited by the actual conditions at that time, it did not arouse enough attention. In past decades,

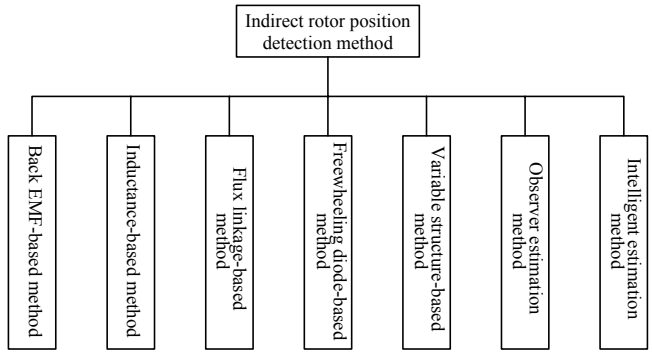


Figure 1.4 Indirect rotor-position-detection methods.

with the improvement of performance of MCU and the upgrading of DSP products, this method has gained rapid development and been applied to actual control systems of BLDC motors [35–37].

The terminal-voltage-based method, an indirect rotor-position-detection method, is actually a changed form of the EMF-based method. It only detects the terminal voltage of each phase, so that the rotor position is acquired through the change of the terminal voltage, whereas the change is actually the reflection for the variation of back-EMF in windings along with the rotor position. However, the terminal-voltage-based method further simplifies the interface circuit, which makes the back-EMF-based method more practical [9,18].

The variable-structure-based method refers to the position-sensorless control that is achieved by making appropriate changes on rotor or stator structure. For instance, adding an auxiliary rotor winding in the surface-mounted-type rotor BLDC motor to get rotor position signals [38], or setting nonmagnetic materials on the rotor surface in order to get the rotor position from detecting the disconnected phase voltage variation caused by eddy-current reaction [39]. In addition, Matsuse *et al*. obtained the rotor position by designing the closed stator slot type motor [40].

As the development of intelligent control is promoting motor control, using fuzzy control, neural networks and other intelligent algorithms to establish the relationship between voltage signals, current signals and rotor position signals is a new approach to position-sensorless detection, which has higher control precision [41–43]. However, compared with traditional position-sensorless control methods, it has more complex algorithms and takes more time in computation, hence the cost is increased.

It is difficult to achieve a direct start for a BLDC motor using position-sensorless control, so the starting mode is always a research focus. The three-step starting technique by using the back-EMF-based method has been more mature. From the start to the stable operation of the motor, this method can be divided into the following three steps: position fixing for rotor, acceleration and switching. Other starting techniques under the position-sensorless control, such as the rotor prelocation method, increasing-frequency and increasing-voltage synchronous methods and the short time measuring pulse rotor orientation starting method, have certain applications.

1.3.2 Torque-Ripple Reduction

Torque-ripple reduction is always an important issue in BLDC motor control systems. As in other motors, some phenomena like the cogging effect and the eddy-current effect cannot be completely avoided in BLDC motor design. Therefore, cogging torque, which should be considered in torque-ripple reduction of BLDC motors, can be restrained with good results by using skewed and fractional slots.

In addition, electronic commutation is usually implemented in BLDC motors, and the presence of motor winding inductance makes it difficult for the phase current to achieve the ideal square-wave current, which may also bring commutation torque ripple to the system. Therefore, to restrain the commutation torque ripple is also an important research, on which many scholars have made a lot of efforts.

The principle of the BLDC motor and the necessity of existence of torque ripple are discussed in [44]. In [45,46], phase voltage and current are transformed with Fourier-series decomposition, and the torque model with fundamental and higher harmonics is derived. Moreover, the purpose

of eliminating torque harmonics is achieved by adjusting the conducting phase of the windings to compensate appropriately. Although it has a large amount of computation, it has higher control precision. Considering the fact that the total current is decreasing during commutation, the overlapping commutation method is presented in [47] by preconducting the awaiting commutation winding, which makes all three phases conducted at the beginning of commutation to ensure that the amplitude of current is a constant value. The relationship among the amplitude of commutation torque ripples, commutation intervals and speed is discussed in [48]. By using the optimum weight method of stator current harmonics, torque ripples caused by electromagnetic torque and cogging torque are effectively reduced with a current regulator and other equipment in [49]. In 1997, Lim *et al*. [50] presented a method to eliminate the torque ripples by regulating the turn-off angle of a voltage source inverter, which is not only suitable for the constant-voltage constant-frequency (CVCF) systems, but also for the VVVF system. From the perspective of commutation instant, the relationships among commutation instants, back-EMF and torque ripple, and that between commutation time and motor speed are discussed in [51]. In addition, torque ripples are effectively restrained by using a direct torque method to control the BLDC motor in [52]. Another torque-ripple reduction is achieved by dynamically changing the input voltage in [53].

Chinese scholars have also done lots of research on torque-ripple reduction of BLDC motors. Torque ripple caused by armature reaction is analyzed in [54]. The corresponding methods to restrain the effects are proposed from aspects of magnetic circuit design and switching phase control. In [55], by using back-EMF, phase current and motor speed as the input signals and torque as the output to construct a torque estimator, the indirect measurement method with a torque estimator is presented. The method achieves the online estimation of torque and makes appropriate compensation to different motor operating conditions. Although it requires complex computation, it can control the torque online and restrain the torque ripple under most operating conditions without measuring the instantaneous torque. The BLDC motor commutation torque-ripple reduction method based on an artificial neural network is presented in [16]. In this method, two three-layer forward-feedback artificial neural networks are trained online and offline, respectively. The error feedback algorithm is used to modify the connected weight value between each cell. One network is used for online commutation state estimation, while the other is used for regulating the voltage instantaneously during commutation, which forms a voltage self-tuning regulator. This regulator, which makes the current decreasing rate approximately equal to the rate of rising during commutation by means of regulating the terminal voltage, maintains the amplitude of the current at a constant value and achieves the reduction of torque ripple. Note that accurate knowledge of parameters of the system is not required in this method, so it shows good ability to adapt to environmental changes. In [56], the motor is equivalent to a serial object that is constructed by two nonlinear systems: a torque subsystem and a speed subsystem. The active disturbance rejection control technique is used to design two first-order active disturbance rejection controllers to achieve the inner and outer closed-loop control for the motor. By implementing the extended state observers (ESO) to observe the torque, torque-ripple reduction is achieved with the help of tracking differentiator (TD) and nonlinear states error feedback (NLSEF) [57]. The above-mentioned technologies have contributed to the reduction of BLDC motor torque ripple, and hence improved the performance of the control system.

Overall, the reasons for BLDC motor torque ripple are complex and corresponding control methods can be used for different situations where each method has its own advantages

and applications. Meanwhile, the existing torque-ripple reduction methods, which do not fundamentally eliminate the torque ripple, are presented as an improvement or compensation for motor structure and control schemes. Thus, torque-ripple reduction remains for further study.

1.3.3 Hardware Implementation

Similar to electrical components, BLDC motor controllers have experienced the development process from discrete element control to digital programmable integrated circuit. A commutation logical signal circuit composed of gate circuits is shown in Figure 1.5.

In general, a BLDC motor designed with discrete components has complex structure and large size, and its reliability and versatility are poor, which makes it unsuitable for mass production. Therefore, application-specific integrated circuit (ASIC) controllers, FPGA, MCU and DSP controllers are widely used to control the BLDC motor.

Currently, many semiconductor manufactures from developed countries, can provide their own ASIC for motor control. For example, American companies ON Semiconductor and Motorola developed the MC33035 and MC33039 BLDC motor control chips, and also Micro Linear Corporation designed the position-sensorless control chips ML4425/4428.

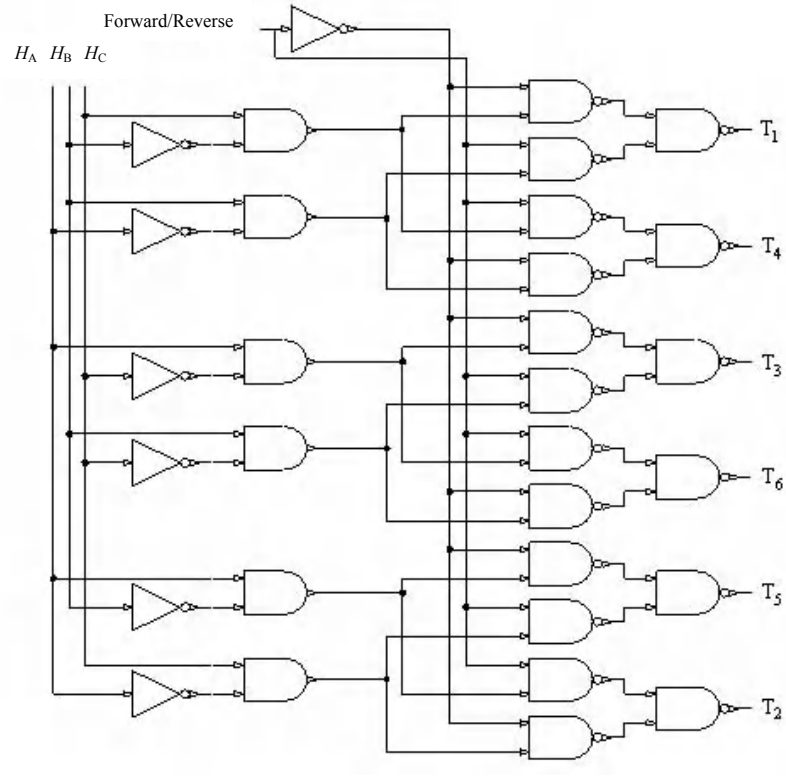


Figure 1.5 Commutation logical signal circuit.

ASIC controllers have the advantages of simple structure, high cost–performance ratio and fewer peripheral devices compared with discrete components. However, there are some limitations and the expandability is not good, so it is difficult to upgrade or change its functions. Consequently, considering the controllers' design of hardware and software and other function in the future, FPGA, MCU and DSP, which have the advantages of perfect functions and easy to control, could be implemented to control BLDC motor, with the condition that the corresponding cost may be higher than that of ASIC controllers. FPGA can be programmed with VHDL, Verilog or the C language, with the advantages of flexibility, static reprogrammable and online dynamic reconstruction, which means the corresponding hardware can be easily modified with the interface functions defined according to the users' requirements. MCU and DSP both have ample peripheral interfaces. The difference is that MCU is commonly used for simple motor control systems while the DSP is used for intelligent control systems due to its powerful computing and data processing capabilities. Typical MCU or DSP control BLDC motor system is shown in Figure 1.6.

Economic and practical BLDC motor controllers can be achieved by using various types of MCU. At the beginning, the most widely used MCUs were MCS-51/96 series products, which have now been extended to PIC16F877A, MSP430F149, MC68HC908MR16, LPC2101 and other products from different companies. Moreover, many companies have introduced specific MCUs for BLDC motor control systems. Chip ST72141 from ST Company is a specific MCU for BLDC motor, which consists of their back-EMF detection patented technology. C50X series chips from Siemens are also made for BLDC motor control systems. For example, inside the C504 chips, there are hardware commutation circuits. When the three-phase rotor-position detector detects and transmits the position signal to the chip, the commutation signals in the main circuit can be controlled by the chip, which does not need to use software for processing. As a result, it can greatly reduce the difficulty of system development and improve the reliability of commutation. Also, the chip C508 can drive two BLDC motors at the same time. Although the price of MCU is relatively lower, its processing capacity is finite, especially when large volumes of data need to be dealt with for the requirements of real time and high precision, the MCU often cannot meet the requirements of computing speed. In some specific

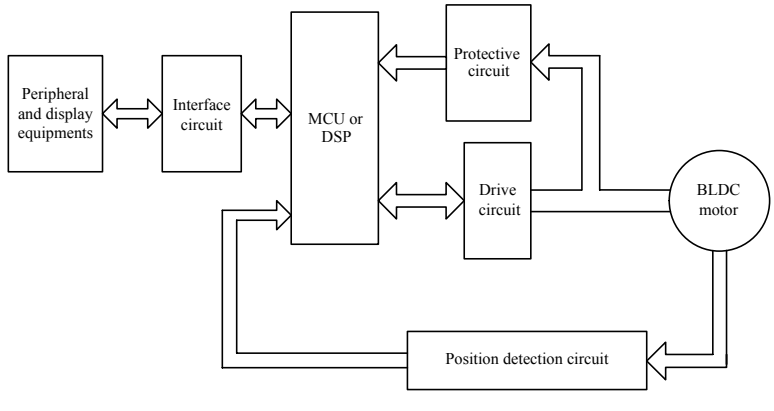


Figure 1.6 Typical BLDC motor control system.

applications, requiring cooperation with multiple motors, using an MCU and its interface circuits makes the hardware circuit more complex, where it is difficult to achieve digital control for motor speed and current. In this condition, generally, DSP, FPGA and "DSP + FPGA" schemes can be implemented to design the BLDC motor control system. A BLDC motor control system consisting of DSP, FPGA, signal conditioning comparison circuit and other subsystems is presented in [58], as shown in Figure 1.7. In the signal-conditioning comparison subsystem, the signals from voltage and current sensors are conditioned and transmitted to the DSP subsystem for A/D sampling. The signals from each phase are compared with the bound of the chopping current from D/A part of the DSP subsystem. The comparison results, which are a series of high-level and low-level signals, are transmitted to the FPGA subsystem, in which the speed signals are compounded and transmitted to DSP. And then, according to the command signal, position signal and chopping signal from the DSP, control signals of power switches are compounded logically and generated. Commonly used power switches include MOSFETs, IGBTs, intelligent power modules (IPM) and so on. In the DSP subsystem, speed command, boot command and current/voltage feedback signals are received. The state of the motor and the bound of the chopping signal are also decided. Also, it has the functions of data, alarm and state display and feedback output speed signals, etc.

At present, the DSP products have developed to the sixth generation, with abundant models and specifications and low price. As the improved Harvard structure and pipeline mechanism are introduced in DSP devices, its computing speed is much faster than that of MCUs, and especially, due to highly specialized instruction set provided by DSP, the computing speed of digital filters is improved, which brings unique advantages on implementation of controller rules, vector control and matrix transformation aspects. Besides, there are many such specific DSP chips that use the CPU as the core and integrate different peripheral components to achieve complex control functions. It reduces the requirements of peripheral components and the cost of the system, which improves the reliability and is propitious for confidentiality of proprietary technologies. For example, TMS320LF2407 from the American TI Company is a type of dedicated motor control DSP chip with low price and powerful functions. The motor control scheme is greatly simplified by 2 EVENT managers, 6 CAPTURE units, 14 PWM output signals and teeming I/O interfaces. TMS320F2812 further improves the accuracy of computation to 32-bit and develops the processing capacity of the system with the frequency

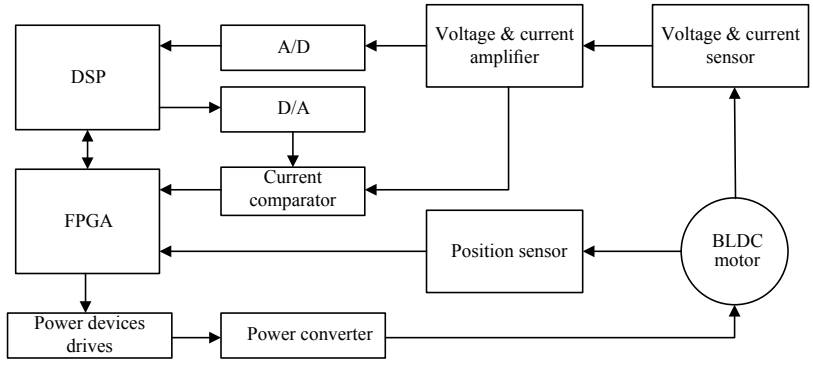


Figure 1.7 BLDC motor control scheme based on DSP and FPGA.

up to 150 MIPS. A 128 kB flash memory, 4 kB boot ROM, math tables and 2 kB OTP ROM are integrated to the DSP of this series product, which greatly improves the flexibility of the applications. The codes and instructions are completely compatible with F240x series DSPs, which ensures the sustainability for the project and product design. Many intelligent control algorithms are achieved with the powerful computation capability of DSP [14–19,59,60], which improves the accuracy and stability of motor control, thereby full digitalization intelligent control of BLDC motor becomes the research focus in recent years. Although the existing advanced control algorithms of BLDC motor based on the DSP are not mature enough, they will be widely used as the computing speed and memory capacity of DSP are improving.

1.4 Future of BLDC Motor Drives

BLCDM is mainly composed of motor body, power drive circuit and position sensor, and it involves motor technology, power electronics, detection and sensor technology, control theory and technology. Hence, the emergence of new electronic technology, new power devices and control methods, will further improve the development and application of BLDC motors.

1.4.1 Impacts of Power Electronics and Microprocessors on BLDC Motor

(1) Miniaturization and integration
The development of microelectromechanical system (MEMS) enables motor control system development towards the direction of a highly integrated control and sensor circuit. For example, current, voltage, and speed signals feed back after being fused, which makes BLDC motor control systems simpler and more reliable. Moreover, as the BLDC motor rotors are made of rare-earth permanent magnet materials and there is no heat source at the rotor side, the internal temperature rise is smaller than that of traditional DC motor, which enables the inverter control circuit to be installed into the motor. Take the 100-kW-type BLDC motor from the French company Alsthom as an example, its total weight is only 28 kg including the inverter, which is installed at the stator side. So the inverter and motor are combined, which makes the BLDC motor and power electronics more closely and improves the added value of products, and the whole control system hereby develops towards the direction of miniaturization and integration. It is worth noting that, currently, due to the limitation of the technologies, these integrated products are mainly used in the main drive motor of disk drive and low-power BLDC motor control systems like fan drives used in equipments. For general industrial BLDC motor control systems, whether the electronic circuit controllers are installed inside the motor, depends on many factors, such as the actual operating condition, the cost of the system, the reliability of the circuit and maintainability and so forth.

(2) Full digitalization of controllers
The improvement of BLDC motor performance, which is related to the permanent magnet materials of rotors and electronic drive circuit, is closely bound up with the controllers. Therefore, in order to improve the overall performance of the control system, we can consider enhancing the performance of controllers. The emergence of high-speed microprocessors and high-density PLC technology provides a reliable guarantee and

feasible solution. For example, in some of the applications that are strict on cost and space, adding the position sensor is impractical and unacceptable, whereas the inherent high-speed computation of DSP can be used to achieve position-sensorless control of BLDC motor. Plenty of hardware, such as traditional PID analog circuits, digital signal processing circuits and logical judging circuits, can be accomplished with software, thus further reducing the size of the hardware circuit and improving the reliability and efficiency of the system. In addition, some complex control algorithms can be realized with DSP, CPLD and FPGA chips, which not only improve the reliability of BLDC motor control systems, but also provide a solid foundation for development towards generalization of the interface and full digitalization of the control system. Full digitalization enables the structure of system hardware to be simpler and improves the application of flexible control algorithm. It is also easy for data transmission with the upper level and the remote control system, which facilitates the monitoring and diagnosis of system failures. A typical block diagram of network remote control for a BLDC motor is shown as Figure 1.8. Remote speed control of a BLDC motor can be achieved with speed and current regulator, the network monitoring and diagnosis functions for the whole control system can be realized within the supervision system.

(3) Green PWM modulation and high-efficiency realization

In BLDC motor control systems, when the three-phase six-state 120 degree two-phase conduction mode is implemented in the inverter, each period has a sector that holds 60 electrical degrees, where each power switch is conducted through a 120° electrical angle in each period. According to their different modulation modes during the conducted period, the control modes of PWM for BLDC motor can be classified as half-bridge modulation and full-bridge modulation. The half-bridge modulation consists of four types: H_PWM-L_ON, H_ON-L_PWM, ON_PWM and PWM_ON, whose characteristic is that in each sector of 60 electrical degrees, one power switch remains normally open and the other is used with PWM control. The full-bridge modulation mode H_PWM-L_PWM can be described as follows, in each sector of 60 electrical degrees, the power switches on both upper and lower legs are chopping at the same time. In these modulation modes, H_PWM-L_ON and H_ON-L_PWM are single-sideband modulation and the other three

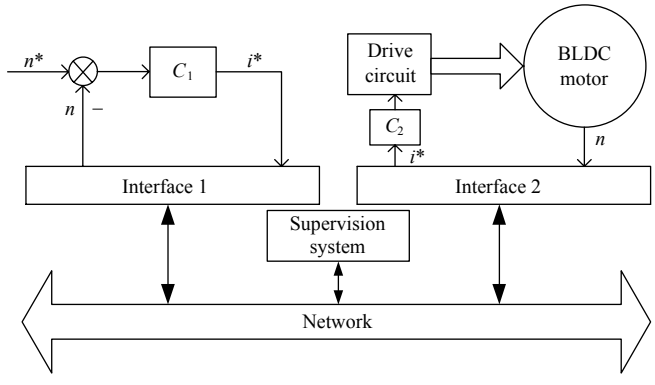


Figure 1.8 Block diagram of remote network control for BLDC motor.

modes are double-sideband modulation. Each modulation mode has its merits and demerits, so users should consider the torque ripple, system efficiency, position-sensorless control methods and other factors to make a rational choice. When a BLDC motor control system is driven by bipolar power transistor (BPT), the switching frequency of the drive circuit is usually 2–5 kHz. The noise caused in this range of frequency is just in the human audible region, which is detrimental to human health. Meantime, when the winding inductance is not large enough, it will result in unsmooth current waveforms with large ripples. The range of switching frequency can be increased to tens of kHz after MOSFETs and IGBTs are used, by which both electromagnetic noise and current waveform are ameliorated. Therefore, using soft switching and other new techniques to reduce switching loss, prolong the switching life and guarantee unvaried or improved efficiency of the system, the green PWM modulation for BLDC motor control systems can be achieved by increasing the switching frequency of the drive circuit. While in the condition that the switching frequency of power switch is restrained, new types of modulation can be used to increase the operating frequency of PWM, so as to reduce the torque ripple and enhance the system efficiency. Furthermore, motor drive power switches, especially the MOSFET, have a large voltage drop and loss when the current is large. Therefore, within the allowable range, high-voltage low-current power switches or power supplies should be used for controlling, so that the ratio between the power switch voltage drop and DC bus voltage is smaller, which can further improve the efficiency of the system.

1.4.2 Permanent Magnet and Design Considerations

Miniaturization, low weight and high efficiency of motors are closely linked to the development of the magnetic material. An early magnetic material is Al-Ni-Co, which was successfully developed in the 1930s. It has higher remanent magnetic induction density and lower coercivity. Co is contained in the alloy. It is expensive, whereas it has good temperature characteristic and is widely used in instrument-type permanent-magnet machines that requires good temperature stability. The later developed ferrite magnetic materials, in which barium ferrite and strontium ferrite are the two most common types, have lower remanent magnetic induction density and higher coercivity with lower price, which made them occupy the leading position for a long time. Rare-earth samarium–cobalt permanent magnet material, the second generation of rare-earth permanent magnet material developed in the mid-1960s, has relatively high remanent magnetic induction density and coercivity, which greatly increase the magnetic energy product. Its Curie temperature is up to 710–800 °C and the magnetic stability is good. However, the price of this alloy is high, which limits its promotion and application. Hence, it is usually used in the aerospace and military products where the price is not the main issue. In 1983, Japanese workers found the third generation of the rare-earth permanent magnet material Nd-Fe-B, leading to a revolution of magnetic materials. This material does not contain expensive alloying elements, and has a high magnetic energy product. Both neodymium and samarium are rare-earth elements, but the price of Nd is lower and the reserves are ten times more than that of Sm. Accordingly, Nd-Fe-B material was rapidly promoted and used in industrial applications and permanent-magnet machines [61].

Compared with traditional excited motors, permanent-magnet machines made of Nd-Fe-B material have the advantages of easy construction, small size and light weight. In the same condition, the number of turns of armature winding is decreased as the performance of magnetic

material is improving. Take the 70-W micromotor from the Philips Company of the Netherlands as an example, the volume of rare-earth PM motors is just one-quarter of the current-excited motors and half of the ferrite excited motors. China is a country with rich mineral deposits of rare-earth elements, of which the production counts for more than 90 per cent of the total output all over the world in recent years. In particular, the improved performance of third-generation Nd-Fe-B magnetic steel has provided a solid foundation for mass production of BLDC motors and PMSMs. The recent nanocomposite permanent magnet material is compounded of hard magnetic phase with high coercivity and soft magnetic phase with high saturated magnetic moments. The theoretical magnetic energy product of nanocrystal material is more than 800 kJ/m^3, which is much more than that of Nd-Fe-B material. Although the mineral resource of Nd-Fe-B is abundant in China, the productive procession and technological management in this area obviously fell behind the developed countries. The good news is that good results have been achieved in the research of new rare-earth permanent magnet material by Peking University, Chinese Academy of Sciences and Central Iron and Steel Research Institute. It is believed that, in the near future, China will become a big player not only in production, but also in processing and applications for rare-earth materials.

Throughout the history of motors, when a new permanent material appears, there is a new revolution for the structure and functions of motors, which promotes the control theory, computation algorithms and structural machinability to a new stage. In the future, as new permanent-magnet materials emerge and the performance is improved, the research of BLDC motor and related products can be further developed. Hence, the performance and functions of motors will be further improved, in particular it will be more widely used in industrial products and civilian industry products. Note that adopting new conductive and insulating materials, and improving the performance of BLDC motors from the motor structure, are the important development directions in the future. The bonded permanent magnet, orientation of permanent magnet materials and magnetizing processing technology, which cannot be separated from materials science, are required to be developed too.

1.4.3 New Types of BLDC Motor

In BLDC motor control systems, speed and torque ripple are always problems that require further solution, especially in the application of audiovisual equipments, aerospace electric equipments and computers, where stable operation, high precision and low noise are requested. Most of the motors used in these applications have low power, small size and compact form, and thus are usually difficult to change. To improve the performance, genetic algorithms (GA), niche algorithms (Niche) and others are implemented to optimize the design of the motor. Through simulation, analysis and comparisons, the structure of magnetic poles and the shape of the air-gap magnetic field are researched and appropriate pole-pair numbers, tooth numbers and slot dimensions are determined. Hence, the demands for power, speed and efficiency are satisfied. At present, many new types of BLDC motor are springing up, such as the slotless type BLDC motor, the coreless-type BLDC motor, the axial-field disc-type BLDC motor and other types of BLDC motor. The slotless-type BLDC motor, in which the cogging parts of stator core in traditional motors are abrogated and the stator windings are directly settled on the yoke of the stator core, have a bigger air gap and the core loss is just the loss at the yoke, whereas in the coreless-type BLDC motor, iron loss is totally eliminated, so it has better

performance and is suitable for high-speed applications. Although both types above have reduced the loss, the structure processing technique is more complex and techniques of inserting winding and molding should be improved. The 2057 series coreless BLDC motor promoted by the MicroMo Electronics Company, which can output torque up to 0.018 N m and speed up to 58 000 r/min, are suitable for surgery, dentistry and other hand-held medical equipments. The axial-field disc-type BLDC motor is a type of motor that can achieve low noise and vibration, small torque ripple, high efficiency and power density, under the condition of small capacity. Corresponding with brushed DC motors, other types of BLDC motor consist of BLDC torque motors, BLDC linear motors, low-inertia BLDC motors, BLDC plane motors, BLDC spherical motors, and so on [62,63]. The optimization of the motor design scheme is attributed to nonlinear programming problems of multiobject functions in [64], and it can be achieved by implementing the fuzzy niche genetic algorithm. The designed motor has the advantages of rapid increase of electromagnetic torque and small commutation torque ripple. The corresponding optimization flowchart is shown in Figure 1.9. In conclusion, researching

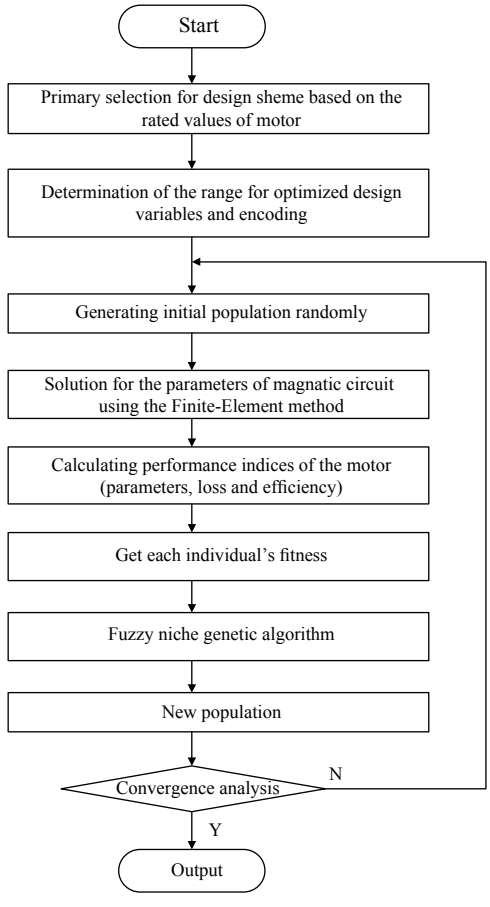

Start
Primary selection for design sheme based on the rated values of motor
Determination of the range for optimized design variables and encoding
Generating initial population randomly
Solution for the parameters of magnatic circuit using the Finite-Element method
Calculating performance indices of the motor (parameters, loss and efficiency)
Get each individual's fitness
Fuzzy niche genetic algorithm
New population
Convergence analysis
N
Y
Output

Figure 1.9 Flowchart of motor design optimization based on fuzzy niche genetic algorithm.

and developing from the aspect of motor structure is one of the major development directions for BLDC motors.

1.4.4 Applications of Advanced Control Strategies

In modern industry, the requirement for motor performance is increasing. The improvement can be achieved by optimizing the motor design and the control of power electronic devices. Also, it can be realized by implementing the advanced control strategies. A BLDC motor control system is a typical nonlinear and multivariable coupling system. The traditional PID control algorithm is simple and easy to realize, but it is difficult to meet the requirements of high precision servocontrol systems. Nonlinear control methods, based on the modern control theory and intelligent control theory, have established the foundation for high-quality dynamic and stable performance and are widely used in BLDC motor control systems. Fuzzy control, neural network, variable structure control, robust control, adaptive control and other advanced control strategies are adopted in the control of BLDC motor [58,59,65–80]. The problem with these methods is that the control is relatively complex, which is difficult to implement. However, as the development of digital control technology and the processing speed of DSP are improving, more advanced control strategies will be used in BLDC motor control systems, which will greatly enhance the performance of the control systems. Meanwhile, while the processing speed of DSP is limited, the practical applications of control algorithms should be focused on, in order to comprehensively promote the BLDC motor control system towards the direction of small size, low weight, intelligence, high efficiency and energy conservation.

1.5 Other Kinds of PM Motors

The introduction of high energy density rare-earth magnets such as Nd-Fe-B, has dramatically increased the range of applications of PM motors. Besides the BLDC motor, other common types of PM motors used in industry are:

- Brush PM motors – Conventional DC machines with mechanical commutators and brushes where permanent magnets provide the excitation field.
- PM synchronous motors – Conventional synchronous machines where permanent magnets replace the DC rotor excitation winding.
- Line-start PM synchronous motors – Synchronous machines equipped with a squirrel-cage induction-type rotor winding for line starting. Permanent magnets embedded in the cage synchronize the motor.
- Doubly salient PM motor – Switched reluctance motor with PM embedded in the stator or rotor side, where the air-gap magnet flux density is from both the winding and the permanent magnet.

In addition, PM motors in which the magnetic flux travels in the axial direction are classified as axial-gap motors. They can have multiple disk or pancake-shaped rotors and stators. The stator–rotor–stator configuration is typical.

Questions

1. Describe some advances in BLDC motor drives.
2. Give some new types of BLDC motor and explain how they work.
3. Describe the advantages of the application of advanced control strategies for BLDC motors.
4. Explain why the BLDC motors are widely used in industries.

References

1. Pillay, P., Krishnan, R. (1991) Application characteristics of permanent magnet synchronous and brushless DC motors for servo drives. *IEEE Transactions on Industry Application*, **27**(5), 986–996.
2. Pillay, P., Krishnan, R. (1989) Modeling, simulation, and analysis of permanent-magnet motor drives, part II: the brushless DC motor drive. *IEEE Transactions on Industry Application*, **25**(2), 274–279.
3. Hemati, N., Leu, M. C. (1992) A complete model characterization of brushless DC motors. *IEEE Transactions on Industry Application*, **28**(1), 172–180.
4. IEEE. (1984) IEEE Standard Dictionary of Electrical Terms, ANSI/IEEE Std. 100–1984. USA.
5. NEMA. (1987) Motion/position Control Motors and Controls, MG7-1987. USA.
6. Inoue, K., Nakaoka, M. (1998) Autotuning gain parameter implementation with fuzzy learning control scheme for DC brushless servo system. *IEE Proceedings-Control Theory and Applications*, **145**(5), 419–427.
7. Ye, J. H. (1982) *Brushless DC Motor.* Science Press, Beijing (in Chinese).
8. Zhang, C. (1996) *Principle and Application of Brushless DC Motor.* China Machine Press, Beijing (in Chinese).
9. Guo, Q. D., Zhao, X. M. (2008) *Principle and Technical Application of Brushless DC Motor.* China Electric Power Press, Beijing (in Chinese).
10. Liu, G., Wang, Z. Q., Fang, J. Q. (2008) *Permanent Magnet Brushless DC Motor Control and Application*. China Machine Press, Beijing (in Chinese).
11. Harrison, D. B., Rye, N. Y. (1955) Commutatorless direct current motor. United States Patent Office, 2,719,944.
12. Wang, C. Y., Xia, J. Q., Yang, J. Y. (2006) *Modern Control Technology for Electric Machines*. China Machine Press, Beijing (in Chinese).
13. Xia, C. L., Guo, P. J., Shi, T. N., *et al.* (2004) Speed control of brushless DC motor using genetic algorithm based fuzzy controller. *IEEE International Conference on Intelligent Mechatronics and Automation*, Japan, 460–464.
14. Wang, J.Current direct control and torque analysis of brushless DC motor based on RBF. Tianjin: Tianjin University Master Thesis, 2003 (in Chinese).
15. Xia, C. L., Liu, J. H., Yu, W. (2006) Variable structure control of BLDCM based on extended state observer. *Proceedings of the CSEE*, **26**(20), 139–143 (in Chinese).
16. Xia, C. L., Wen, D., Wang, J. (2002) A new approach of minimizing commutation torque ripple for brushless DC motor based on adaptive ANN. *Proceedings of the CSEE*, **22**(1), 54–58 (in Chinese).
17. Xia, C. L., Wang, J., Shi, T. N. (2003) Direct control of currents based on adaptive RBF neural network for brushless DC motors. *Proceedings of the CSEE*, **23**(6), 123–127 (in Chinese).
18. Wen, D. Position sensorless control and torque ripple research of brushless DC motor based on ANN. Tianjin: Tianjin University Master Thesis, 2002 (in Chinese).
19. Xia, C. L., Guo, P. J., Shi, T. N. (2005) Control of brushless DC motor using genetic algorithm based fuzzy controller. *Proceedings of the CSEE*, **25**(11), 129–133 (in Chinese).
20. Kuo, J. L., Chang, Z. S. (2008) Intelligent sensorless control of two-phase linear brushless DC motor based on a recurrent fuzzy neural network. *Control and Intelligent Systems*, **36**(2), 161–168.
21. Editorial Committee of China Machinery Industry Yearbook. (2004–2008) *China Electrical Equipment Industry Yearbook*. China Machine Press, Beijing (in Chinese).
22. Guo, J. L., Chen, S. Y. (2007) How to choose driving motor for electric vehicle. *Auto Electric Parts*, **1**, 9–12 (in Chinese).
23. Xia, C. L., Xue, X. D. (1999) Design of the brushless DC motor for the air-conditioner in the automobile. *Micromotors Servo Technique*, **3**, 7–8 (in Chinese).
24. Xia, C. L., Shi, T. N. (2001) Simulation of non-bridge brushless DC motor for the air-conditioner in the automobile. *Micromotors Servo Technique*, **3**, 7–9 (in Chinese).

25. Cheng, Q., Chen, H. B. (2005) The application of permanent magnet brushless DC motor in air-condition compressor. *Journal of Hubei University of Technology*, **20**(1), 41–43 (in Chinese).
26. Ma, R. Q., Liu, W. G., Liu, J. L. (2004) Research of REPM brushless linear motor in compressor. *Micromotors Servo Technique*, **37**(6), 42–46 (in Chinese).
27. Kenjo, T., Nagamori, S. (1985) *Permanent Magnet and Brushless DC Motors*. Oxford University Press, New York.
28. Mieslinger, W. (1969) Control circuit for a commutatorless D.C. motor. United States Patent Office, 3,475,668, patented.
29. Iizuka, K., Uzuhashi, H., Kano, M., *et al.* (1985) Microcomputer control for sensorless brushless motor. *IEEE Transactions on Industry Applications*, **IA-21**, 595–601.
30. Lin, R. L., Hu, M. T., Chen, S. C., *et al.* (1989) Using phase-current sensing circuit as the position sensor for brushless DC motors without shaft position sensor. The 15th Annual Conference of IEEE Industrial Electronics Society, USA, **1**: 215–218.
31. Ogasawara, S., Akagi, H. (1990) An approach to position sensorless drives for brushless DC motors. Conference Record of the 1990 IEEE Industry Applications Society Annual Meeting, USA, **1**, 443–447.
32. Matsui, N., Takeshita, T., Yasuda, K. (1992) A new sensorless drive of brushless DC motor. Proceedings of the 1992 International Conference on Industrial Electronics, Control, Instrumentation, and Automation. Power Electronics and Motion Control, USA, **1**, 430–435.
33. Ertugrul, N., Acarnley, P. (1994) A new algorithm for sensorless operation of permanent magnet motors. *IEEE Transactions on Industry Application*, **30**(1), 126–133.
34. Dhaouadi, R., Mohan, N., Nourum, L. (1991) Design and Implementation of an extended Kalman filter for the state estimation of a permanent magnet synchronous motor. *IEEE Transactions on Power Electronics*, **6**(3), 491–497.
35. Terzic, B., Jadric, M. (2001) Design and implementation of the extended Kalman filter for the speed and rotor position estimation of brushless DC motor. *IEEE Transactions on Industry Electronics*, **48**(6), 1065–1073.
36. Bolognani, S., Tubiana, L., Zigliotto, M. (2003) Extended Kalman filter tuning in sensorless PMSM drives. *IEEE Transactions on Industry Application*, **39**(6), 1741–1747.
37. Chen, W.Rotor position detection and model reference adaptive control of brushless DC motor based on Kalman filters. Tianjin: Tianjin University Master Thesis, 2003 (in Chinese).
38. Nondahl, T. A., Ray, C., Schmidt, P. B., *et al.* (1999) A permanent-magnet rotor containing an electrical winding to improve detection of rotor angular position. *IEEE Transactions on Industry Application*, **35**(4), 819–824.
39. Tomita, M., Doki, S., Okuma, S., *et al.* (1999) Sensorless rotor position estimation at standstill of cylindrical brushless DC motors using opened phase voltage change caused by eddy currents. *Electrical Engineering in Japan*, **126**(1), 52–60.
40. Matsuse, K., Baba, T., Masukane, I., *et al.* (2003) Position sensorless starting method and driving characteristics of closed-slot small permanent-magnet motor. *IEEE Transactions on Industry Application*, **39**(2), 451–456.
41. Shi, T. N., Tian, Y., Xia, C. L. (2007) Position sensorless control based on wavelet neural network for PM brushless DC motors. *Journal of Tianjin University*, **40**(2), 190–194 (in Chinese).
42. Yang, X. J. Sensorless control for brushless DC motor. Tianjin: Tianjin University Master Thesis, 2002 (in Chinese).
43. Fang, W. Z., He, Y. K. (1998) Back electromotive force prediction using artificial neural network for brushless DC motor. *Micromotors Servo Technique*, **31**(2), 7–11, 24 (in Chinese).
44. Jahns, T. M. (1984) Torque production in permanent-magnet synchronous motor drives with rectangular current excitation. *IEEE Transactions on Industry Application*, **IA-20**(4), 803–813.
45. Hoang, L. H., Robert, P., Feuillet, R. (1986) Minimization of torque ripple in brushless DC motor drives. *IEEE Transactions on Industry Application*, **IA-22**(4), 748–755.
46. Pillay, P., Krishnan, R. (1988) An investigation into the torque behavior of a brushless DC motor drive. IEEE Industry Applications Society Annual Meeting, USA, **1**, 201–208.
47. Murai, Y., Kawase, Y., Ohashi, K., *et al.* (1987) Torque ripple improvement for brushless DC miniature motors. IEEE Industry Applications Society Annual Meeting, USA, 21–26.
48. Carlson, R., Lajoie-Mazenc, M., Fagundes, J. C. S (1992) Analysis of torque ripple due to phase commutation in brushless DC machines. *IEEE Transactions on Industry Application*, **28**(3), 632–638.
49. Hung, J. Y., Ding, Z. (1993) Design of currents to reduce torque ripple in brushless permanent magnet motors. *IEE Proceedings-B, Electric Power Applications*, **140**(4), 260–266.

50. Lim, Y. H., Kook, Y. S., Ko, Y. (1997) A new technique of reducing torque ripples for BDCM drives. *IEEE Transactions on Industrial Electronics*, **44**(5), 735–739.
51. Kang, B. H., Kim, C. J., Mok, H. S. (2001) Analysis of torque ripple in BLDC motor with commutation time. IEEE International Symposium on Industrial Electronics Proceedings, KOREA, 1044–1048.
52. Liu, Y., Zhu, Z. Q., Howe, D. (2005) Direct torque control of brushless DC drives with reduced torque ripple. *IEEE Transactions on Industry Application*, **41**(2), 599–608.
53. Nam, K. Y., Lee, W. T., Lee, C. M., *et al.* (2006) Reducing torque ripple of brushless DC motor by varying input voltage. *IEEE Transactions on Magnetics*, **42**(4), 1307–1310.
54. Zhang, Y. M., Xia, P. C. (1999) The armature reaction of the brushless DC servo motor. *Micromotors Servo Technique*, **32**(1), 10–12 (in Chinese).
55. Zhang, Z. Z. (1999) Study on Digital simulation of ripple torque of brushless DC motor system. *Micromotors Servo Technique*, **32**(5), 3–5 (in Chinese).
56. Xia, C. L., Yu, W., Li, Z. Q. (2006) Torque ripple reduction of PM brushless DC motors based on auto-disturbances-rejection controller. *Proceedings of the CSEE*. **26**(24), pp. 137–142 (in Chinese).
57. Xia, C. L., Li, Z. J., Yang, R. (2005) Control system of brushless DC motor based on active-disturbance rejection controller. *Proceedings of the CSEE*. **25**(2), 82–86 (in Chinese).
58. Liu, J. H. Sliding variable structure control for PM brushless DC motor. Tianjin: Tianjin University Master Thesis, 2005 (in Chinese).
59. Sharkawi, M. A., Samahy, A. A., Sayed, M. L. (1994) High performance drive of DC brushless motors using neural network. *IEEE Transactions on Energy Conversion*, **9**(2), 317–322.
60. Rubaai, A., Ricketts, D., Kankam, M. D. (2002) Development and implementation of an adaptive fuzzy-neural-network controller for brushless drives. *IEEE Transactions on Industry Applications*, **38**(2), 441–447.
61. Tang, R. Y. (2006) *Modern Permanent Magnet Machines-Theory and Design*, China Machine Press, Beijing (in Chinese).
62. Wang, F. X., Wang, J. Q., Kong, Z. G. (2004) Study on brushless DC motor with passive magnetic bearings. *Proceedings of the CSEE*. **24**(5), 90–95 (in Chinese).
63. Ji, P., Song, W., Yang, Y. B. (2003) Application situation of PM brushless motors. *Electrical Machinery Technology*, (4), 32–36 (in Chinese).
64. Chen, W. Study on torque ripple suppression technique of permanent magnet brushless DC motor. Tianjin: Tianjin University PhD Thesis, 2006 (in Chinese).
65. Lee, C. K., Kwok, N. M. (1995) A variable structure controller with adaptive switching surfaces brushless DC motor. Proceedings of the American Control Conference, USA, **1**, 1033–1034.
66. Xia, C. L., Yang, X. J., Shi, T. N. (2002) Robust speed controller design for brushless motor drive. *Advanced Technology of Electrical Engineering and Energy*, **21**(3), 5–8 (in Chinese).
67. Xiao, B. X., Tang, Z. Q., Jiang, H. B. (1999) Application of adaptive control on brushless DC motor speed control system. *Journal of Hefei University of Technology (Natural Science)*. **22**(6), 94–97 (in Chinese).
68. Xia, C. L., Fang, H. W., Chen, W., *et al.* (2006) Ant colony algorithm based fuzzy control for a brushless DC motor. IEEE Proceedings of the World Congress on Intelligent Control and Automation, China, 6498–6502.
69. Chen, W., Xia, C. L. (2006) Sensorless control of brushless DC motor based on fuzzy logic. IEEE Proceedings of the World Congress on Intelligent Control and Automation, China, 6298–6302.
70. Xia, C. L., Chen, W. (2005) Sensorless control of brushless DC motors at low speed using neural networks. IEEE International Conference on Machine Learning and Cybernetics, China, 1099–1103.
71. Xia, C. L., Yang, X. J., Shi, T. N. (2001) A speed observer for brushless DC motor. *Micromotors Servo Technique*, **34**(6), 27–29 (in Chinese).
72. Xia, C. L., Li, Z. Q., Wang, M. C. (2005) Single neural PID model reference adaptive control for PM brushless DC motors based on RBF neural network on-line identification. *Transactions of China Electrotechnical Society.* **20**(11), 65–69 (in Chinese).
73. Li, Z. Q., Xia, C. L. (2006) Speed control of brushless DC motor based on CMAC and PID controller. IEEE Proceedings of the World Congress on Intelligent Control and Automation, China, 6318–6322.
74. Xia, C. L., Liu, J. H., Yu, W., *et al.* (2005) Variable structure control of BLDCM based on extended state observer. IEEE International Conference on Mechatronics and Automation, Canada, 568–571.
75. Xia, C. L., Zhang, M. H., Wang, Y. F. (2008) The direct torque control for permanent magnet brushless DC motors. *Proceedings of the CSEE*. **28**(6), 104–109 (in Chinese).

76. Zhang, M. H., Xia, C. L. (2007) Speed control of brushless DC motor based on single neural PID and wavelet neuron network. IEEE International Conference on Control and Automation, China, 621–624.
77. Wang, Y. F., Xia, C. L. (2007) Adaptive speed control for brushless DC motors based on genetic algorithm and RBF neural network. IEEE International Conference on Control and Automation, China, 1219–1222.
78. Liu, D., Xia, C. L., Zhang, M. H., *et al.* (2007) Control of brushless DC motor using fuzzy set based immune feedback PID controller. IEEE International Symposium on Industrial Electronics, Spain, 1045–1049.
79. Tian, Y., Shi, T. N., Xia, C. L. (2007) Sensorless position control using adaptive wavelet neural network for PM BLDCM. IEEE International Symposium on Industrial Electronics, Spain, 2848–2852.
80. Fang, H. W., Xia, C. L., Chen, Z. W., *et al.* (2007) Position servo control of brushless DC motor based on the second discrete filter. IEEE International Conference on Robotics and Biomimetics, China, 1838–1842.

2

Mathematical Model and Characteristics Analysis of the BLDC Motor

The mathematical model of the BLDC motor is fundamental for the corresponding performance analysis and control system design. The structure characteristics and working modes of the BLDC motor should be considered when we are building its model. The BLDC motor generally consists of three parts: the motor structure, the power driving circuit, and the position sensor. Moreover, there are various structures and different driving modes. In the first section of this chapter, we will introduce several existing structures and driving modes of BLDC motors. The common mathematical models, which mainly include differential equation model, transfer function model, and state-space model, are presented in the second section. Finally, the steady and dynamic characteristics are analyzed and the variations of current and torque during commutation are discussed in detail.

2.1 Structure and Drive Modes

2.1.1 Basic Structure

The main design principle of a BLDC motor is to replace the mechanical commutator by using an electrical switch circuit. In traditional DC motors, the brushes are used for commutation, making the directions of the main magnetic field and the armature magnetic field perpendicular to each other when the motor is running. For the purpose of realizing commutation without mechanical contact, brushes were abandoned after the "inverted DC motor" was developed in which armature winding and magnet steel are placed on the stator and rotor sides separately. In order to control the motor's rotation speed and direction, a rotor-position sensor, a control circuit, together with a power inverter must be included in a BLDC motor system. Figure 2.1 shows a BLDC motor experimental system.

Compared with other kinds of motors, the BLDC motor is excited by a square wave, so that the motor has lots of advantages, such as higher permanent magnet utilization, smaller size,

Permanent Magnet Brushless DC Motor Drives and Controls, First Edition. Chang-liang Xia.
© 2012 Science Press. Published 2012 by John Wiley & Sons Singapore Pte. Ltd.

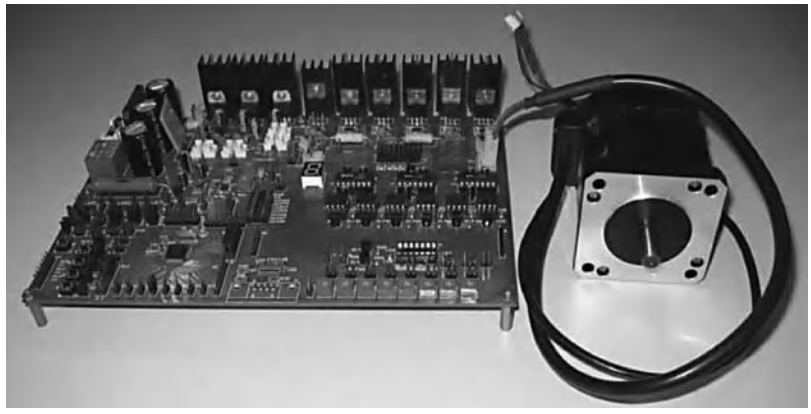


Figure 2.1 The BLDC motor experimental system.

larger motor torque, higher efficiency and reliability. Therefore, the BLDC motor plays an important role in product quality improvement, service life extension and energy saving. These superiorities are becoming even more evident along with the presence of higher performance and lower price of new types of NdFeB.

The BLDC motor's structure contains a stator with armature winding and a rotor with a permanent magnet, which is similar to PMSM. The cross-sectional image of a four-pole BLDC motor is shown in Figure 2.2.

2.1.1.1 Stator Cores

The stator structure of the BLDC motor is similar to that of a general synchronous motor or an induction motor. Single- or multiple-phase symmetric windings are embedded in the iron core, which can be connected in "Y" or "Δ" type. Considering the performance and the cost of the system, the Y-type is mostly used, in which the three phase windings are connected symmetrically without a neutral point. Note that in the traditional brush DC motor, the armature winding is placed at the rotor, whereas the armature winding is installed at the stator side in the BLDC motor, causing less heating.

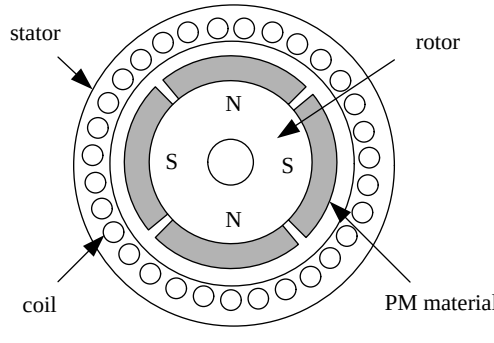


Figure 2.2 Cross-sectional image of a BLDC motor.

2.1.1.2 Windings

The common winding types used in BLDC motors are concentrated full-pitch windings, distributed full-pitch windings, distributed short-pitch windings, etc. The different types of windings can affect the waveform of the back-EMF and the performance of the motor.

(1) For the concentrated full-pitch winding, the wires of the same phase are placed in one cog, and therefore the air-gap flux density in the motor is the same. By adding the back-EMF generated by wires of each phase, we can get the waveform of the total back-EMF, which has a similar shape as the air-gap flux density. Furthermore, the platform width of the back-EMF waveform is the same as that of the air-gap flux density waveform. Thus, the concentrated full-pitch winding can produce a better trapezoidal back-EMF.
(2) For the purpose of cooling the winding effectively through the inner surface space of the stator, the coil winding can be dispersed evenly at the surface of the stator, which is called distributed winding. Under normal circumstances, it is hard for the spatial distribution of air-gap flux density to form an ideal square wave.
(3) On the other hand, application of the short-pitch winding makes it possible to shorten the connecting wires at the end of the winding. This can be helpful to save copper material and weaken the torque harmonics.

2.1.1.3 PM Rotor

The BLDC motor's rotor is constituted by permanent magnets with certain pole pairs embedded in the surface or the inside of the iron core. At present, the permanent magnets are usually made using rare-earth permanent magnetic materials like NdFeB, which have the advantages of high coercivity and remanence intensity. The permanent magnetic steels, in the BLDC motors as well as the brushed motors, are used to produce a sufficient magnetic field in the air gap. The only difference between them is that in BLDC motors, PM steels are installed on the rotor side, whereas they are placed on the stator side in brushed motors. Three typical structures of the BLDC motor rotors are as follows.

(1) Surface-mounted PM rotor. For the surface-mounted PM rotor, on the surface of the iron core there is mounted radial magnetized tile-shaped rare-earth permanent magnet. Furthermore, the tile-shaped poles can be assembled by rectangle strips so as to cut the costs of the motor. In the design procedure of the motor, the designer always adopts this structure with its pole arc width larger than 120 degree electric angle in order to generate a square air-gap flux density and decrease torque ripple.
(2) Magnet-embedded rotor. When the rectangular permanent magnets are embedded into the iron core of the rotor, we call it a magnet-embedded rotor. Since the magnetism gathering technology can provide larger flux, the flux under one polar pitch is produced by two adjacent poles in parallel. In this case, magnetism-isolating technology or a stainless steel shaft should be adopted.
(3) Magnetic loop rotor. For the magnetic loop rotor, a rare-earth PM ring magnetized radially in multiple poles through a special way is overlapped around the iron core. Note that it is usually used in low-power motors.

2.1.1.4 Position Sensor

The position sensors installed in the motor can detect the rotor position and transform it into an electrical signal, providing the correct commutation information for the logic switch circuit. Hence, the proper current commutation of the windings is obtained according to rotor position information, and the PM rotor will rotate continuously because of the stepping rotating magnetic field generated by the current in the air gap.

There are various kinds of position sensors and each has its own characteristics. At present, a wide range of electromagnetic, photoelectric and magnetic sensors have been used in BLDC motors. The Hall sensor, as a kind of magnetic sensor, has the advantages of compact volume, low price and convenient operation. Therefore, it is commonly used in BLDC motor control systems as the rotor-position detector.

2.1.2 General Design Method

The generally used methods of BLDC motor design mainly contain an electromagnetic design method (EMDM) and a field-circuit method (FCM). The EMDM is used more frequently than the FCM for its simplicity. However, the FCM can be used to get more accurate results, because it is allowed to check the magnetic field of the design scheme with the finite element method and make corresponding appropriate adjustments.

The EMDM is the traditional design method of BLDC motors. It mainly includes four steps: (1) Confirm the rotor structure according to the technical requirements; (2) Determine the magnetic load B_δ according to the rotor structure and the performance of permanent magnet; (3) Decide the electrical load A by B_δ; (4) Determine the basic size D, L according to A and B_δ. Note that this method is easy to implement in practice. But its calculation precision is relatively poor.

The FCM of BLDC motor design is based on the analysis of finite elements of magnetic field, where the magnetic and circuit parameters are obtained from the finite-element analysis and the electrical circuit, respectively. The high-precision analysis of magnetic field (generally the 2D calculation of the magnetic field will meet the design requirements) is the main advantage of the method. But the amplitude and phase position of the equivalent current will change when the magnetic field is analyzed. So, the magnetic-field analysis and the circuit calculation must be carried out synchronously. Generally, the main procedure of the FCM design method is shown as Figure 2.3. As for the design optimization of BLDC motor, it will be discussed in Section 5.5.

2.1.3 Drive Modes

2.1.3.1 Half-Bridge Mode

For Y-connected BLDC motors, the generally used three-phase half-bridge driving circuit is shown in Figure 2.4. In the figure, L_A, L_B and L_C represent the windings of phase A, B, and C, respectively, and the power switches T_1, T_2 and T_3 are connected to the three-phase windings in series. The rotor position signals H_A, H_B and H_C are used to drive the power switches after being amplified so as to control the motor commutation. During the commutation process, the rotating step magnetic field generated by each stator winding in the air gap has three

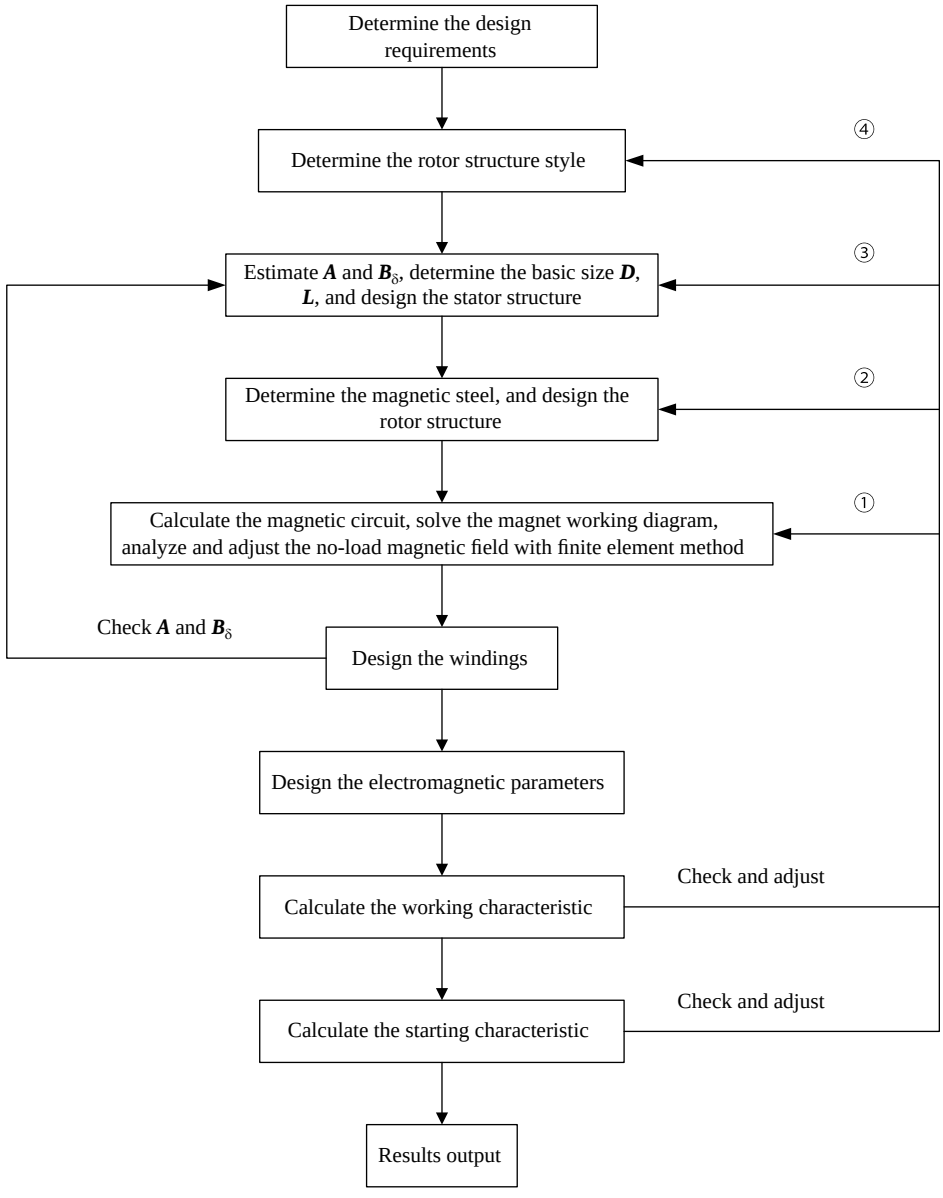

Determine the design requirements
Determine the rotor structure style
④
Estimate A and B_δ, determine the basic size D, L, and design the stator structure
③
Determine the magnetic steel, and design the rotor structure
②
Calculate the magnetic circuit, solve the magnet working diagram, analyze and adjust the no-load magnetic field with finite element method
①
Check A and B_δ
Design the windings
Design the electromagnetic parameters
Calculate the working characteristic
Check and adjust
Calculate the starting characteristic
Check and adjust
Results output

Figure 2.3 Flowchart of BLDC motor design.

magnetic states in the range of 360° electrical angle, where each state holds on a 120° electrical angle.

Although the three-phase half-bridge driving BLDC motor control system has the advantages of fewer drive components, lower cost, easy to control, it is seldom used because of its disadvantages of large torque ripples and low utilization of the windings. In this condition, each winding is conducted only 1/3 of the period.

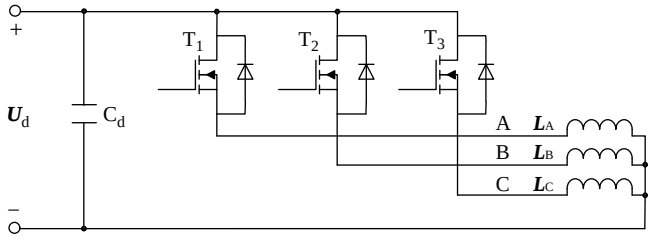


Figure 2.4 Half-bridge driving circuit.

2.1.3.2 Full-Bridge Mode

In the following content we will introduce the full-bridge driving circuit while taking the three-phase Y-connected BLDC motor as an example. Figure 2.5 shows the schematic diagram of the full-bridge driving circuit. In the diagram, power switches T_1, T_2, T_3, T_4, T_5 and T_6 are used to turn on or turn off the currents of the windings according to the logic signals produced by Hall sensors. The mainly used conduction modes are the two-phase conduction mode and the three-phase conduction mode.

1) Two-phase conduction mode

The principle of the two-phase mode is conducting two of the motor windings all the time as well as suspending the third one. The conduction order and instant are determined by the rotor position information that is generated by the sensors. In this condition, the synthetic rotating magnetic field generated by the stator is a step field instead of a continuous one. The bridge converter commutates once the rotor rotates a 60° electrical angle, and the magnetic status is consequently changed. So, there are six magnetic statuses and two phase windings are conducting in each state. The time of current flowing continuously in each winding is 120° electric angles.

In the two-phase mode, there is only one upper bridge switch conducted at a time, which produces the forward flowing current in the corresponding winding, resulting in a torque. Similarly, another torque is produced by the backward current because of the lower bridge switch conduction. The sum of these torques constitutes the synthetic torque, which rotates 60°

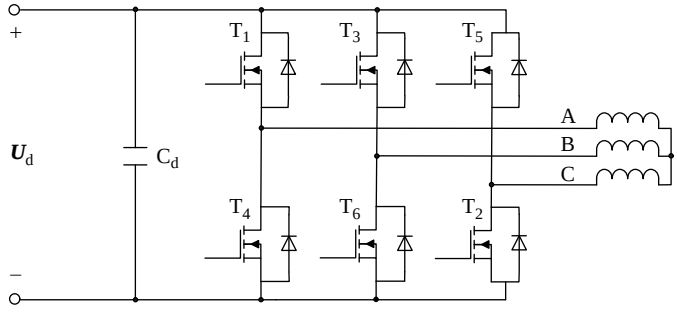


Figure 2.5 Full-bridge driving circuit.

electrical angles at each commutation period. Therefore, the torque ripples are much smaller than that of a half-bridge driving system because the direction of torque changes six times in one cycle.

2) Three-phase conduction mode
In the three-phase conduction mode, there are three power switches of the bridge energized every moment. Compared with the two-phase conduction mode, the three-phase conduction mode has the same driving circuit as shown in Figure 2.5. The only difference between these two modes is the order of conducting, and each power switch conducts 180° in the three-phase conduction mode.

The three-phase conduction mode can further increase the utilization of the windings as well as reduce the torque ripples. However, it should be noted that the three-phase conduction mode may possibly lead to the upper and lower switches of the same bridge being conducted at the same time.

The principle diagram of a Δ-connected three-phase full-bridge BLDC motor control system is shown in Figure 2.6. As shown in the figure, there are few differences between Δ–connected and Y- connected driving circuits. The only thing we need to do is consider the connection point of phase A and B in the Δ-connected motor as the point A in the Y-connected motor, while the connection point of phase B and C as B point, and the connection point of phase C and A as C point.

2.1.3.3 C-Dump Mode

In some applications of BLDC motors, good control performance, low cost and small size are all required. In order to meet these requirements, a compromised method between half-bridge control and full-bridge control was proposed by Walter and Stephen [1], which is called a C-Dump driving circuit. As shown in the Figure 2.7, only four power switches are used in the C-Dump driving circuit of the three-phase BLDC motor. The four-quadrant operation of the motor can be achieved through this driving mode.

Compared with the full-bridge driving mode, there are fewer power switches and energy losses under the C-dump driving mode. However, larger commutation torque ripples may be produced.

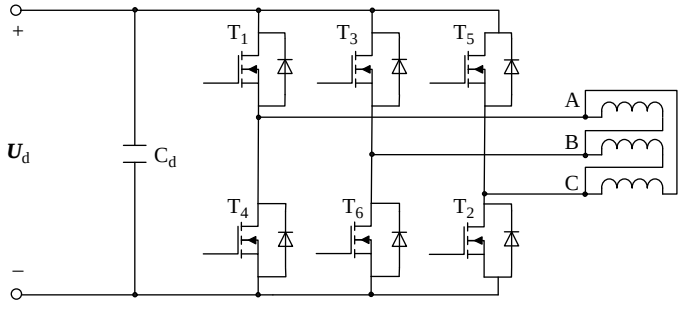


Figure 2.6 Full-bridge driving circuit for Δ–connected motor.

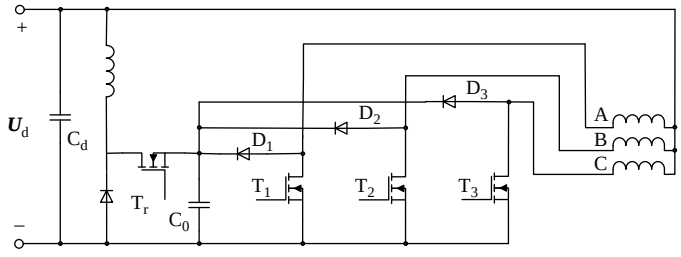


Figure 2.7 C-dump driving circuit.

2.1.3.4 H-Bridge Mode

Figure 2.8 shows the principle of the H-bridge power inverter. The typical feature of the H-bridge is that each winding is controlled by an H-bridge power inverter separately. The current of the BLDC motor can be controlled by this driving circuit easily. Moreover, the four-quadrant operation can also be achieved with this driving mode.

Note that each H-bridge power inverter has 4 power switches for one phase winding. So, it is usually used in single-phase or two-phase BLDC motors. A delay control of the driving signals must be taken to prevent the upper and lower switches of the same bridge arm from being conducting at the same time. This means that the switches of one side will conduct under the condition that the switches of the other side have been turned off reliably. Consequently, the dead-band time has to be longer than the turn-off time of the corresponding power switch [2].

2.1.3.5 Four-Switch Mode

The structure of four-switch driving circuit is shown in Figure 2.9. In the topology, one bridge of the full-bridge driving circuit is replaced with two capacitances. The neutral point of the two capacitances is connected to the phase-C winding. Thus, two power switches are saved in the four-switch driving circuit so that the system has lower cost and less loss, whereas the control algorithm will be more complicated [3].

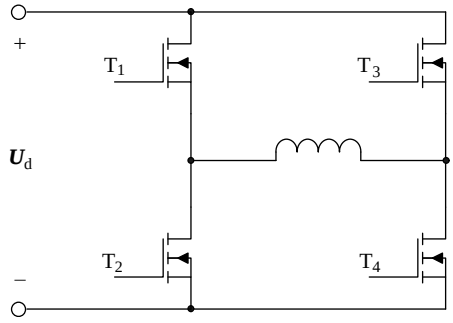


Figure 2.8 H-bridge driving circuit.

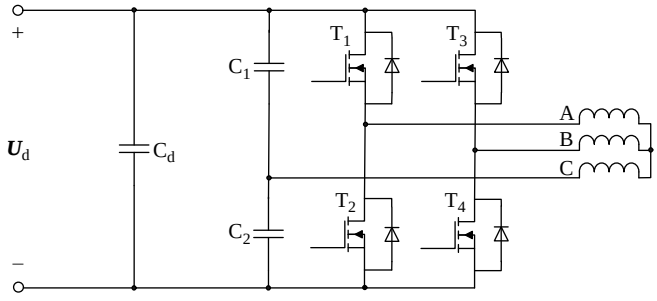


Figure 2.9 Four-switch driving circuit.

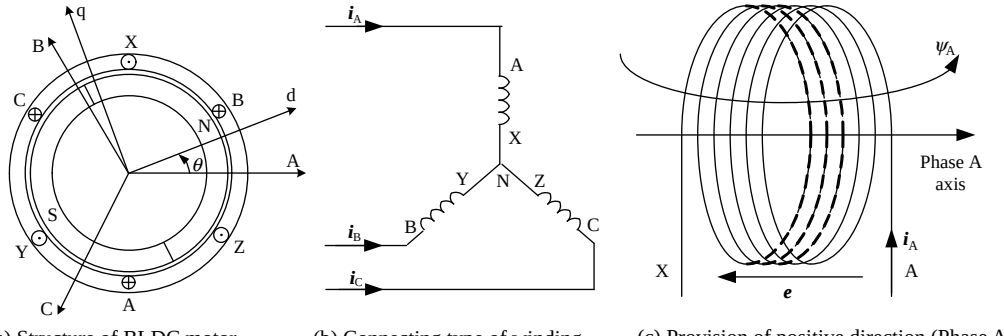
2.2 Mathematical Model

2.2.1 Differential Equations

In this section, the differential equation model is built for a three-phase two-pole BLDC motor. The stator has a Y-connected concentrated full-pitch winding, and the inner rotor has a nonsalient pole structure. Three Hall sensors are placed symmetrically at 120° interval. Furthermore, the following assumptions are made to build the differential equation of the BLDC motor [4–6].

(1) Ignore the core saturation, as well as the eddy current losses and the hysteresis losses.
(2) Ignore the armature reaction, and the distribution of air-gap magnetic field is thought to be a trapezoidal wave with a flat-top width of 120° electrical angle.
(3) Ignore the cogging effect and suppose the conductors are distributed continuously and evenly on the surface of the armature.
(4) Power switches and flywheel diodes of the inverter circuit have ideal switch features.

Hence, the simplified schematic diagram of the motor can be obtained as shown in Figure 2.10.



(a) Structure of BLDC motor (b) Connecting type of winding (c) Provision of positive direction (Phase A)

Figure 2.10 Schematic diagram of the BLDC motor.

Under the positive direction shown in Figure 2.10, the phase voltage of each winding, which includes the resistance voltage drop and the induced EMF, can be expressed as

$$u_x = R_x i_x + e_{\psi x} \tag{2.1}$$

where

u_x — phase voltage, in which subscript x denotes phase A, B and C;
i_x — phase current;
$e_{\psi x}$ — phase-induced EMF;
R_x — phase resistance. For three-phase symmetrical winding, there exists $R_A = R_B = R_C = R$.

The winding-induced EMF is equal to the change rate of the flux. Since the positive direction of induced EMF and flux linkage defined in Figure 2.10 is opposite to that of the right-hand screw rule, the induced EMF can be written as

$$e_{\psi x} = \frac{\mathrm{d}\psi_x}{\mathrm{d}t} \tag{2.2}$$

Taking phase A for example, the flux is given as

$$\psi_A = L_A i_A + M_{AB} i_B + M_{AC} i_C + \psi_{pm}(\theta) \tag{2.3}$$

where

$\psi_{pm}(\theta)$ — PM flux linkage of phase A;
θ — position angle of rotor, the angle between rotor d-axis and the axis of phase A;
L_A — self-inductance of phase A;
M_{AB}, M_{AC} — mutual inductance of phase A with phase B and phase C.

The magnitude of $\psi_{pm}(\theta)$ depends on the magnetic field distribution of the PM in the air gap. The radial component of PM air-gap magnetic field distributes as a trapezoidal profile along the inner surface of the stator, is shown in Figure 2.11.

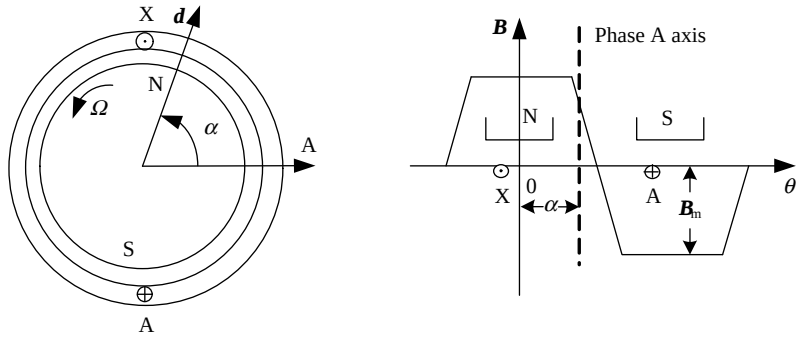
As shown in Figure 2.11, when the rotor rotates anticlockwise, the winding AX moves in the forward direction along the θ-axis. Then, the effective flux of phase A will change with regard to the rotor position. When the rotor position is α, the PM flux of phase A is

$$\psi_{pm}(\alpha) = N\phi_{pm}(\alpha) \tag{2.4}$$

$$\varphi_{pm}(\alpha) = \int_{-\frac{\pi}{2}+\alpha}^{\frac{\pi}{2}+\alpha} B(\theta)\mathrm{S}\mathrm{d}\theta \tag{2.5}$$

where

Φ_{pm} (α) — PM flux of phase A when the rotor position angle is α;
$B(\theta)$ — PM rotor radial flux density in the air gap, which is in a trapezoidal distribution along θ;



(a) Rotor position (b) Flux distribution

Figure 2.11 PM flux of phase A.

N — turns of winding;
S — product of rotor radius and effective length of conductors.

Substituting Equations (2.2)–(2.5) into Equation (2.1), we can get

$$\begin{aligned} u_A &= Ri_A + \frac{d}{dt}(L_A i_A + M_{AB} i_B + M_{AC} i_C + \psi_{pm}) \\ &= Ri_A + \frac{d}{dt}(L_A i_A + M_{AB} i_B + M_{AC} i_C) + \frac{d}{dt}\left[NS\int_{-\frac{\pi}{2}+\theta}^{\frac{\pi}{2}+\theta} B(x)dx\right] \\ &= Ri_A + \frac{d}{dt}(L_A i_A + M_{AB} i_B + M_{AC} i_C) + e_A \end{aligned} \tag{2.6}$$

where e_A represents the back-EMF of phase A.

Equation (2.6) includes a derivative operation of the product of inductance and current, where the self-inductance and the mutual inductance of the winding is proportional to N^2 (N represents the number of turns) and the permeance of the corresponding magnetic circuit. That is

$$L_A = N^2 \Lambda_A \tag{2.7}$$

$$M_{AB} = N^2 \Lambda_{AB} \tag{2.8}$$

where

Λ_A — permeance of self-inductance flux in phase A;
Λ_{AB} — permeance of mutual inductance flux between phase A and phase B.

The permeability of salient pole rotor differs in directions of the d-axis and the q-axis, consequently the self-inductance and mutual inductance of winding changes with the rotor position [7]. Therefore, the inductance also changes with the rotor position. But for the nonsalient pole rotor, the flux is isotropic in all directions. Hence, the permeability of the magnetic circuit cannot be affected by rotor position. So, the self-inductance and mutual inductance will not vary with time. The effect of rotor saliency on winding inductance is shown in Figure 2.12.

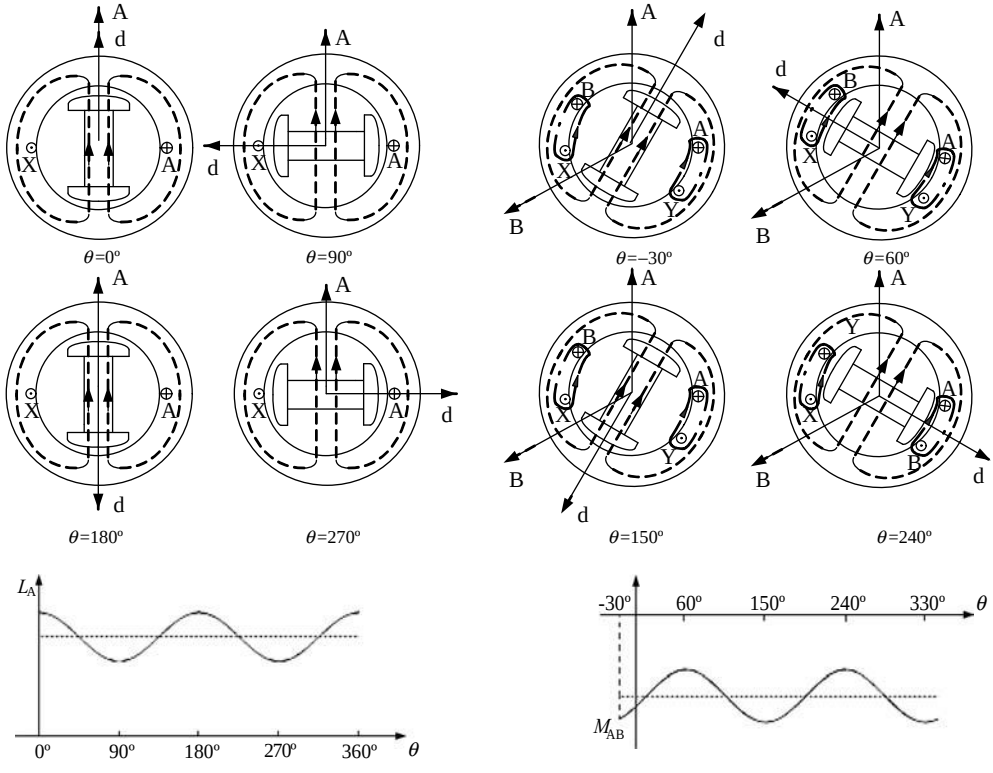


Figure 2.12 Effect of rotor saliency on magnetic circuit.

Generally, the surface-mounted salient-pole rotor is used for BLDC motors. In this condition, the winding inductance will not change with the time. Further, as the three-phase stator windings are symmetrical, the self-inductances will be equal, and so as the mutual inductance. That is $L_A = L_B = L_C = L$, $M_{AB} = M_{BA} = M_{BC} = M_{CB} = M_{AC} = M_{CA} = M$. Substituting them into Equation (2.6), we can get

$$u_A = Ri_A + L\frac{di_A}{dt} + M\frac{di_B}{dt} + M\frac{di_C}{dt} + e_A \tag{2.9}$$

in which

$$\begin{aligned} e_A &= \frac{d}{dt}\left[NS\int_{-\frac{\pi}{2}+\theta}^{\frac{\pi}{2}+\theta} B(x)dx\right] \\ &= NS\left[B\left(\frac{\pi}{2}+\theta\right) - B\left(-\frac{\pi}{2}+\theta\right)\right]\frac{d\theta}{dt} \\ &= NS\omega\left[B\left(\frac{\pi}{2}+\theta\right) - B\left(-\frac{\pi}{2}+\theta\right)\right] \end{aligned} \tag{2.10}$$

where ω is the electrical angular speed of motor.

According to the distribution of magnetic density in the air gap as shown in Figure 2.11(b), together with $B(\theta)$ having a period of 2π and $B(\theta+\pi) = -B(\theta)$, we can get

$$\begin{aligned} e_A &= NS\omega\left[B\left(\frac{\pi}{2}+\theta\right) - B\left(-\frac{\pi}{2}+\theta\right)\right] \\ &= NS\omega\left[B\left(\frac{\pi}{2}+\theta\right) - B\left(\frac{\pi}{2}+\theta+\pi-2\pi\right)\right] \\ &= 2NS\omega B\left(\frac{\pi}{2}+\theta\right) \end{aligned} \tag{2.11}$$

Then, the θ-dependent back-EMF wave of phase A is $\pi/2$ ahead of the distribution of the magnetic density in air gap, and e_A can be expressed as

$$e_A = 2NS\omega B_m f_A(\theta) = \omega\psi_m f_A(\theta) \tag{2.12}$$

where

B_m — maximum value of PM density distribution in air gap;
ψ_m — maximum value of PM flux linkage of each winding, $\psi_m = 2NSB_m$;
$f_A(\theta)$ — back-EMF waveform function of phase A.

Note that the $f_A(\theta)$ has a trapezoidal distribution with the rotor position, and its maximum and minimum values are, respectively, 1 and –1. The corresponding waveform and its phase relationship with $B(\theta)$ and e_A are shown in Figure 2.13. As for the three-phase symmetrical windings, there also exist $f_B(\theta) = f_A(\theta - 2\pi/3)$, and $f_C(\theta) = f_A(\theta + 2\pi/3)$.

It can be seen from Equation (2.10) that e_A is a rotating back-EMF that is produced by the winding flux linkage caused by the rotating rotor.

As the currents of the three phases satisfy

$$i_A + i_B + i_C = 0 \tag{2.13}$$

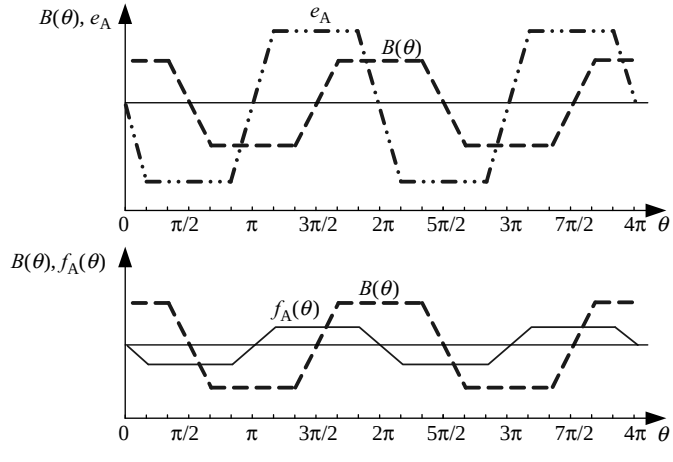


Figure 2.13 Phase relationship between $B(\theta)$, e_A, and $f_A(\theta)$.

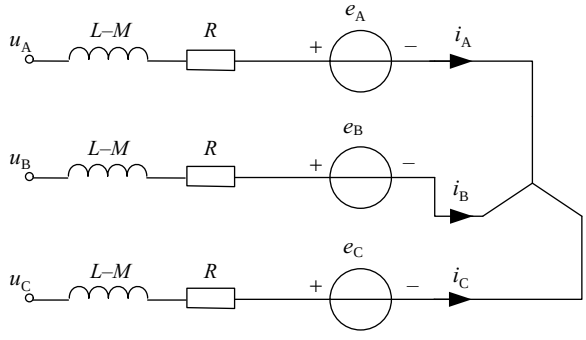


Figure 2.14 Equivalent circuit of the BLDC motor.

Equation (2.9) can be further simplified as

$$u_A = Ri_A + (L - M)\frac{di_A}{dt} + e_A \tag{2.14}$$

Then, the matrix form of phase voltage equation of BLDC motor can be expressed as

$$\begin{bmatrix} u_A \\ u_B \\ u_C \end{bmatrix} = \begin{bmatrix} R & 0 & 0 \\ 0 & R & 0 \\ 0 & 0 & R \end{bmatrix} \begin{bmatrix} i_A \\ i_B \\ i_C \end{bmatrix} + \begin{bmatrix} L-M & 0 & 0 \\ 0 & L-M & 0 \\ 0 & 0 & L-M \end{bmatrix} \frac{d}{dt} \begin{bmatrix} i_A \\ i_B \\ i_C \end{bmatrix} + \begin{bmatrix} e_A \\ e_B \\ e_C \end{bmatrix} \tag{2.15}$$

According to Equation (2.15), the equivalent circuit of the BLDC motor can be shown as in Figure 2.14.

In most practical applications of BLDC motors, the stator windings are Y-connected in which there is no neutral point brought out so that the phase voltages are difficult to detect. Thus, the mathematical model based on phase voltage is not applicable in some cases. In contrast, the line voltage is easy to measure. It is approximately equal to the DC bus voltage when the relevant power transistors are turned on. Therefore, the mathematical model based on line voltage is more suited to the practical system.

The line voltage equation can be obtained through subtraction calculation of the phase-voltage equation as

$$\begin{bmatrix} u_{AB} \\ u_{BC} \\ u_{CA} \end{bmatrix} = \begin{bmatrix} R & -R & 0 \\ 0 & R & -R \\ -R & 0 & R \end{bmatrix} \begin{bmatrix} i_A \\ i_B \\ i_C \end{bmatrix} + \begin{bmatrix} L-M & M-L & 0 \\ 0 & L-M & M-L \\ M-L & 0 & L-M \end{bmatrix} \frac{d}{dt} \begin{bmatrix} i_A \\ i_B \\ i_C \end{bmatrix} + \begin{bmatrix} e_A - e_B \\ e_B - e_C \\ e_C - e_A \end{bmatrix} \tag{2.16}$$

Similar to DC motors, the analysis of power and torque for the BLDC motor can be carried out from the perspective of energy transfer. When the motor is operating, the power from the source is absorbed, and although a little is turned into copper loss and iron loss, most of the power is transferred through the air gap to the rotor by the torque effect. The power transferred to the rotor, which is called the electromagnetic power, equals the sum of the product of current and back-EMF of the three phases. That is

$$P_e = e_A i_A + e_B i_B + e_C i_C \tag{2.17}$$

Ignoring the mechanical loss and stray loss, the electromagnetic power is totally turned into kinetic energy, so

$$P_e = T_e \Omega \tag{2.18}$$

where

T_e — electromagnetic torque;
Ω — angular velocity of rotation.

Hence, from Equations (2.17) and (2.18), we can get

$$T_e = \frac{e_A i_A + e_B i_B + e_C i_C}{\Omega} \tag{2.19}$$

Substituting Equation (2.12) into Equation (2.19), another form of the torque equation can be represented as

$$T_e = p[\psi_m f_A(\theta) i_A + \psi_m f_B(\theta) i_B + \psi_m f_C(\theta) i_C] \tag{2.20}$$

where p is the number of pole pairs.

When the BLDC motor runs in the 120° conduction mode and the corresponding transient commutation process is ignored, the currents that have the same amplitude and the opposite direction only flow through two-phase windings of the Y-connected motor at any time. Note that the symbols of $f(\theta)$ at the flat-top position are opposite to each other for different windings, so Equation (2.20) can be further simplified as

$$T_e = 2p\psi_m i_A = K_T i \tag{2.21}$$

where

K_T — the torque coefficient;
i — the steady phase current.

In order to build a complete mathematical model of the electromechanical system, the motion equation has to be included as

$$T_e - T_L = J \frac{d\Omega}{dt} + B_v \Omega \tag{2.22}$$

where

T_L — load torque;
J — rotor moment of inertia;
B_v — viscous friction coefficient.

Thus, Equations (2.15), (2.19) and (2.22) constitute the differential equation mathematical model of the BLDC motor.

2.2.2 *Transfer Functions*

The transfer function is one of the most important concepts of control theory, and the transfer-function-based mathematical models are widely used in automatic control fields. Some control design and analysis methods, such as the root-locus method and the frequency-response method, are also developed based on the system transfer function.

The transfer function of the BLDC motor is significant for the performance analysis and control design of the motor. Compared with the traditional brushed DC motor, the windings of the BLDC motor are energized according to the rotor position, and the motor is usually designed to be three-phase or multiphase. However, for each conducted phase winding, the mechanisms of back-EMF and electromagnetic torque are all the same with those of the traditional brushed DC motor, thus similar analysis methods can be adopted.

Suppose that the three-phase BLDC motor is controlled by the full-bridge driving in the two-phase conduction mode, then when the windings of phase A and B are conducted, there exists

$$\begin{cases} i_{\mathrm{A}} = -i_{\mathrm{B}} = i \\ \dfrac{\mathrm{d}i_{\mathrm{A}}}{\mathrm{d}t} = -\dfrac{\mathrm{d}i_{\mathrm{B}}}{\mathrm{d}t} = \dfrac{\mathrm{d}i}{\mathrm{d}t} \end{cases} \tag{2.23}$$

Thus, the line-voltage U_{AB} in Equation (2.16) can be rewritten as

$$u_{\mathrm{AB}} = 2Ri + 2(L - M)\frac{\mathrm{d}i}{\mathrm{d}t} + (e_{\mathrm{A}} - e_{\mathrm{B}}) \tag{2.24}$$

Take the transient process out of consideration (i.e. ignore the trapezoid bevel edge), then the steady e_{A} and e_{B} are equal in amplitude and opposite in direction when phases A and B are turned on. So, Equation (2.24) can be expressed as

$$u_{\mathrm{AB}} = U_{\mathrm{d}} = 2Ri + 2(L - M)\frac{\mathrm{d}i}{\mathrm{d}t} + 2e_{\mathrm{A}} = r_{\mathrm{a}}i + L_{\mathrm{a}}\frac{\mathrm{d}i}{\mathrm{d}t} + k_{\mathrm{e}}\Omega \tag{2.25}$$

where

U_{d} — DC bus voltage;
r_{a} — line resistance of winding, $r_{\mathrm{a}} = 2R$;
L_{a} — equivalent line inductance of winding, $L_{\mathrm{a}} = 2(L - M)$;
k_{e} — coefficient of line back-EMF, $k_{\mathrm{e}} = 2p\psi_{\mathrm{m}} = 4pNSB_{\mathrm{m}}$.

Equation (2.25) is exactly the armature voltage loop equation when two phase windings are excited, and the corresponding equivalent circuit is shown in Figure 2.15.

Note that the equivalent circuit shown in Figure 2.15 could be adopted in three-phase half-bridge driving and three-phase full-bridge driving modes of the BLDC motor with specific k_{e} and K_{T} too.

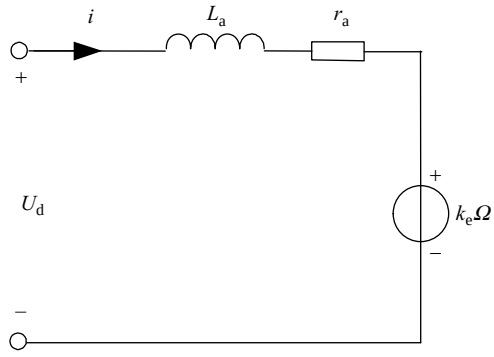


Figure 2.15 Equivalent circuit of the BLDC motor with two phase windings excited.

In Equation (2.25), if the current can be expressed by angular velocity, then we can get the transfer function of motor by obtaining the relationship between bus voltage and angular velocity. So, substituting Equation (2.21) into Equation (2.22), we get

$$K_T i - T_L = J\frac{d\Omega}{dt} + B_v\Omega \tag{2.26}$$

First, when the BLDC motor runs with no load, the current is given as

$$i = \frac{J}{K_T}\frac{d\Omega}{dt} + \frac{B_v}{K_T}\Omega \tag{2.27}$$

Substituting Equation (2.27) into Equation (2.25), we get

$$U_d = r_a\left(\frac{J}{K_T}\frac{d\Omega}{dt} + \frac{B_v}{K_T}\Omega\right) + L_a\frac{d}{dt}\left(\frac{J}{K_T}\frac{d\Omega}{dt} + \frac{B_v}{K_T}\Omega\right) + k_e\Omega \tag{2.28}$$

Also, it can be rearranged as

$$U_d = \frac{L_a J}{K_T}\frac{d^2\Omega}{dt^2} + \frac{r_a J + L_a B_v}{K_T}\frac{d\Omega}{dt} + \frac{r_a B_v + k_e K_T}{K_T}\Omega \tag{2.29}$$

By Laplace transformation of Equation (2.29), the transfer function of a BLDC motor can be expressed as

$$G_u(s) = \frac{\Omega(s)}{U_d(s)} = \frac{K_T}{L_a J s^2 + (r_a J + L_a B_v)s + (r_a B_v + k_e K_T)} \tag{2.30}$$

Thus, the structure of a BLDC motor control system with no load can be built as shown in Figure 2.16.

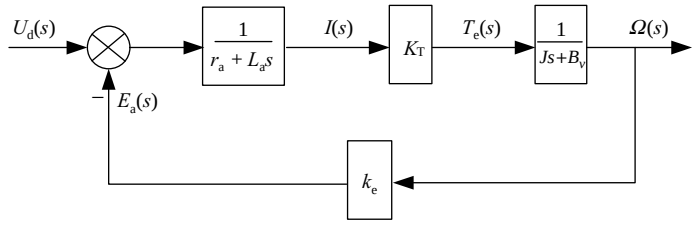


Figure 2.16 Structure of BLDC motor control system with no load.

Equation (2.30) implies that the BLDC motor can be considered as a second-order system, so it can be rearranged as

$$G_u(s) = \frac{K_T}{r_a B_v + k_e K_T} \frac{\omega_n^2}{(s^2 + 2\xi\omega_n s + \omega_n^2)} \tag{2.31}$$

where

$\omega_n = \sqrt{\dfrac{r_a B_v + k_e K_T}{L_a J}}$— natural frequency of the second-order system;

$\xi = \dfrac{1}{2} \dfrac{r_a J + L_a B_v}{\sqrt{L_a J}\sqrt{(r_a B_v + k_e K_T)}}$— damping ratio of the second-order system.

It can be seen from Equation (2.31) that the two roots of the characteristic equation for the BLDC motor's second-order system are $s_{1,2} = -\xi\omega_n \pm \omega_n\sqrt{\xi^2 - 1}$. So the system response time is determined by ω_n and ξ. For unit step input, the convergence speed of the response curve depends on ω_n. A larger ω_n generally leads to a faster convergence speed. Meanwhile, the parameter ξ will determine the character of eigenvalues and the shape of the response curve. The system runs underdamping, critical damping and overdamping states, respectively, when $0 < \xi < 1$, $\xi = 1$, and $\xi > 1$. The response curves for different damping ratios are shown in Figure 2.17.

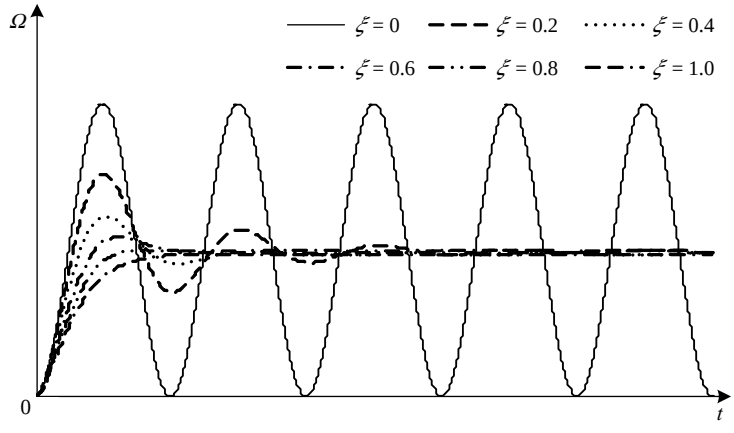


Figure 2.17 Response curves of BLDC motor.

Let the mechanical time constant be $t_m = \dfrac{r_a J + L_a B_v}{r_a B_v + k_e K_T}$ and the electromagnetic time constant be $t_e = \dfrac{L_a J}{r_a J + L_a B_v}$, then Equation (2.30) can be rewritten as

$$G_u(s) = \frac{K_T}{r_a B_v + k_e k_T} \frac{1}{(s^2 t_m t_e + s t_m + 1)} \tag{2.32}$$

Generally speaking, the mechanical time constant is much larger than the electromagnetic time constant, i.e. $t_m \gg t_e$, so the transfer function expressed in Equation (2.32) can be further simplified as

$$\begin{aligned} G_u(s) &\approx \frac{K_T}{r_a B_v + k_e K_T} \frac{1}{(s^2 t_m t_e + s t_m + s t_e + 1)} \\ &= \frac{K_T}{r_a B_v + k_e K_T} \frac{1}{(s t_m + 1)(s t_e + 1)} \end{aligned} \tag{2.33}$$

It is seen from Equation (2.33) that the transfer function of BLDC motor can be expressed by two inertia elements in series [8]. Figure 2.18 shows the corresponding speed responding process with step input.

In Figure 2.18, we can learn the physical meaning of time constant in a transfer function. When a step voltage is applied to the input, first the current will respond to voltage change through the $1/(st_e + 1)$ link, and its time constant is t_e. Then, the speed will respond to the current change through the $1/(st_m + 1)$ link, where t_m is the corresponding time constant. Figure 2.18 has shown the interconnection between armature current and angular speed.

If the effect of electromagnetic time constant is ignored, i.e. the armature inductance is negligible, then L_a can be deemed to be zero, so Equation (2.32) can be simplified into a first-order model as

$$G_u(s) = \frac{K_T}{r_a B_v + k_e K_T} \frac{1}{s t_m + 1} \tag{2.34}$$

The corresponding system structure diagram is shown in Figure 2.19.

Further, the step response of Equation (2.34) is given by

$$\Omega(t) = \frac{K_T U_d}{r_a B_v + k_e K_T} (1 - e^{-t/t_m}) \tag{2.35}$$

Figure 2.20 shows the corresponding response curve.

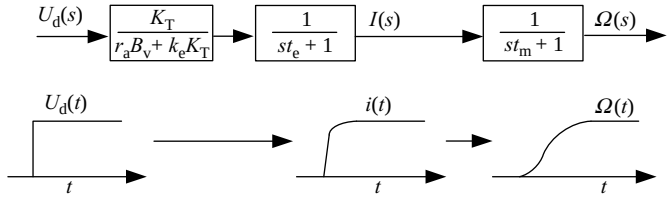


Figure 2.18 Speed responding process with step input.

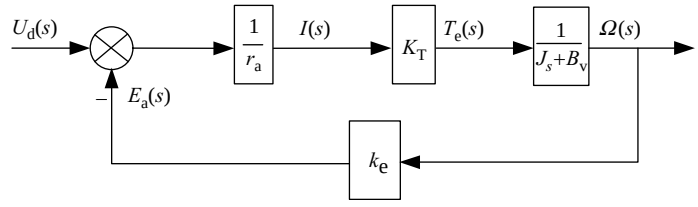


Figure 2.19 System structure diagram of BLDC motor with the armature inductance neglected.

It is known from Figure 2.20 that a smaller t_m leads to a shorter settling time of $\Omega(t)$. For a speed-control system, it is desirable that the delay time of speed response be short enough. If the mechanical time constant is big, a rational closed control system should be designed to increase the response speed. For example, a voltage or current amplifier with large gain used in an analog control system as well as the larger proportional gain of PI controller in digital control system can all increase the open-loop gain of the system. Consequently, the rise time of the speed response will be reduced. However, too large a gain would bring more losses of power switches so as to reduce the efficiency of system. Furthermore, from the control viewpoint, a large proportional gain may cause oscillation and instability. Therefore, the stability and the system response speed should be considered together in system design. The response speed should be increased under the condition of stability.

In the following, the transfer function and speed step response of a BLDC motor when the load torque is not zero will be discussed. In this condition, the load torque can be regarded as an input of the system, as shown in Figure 2.21.

For such a system, the superposition principle holds. Thus, the output of the system equals the sum of outputs when $U_d(s)$ and $T_L(s)$ are applied to the system, respectively. In Figure 2.21, when $U_d(s) = 0$ holds, then

$$\left[-k_e \frac{1}{r_a + L_a s} K_T \Omega(s) - T_L(s)\right] \frac{1}{Js + B_v} = \Omega(s) \tag{2.36}$$

So

$$\Omega(s)\left[\frac{(r_a + L_a s)(Js + B_v) + k_e K_T}{(r_a + L_a s)}\right] = -T_L(s) \tag{2.37}$$

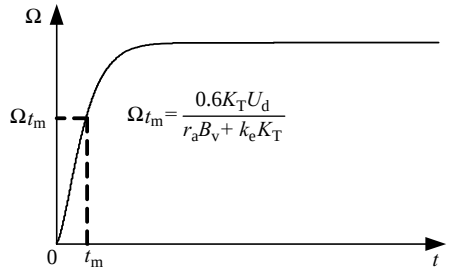


Figure 2.20 Speed step response of BLDC motor neglecting the armature inductance.

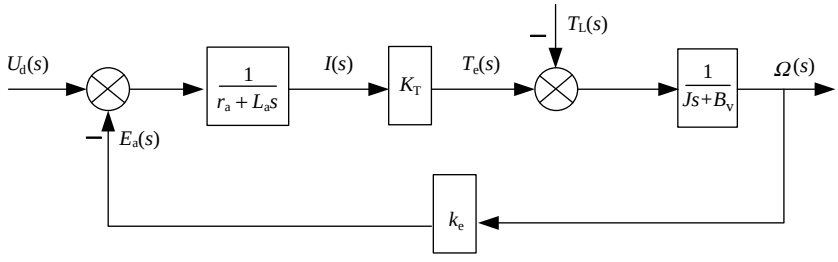


Figure 2.21 Structure diagram of BLDC motor with load torque.

Then, the transfer function between load torque and speed is

$$G_{\mathrm{L}}(s) = \frac{\Omega(s)}{T_{\mathrm{L}}(s)} = -\frac{r_{\mathrm{a}} + L_{\mathrm{a}}s}{L_{\mathrm{a}}Js^2 + (r_{\mathrm{a}}J + L_{\mathrm{a}}B_{\mathrm{v}})s + (r_{\mathrm{a}}B_{\mathrm{v}} + k_{\mathrm{e}}K_{\mathrm{T}})} \tag{2.38}$$

Therefore, the speed response of a BLDC motor affected together by voltage and load torque is given by

$$\begin{aligned}\Omega(s) &= G_{\mathrm{u}}(s)U_{\mathrm{d}}(s) + G_{\mathrm{L}}(s)T_{\mathrm{L}}(s) \\ &= \frac{K_{\mathrm{T}}U_{\mathrm{d}}(s)}{L_{\mathrm{a}}Js^2 + (r_{\mathrm{a}}J + L_{\mathrm{a}}B_{\mathrm{v}})s + (r_{\mathrm{a}}B_{\mathrm{v}} + k_{\mathrm{e}}K_{\mathrm{T}})} - \frac{(r_{\mathrm{a}} + L_{\mathrm{a}}s)T_{\mathrm{L}}(s)}{L_{\mathrm{a}}Js^2 + (r_{\mathrm{a}}J + L_{\mathrm{a}}B_{\mathrm{v}})s + (r_{\mathrm{a}}B_{\mathrm{v}} + k_{\mathrm{e}}K_{\mathrm{T}})}\end{aligned} \tag{2.39}$$

2.2.3 State-Space Equations

In modern control theory, the motion state of control system relies on its state equation. The state-space equation method is one of the most important analysis methods in modern control theory. From the state equation we can get all the independent variables and then determine all the motion states of the system. A group of first-order differential equations with state variables is used in the state-space method to describe the dynamic characteristics of the system. Since it is helpful to the realization of different digital control algorithms, the state-space method is becoming more and more popular in designing control systems with the fast development of computer techniques. Especially in recent years, computer on-line control systems such as optimal control, Kalman filters, dynamic system identification, self-adaptive filters and self-adaptive control have been applied to motor control. All these control techniques are based on the state equation.

The state equations of a BLDC motor can be obtained by the algebraic transformation of the differential equation model. First, appropriate variables should be selected as state variables. The selection of state variables is not unique, but they should be independent of each other. Moreover, the number of state variables should be equal to the order of the differential equation. Currents of three phase windings and the angular speed are selected here as state variables, and the fourth-order state equation is then derived as

$$\dot{\boldsymbol{x}} = \boldsymbol{A}\boldsymbol{x} + \boldsymbol{B}\boldsymbol{u} \tag{2.40}$$

where $\boldsymbol{x} = [\, i_{\mathrm{A}} \quad i_{\mathrm{B}} \quad i_{\mathrm{C}} \quad \Omega \,]^{\mathrm{T}}$;

$$\boldsymbol{u} = [\, u_{\mathrm{A}} \quad u_{\mathrm{B}} \quad u_{\mathrm{C}} \quad T_{\mathrm{L}} \,]^{\mathrm{T}};$$

$$\boldsymbol{A} = \begin{bmatrix} -\dfrac{R}{L-M} & 0 & 0 & -\dfrac{p\psi_{\mathrm{pm}}(\theta)}{L-M} \\ 0 & -\dfrac{R}{L-M} & 0 & -\dfrac{p\psi_{\mathrm{pm}}\left(\theta-\dfrac{2\pi}{3}\right)}{L-M} \\ 0 & 0 & -\dfrac{R}{L-M} & -\dfrac{p\psi_{\mathrm{pm}}\left(\theta-\dfrac{4\pi}{3}\right)}{L-M} \\ \dfrac{p}{J}\psi_{\mathrm{pm}}(\theta) & \dfrac{p}{J}\psi_{\mathrm{pm}}\left(\theta-\dfrac{2\pi}{3}\right) & \dfrac{p}{J}\psi_{\mathrm{pm}}\left(\theta-\dfrac{4\pi}{3}\right) & -\dfrac{B_{\mathrm{v}}}{J} \end{bmatrix};$$

$$\boldsymbol{B} = \begin{bmatrix} \dfrac{1}{L-M} & 0 & 0 & 0 \\ 0 & \dfrac{1}{L-M} & 0 & 0 \\ 0 & 0 & \dfrac{1}{L-M} & 0 \\ 0 & 0 & 0 & -\dfrac{1}{J} \end{bmatrix}.$$

In Equation (2.40), the angular position of the rotor can be detected by a position sensor. As the armature reaction is ignored, the PM flux linkage $\psi_{\mathrm{pm}}(\theta)$ is only a function of θ, which is independent of current and speed. Hence, $\psi_{\mathrm{pm}}(\theta)$ can be regarded as a coefficient of the equation. As θ changes with regard to time when the motor is running, matrix $\boldsymbol{A}$ is time-varying. Thus, the state equation represented as Equation (2.40) denotes a time-varying multiple-input multiple-output (MIMO) continuous linear system.

The controllability of a linear system is the base of optimal control and optimal estimation, so it should be determined. Assume the controllability matrix is

$$\boldsymbol{M} = [\, \boldsymbol{M}_0 \quad \boldsymbol{M}_1 \quad \boldsymbol{M}_2 \quad \boldsymbol{M}_3 \,] \tag{2.41}$$

where $\boldsymbol{M}_0 = \boldsymbol{B}$, $\boldsymbol{M}_{\mathrm{i}}(t) = \boldsymbol{A}^i\boldsymbol{B}$, $i = 1, 2, 3$.

Then, matrix $\boldsymbol{M}$ can be transformed to

$$\boldsymbol{M} = \begin{bmatrix} \lambda & 0 & 0 & 0 & & & \\ 0 & \lambda & 0 & 0 & & & \\ 0 & 0 & \lambda & 0 & \boldsymbol{M}_1 & \boldsymbol{M}_2 & \boldsymbol{M}_3 \\ 0 & 0 & 0 & -\dfrac{1}{J} & & & \end{bmatrix} \tag{2.42}$$

where $\lambda = 1/(L-M)$.

The matrix M meets the condition of rank $[\boldsymbol{M}] = 4$. So, the system represented by Equation (2.40) is controllable and all the poles of the system can be arbitrarily placed by state feedback.

2.3 Characteristics Analysis

2.3.1 Starting Characteristics

The starting characteristics are the variation curves of the speed and current in the process of the speed rising from 0 to the stable value under constant DC bus voltage. At the instant of starting, both the speed and back-EMF are 0, and the armature current can be represented as

$$I = \frac{U_{\mathrm{d}} - \Delta U}{r_{\mathrm{a}}} \tag{2.43}$$

where ΔU is the voltage drop of the power switches of the bridge inverter.

The curves of speed and armature current in the starting process are shown in Figure 2.22.

It can be seen from Figure 2.22 that, since the voltage drop of the power switches and the armature winding resistance are all small, the starting current will be large in a short period of time. It may reach several times or more than ten times the normal operating current. Within the allowable range, the large starting current is helpful to the acceleration of the rotor so that the motor can quickly start even under full load. For example, if the motor runs under rated operating conditions, both the startup speed and back-EMF will be 0. Moreover, the armature current increases rapidly in the instant of starting. Thus, the electromagnetic torque is much larger than the load torque so that the speed increases rapidly. Consequently, the back-EMF will increase so that the growth of armature current becomes slower until it reaches the maximum. Then, the armature current begins to decrease. The decreased current will lead to a decrease of the electromagnetic torque, so the rising acceleration of the speed becomes smaller. When the electromagnetic torque and load torque achieve the dynamic balance, the speed will stay in the rating value, i.e. the BLDC motor will maintain steady-state operation.

Without considering the limit of the starting current, the shape of the speed curve in Figure 2.22 is determined by the damping ratio of the motor. According to the transfer function of the motor, when the damping ratio is $0 < \xi < 1$, the system is in the underdamped condition, the speed and current will become stable after a process with overshoot and oscillation, as shown in Figure 2.23. It can be seen that the shape of the speed step response in Figures 2.22 and 2.23 are in accord with that in Figure 2.17. In practice, due to the restrictions on the armature current, the speed and current oscillations shown in Figure 2.23 will not appear when the motor is starting.

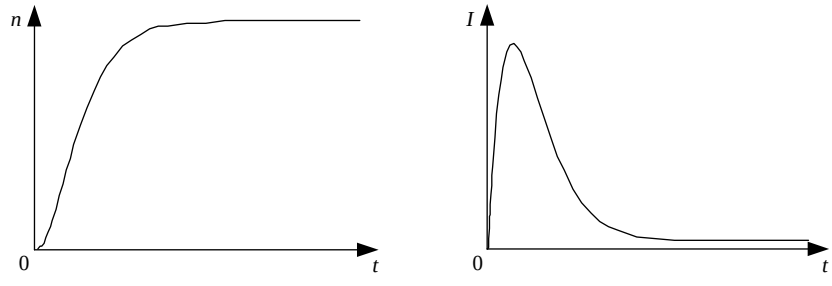


Figure 2.22 Curves of speed and current during the starting process.

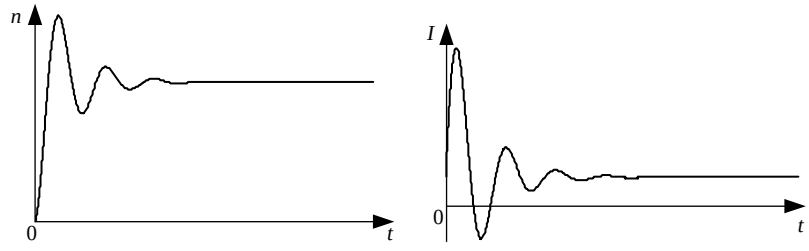


Figure 2.23 Overshoot and oscillation in starting process.

In the motor control system, power switches of driving circuit are more sensitive to the overcurrent. If the current exceeds its upper limit, the power switches will suffer from breakdown in a short period of time. For example, the enduring time of overcurrent for IGBT is normally less than 10 μs. Generally, large-capacity power switches are chosen to stand the high starting current. However, the rated current of the motor is much smaller than the starting current. Thus, the current of the power switch is less than its rated value during most of the normal running. In this condition, the utilization efficiency of the switches decreases so that its cost increases. Therefore, in the design of the driving circuits, it is better to select suitable power switches according to the starting characteristics and working requirements of the motor. In addition, the starting current has to be limited appropriately. Note that the starting current should increase as much as possible to improve the dynamic response speed when the safety of the power switches is ensured. Since the magnetic field has a trapezoidal distribution in the air gap of the BLDC motor, then if the phase winding conducts in the trapezoidal bevel edge of the back-EMF, the back-EMF will be smaller. Thus, the armature current is becoming larger. So, compared to the traditional DC motor, the starting current of the BLDC motor may be larger. This should be considered in the design of the driving circuits.

2.3.2 Steady-State Operation

2.3.2.1 Operating Characteristics

The operating characteristics indicate the relationships between armature current, motor efficiency and output torque with a constant DC bus voltage U_d.

According to Equation (2.21), the armature current will increase with the increasing of load torque so that the electromagnetic torque can balance the load torque. Hence, stable running of the motor is assured.

Since the input power of the motor can be given as

$$P_1 = U_d I = r_a I^2 + \frac{\pi}{30} k_e n I + \Delta U I \tag{2.44}$$

and

$$P_1 = P_{Cu} + P_e + P_T \tag{2.45}$$

where

n — the motor speed;
P_{Cu} — the armature copper loss ($P_{Cu} = r_a I^2$);
P_e — electromagnetic power ($P_e = k_e \Omega I$);
P_T — the loss of bridge power switches ($P_T = \Delta UI$), which is related to the characteristics of power electronic switches and the voltage applied on the corresponding gate terminal of the switch. Here, it is approximately considered a constant.

As shown in Equation (2.45), the input power consists of the electromagnetic power P_e and the loss $P_{Cu} + P_T$. P_e is the power consumed to overcome the back-EMF. It can be turned into mechanical energy through the magnetic field, which will act on the rotor in the form of electromagnetic torque. So, taking the loss of load into account, the power transfer can be expressed as

$$P_e = (T_L + T_0)\Omega = P_2 + P_0 \tag{2.46}$$

where

T_L — load torque;
T_0 — no-load torque corresponding to no-load loss ($T_0 = P_0/\Omega$);
P_2 — output power ($P_2 = T_L \Omega$);
P_0 — no-load loss, including the core loss and mechanical friction loss.

Thus, the efficiency of the motor is given as

$$\eta = \frac{P_2}{P_1} = \frac{P_1 - (P_{Cu} + P_T + P_0)}{P_1} = 1 - \frac{\sum P}{P_1} \tag{2.47}$$

Hence, Equation (2.47) can be further rewritten as

$$\eta = 1 - \frac{r_a}{U_d} I - \frac{P_T + P_0}{U_d I} \tag{2.48}$$

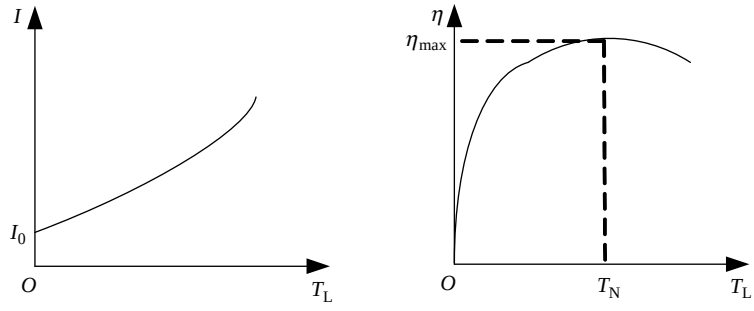
In order to find the extreme value of Equation (2.48), the derivative of η with respect to I should be equal to 0 as

$$\frac{d\eta}{dI} = -\frac{r_a}{U_d} + \frac{P_T + P_0}{U_d I^2} = 0 \tag{2.49}$$

Further, we can get

$$P_T + P_0 = r_a I^2 = P_{Cu} \tag{2.50}$$

Note that the $P_T + P_0$ in Equation (2.50) will not change with load variation, so it is defined as the invariable loss. But the copper loss P_{Cu} changes with the load variation, so it is called the



(a) Armature current (b) Efficiency

Figure 2.24 Curves of armature current and efficiency.

variable loss. Equation (2.50) shows that when the variable loss equals the invariable loss, the maximum efficiency of the motor is achieved. Figure 2.24 shows the curves of armature current and efficiency of the BLDC motor with varied load torque and constant U_d.

2.3.2.2 Regulation Characteristic

Regulation characteristic denotes the relationship between the speed and U_d with constant electromagnetic torque T_e. If the loss of power switches is negligible, when the motor works in steady state, there exist

$$U_d = r_a I + \frac{\pi}{30} k_e n \tag{2.51}$$

and

$$K_T I - T_L = \frac{\pi}{30} B_v n \tag{2.52}$$

Then

$$n = \frac{30K_T}{\pi K_T k_e + \pi r_a B_v} U_d - \frac{30r_a}{\pi K_T k_e + \pi r_a B_v} T_L \tag{2.53}$$

Figure 2.25 shows the n–U_d curves with different electromagnetic torques, where $T_{e1} < T_{e2} < T_{e3} < T_{e4}$.

It can be seen from Figure 2.25 that there exists a dead zone in regulation characteristics. When U_d changes within the dead zone, the electromagnetic torque is not big enough to overcome the load torque to start the motor so that the speed is always zero. Only when the U_d is greater than the threshold voltage can the motor start and run in the steady state. Moreover, the greater the U_d, the bigger the steady-state speed.

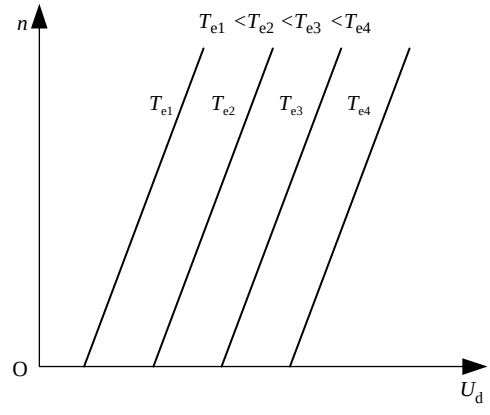


Figure 2.25 Regulation characteristics of BLDC motor.

2.3.2.3 Mechanical Characteristic

Mechanical characteristics denote the relationship between speed and electromagnetic torque with constant U_d. It can be derived from Equation (2.51) that

$$T_e = K_T \frac{30U_d - \pi k_e n}{30r_a} \tag{2.54}$$

such that

$$n = \frac{30}{\pi} \frac{K_T U_d - r_a T_e}{k_e K_T} \tag{2.55}$$

From Equation (2.55), we can obtain curves of mechanical characteristics with different U_d, as shown in Figure 2.26. In the figure, $U_{d1} > U_{d2} > U_{d3} > U_{d4}$.

Note that Equation (2.55) is a linear equation. In practice, due to influences from the variable loss and the armature reaction, the curve of mechanical characteristics is only considered as approximately linear. As shown in Figure 2.26, with a certain DC bus voltage U_d, the speed of the motor decreases on increasing the electromagnetic torque. Moreover, the curve will shift upward as U_d increases. Since the power electronic switches with nonlinear saturation characteristics are used for the commutation of BLDC motors, the voltage drop of the power switch will increase rapidly with increasing armature current when the motor runs near the stalled condition. So, there will be a significant downward bending phenomenon at the end of the curve of the mechanical characteristics, as shown in Figure 2.26 [9].

As discussed above, the mechanical characteristics of BLDC motor are similar to those of a separately excited DC motor. The no-load point of the mechanical characteristics may be altered by changing the DC bus voltage. Therefore, the speed control of a BLDC motor is usually carried out by means of PWM modulation.

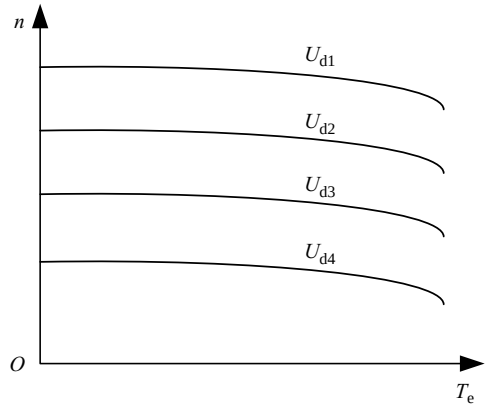


Figure 2.26 Mechanical characteristics of BLDC motor.

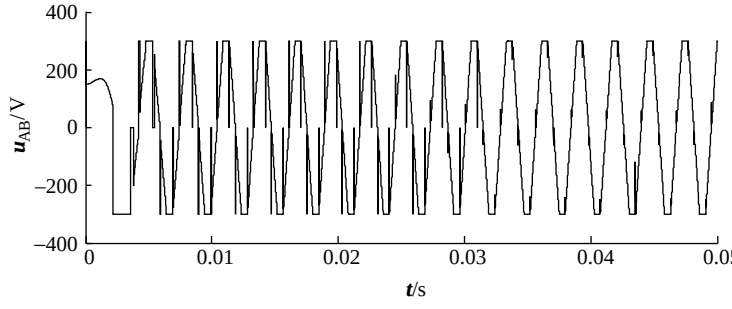
2.3.3 *Dynamic Characteristics*

In this section, the dynamic characteristics of a BLDC motor refer to the motor transient process with free acceleration and load torque variation. Figure 2.27 shows the simulation waveform of the accelerating procedure for the BLDC motor from stall state to maximum speed with no load and constant voltage power supply. The corresponding motor parameters are shown as follows: the stator resistance $R = 0.620\,\Omega$, the stator equivalent inductance $L - M = 1.000 \times 10^{-3}$ H, $\psi_m = 0.066$ Wb, the moment of inertia $J = 0.362 \times 10^{-3}\,\text{kg m}^2$, the viscous friction coefficient $B_v = 9.444 \times 10^{-5}\,\text{N m s}$, the number of pole pairs $p = 4$, and $U_d = 300$ V. The topology of the driving circuit is the DC power-supply–inverter structure, where the inverter works in 120° conduction mode.

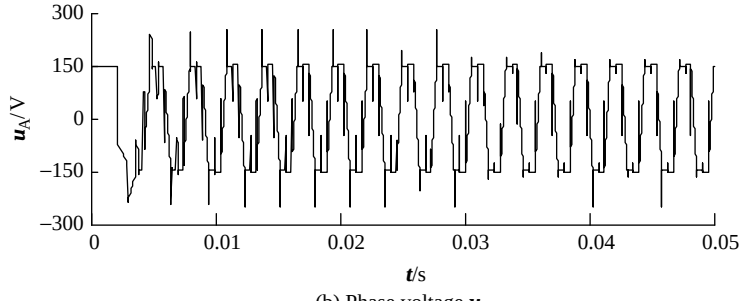
It can be seen from Figure 2.27 that the phase voltage and line voltage have a degree of slope due to the effect of the trapezoidal back-EMF. Moreover, there are narrow pulses in the voltage waveform. This is because of the voltage mutation caused by the conduction of the freewheeling diode during the commutation period. The width of the narrow pulse is equal to the commutation period, which is dependent on the electromagnetic time constant and the running state of the motor. The variation of phase current and torque is similar to that analyzed in the starting process. The starting current and torque achieve more than 10 times their rating values, respectively. But the steady current and torque are small at the no-load condition. Note that the damping in the simulation is rather large, thus the speed curve in Figure 2.27 directly gets to the steady state without overshoot. The variation of the envelope of back-EMF waveform is consistent with that of the speed curves.

The simulation results of the free acceleration process of the motor with the load torque $T_L = 6\,\text{N m}$ are shown in Figure 2.28.

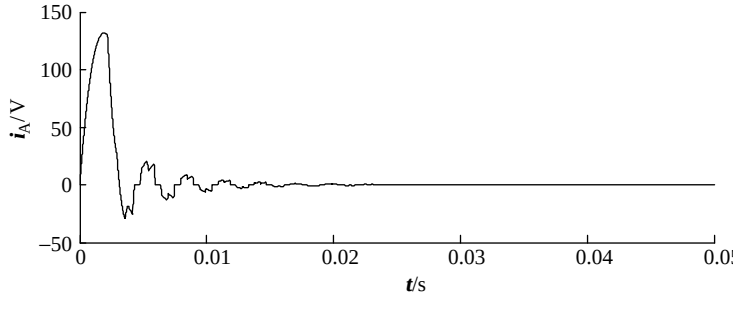
In this condition, the average of winding current is bigger, and the freewheeling process will last a longer time during the commutation period, so that its influence on line or phase voltage is also larger. Hence, in Figure 2.28, narrow pulses still exist in the voltage waveform at the steady state. As for the current, the maximum of the starting current is approximately the same as that in the no-load state. But the time is slightly longer to reach its maximum value, so the heating of the motor and driving circuit is more serious. Generally, a series resistance or a



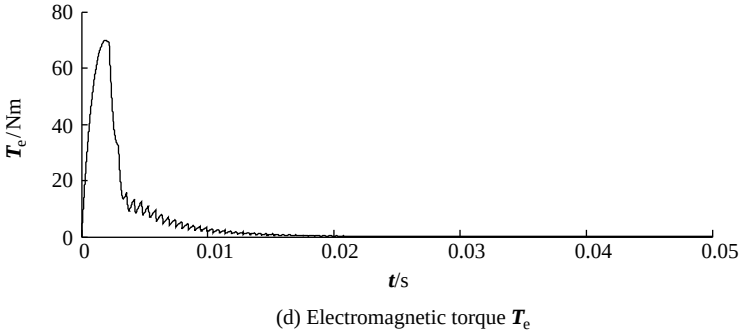
(a) Line voltage u_{AB}



(b) Phase voltage u_A

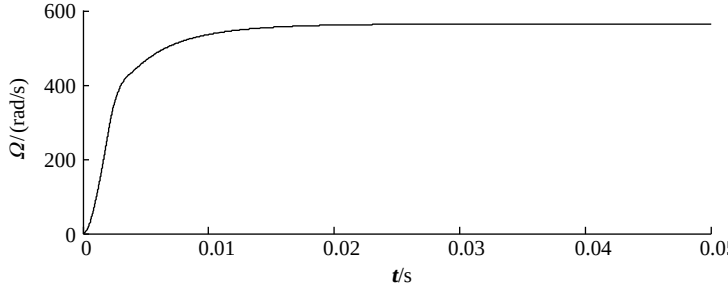


(c) Phase current i_A

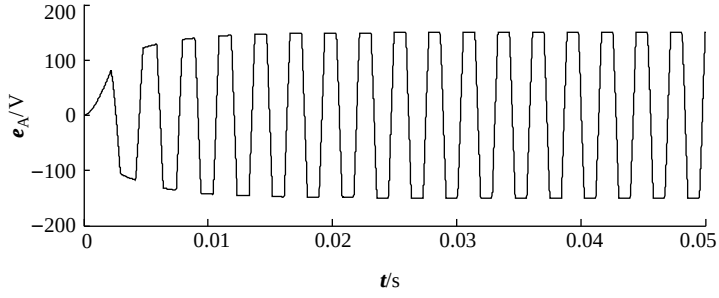


(d) Electromagnetic torque T_e

Figure 2.27 Dynamic process of free acceleration with no load.



(e) Angular velocity Ω



(f) Phase back-EMF e_A

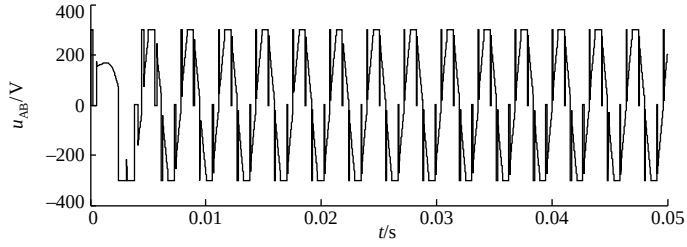
Figure 2.27 (*Continued*).

decreasing voltage can be used to limit the starting current. In addition, the current and torque ripple is more obvious in steady state in this situation.

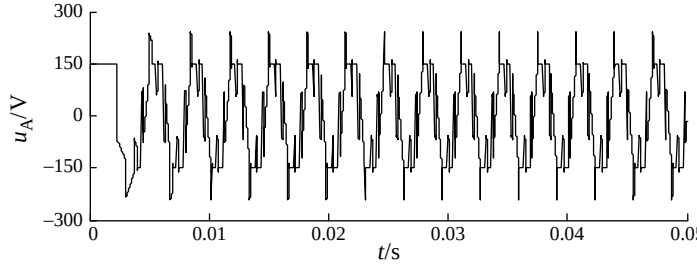
The dynamic simulation results of the BLDC motor with step load are shown in Figure 2.29.

In Figure 2.29, the motor starts with no load, and then accelerates freely to the steady state. Note that when the load increases suddenly (i.e. jumps from 0 to 6 N m at 0.025 s), the motor speed will decrease with the cycle of the phase voltage and phase current becoming longer. The increase in the current will lead to an increase of the torque so as to balance the increased load torque. In addition, the amplitudes of the current and torque ripple are also increased. When the load decreases suddenly (i.e. varies from 6 N m to 4 N m at 0.045 s), the motor speed will increase with the cycle of the voltage and current becoming shorter. Moreover, the amplitude and the ripple of the current and the torque will become smaller. As discussed above, the speed is high enough at 0.025 s, i.e. the back-EMF is large enough. So, the current cannot quickly respond to the sudden increase of the load with constant bus voltage. Hence, the change of speed is relatively slow. In this condition, the boost circuits can be used to increase the voltage so as to accelerate the response speed of the current. Similarly, when the load decreases suddenly, we can use the PWM control method to reduce the voltage of the armature winding.

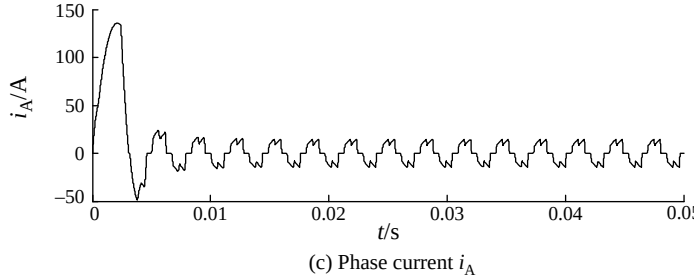
In summary, we can see that the response speed of dynamic process of BLDC motor is quick. It is mainly determined by its merits, such as high power density, large torque output and small size. In addition, the simulation results show that the torque ripple of the BLDC motor is



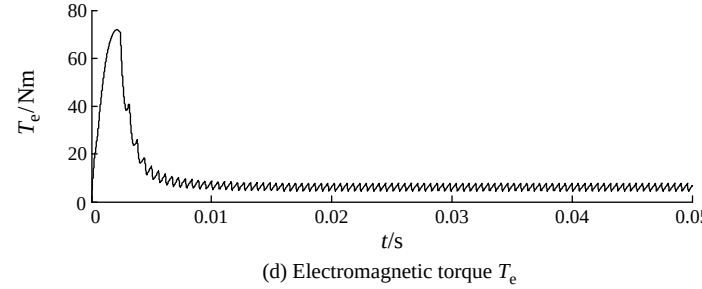
(a) Line voltage u_{AB}



(b) Phase voltage u_A

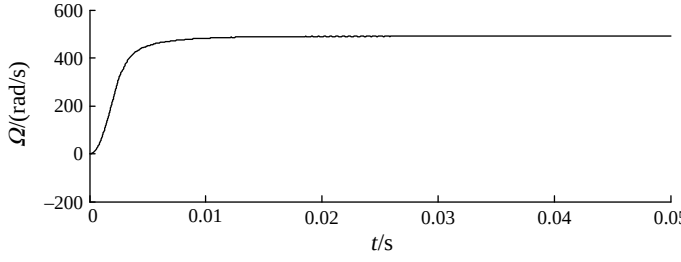


(c) Phase current i_A

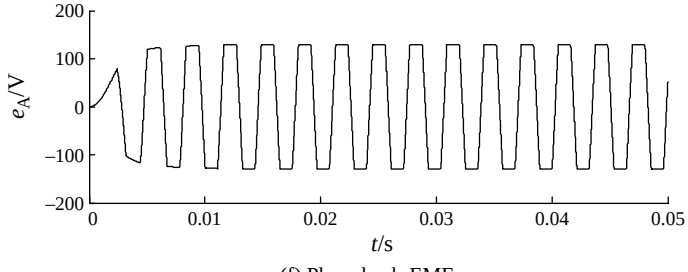


(d) Electromagnetic torque T_e

Figure 2.28 Free acceleration process with load $T_L = 6\,\text{Nm}$.



(e) Angular speed Ω



(f) Phase back-EMF e_A

Figure 2.28 (*Cotninued*).

slightly large. This shortcoming has limited its applications in high-performance driving systems. Hence, how to limit the torque ripple is one of the hot issues of the BLDC motor.

2.3.4 Load Matching

Of the various types of BLDC motors, if the motor with small mechanical time constant is coupled with large inertial load, then it will lose the advantage of having a small moment of inertia. On the other hand, when the motor with a big moment of inertia is used to drive light load, the motor efficiency may be reduced. The most important property of a BLDC motor is that it is able to meet the power converter and load requirements. From this viewpoint, we shall consider the following fundamental issues with which to select the motor suitable for a given load.

2.3.4.1 Torque Matching and Stable Running

One way to evaluate whether the torque capabilities of a motor meet the requirement of a given load is to compare its mechanical characteristic curve with the corresponding speed–torque curve of the load. At any time during acceleration or full speed, the amount of torque produced by the motor must exceed the load torque requirements. Further, to ensure the stable operation of the motor drive system, there should be a crossing point between the mechanical characteristic curve and the speed-torque curve, as shown in Figure 2.30. It should be noted that the most accurate way to obtain the speed-torque curve of the BLDC motor and a given load is from the corresponding equipment manufacture. Besides the steady-state torque and acceleration torque, the starting torque should be considered in practice too.

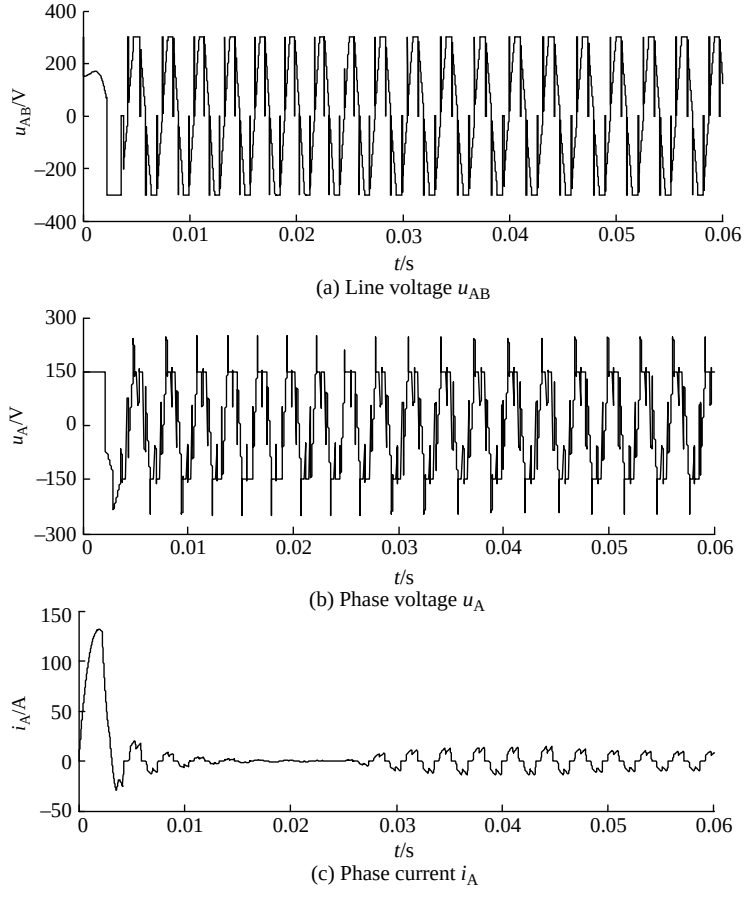
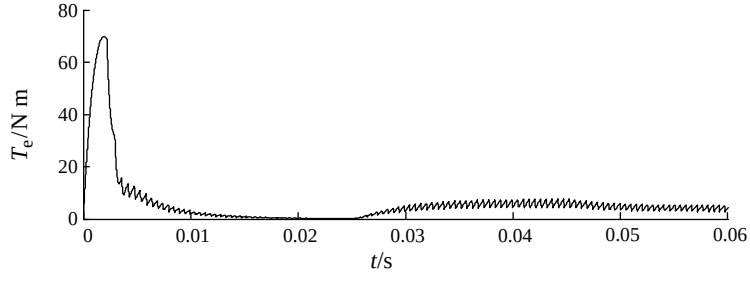


Figure 2.29 Dynamic process of the BLDC motor with step load.

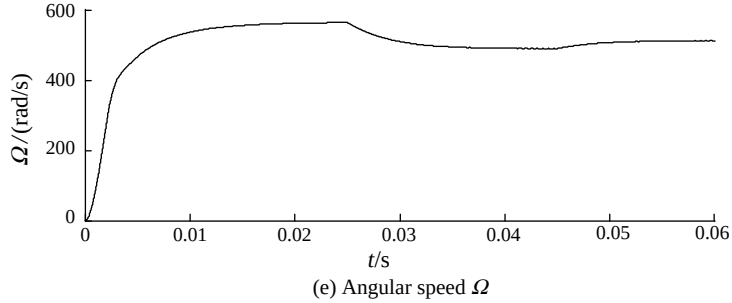
2.3.4.2 Mechanical Transmission

Generally, motor speeds and load speeds do not match up very well. This situation in the motor industry makes the requirement for mechanical transmission of some type a necessity, and most often it includes gear reduction, like in the BLDC motor application for elevator door driving. Gear reducers have been engineered over the years in many forms, complex, simple, low and high accuracy, low and high efficiency. There are also belt and pulley reducers, clutch systems, and recently more exotic systems like magnetic couplings, all with the intent of matching the motor speed to the required speed of the load.

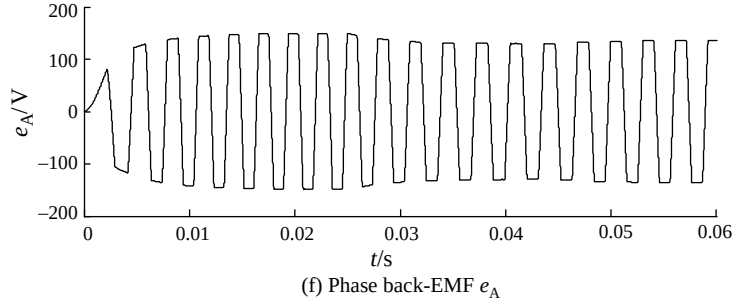
The most significant contribution of gear reducers is the multiplication of torque output of the motor, or said in reverse, the reduction of the load torque requirement by the ratio of the reducer (minus efficiency losses). Due to the relatively low cost of mechanical solutions, gear reduction is the most inexpensive way to gain torque. In high-performance systems, a torque increase comes at a relatively high price if it has to be derived directly from the motor and drive system. This is based on the cost of power electronics and permanent magnets. In this condition, in order to match the load and motor, the input to the power converter is manipulated



(d) Electromagnetic torque T_e



(e) Angular speed Ω



(f) Phase back-EMF e_A

Figure 2.29 (*Continued*).

by the controller. For further design information about the load matching of motor driving, please refer to [8] and other related books.

2.3.5 *Commutation Transients*

Note that the current and back-EMF will both change during the transient process of the commutation. Further, the interaction between them can result in commutation torque ripples.

Taking the three-phase symmetrical winding and Y-connected BLDC motor with full-bridge driving as an example, the voltage equation can be given as

$$u_x = Ri_x + (L - M)\mathrm{d}i_x/\mathrm{d}t + e_x \quad x = A, B, C \tag{2.56}$$

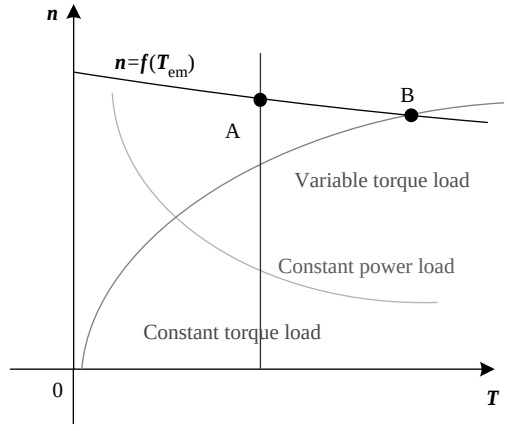


Figure 2.30 Speed–torque curves matching between BLDC motor and various loads.

where

u_x — phase voltage;
i_x — phase current;
e_x — phase back-EMF;
R — phase resistance;
L — self-inductance of phase winding;
M — mutual inductance of phase winding.

And the electromagnetic torque equation is

$$T_e = (e_A i_A + e_B i_B + e_C i_C)/\Omega \tag{2.57}$$

where Ω is the mechanical angular speed of the motor.

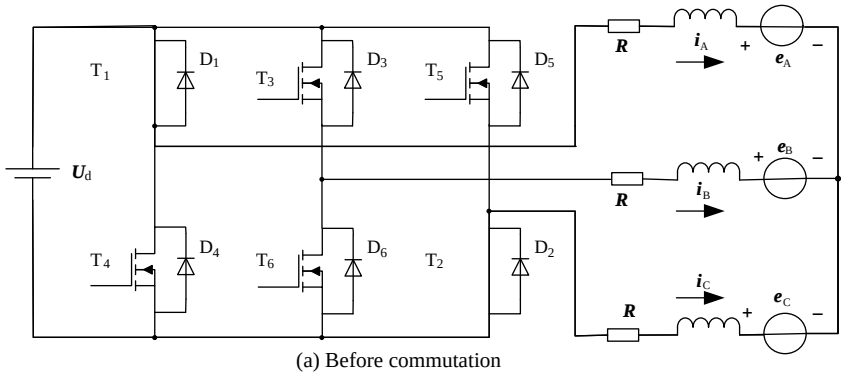
From Equation (2.57), we can see that in order to maintain the electromagnetic torque constant, the sum of $e_A i_A$, $e_B i_B$ and $e_C i_C$ must be constant when the speed is kept constant. Assume that the air-gap magnetic field in the motor is the ideal trapezoidal wave with same distributed shape as the back-EMF. Therefore, the armature current i_x must be square wave and in phase with e_x so as to maintain the torque constant.

For the three-phase BLDC motor with full-bridge driving, only two phases of the armature windings are conducted with the other phase nonenergized during the steady state, as shown in Figure 2.31(a).

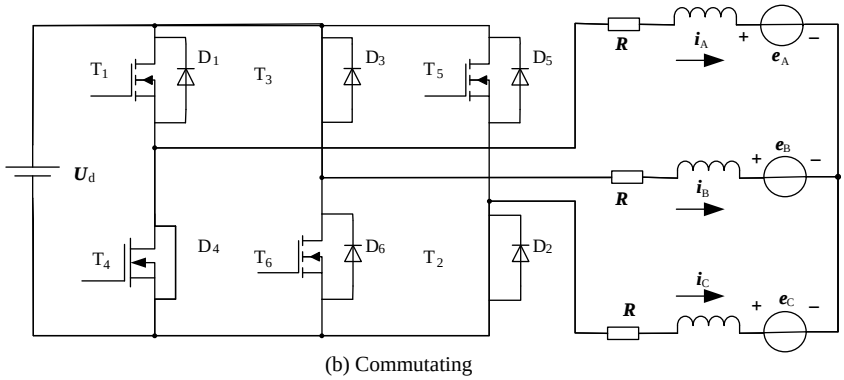
Assume that phases A and C are conducted before commutation, then $i_C = -i_A$, $i_B = 0$, $e_C = -e_A$, so it can be derived from Equation (2.57) that

$$T_e = 2e_C i_C/\Omega \tag{2.58}$$

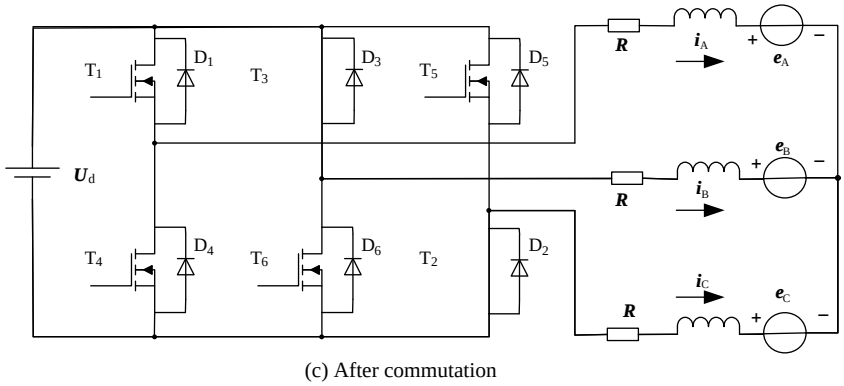
Furthermore, assume that $i_C = -I$, $e_C = -E$, then the electromagnetic torque $T = 2EI/\Omega$ is the average torque. After the controller sends out the commutation signals, T_1 will turn off with T_3 conducted, as shown in Figure 2.31(b).



(a) Before commutation



(b) Commutating



(c) After commutation

Figure 2.31 The diagram of commutation.

Hence, if the phase resistance is ignored and the back-EMF is assumed to be the ideal trapezoidal wave, the change of the phase currents can be represented as

$$\begin{cases} \dfrac{\mathrm{d}i_{\mathrm{A}}}{\mathrm{d}t} = -\dfrac{U_{\mathrm{d}} + 2E}{3(L-M)} \\ \dfrac{\mathrm{d}i_{\mathrm{B}}}{\mathrm{d}t} = \dfrac{2(U_{\mathrm{d}} - E)}{3(L-M)} \\ \dfrac{\mathrm{d}i_{\mathrm{C}}}{\mathrm{d}t} = -\dfrac{U_{\mathrm{d}} - 4E}{3(L-M)} \end{cases} \tag{2.59}$$

Since the duration of commutation is very short, then we can assume that $e_A = E$ in this process. The relationship between the phase currents and the time at the moment of commutation can be derived from Equation (2.59) as

$$\begin{cases} i_A = I - \dfrac{U_d + 2E}{3(L-M)}t \\ i_B = \dfrac{2(U_d - E)}{3(L-M)}t \\ i_C = -I - \dfrac{U_d - 4E}{3(L-M)}t \end{cases} \tag{2.60}$$

At this moment, i_A still exists. Thus, the current will flow through the freewheeling diode until i_A decreases to zero, as shown in Figure 2.31(c). During this process, i_B increases from zero to I, and still satisfies

$$i_A + i_B + i_C = 0 \tag{2.61}$$

After the commutation, $i_A = 0$, $i_C = -i_B$. We define t_1 as the time for i_A decreasing from I to 0, whereas t_2 as the time for i_B increasing from 0 to I. The corresponding variation process of each phase current is shown in Figure 2.32.

From Equation (2.58) we can know that the torque is proportional to $e_C i_C$ before commutation. During the process of commutation, amplitude of i_C is greater than I when $t_1 > t_2$ (see Figure 2.32(a)). When $t_1 = t_2$ (see Figure 2.32(b)), the amplitude of i_C remains constant. And when $t_1 < t_2$ (Figure 2.32(c)), the amplitude of i_C is less than I. Thus, from Equation (2.60) we can get the time for i_A decreasing from I to 0 as

$$t_{fa} = \frac{3(L-M)I}{U_d + 2E} \tag{2.62}$$

After t_{fa} passed, i_B can be given as

$$i_B(t_{fa}) = \frac{2(U_d - E)}{U_d + 2E}I \tag{2.63}$$

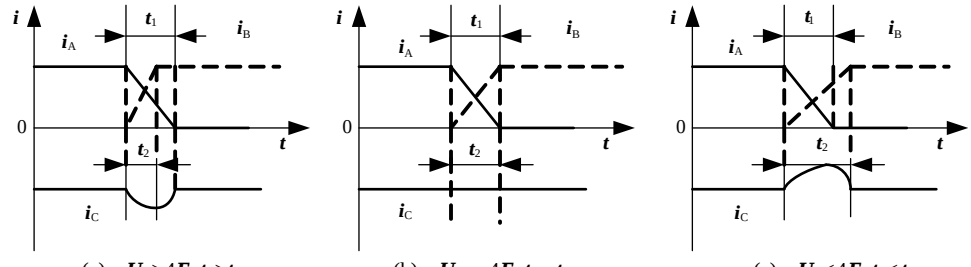


Figure 2.32 Phase current in commutation under different conditions.

From Equation (2.63) we can obtain the following conclusions during the commutation:

(1) When $U_d > 4E$, $t_1 > t_2$, the torque increases.
(2) When $U_d = 4E$, $t_1 = t_2$, the torque remains constant.
(3) When $U_d < 4E$, $t_1 < t_2$, the torque reduces.

Thus, when $U_d = 4E$, changes of amplitude of i_C can be avoided so that the commutation torque ripple will not appear. However, $U_d = 4E$ is not the steady state of the motor. In this condition, the motor is in acceleration. The back-EMF E will increase with the increasing of the motor speed such that $U_d < 4E$. Therefore, even in the steady state, commutation torque ripple still exists in the BLDC motor, which is related to the speed [10]. Hence, by choosing a proper commutation strategy, such as advanced conducting of the phase current and the PWM modulation method, we can limit the commutation torque ripple to some extent.

Questions

1. What is the use of position sensor in BLDC motors?
2. List at least four driving circuits for the BLDC motor control system and summarize their advantages and disadvantages.
3. Try to model a BLDC motor with differential equation, transfer equation and state-space equation, respectively, in MATLAB.
4. Explain why the current of the BLDC motor is larger at the starting time than that at the steady state?
5. In what condition can the BLDC motor achieve its maximum efficiency?
6. Why does the narrow pulse exist in the voltage waveform during the control of BLDC motors?
7. Give some methods for limiting the commutation torque ripple of BLDC motors.
8. Present some practical techniques of load matching for BLDC motor driving.

References

1. Walter, N. A., Stephen, L. H. (2003) *Electric Motor Control*. Thomson/Delmar Learning, Australia.
2. Xie, B. C., Ren, Y. D. (2005) *DSP Control Technology and Its Application of Motor.* Beihang University Press, Beijing (in Chinese).
3. Fu, Q., Lin, H., He, B. (2006) A novel direct current control of four-switch three-phase brushless DC motor. *Journal of Chinese Electrical Engineering Science*, **26**(4), 148–153 (in Chinese).
4. Krause, P. C. (1986) *Analysis of Electric Machinery.* Kinsport Press Inc., Kinsport Town.
5. Pillay, P., Krishnan, R. (1989) Modeling, simulation, and analysis of permanent-magnet motor drives, part II: the brushless DC motor drive. *IEEE Transactions on Industry Application*, **25**(2), 274–279.
6. Pillay, P., Krishnan, R. (1989) Modeling, simulation, and analysis of permanent-magnet motor drives, part I: the permanent-magnet synchronous motor drive. *IEEE Transactions on Industry Application*, **25**(2), 265–273.
7. Gao, J. D., Wang, X. H., Li, F. H. (2005) *AC Motor and Its Analysis*. (2nd edn). Tsinghua University Press, Beijing (in Chinese).
8. Kenjo, T., Nagamori, S. (1985) *Permanent Magnet and Brushless DC Motors*. Oxford University Press, New York.
9. Ye, J. H. (1982) *BLDC Motor.* Science Press, Beijing (in Chinese).
10. Xia, C. L., Wen, D., Wang, J. (2002) A new approach of minimizing commutation torque ripple for brushless DC motor based on adaptive ANN. *Journal of Chinese Electrical Engineering Science*, **22**(1), 54–58 (in Chinese).

3

Simulation for BLDC Motor Drives

The research of motor control systems has high requirements for hardware and experimental conditions. Moreover, some experiments may cause damage to the motor and other equipment, which to some degree increases the cost of the research, and also brings great difficulty to the experiment. The introduction of computer simulation can effectively help to reduce such difficulties. When applied in modern motor control systems, computer simulation plays a significant role in helping researchers to design and analyze control system more conveniently, as well as quickening product development and cutting down the cost of research. At present, the software commonly used in simulation for motor control systems involves MATLAB/Simulink, ACSL, SPICE, Saber, etc., among which MATLAB/Simulink has fairly wide application. Simulink has a specific toolkit for motor control system simulation, and its demos cover almost all the common types of DC and AC driving system, including the models of high-performance motor control strategies, such as vector control, direct torque control, etc. In addition, Simulink has a user-friendly interface, an easy operation method, and strong capability of data analysis based on MATLAB, all of which are vital to its wide application. This chapter mainly introduces the example of a BLDC motor control system model based on MATLAB 7.1/Simulink 6.3, and then the corresponding analysis of system performance is given in accordance with the simulation.

3.1 S-Function Simulation

An S-function is a computer language description of a Simulink block, which can be used to expand the simulation capability of Simulink. It can be written in MATLAB language, as well as in computer languages such as C, C++, Ada, FORTRAN, etc. S-functions are compiled by MATLAB as MEX-files, and then will become dynamic linking subfunctions that MATLAB can automatically call and execute. Users can also construct their own S-function models to realize the function that is not found in the Simulink standard modules, so that the function of the simulation models will be more complete and more customized.

Permanent Magnet Brushless DC Motor Drives and Controls, First Edition. Chang-liang Xia.
© 2012 Science Press. Published 2012 by John Wiley & Sons Singapore Pte. Ltd.

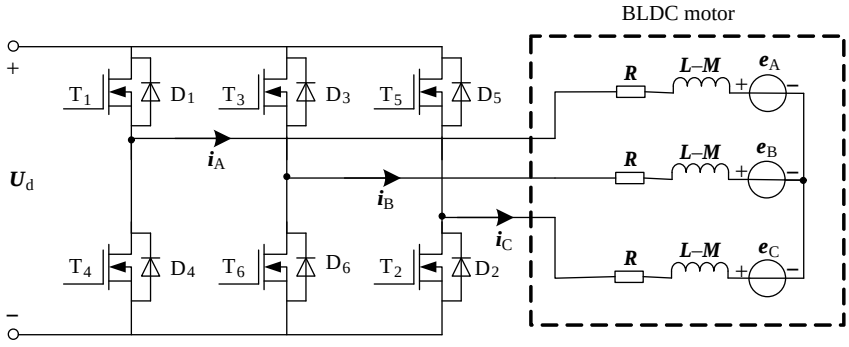


Figure 3.1 The structure of a BLDC motor simulation system.

The S-function simulation example in this chapter is written in MATLAB language. The structure of the simulation system is shown in Figure 3.1.

In the model, the commutation logic control and the motor are both realized by S-function programming, and they are respectively masked as two subsystems: "Control" and "BLDC_Motor". The whole simulation model of BLDC motor control system is shown in Figure 3.2.

In the Figure 3.2, the module "Memory" is mainly used to delay the output Hall signal of the motor with an integral step, so as to avoid algebraic loop in the simulation.

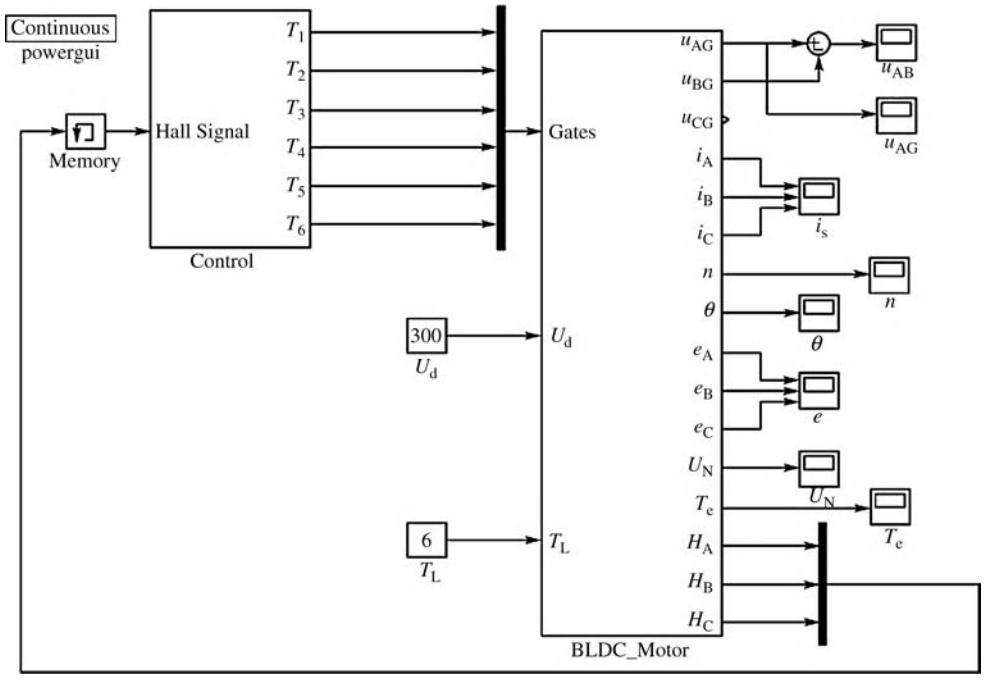


Figure 3.2 S-function simulation model for a BLDC motor control system.

The core of the subsystem "BLDC_Motor" is an S-function module named "BLDC_Motor", whose inputs include:

(1) The gate signal, Gates, is a vector, and its elements are the signals T_1, T_2, . . ., and T_6, which correspond to the gate signals of power devices in Figure 3.1. According to the output signals of Hall position sensors and the control algorithm, the subsystem "Control" calculates the values of T_1, T_2, . . ., and T_6, which are Boolean variables, namely 0 or 1.
(2) The DC voltage U_d of the bridge inverter is given by a constant module in Figure 3.2, and thus its value can be adjusted as needed.
(3) The load torque T_L is also given by a constant module and thus it is adjustable.

And the outputs of the "BLDC_motor" module include:

(1) Three phase to ground voltages u_{AG}, u_{BG} and u_{CG}.
(2) Phase currents i_A, i_B and i_C.
(3) The rotor speed n.
(4) The rotor position angle θ, which stands for the angle between the rotor d-axis and the axis of phase-A winding of the stator.
(5) The phase back-EMF of the windings e_A, e_B and e_C.
(6) The neutral to ground voltage U_N of the three phase windings.
(7) The electromagnetic torque T_e.
(8) The output signals of Hall position sensors H_A, H_B and H_C.

The variables in the model are all in SI unit except the rotor speed, whose unit is r/min. Signal variables, including Hall signal and gate signal, have no units.

Double click the module "BLDC_Motor", and there pops up a dialog box for parameter setting, as shown in Figure 3.3.

The parameters of the motor mainly include:

(1) Stator resistance $R(\Omega)$, inductance L(H), mutual inductance M(H) and the back-EMF coefficient of each phase of the motor K_e (V/(rad/s)).
(2) Number of pairs of poles p, moment of inertia J (kg m^2).
(3) Torque at no load T_0 (N m), the rotor angle at start-up θ_0 (rad).
(4) Viscous friction coefficient B_v (N m s), starting friction torque T_{b0} (N m).
(5) The voltage of the MOSFET while conducting V_T(V), the voltage of the freewheeling diode while conducting V_D(V).

The main calculating process of the S-function corresponding to the module "BLDC_Motor" is shown as follows:

(1) The calculation of back-EMF and Hall signal [1]. This is chiefly achieved by the lookup table, among which the calculation of the peek value of back-EMF is shown as Equation (2.12), and the lookup function corresponds to the back-EMF waveform distribution function as shown in Figure 2.13.
(2) Calculate the differential of the current state variable. The modeling of a BLDC motor needs to choose three phase currents, rotor speed and angle as state variables. The aim of

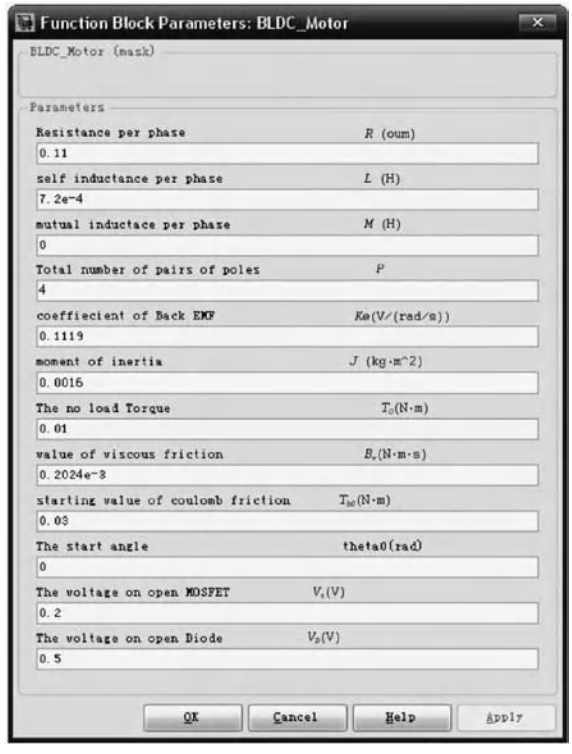


Figure 3.3 A BLDC motor simulation parameter setting.

this part is to calculate the differential of currents. During this process, all the running conditions should be taken into consideration before categorization on the basis of the values of T_1, T_2, . . ., and T_6. In order to avoid the situation that two power devices on the same bridge are conducting at the same time, we should make sure of T_1 & $T_4 = T_3$ & $T_6 = T_5$ & $T_2 = 0$. Now set the flag variable as

$$\text{flag} = (T_1|T_4) \times 4 + (T_3|T_6) \times 2 + (T_5|T_2) \tag{3.1}$$

Hence, the value of flag is an integer between 0 and 7, which represent 8 operating states of the inverter, as shown in Table 3.1.

It can be seen from Table 3.1 that according to the different operating modes (120° conducting or 180° conducting) of the inverter, when the PWM control mode and the setting of dead zone are taken into account, the motor can be operated at any one of the 8 states mentioned above. Thus, the windings of the motor can be in one of the conducting states like no phase conducting, only one phase conducting, only two phases conducting and all the three phases conducting. The state that only two phases are conducting is rather common when the ON_PWM control mode is implemented, in which case the circuit is fairly complicated. Now take the situation that flag = 2 for an example.

The fact that flag = 2 indicates that the upper bridge or the lower bridge of the phase B is conducted, and thus the input voltage of phase B is easily obtained. To begin with, it is

Table 3.1 The operating states of the BLDC motor inverter

Flag	Conducting state
0	No power device of the inverter conducting, no input voltage in any of the three phase windings.
1	T_1, T_3, T_4 and T_6 turned off, phase A and phase B open or freewheeling, phase C conducted.
2	T_1, T_2, T_4 and T_5 turned off, phase A and phase C open or freewheeling, phase B conducted.
3	T_1 and T_4 turned off, phase A open or freewheeling, phase B and phase C conducted.
4	T_2, T_3, T_5 and T_6 turned off, phase B and phase C open or freewheeling, phase A conducted.
5	T_3 and T_6 turned off, phase B open or freewheeling, phase A and phase C conducted.
6	T_2 and T_5 turned off, phase C open or freewheeling, phase A and phase B conducted.
7	When there is a power device conducting in each phase of the inverter or when the three upper bridges are conducting at the same time, there is no input voltage in the three phase windings; in other cases, there are input voltages.

judged according to the value of the signal T_3. If the upper bridge is conducted, then

$$u_{BG} = U_d - V_T \tag{3.2}$$

Otherwise, the lower bridge is conducted, and the terminal voltage of phase B is

$$u_{BG} = V_T \tag{3.3}$$

In this condition, the phase working in PWM control modes, either phase A or phase B, is at PWM low level, during which the current flows through the freewheeling diodes. The other phase is open or in the state of commutation with freewheeling diodes. According to the different states of circuit mentioned above, the phase current and terminal voltage of each phase can be determined, and together with motor parameters and the three-phase back-EMF calculated in stage (1), the derivative of current can be solved. In the program, the phase with zero crossing current is simplified, both current and derivative of current are set 0. In the mode of unilateral modulation, with the coaction of neutral point voltage jump and back-EMF of the windings, the terminal voltage of the unexcited phase will be higher than U_d or become negative, which cause the current to flow through another freewheeling diode of this bridge and increase inversely, thus forming the back-EMF current, as shown in Figure 3.4.

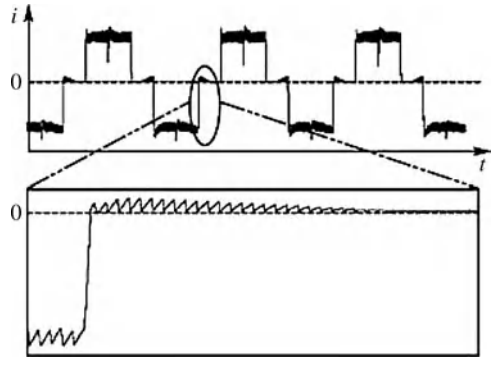


Figure 3.4 The back-EMF current.

Table 3.2 Phase currents relationship

	$i_A = 0$	$i_A > 0$	$i_A < 0$
$i_C = 0$	As the sum of three phase current is 0, thus $i_B = 0$, and the motor is at the moment of start-up.	Phase C is turned off; phase A is at the low level of PWM, and freewheels through D_4; $i_B = -i_A$.	Phase C is turned off, phase A is at the low level of PWM, and freewheels through D_1; $i_B = -i_A$.
$i_C > 0$	Phase A is turned off; phase C is at the low level of PWM, and freewheels through D_2; $i_B = -i_C$.	Transient process during which phase C freewheels though D_2 and phase A freewheels through D_4; $i_B = -(i_A + i_C)$.	Transient process during which phase C freewheels though D_2 and phase A freewheels through D_1; $i_B = -(i_A + i_C)$.
$i_C < 0$	Phase A is turned off; phase C is at the low level of PWM, and freewheels through D_5; $i_B = -i_C$.	Transient process during which phase C freewheels though D_5 and phase A freewheels through D_4; $i_B = -(i_A + i_C)$.	Transient process during which phase C freewheels though D_5 and phase A freewheels through D_1; $i_B = -(i_A + i_C)$.

The circuit state is closely related to the intensity and direction of current. Take the freewheeling phase for example, and then when the current decreases to 0, the structure of the circuit changes as the freewheeling diode closes, resulting in the neutral point voltage and terminal voltage jump, and consequently the derivative of current jump. While the motor is running, the value of current is shown in Table 3.2.

To calculate the differential of the current under different circumstances, it is necessary to obtain the relevant voltage variable in advance. This calculation process can be performed on the basis of categorized analysis of Table 3.2. Take the circumstance that $i_A = 0$, $i_C > 0$ for example. In this case, the current freewheels through the diode in phase C, thus

$$u_{CG} = -V_D \tag{3.4}$$

$$U_N = ((u_{BG} + u_{CG}) - (e_B + e_C))/2 \tag{3.5}$$

$$U_{AG} = U_N + e_A \tag{3.6}$$

According to the voltage equation, the differential of the currents in phase B and phase C are, respectively, given as

$$\frac{di_B}{dt} = ((u_{BG} - U_N) - e_B - R \times i_B)/(L - M) \tag{3.7}$$

and

$$\frac{di_C}{dt} = ((u_{CG} - U_N) - e_C - R \times i_C)/(L - M) \tag{3.8}$$

Note that once the current of the nonexcited phase decreases to zero, it will remain zero before the next conducting instant. So, the differential of the current is also zero, namely

$$\frac{\mathrm{d}i_{\mathrm{A}}}{\mathrm{d}t} = 0 \tag{3.9}$$

Similarly, the corresponding voltage variable and state variable differential can be calculated for other conditions of i_{A} and i_{C}.

(3) The calculation of torque and angular speed. With the calculated three phase currents and back-EMF, the electromagnetic torque is given as

$$T_{\mathrm{e}} = p \times K_{\mathrm{e}} \times (f_{\mathrm{A}} \times i_{\mathrm{A}} + f_{\mathrm{B}} \times i_{\mathrm{B}} + f_{\mathrm{C}} \times i_{\mathrm{C}}) \tag{3.10}$$

The angular speed is also a state variable, and its state equation can be obtained according to the motion equation of the motor. Note that the motion state of the motor is relevant to the characteristic of the load. Here, the load is assumed to be a frictional constant torque load. At the instant of start-up, the electromagnetic torque has to offset the static friction and the load torque. Thus, the differential of angular speed is given as

$$\frac{\mathrm{d}\Omega}{\mathrm{d}t} = (\mathrm{sgn}(T_{\mathrm{e}}) \times (\mathrm{abs}(T_{\mathrm{e}}) - (T_{\mathrm{L}} + T_0) - T_{\mathrm{b0}}))/J \tag{3.11}$$

When the angular speed is not equal to zero, the static frictional force in Equation (3.11) turns into the sliding frictional force, so

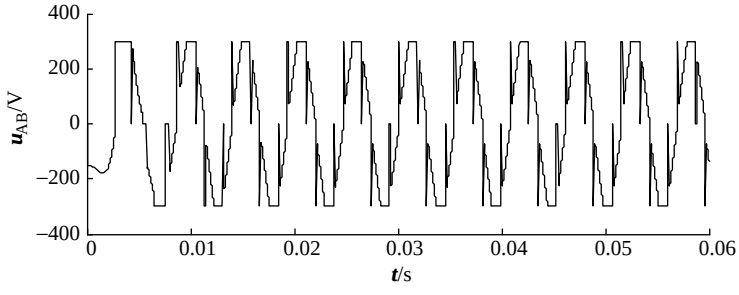
$$\frac{\mathrm{d}\Omega}{\mathrm{d}t} = (T_{\mathrm{e}} - \mathrm{sgn}(\Omega) \times T_{\mathrm{L}} - T_0 - B_{\mathrm{v}} \times \Omega)/J \tag{3.12}$$

The simulation results for open-loop operation of the motor are shown in Figure 3.5.

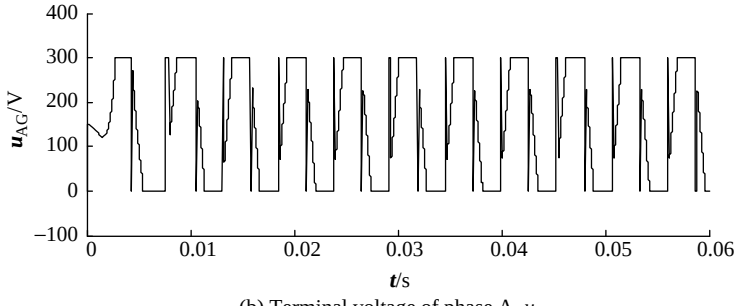
It can be seen from Figure 3.5 that, when no measures are taken to limit the current, both the current and torque are too big at start-up, and the speed will rise to its maximum in a rather short period of time. Due to the high speed, the compound back-EMF of the two windings are greater than the line back-EMF, so the bus current flows from the motor to the power source. Thus, the electromagnetic torque becomes negative and the motor works at braking state. In this situation, the mechanical energy of the rotor is transformed into electrical energy stored in the source, and the rotor speed starts to decrease. When the compound back-EMF is once again lower than the line voltage on decreasing the rotor speed, the current begins to flow from the source to the windings again. Thus, the electromagnetic torque becomes positive, and the motor operates as a motor again.

3.2 Graphical Simulation

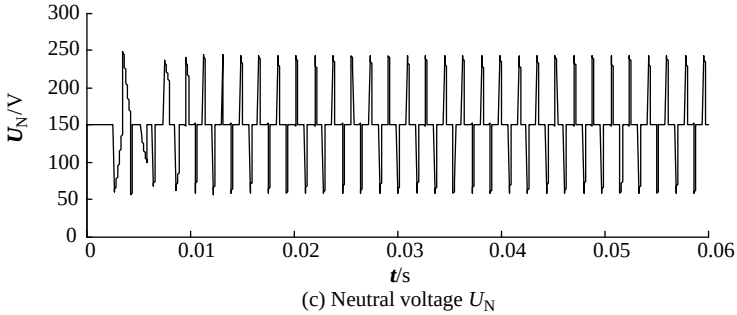
Simulink can employ all sorts of modules arranged as libraries to achieve dynamic system graphical modeling. Besides the commonly used modules, Simulink provides module libraries in the form of the toolbox for different research areas, including the power system simulation library SimPowerSystem.



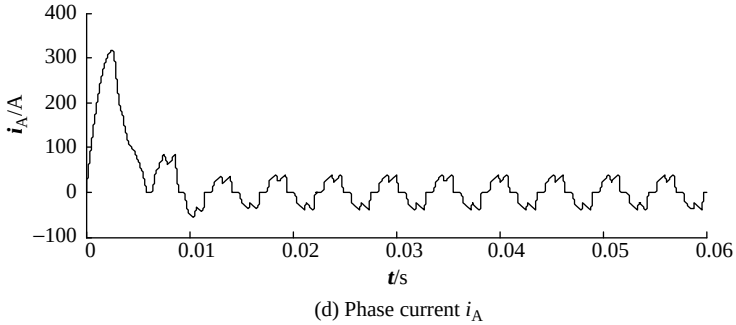
(a) Line voltage u_{AB}



(b) Terminal voltage of phase A, u_{AG}

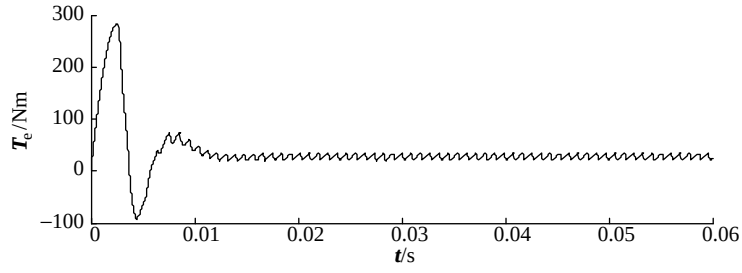


(c) Neutral voltage U_N

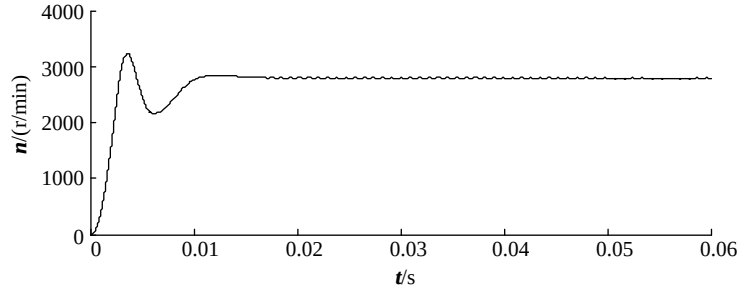


(d) Phase current i_A

Figure 3.5 Simulation results of BLDC S-function modeling.



(e) Electromagnetic torque T_e



(f) Rotor speed n

Figure 3.5 (*Continued*)

The SimPowerSystem library offers fairly accurate models of many components used in power systems, such as power sources, transformers, motors, loads, etc. In the meantime, it provides libraries of specific application systems, including various motor drive system models. Moreover, it is a GUI-based tool with intuitive graphics capability and excellent data-processing ability. Users can use SimPowerSystem for the modeling of motor drive systems, as well as control strategies design, real-time recording of motor variables and qualitative or quantitative performance analysis of the motor operation. Note that when the SimPowerSystem library is employed for modeling, the following have to be paid attention to:

(1) The connection between electrical models and the common Simulink models. The terminals of the modules in SimPowerSystem are usually denoted by the sign "□", while the terminals of the ones in Simulink are usually denoted by the sign ">". These two types of terminals cannot be connected directly. Some "interface modules", like controlled modules or measuring modules are used for the connection between them. For example, the output signals of the sources in Simulink, such as sinusoidal, stepping and constant ones, must be transformed by controlled modules before they are connected to modules in Powerlib, like inductance and capacitance. By contrast, signals like voltage and current in electrical modules must be transformed by measuring modules before being connected to modules in Simulink like "Math Operations" or "Sinks".
(2) The measurement of voltage and current. In electrical models, branch voltage and current are usually measured by voltage and current measurement modules or a multimeter module. There is a positive or negative sign marked at the terminals of voltage and current measurement modules, so that the polarity of the measured signal can be judged conveniently. Slightly different from that, a multimeter module needs to select the

pull-down menu in the parameter setting dialog of the electrical module, and then the voltage and current signals are chosen to be measured. So that they will be displayed in the multimeter module, which are ready to be selected by users.

(3) The connection of inductance and capacitance. Inductance cannot be directly connected in series with a current source, while capacitance cannot be in parallel connection directly with a voltage source. If the above direct connections are inevitable in the modeling, the inductance and capacitance can be connected in parallel with a certain resistance before they are connected.

3.2.1 Simulation of Double Closed-Loop Speed-Control System

Since double closed-loop speed-control system is one of the most common motor control systems, an example of the modeling for a BLDC motor double closed-loop speed-control system based on SimPowerSystem is given below. The block diagram of the simulation system is shown in Figure 3.6.

The whole system is comprised of four parts:

(1) The main power circuit. It is a VVVF AC–DC–AC circuit, mainly including a three-phase AC voltage source, a bridge rectifier, a bridge inverter and a DC filtering capacitance. The RMS value of line voltage of a three-phase AC voltage source is 217 V, and its frequency is 50 Hz. Both the rectifier and inverter are implemented by the "Universal Bridge" module in SimPowerSystem, and the value of the DC filtering capacitance is set to 4400 μF.

(2) The motor. The module "Permanent Magnetic Synchronous Motor" is selected with the waveform of air-gap magnetic flux density being trapezoidal and the width of its flat part is 120 electrical degrees.

(3) Measurement unit. This unit consists of several bus-selecting modules "Bus Selector", which is used to measure the variables of the motor when it is operating, such as voltage, current and rotor speed.

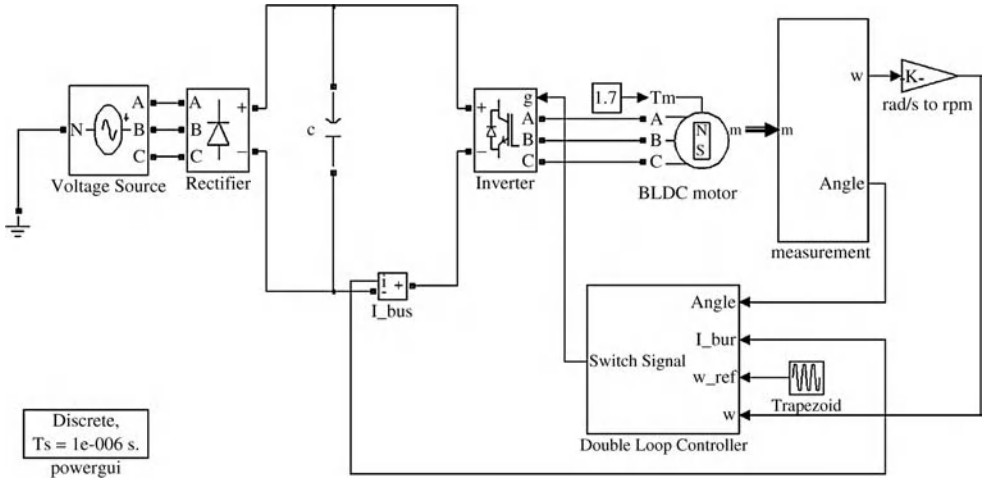


Figure 3.6 The block diagram the of BLDC motor double closed loop speed-control system.

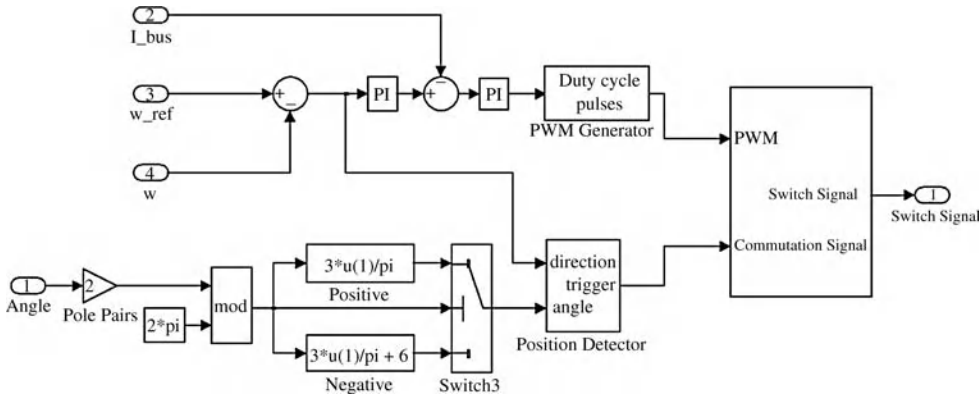


Figure 3.7 Double closed-loop controller module diagram.

(4) Controller unit. Double closed-loop speed regulation is implemented by the subsystem named "Double Loop Controller". Its input variables are the rotor position angle, the bus current, the reference and measured speed, and it outputs six PWM pulses, of which the frequency is 20 kHz, to the bridge inverter. The related block diagram of the controller is shown in Figure 3.7.

Through the logic AND operation between the commutation signal and the PWM signal of the BLDC motor, the controller will obtain the gate signal, which determines whether the inverter is on or off. The commutation signal is obtained by detecting the rotor position angle, which is transferred to the "Position Detector" unit after complementation and absolute value operation. In order to implement the electromagnetic braking and motor reversing rotation, the "Position Detector" unit must be able to determine whether the controller adopts forward rotation or reversing rotation commutation according to the error between the reference speed and the measured speed. When the speed is too high, electromagnetic braking can be achieved only by changing the commutation sequence, so as to decrease the speed.

When two of the three windings of the motor are excited, the rotor will possibly be pulled to one of the six different space positions, as shown in Table 3.3. Thus, the commutation sequence of the module "Permanent Magnetic Synchronous Motor" is determined.

According to Table 3.3, the schematic diagram of space vector of the BLDC motor can be obtained, as shown in Figure 3.8. In Figure 3.8, the space of 360 degrees of electrical angle is divided by the current space vector into six sectors, which are labeled by 0, 1, 2, 3, 4 and 5, respectively. The current space vector I_{CB} is located at the 0° axis, which is the reference position of rotor angle. During simulation, the position of the rotor at any instant is transformed into the label of the corresponding sector. According to this label and the direction command, the subsystem "Position Detector" outputs the commutation signal.

Table 3.3 Conducting phase and rotor position of the BLDC motor

Conducting phase	AB	AC	BC	BA	CA	CB
Rotor position angle (rad)	$\pi/3$	$2\pi/3$	π	$4\pi/3$	$5\pi/3$	2π

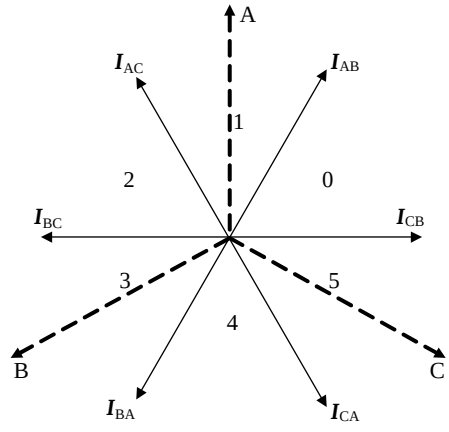


Figure 3.8 The BLDC motor current space vector.

The PWM signal is generated by the subsystem "PWM Generator", and its duty cycle is calculated by a PI controller of the current loop.

Figure 3.9 is the simulation results of the BLDC motor double closed-loop speed-control system with a constant reference speed.

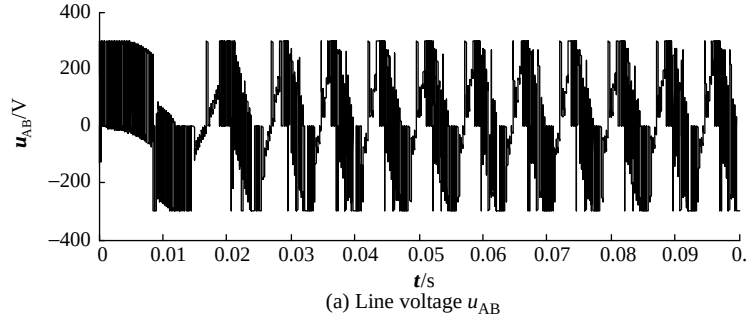
In the figure, the reference speed is 2000 r/min, and the motor starts with a rating load. Compared with the simulation waveforms in Figure 3.5, the waveforms of the line voltage and terminal voltage of double closed-loop control are PWM waveforms, the envelope of which is the same as the voltage waveform in Figure 3.5. The equivalent voltage of the winding is determined by the duty cycle of PWM.

In the simulation system, the output of the speed PI controller is limited within twice the rated current. From Figure 3.9, it can be seen that during the start-up procedure the phase current arrives at the limited value within a rather short period of time, so that the motor starts at the permitted highest current. The torque changes in the same way as that of the amplitude of current. This means that during the start-up procedure the torque arrives at its permitted highest value, and then with increasing speed and decreasing current, it decreases gradually until settling down to the load torque. As they are limited, the current and torque are lower than they are at open-loop operation during the start-up procedure. Thus, the rotor acceleration is smaller and a longer time is necessary for getting to the rated speed.

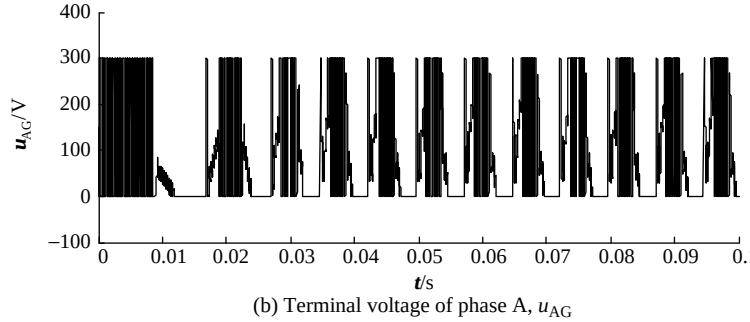
Figure 3.10 shows the simulation results at the condition that the reference speed is a ramp signal and the load changes from 0 to the rated value at 0.05 s.

In Figure 3.10, the reference speed varies from 0 to 2000 r/min during a period of 0.04 s. The change of line voltage and terminal voltage is similar to that in Figure 3.9. They are all PWM waveforms, and the cycle of its envelope reduces with increasing speed.

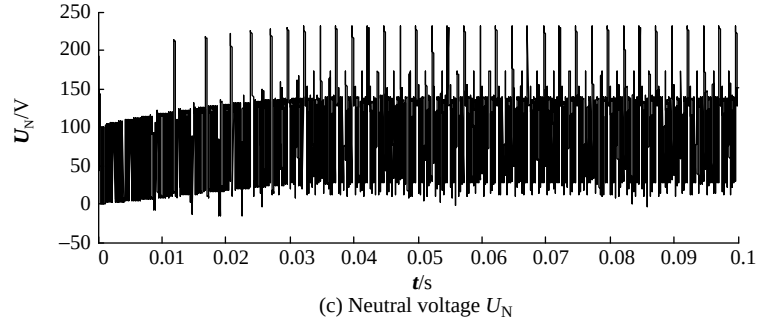
As the motor starts with no load, and the reference speed is the ramp signal, the starting current is rather small. When the rotor has finished its accelerating procedure and the load torque is still 0, the current is about 0. If the load changes to the rated value, the current will increase quickly. During the start-up procedure, the rotor approximately rotates with constant acceleration, and thus the torque remains constant before 0.04 s. When the load changes suddenly, the electromagnetic torque increases with ascending current, so that the torque can



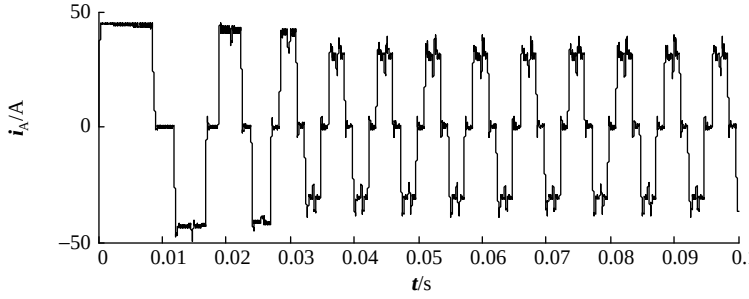
(a) Line voltage u_{AB}



(b) Terminal voltage of phase A, u_{AG}

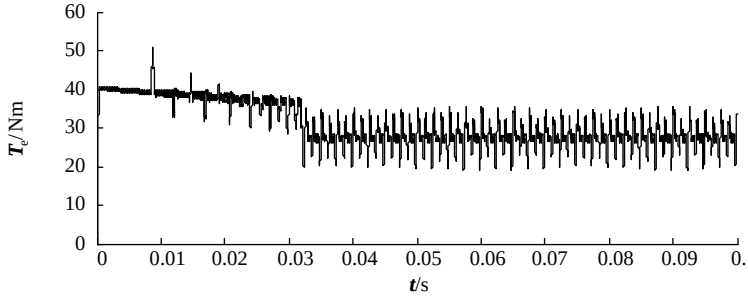


(c) Neutral voltage U_N

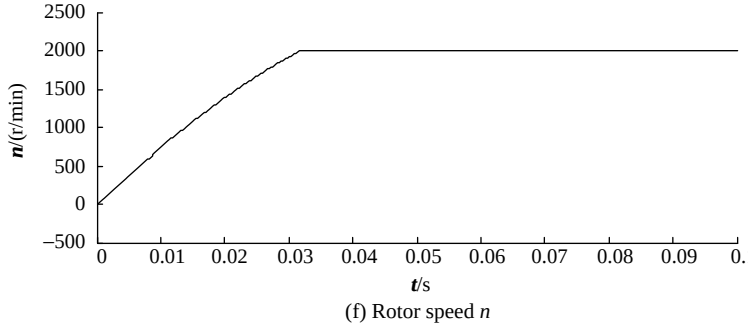


(d) Phase current i_A

Figure 3.9 Start-up process simulation of the motor with constant reference speed.



(e) Electromagnetic torque T_e



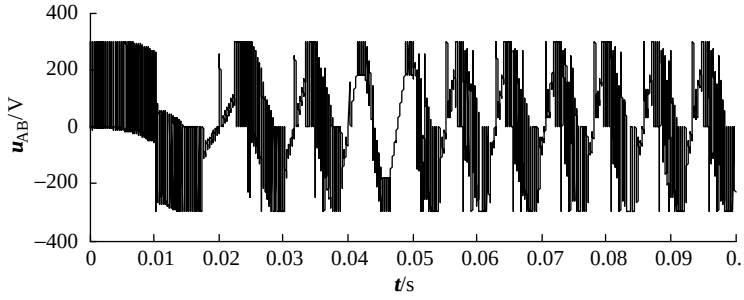
(f) Rotor speed n

Figure 3.9 (*Continued*)

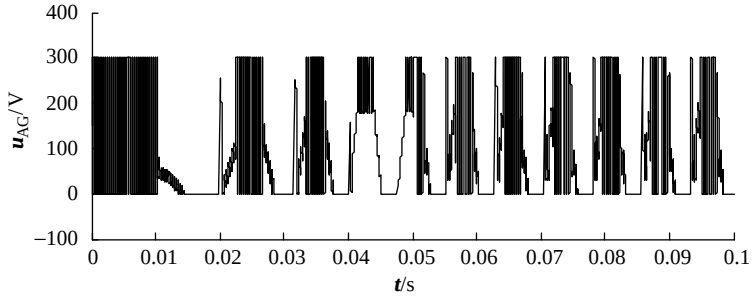
be adjusted quickly. From Figure 3.10, it can be concluded that under the control of the double closed-loop controller, the speed can track its reference fairly well when the motor runs with no load. The moment the load increases, the speed begins to decrease, and then the speed is increased by increasing the output duty cycle of PWM. Thus, under the control of a PI controller, nonstatic error control will be achieved. Moreover, this process will get faster with appropriate parameter selection by the PI controller. So, it can be summarized that the BLDC motor has a rather quick response and strong antidisturbance ability when controlled in double closed-loop mode.

3.2.2 Advanced Conduction of Phase Current for BLDC Motor Control

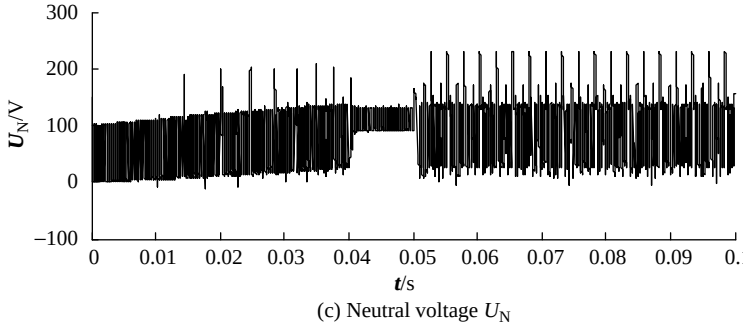
When the reference speed is lower than the rated value, speed regulation can be achieved by changing the terminal voltage of the windings. However, when the reference speed is higher than the rated value, the back-EMF is fairly high, and the voltage of the winding can no longer be increased. So that the windings current is not enough to generate higher torque, this will cause the difficulty of increasing the speed of the motor. Thus, the range of speed is restricted. Therefore, the key of speed regulation above the rated value is to avoid the restriction of current increasing imposed by back-EMF. For a separately excited DC motor, the main magnetic field can be attenuated by adjusting the exciting current, so that the back-EMF is decreased, and the rotor speed is increased. For a permanent magnetic synchronous motor, field weakening and speed increasing will be achieved with the current vector control method.



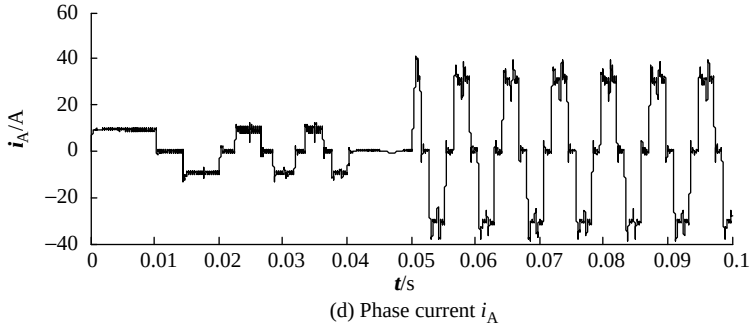
(a) Line voltage u_{AB}



(b) Terminal voltage of phase A, u_{AG}

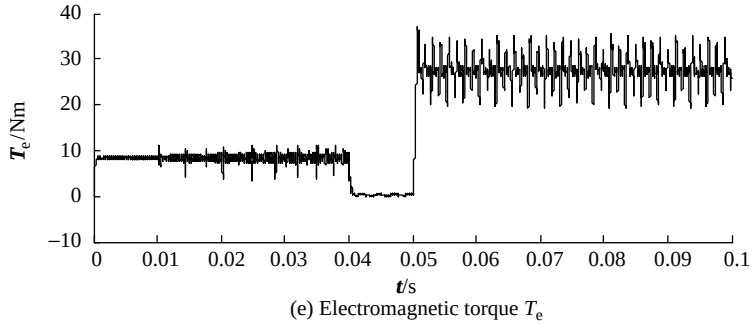


(c) Neutral voltage U_N

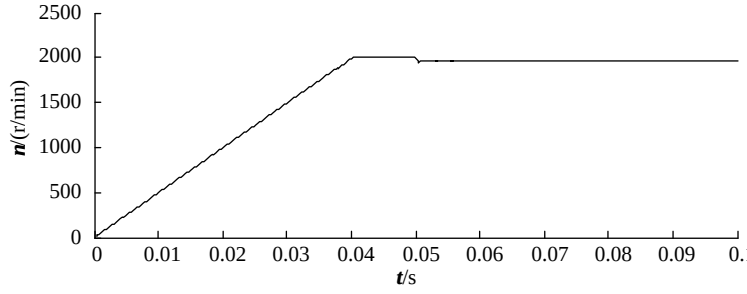


(d) Phase current i_A

Figure 3.10 Simulation results with ramp input and varied load.



(e) Electromagnetic torque T_e



(f) Rotor speed n

Figure 3.10 (*Continued*)

As a permanent magnetic rotor is used in the BLDC motor, the field excitation is not adjustable. In addition, since the air-gap magnetic field is trapezoidal, the analysis method based on vector control has high error. Therefore, different from these two types of motor, when the reference speed is higher than the rated value, the advanced conduction of phase current is usually adopted to expand the speed range of BLDC motor [2–7]. The corresponding principle is shown in Figure 3.11.

Take phase A for example, Figure 3.11 shows the relation of the phase current i_A in the advanced conduction of phase current mode, the phase current i_0 in normal conducting mode, and the phase back-EMF e_A. Since the speed is fairly high at this condition, the rotor speed can be assumed to be constant during the current varying period as shown in Figure 3.11. It can be seen from Figure 3.11 that i_A is leading i_0 in phase by α electrical degrees. As it keeps away from the maximum of the back-EMF, i_A increases rapidly during a period shortly after

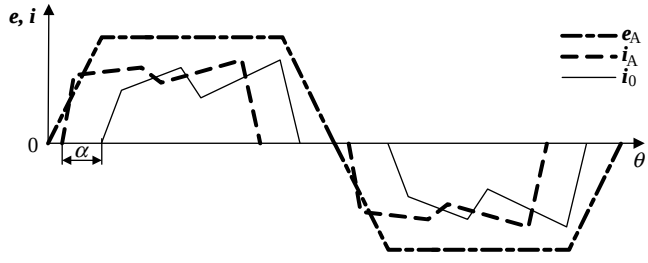


Figure 3.11 The principle for advanced conduction of phase current.

phase A is conducting. The winding of phase A can store much magnetic field energy, compared with the situation in which the phase current is i_0. Subsequently, as the line back-EMF of the windings arrives and remains the maximum, the increase in the current gets slower. If the value of α is rather big, the current will decrease rapidly after its increase. Its waveform is similar to a sinusoidal one. So, the torque ripple will be rather big as the back-EMF is a square wave. As analyzed above, with the advanced conduction of phase current, when the back-EMF arrives at its maximum, i_A is greater than i_0, and the electrical torque increases. Thus, the speed above the rated value is achieved. As a long time of operation at high current will cause severe heating of the motor, this operation mode is usually applied to constant power load, so as to ensure that the current is remained about the rated value.

It is worth noting that the advanced conduction of phase current adopted in the BLDC motor to increase the speed is essentially different from the field-weakening method adopted in separately excited DC motor for speed regulation. The air-gap flux density of the BLDC motor is distributed in a trapezoidal waveform, of which the sloping edge is where the flux density is small and thus the magnetic field is weak. In the normal commutation mode, the phase current begins conducting when the phase back-EMF is equal to the maximum, and the torque-generation process utilizes the magnetic field to the utmost. In the mode of advanced conduction of phase current, only part of the magnetic field at the sloping edge of the air-gap flux density takes part in the electromechanical energy conversion. This means that the effective magnetic field is reduced. Thus, a similar effect of field weakening and speed increasing is achieved like that of the separately excited DC motor. Note that the main field of the motor is not changed here, only the air-gap flux density distribution is changed. Since the sloping edge distribution area of the trapezoidal air-gap flux density is limited, the magnetic-field regulation and speed range expanding ability of the BLDC motor controlled by the advanced conduction of phase current are inferior to those of the electrically excited DC motor.

Figure 3.12 shows the simulation block diagram of the BLDC motor controlled by the advanced conduction of phase current.

In Figure 3.12, the structure of the main circuit is thoroughly the same as that of the double closed-loop control system. They all employ the AC–DC–AC converter structure. Further, the

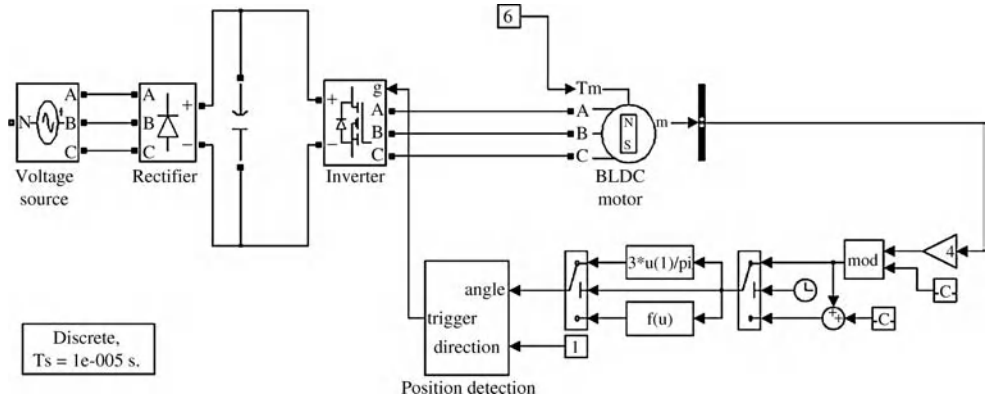


Figure 3.12 Simulation block diagram of the BLDC motor controlled by the advanced conduction of phase current.

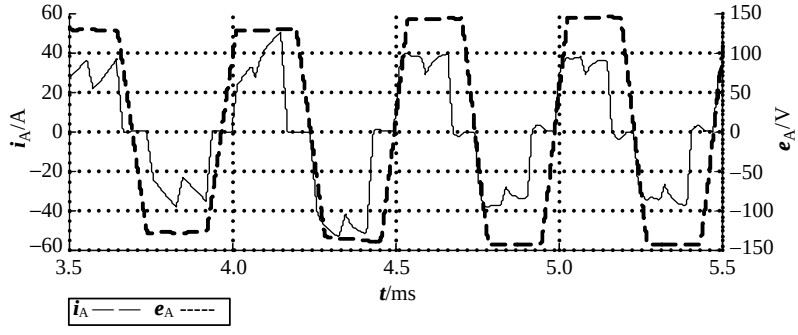


Figure 3.13 The waveforms of phase current and phase back-EMF.

motor starts in normal commutation mode with full load, and then shifts to the mode controlled by advanced conduction of phase current at the steady-state speed. For the convenience of observing how phase current varies with the leading conducting angle, the load torque is set constant.

Figure 3.13 shows the corresponding waveforms of phase current and phase back-EMF of the field weakening speed-control system during the period between 3.5 ms and 5.5 ms, in which α changes abruptly at $t = 4$ ms from 0° to 30°.

It can be seen from Figure 3.13 that the phase and the shape of the phase current have changed. In the normal commutation mode there exist apparent spikes in the vicinity of the maximum of current, while in the advanced conduction of the phase current mode, the current is almost flat, with a trend of decreasing. As analyzed before, this is mainly because the advanced conduction mode causes the increasing of speed and back-EMF, bringing out the difficulty in increasing the current. The simulation results also show that the RMS value of phase current changed from 20 A to 22 A after the abrupt change of the angle α. This is caused by the increment of the current when the back-EMF is still small. Note that the energy stored in the magnetic field is closely related to the windings current. Thus, knowledge of the changing of phase current waveform is helpful for us to comprehend the principle of the advanced conduction of phase current from the viewpoint of energy transfer. In this viewpoint, the energy transferred to the motor by the bridge inverter will be transformed into the output mechanical energy of the motor and the magnetic energy stored in the air gap, without regard to copper loss, iron loss and friction loss. When the BLDC motor is controlled by the advanced conduction of phase current, power switches begin to conduct at the edge of the trapezoid back-EMF, and the corresponding phase current increases rapidly. Before the end of the flat top of the trapezoid, power switches are cut off, and the current of this phase decreases rapidly. If the DC bus voltage and load torque remain unchanged, the RMS value of bus current will also increase, and a greater proportion of the electric energy from the power source will be transformed into mechanical energy, and thus the speed of the motor is increased.

Figure 3.14 shows the corresponding simulation waveforms of electromagnetic torque and speed response as analyzed above.

As shown in Figure 3.14, when α changes suddenly from 0° to 30°, the electromagnetic torque begins to increase, and the rotor starts to accelerate until the torques exerted on the rotor

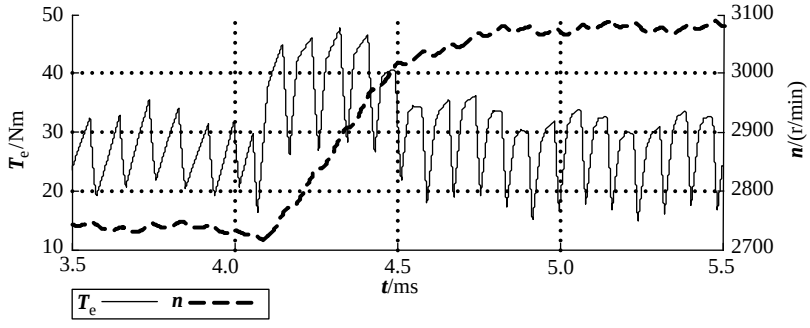


Figure 3.14 Waveforms of electromagnetic torque and speed.

reach the new equilibrium. Since the load torque is constant, the steady-state torque stays unchanged after the change of α, and only the amplitude of torque ripple is slightly augmented.

Figure 3.15 shows the mechanical characteristics of the BLDC motor with different advanced conduction angle. In order to observe the mechanical characteristic in a wide range of torque, the load torque is set from 0 to 70 N m, almost triple the rated value.

As shown in Figure 3.15, the mechanical characteristics curve family of the BLDC motor moves upward with the increasing of α, and the curve with $\alpha = 15°$ is the dividing line. When α is less than 15°, the curves have only slight translation. Note that when α is equal to 7.5°, the mechanical characteristic curve of the motor is nearly the same as that in the normal commutation mode. However, when α is greater than 15°, there is an evident change in the mechanical characteristics. For example, when α is equal to 30°, the speed of the motor with rated load is 3700 r/min, which is 1.32 times the rated speed in normal commutation mode.

Figure 3.16 shows the variation for the RMS value of current with respect to the advanced conduction angle.

Through comparison of the curves in Figure 3.16, it is apparent that when the value of α is large, the phase current corresponding to the same load torque is also high, especially when the speed is greater than the rated value. Therefore, the advanced conduction angle has a significant influence on the current RMS value variation with load change. Since higher phase

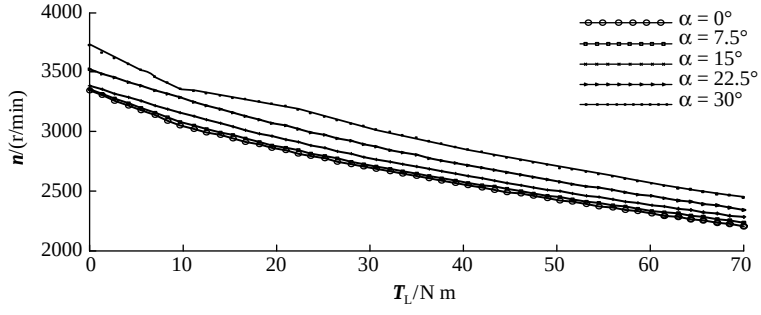


Figure 3.15 Mechanical characteristics corresponding to different advanced conduction angle.

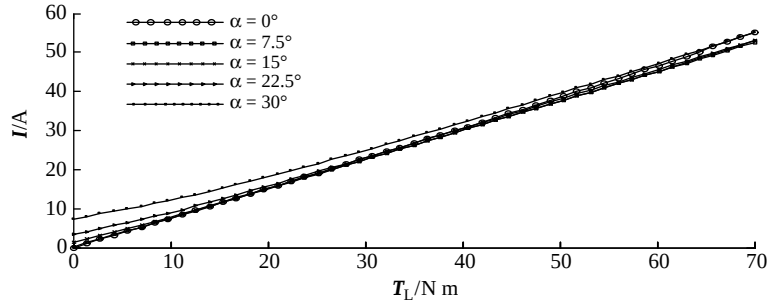


Figure 3.16 The variation of the RMS value of current with respect to the advanced conduction angle.

current will cause higher average torque, a higher speed of the motor will be obtained consequently, which is in accord with the results shown in Figure 3.15. Taking the current restriction of motor continuous working into consideration, the advanced conduction angle is usually not bigger than 30°.

Questions

1. Briefly describe the main calculating process of the S-function corresponding to the module "BLDC_Motor".
2. How many parts does the model of BLDC motor double closed-loop speed-control system presented in this chapter consist of? And what are their functions, respectively?
3. Why is the advanced conduction of phase current adopted when the reference speed is above the rated value? Describe the principle of this method.
4. Try to build a model of BLDC motor closed-loop speed-control system by yourself. Then compare it with that presented in the SimPowerSystem library to see if they work in the same way.

References

1. Pillay, P., Krishman, R. (1989) Modeling, simulation, and analysis of permanent-magnet motor drives, part II: the brushless DC motor drive. *IEEE Transactions on Industry Application*, **25**(2), 274–279.
2. Chan, C. C., Jiang, J. Z., Xia, W., *et al.* (1995) Novel wide range speed control of permanent magnet brushless motor drives. *IEEE Transactions on Power Electronics*, **10**(5), 539–546.
3. Yan, L. (2004) *Flux weakening technology study on permanent magnet brushless DC motor.* Hangzhou: Zhejiang University, PhD Thesis, (in Chinese).
4. Janhns, T. M. (1984) Torque production in permanent-magnet synchronous motor drives with rectangular current excitation. *IEEE Transactions on Industry Application*. IA- **20**(4), 803–813.
5. Lawler, J. S., Bailey, J. M., Mckeever J. W., *et al.* (2002) Limitations of the conventional phase advance method for constant power operation of the brushless DC Motor. IEEE SoutheastCon 2002, Columbia, 174–180.
6. Miti G K, Renfrew A C, Chalmers B J, (2001) Field-weakening regime for brushless DC Motors based on instantaneous power theory. *IEE Proceedings on Electrical Power Application*. 2001, **148**(3): 265–271.
7. Safi, S. K., Acarnley, P. P., Jack, A. G. (1995) Analysis and simulation of the high-speed torque performance of brushless DC motor drives. *Electric Power Applications*, **142**(3), 191–200.

4

Speed Control for BLDC Motor Drives

BLDC motor speed control plays an important role in modern motor control. The control methods are usually divided into two main types: open-loop and closed-loop ones. Dual-closed-loop speed control is common in control systems. The inner loop is the current or torque loop, while the outer loop is the velocity or voltage loop. When the motor works in normal mode or runs below the rated speed, the input voltage of the armature is changed through PWM modulation strategy; while the motor is operated above the rated speed, we usually weaken the flux by means of advancing the exciting current or auxiliary flux to achieve the aim. A BLDC motor speed-control system generally involves many techniques. In this chapter, we mainly focus on the realization of the dual-closed-loop speed control, the intelligent speed-control strategies, and the influence of time-varying motor parameters (resistances, inductances, and moment of inertia) on the motor speed control law.

4.1 Introduction

4.1.1 PID Control Principle

Traditional PID control has been one of the most developed strategies in the linear control systems for over 70 years, which is still commonly used in industrial control systems. The PID controller has been used widely in industrial applications owing to its simplicity, robustness, reliability and easy tuning parameters. The typical structure of PID control is shown in Figure 4.1.

The standard PID controller calculates the deviation $e(t)$ between the reference value and the actual value. Then, the plant is controlled by the variable $u(t)$ with a linear combination of proportional–integral–derivative terms. The corresponding PID control law in continuous form can be expressed as

$$u(t) = K_{\mathrm{P}}\left(e(t) + \frac{1}{T_{\mathrm{I}}}\int_0^t e(t)\mathrm{d}t + T_{\mathrm{D}}\frac{\mathrm{d}e(t)}{\mathrm{d}t}\right) \tag{4.1}$$

Permanent Magnet Brushless DC Motor Drives and Controls, First Edition. Chang-liang Xia.
© 2012 Science Press. Published 2012 by John Wiley & Sons Singapore Pte. Ltd.

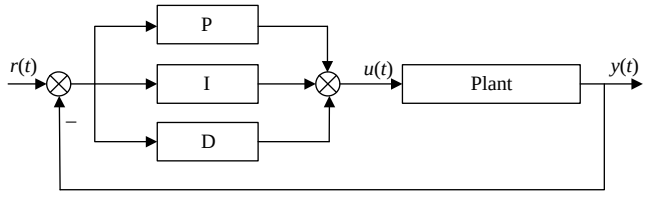


Figure 4.1 Diagram of a PID control system.

where K_P is the proportional gain, T_I is the integral time constant and T_D is the differential time constant.

In practical control system, not all PID controllers are composed of three terms: proportional, integral and differential. PID controllers contain various structure forms, such as proportional controller, proportional–integral controller and proportional–derivative controller, and so on. Among them, the proportional–integral controller is the most commonly used one in the BLDC motor control system. The differential term can effectively reduce the overshoot and maximum dynamic deviation, but it will make the controlled plant easily affected by high-frequency disturbances.

In order to improve system reliability, digital PID controller is often used in modern motor control systems. In this situation, the continuous PID control algorithm cannot be used directly, and Equation (4.1) should be discretized. The difference equation of discrete PID control law, which is also known as the position PID control algorithm, is obtained as

$$\begin{aligned} u(k) &= K_P\left[e(k) + \frac{T}{T_I}\sum_{j=0}^{k} e(j) + \frac{T_D}{T}(e(k) - e(k-1))\right] \\ &= K_P e(k) + K_I\sum_{j=0}^{k} e(j) + K_D(e(k) - e(k-1)) \end{aligned} \tag{4.2}$$

where K_I is the integral coefficient, K_D is the differential coefficient, T is the sampling period, $e(k)$ and $e(k-1)$ are the deviation of inputs at the kth and the $(k-1)$th time, respectively.

A typical digital PID control system is shown in Figure 4.2.

In digital motor control system, PID control law expressed as Equation (4.2) may induce large error and has poor dynamic performance. Thus, the incremental PID control law based on the recursive principle can be adopted, which is expressed as

$$\begin{aligned} \Delta u(k) &= u(k) - u(k-1) \\ &= K_p(e(k) - e(k-1)) + K_I e(k) + K_D(e(k) - 2e(k-1) + e(k-2)) \end{aligned} \tag{4.3}$$

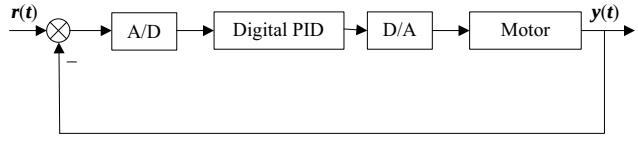


Figure 4.2 Diagram of the digital PID motor control system.

Comparing Equation (4.2) with Equation (4.3), we could find that the calculation complexity of incremental PID control law is much smaller. Moreover, the positional PID control law shown in Equation (4.2) could be deduced from Equation (4.3).

Once the structure of the PID controller is determined, the parameters of the PID controller need to be adjusted. The parameter tuning methods for a continuous PID controller can be used to determine the parameters of a digital PID controller. In practice, the proportional parameter is first tuned, then the integral parameter, and finally the differential parameter. For a PI controller, one tuning method is first to set the integral part to zero, then increase the proportional part until the system response is stable, finally tune the integral part to improve the dynamic response ability and static stability. It is worth noting that the selections of these three parameters are not isolated. In order to obtain the best control performance, they should be considered as a whole in the tuning process. The system performance is also closely related to the choice of sampling period T, so the designer should select it properly. According to Shannon sampling theorem, the sampling frequency must be greater than or equal to twice of the maximum frequency of the sampled signal in order to recover or approximately recover the discrete signal to its original continuous signal. Under this condition, the smaller the sampling period, the closer is the performance of the sampled data control system to the continuous control system. As for closed-loop control systems, especially the motor speed-control system, the controller is usually designed to trace the change of speed quickly. Thus, the sampling period should be as small as possible, whereas the sampling frequency is high enough. In practice, taking the operating frequency of microprocessor, switching frequency of power electronics, time delay of sensors, and the restriction of the conversion ability of A/D and D/A into consideration, the sampling period cannot be too small. Therefore, the system designer should select the sampling period reasonably according to the concrete circumstances. Let T_r be the rising time of the system response and N_r be the sampling frequency, a simple empirical formula for estimating the sampling period T is shown as

$$N_r = \frac{T_r}{T} = 2 - 4 \tag{4.4}$$

Compared with the continuous control system, the digital control system has the following advantages:

(1) The digital devices have higher reliability, flexibility and stability compared with the analog devices.
(2) A digital control system has a higher antidisturbance ability.
(3) A digital control system is more flexible, which has high control precision and could implement complex control algorithms easily.
(4) A digital control system is more suitable to communicate with the top-level application system or the remote control unit so as to construct a distributed control network.

With the development of computer technology and intelligent control theory, various types of PID controllers have appeared, such as trapezoid integration PID, variable-speed integration PID, fuzzy PID, neural-network PID, and so on. Note that these new PID controllers are proposed for those controlled objects that are characterized as nonlinear, coupling, delay, variable structure. These improvements not only enhance the system control performance, but

also expand the application areas of PID controllers. Since each PID controller has its own advantages, disadvantages and application areas, specific requirements and the control performance should be considered when choosing the PID controller structure type.

During the design of a BLDC motor speed controller, it is essential to consider the system's working environment, load characteristics and position-detection methods. The target of control is to achieve wide speed range, small static tracing error, good tracking performance and antidisturbance ability. In a variety of control strategies, the dual-closed-loop PI control technology is the most mature and widely used. The outer loop of the dual-closed-loop speed controller is the speed loop (i.e. the voltage loop), aiming to stabilize the speed and resist-load disturbance. The inner loop is the current loop (i.e. the torque loop), aiming to stabilize current and resist grid voltage fluctuation. In the following two subsections, the antiwindup phenomenon and the intelligent speed-control technologies are analyzed briefly.

4.1.2 Antiwindup Controller

Using a PID controller for single-loop or double-loop speed regulation of BLDC motor has been deeply studied. Usually, it can satisfy general speed-regulation requirements. However, since a BLDC motor is a multivariable nonlinear system, many new problems need to be solved further. Currently, most of BLDC motors adopt PID controller and PWM modulation for speed control. Note that a current limiter is often followed in the speed loop, and PWM can be regarded as another saturation limiter, as shown in Figure 4.3. Therefore, the BLDC motor speed-control system has strong saturation characteristics. When the system enters into the saturation state, the integral part of the controller will inevitably result in a typical windup phenomenon. In more serious situations, it will make the system performance degrade greatly.

There are many ways to design an antiwindup controller, which can be mainly divided into linear structure and nonlinear structure [1]. Their principles are all based on whether the system limits the amplitude of output or not (i.e. whether the output of the controller is equal to the input of controlled objects) so as to prevent or limit the integral effect. The difference between the linear and nonlinear antiwindup controller is that there only exist switch elements or other nonlinear elements in the latter. Antiwindup methods have been used in induction motor and permanent-magnet synchronous motor control. Three new antiwindup design methods have been proposed in [2], and they were performed in FPGA to control an induction motor. A current regulator based on antiwindup is used to realize the flux-weakening control of a surface-mounted permanent magnet motor in [3]. It needs no extra hardware and is easy to implement in software.

All the traditional antiwindup controllers use the difference between the input and the output of the limiter as the feedback signal to avoid or suppress the windup phenomenon in the

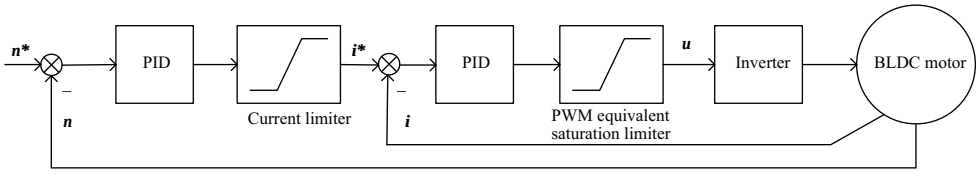


Figure 4.3 Diagram of double closed-loop speed-regulation system for a BLDC motor.

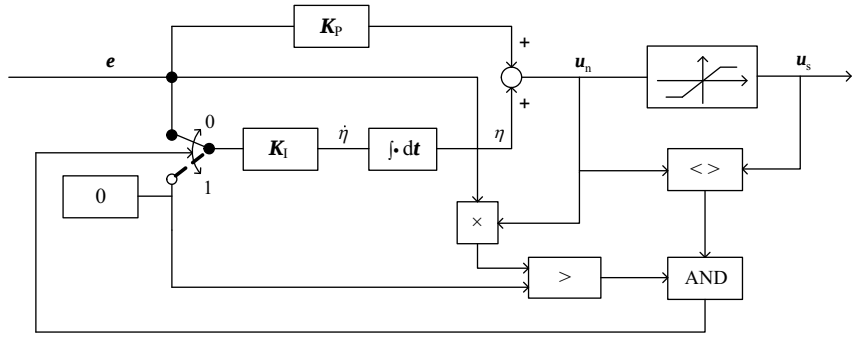


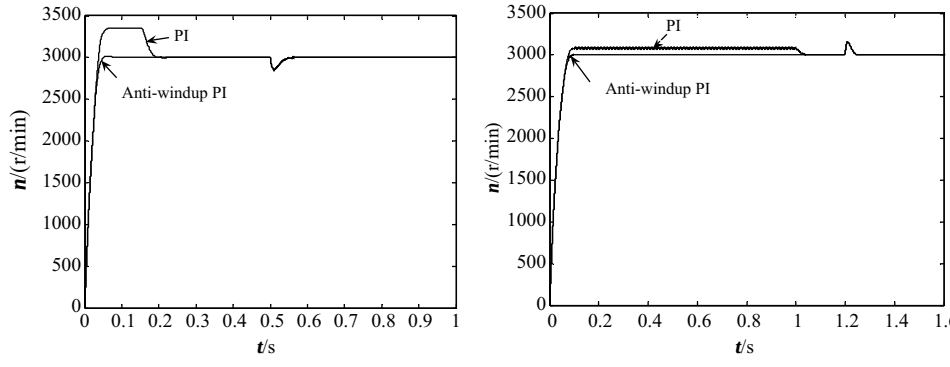
Figure 4.4 An integral clamping antiwindup controller.

control system. Eleven different antiwindup design methods have been proposed in [4], and the integrator clamping antiwindup controller is found to be the best one, whose structure is shown as Figure 4.4. A modified antiwindup controller based on the backcalculation and the integrator clamping is presented in [1], the simulation results have demonstrated that its application on the BLDC motor can make the system overshoot smaller to some extent. But this influence is not obvious and it also needs to reduce the system response speed to achieve this aim. Further, the algorithm of this kind of antiwindup controller is more complex. So, the simple integrator clamping antiwindup PI controller is used here to control the BLDC motor. The corresponding variable structure control law of the controller is

$$\dot{\eta} = \begin{cases} 0 & e \cdot u_n > 0, u_n \neq u_s \\ K_I \cdot e & u_n = u_s \end{cases} \tag{4.5}$$

The speed regulation performance of a BLDC motor with PI and antiwindup PI controller is shown in Figure 4.5.

It can be seen from Figure 4.5 that the antiwindup PI controller has good antidisturbance ability, less overshoot and shorter settling time of the system, and can improve the speed response ability.



(a) Starting with no load (load increases at 0.5 s)

(b) Starting with full load (load decreases at 1.2 s)

Figure 4.5 PI and antiwindup PI control for a BLDC motor.

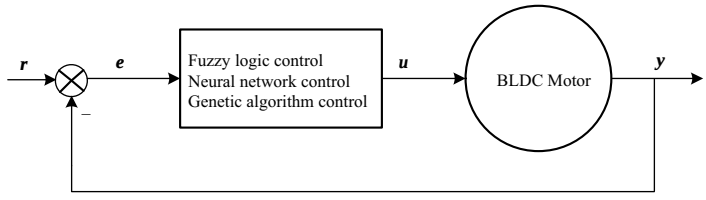
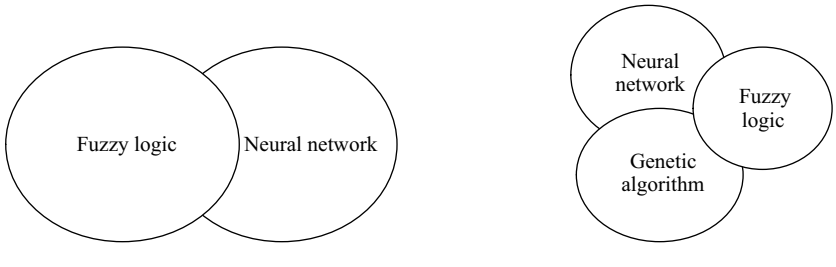


Figure 4.6 Intelligent control diagram for a BLDC motor.

4.1.3 Intelligent Controller

Intelligent control emerges from the combination of automatic control and the concept of artificial intelligence. The common intelligent control methods involve fuzzy logic, neural networks and genetic algorithms, etc. They have been used widely in areas of the motor control, motor parameter identification and state estimation, fault detection and diagnosis. A typical BLDC motor block diagram of an intelligent control system is shown in Figure 4.6. An intelligent control algorithm is independent or not fully dependent on the controlled plant's accurate mathematical model. A fuzzy-logic control system based on expert knowledge database needs less calculations, but it lacks sufficient capacity for the new rules. On the contrary, a neural-network-based motor control system has a strong ability to solve the structure uncertainty and the disturbance of the system, whereas it requires more computing capacity and data storage space. Genetic algorithms, ant-colony algorithms, and artificial immune algorithms are, respectively, created from the human evolution, biology evolution, and artificial immune systems. They can optimize the controller parameters online or offline to achieve a better control performance. Of course, they need longer computation time and larger storage capacity. In practice, in order to improve the reliability of the system, a variety of combined intelligent methods like a fuzzy neural-network controller, a fuzzy-genetic controller, and a fuzzy immune controller are adopted so that they can take advantage of each other. The combination may be a simple superposition or a fully integration, as shown in Figure 4.7. From above, we can know that fuzzy control has the disadvantage of poor learning ability and the advantage of good reasoning ability, while the neural network has poor reasoning ability but good learning ability. So, the combination of them can ensure the fuzzy neural network's good learning and reasoning ability. Moreover, the integration of genetic algorithm for a fuzzy neural network can optimize the fuzzy inference rules and the



(a) Combination of two intelligent control methods (b) Combination of three intelligent control methods

Figure 4.7 Combination of intelligent control methods.

neural-network structure, and improve the system reliability and control accuracy. As far as we know, it is difficult for us to solve all problems in BLDC motor control systems by using only one type of intelligent control methods. So in order to achieve a system-level optimal control performance, intelligent control is usually combined with the traditional linear control and other modern control methods.

4.1.4 Representations of Uncertainty

Uncertainty of the controlled plant (for example, the BLDC motor) usually includes unstructured uncertainty and structured uncertainty. Let $G_0(s)$ be a nominal transfer function, which is a best estimate, in some sense, of the true plant behavior, and let $G(s)$ denote the true transfer function of the plant. Then for BLDC motor, the unstructured uncertainty can be represented in three most commonly used models as follows:

$$G(s) = G_0(s) + \Delta_{\mathrm{a}}(s) \tag{4.6}$$

$$G(s) = G_0(s)[I + \Delta_{\mathrm{i}}(s)] \tag{4.7}$$

or

$$G(s) = [I + \Delta_{\mathrm{o}}(\mathrm{s})]G_{\mathrm{o}}(\mathrm{s}) \tag{4.8}$$

where $\Delta_{\mathbf{a}}(s)$ — additive perturbation;
$\Delta_{\mathbf{i}}(s)$ — input multiplicative perturbation;
$\Delta_{\mathbf{o}}(\mathbf{s})$ — output multiplicative perturbation.

The additive model in Equation (4.6) may be used to pose some robust stabilization problems that have nice solutions, but the multiplicative models in Equations (4.7) and (4.8) are often more realistic, since $\|\Delta_i\|_\infty$and $\|\Delta_o\|_\infty$represent relative rather than absolute magnitudes.

In practical BLDC motor control systems, measurement errors such as current, voltage, speed measurement errors caused by resolution of sensor, the perturbation from system or external factors, and observation error such as torque, back-EMF observation error caused by observation algorithms or the accuracy of model all would lead to unstructured uncertainty.

It is well known that motor operation is strongly affected by the rotor magnetic saliency, saturation, and armature reaction effects. In particular, the saturation of the rotor iron portion around the magnets induces significant distortion of the air-gap flux. Subsequently, the inductance parameters vary as a function of the magnitude and phase angle of the motor current. Moreover, the inductance variation affects both the plant gain and the open-loop electrical time constant of the motor. Hence, the performance of the drive varies at different dynamic and steady-state operating conditions.

Usually, the flux density of the rotor permanent magnets is affected by the temperature variation, and it will be amplified by variations in the stator-winding resistance and the magnetic saturation in the motor. Also, the residual flux density decreases as the

temperature increases through a reversible process. In addition, the inaccuracy of the back-EMF model may degrade the control performance under the condition of sensorless control.

Hence, in BLDC motor control systems, electrical parameters such as stator resistors R_s and inductances L_s are sensitive to environment temperature and motor angle speed, especially when the motor runs at high speeds and full load. Consequently, the electrical time constant will vary with these factors. Random perturbations from load or unmodeled dynamics also affect the system performance. The uncertainty in a BLDC motor could be represented as follows:

$$u_a = R_0 i_a + L_0 \frac{di_a}{dt} + \omega_r \psi_{f0} + d \tag{4.9}$$

$$d = \Delta R i_a + \Delta L \frac{di_a}{dt} + \omega_r \Delta\psi + \varepsilon \tag{4.10}$$

where R_0, L_0 and ψ_{f0} represent stator nominal resistor, nominal inductance and ψ_{f0} nominal flux respectively, $R = R_0 + \Delta R$, $L = L_0 + \Delta L$, $\psi = \psi_{f0} + \Delta\psi$, and ε represents unmodeled dynamics.

In this way, the BLDC motor control system can be modeled more accurately and it will be more suitable in practice.

4.2 Advanced Speed Control for BLDC Motor Drives

4.2.1 Fuzzy Control

As shown in Figure 4.8, a typical fuzzy-control system is composed of a fuzzy controller and a plant. The fuzzy controller involves four components: fuzzification, knowledge database (including the database and rule base), fuzzy inference and defuzzification. Fundamentally, fuzzy control can reflect human reasoning. It is an intelligent control method that is independent of the precise mathematical model of the controlled object. Whether the controlled object is linear or nonlinear, a fuzzy controller can be implemented effectively with good robustness and adaptability.

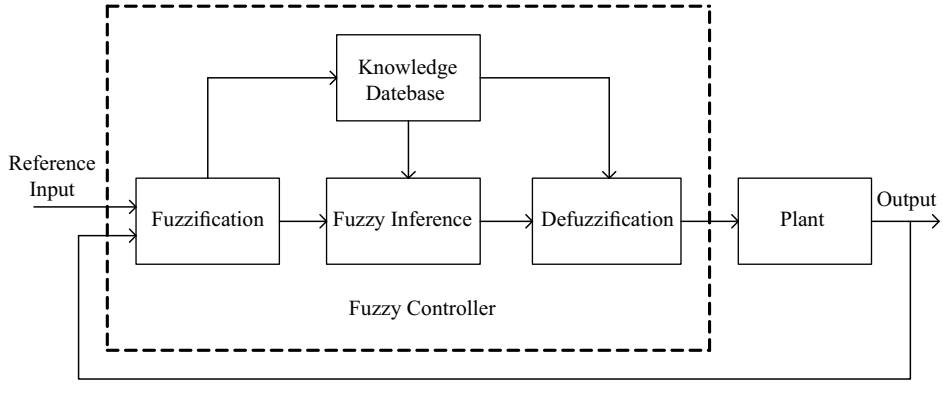


Figure 4.8 Typical diagram of a fuzzy-control system.

Due to the appearance and development of fuzzy theory, fuzzy control has been used widely in motor-control applications. Since the motor load varies greatly in many motor applications, good speed-regulation ability is often essential in all working conditions. Considering the limitation on algorithm time consumption, nonlinear control methods based on fuzzy logic are ideal choices for motor control [5–8]. Currently, the fuzzy-control methods for BLDC motors can be mainly divided into three categories: standard fuzzy controller, fuzzy-PID switch controller and optimized fuzzy controller.

4.2.1.1 Types of Fuzzy Controller

(1) Standard fuzzy controller. A standard fuzzy controller for BLDC motor is shown in Figure 4.9. Based on the principle of fuzzy controller shown in Figure 4.8, the input signal is first fuzzificated, then the control table is constructed according to an expert knowledge database, and finally the control signal is obtained through defuzzification.

In general, a one-dimensional fuzzy controller in Figure 4.9 is usually used for a one-order controlled object. Because only one error signal is chosen as the input variable in this type of controller, its dynamic performance is often poor. In theory, the higher the fuzzy controller's dimension, the better the control performance. However, higher dimension will lead to more complex fuzzy-control rules and control algorithms. So generally the dimension of the fuzzy controller does not exceed 3. To date, the two-dimensional fuzzy controller has been widely used. As shown in Figure 4.9(b), the feedback error e and its differential $\dot{e}$ are used as inputs and the control variable u is used as output.

(2) Fuzzy-PID switch controller. The control strategy is obtained by the integration with a fuzzy controller and conventional PID control as shown in Figure 4.10. When the output of the fuzzy controller is zero, the system switches to the conventional PID controller. Otherwise, the fuzzy controller works. Hence, the fuzzy controller can be used to improve the robustness to uncertainties. It has been proved that the fuzzy-PID switch controller can also reduce the overshoot and the settling time of the whole system.

(3) Optimized fuzzy controller. In order to achieve an optimal operation, a fuzzy controller is used to optimize and adjust the parameters of traditional PID controller by using fuzzy

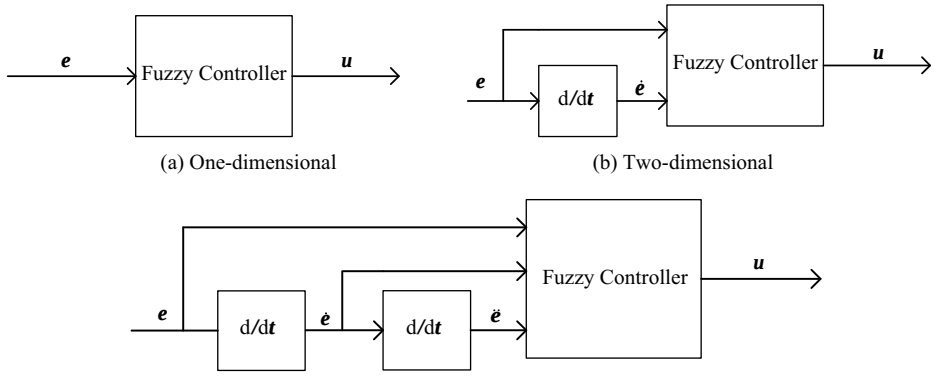


Figure 4.9 The structure of fuzzy controllers.

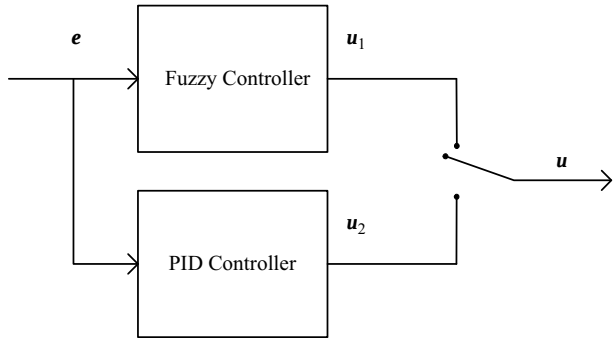


Figure 4.10 Fuzzy-PID switch controller.

rules as shown in Figure 4.11. The controller's parameters are adjusted online according to the actual working conditions. It is an online intelligent parameters adjustment method.

(4) Other types. There are many other types of fuzzy controllers in BLDC motor control systems. Moreover, with the development of the technology, more new fuzzy-control strategies will emerge. Figure 4.12 shows a precompensation fuzzy controller. In certain occasions, the PID controller in Figure 4.12 can be removed (note that when there is no PID controller, u_0 is equal to r^*), the basic idea is to use a fuzzy feedforward compensation controller to compensate the actual reference input to get an ideal reference input signal, then use the traditional double closed-loop controller to control the BLDC motor.

4.2.1.2 General Design Procedures of Fuzzy Controller for BLDC Motor

According to the practical needs in applications of BLDC motor control systems, the two-dimensional fuzzy controller is usually adopted, i.e. using the motor speed error e and its rate of change e_c as inputs of fuzzy controller. Through fuzzification and fuzzy decision, a one-dimensional output is obtained. Then the control signal after defuzzification is used for

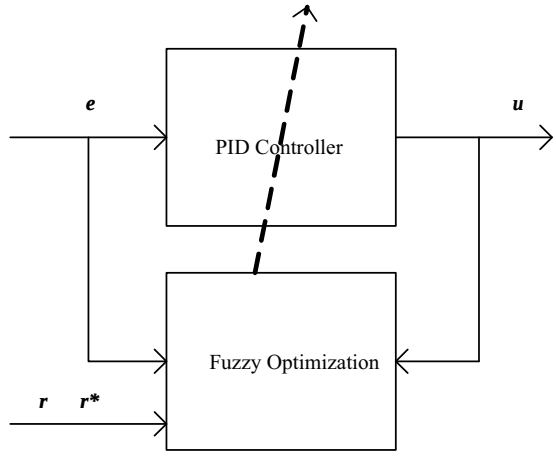


Figure 4.11 Optimized fuzzy controller.

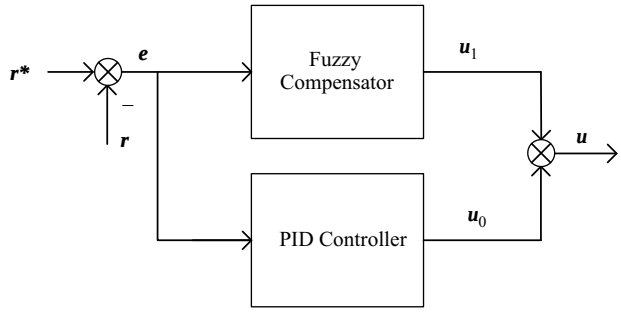


Figure 4.12 Precompensation fuzzy controller.

speed regulation. The two-dimensional fuzzy controllers have been widely used in fuzzy controller for its good performance. The corresponding design procedures are as follows.

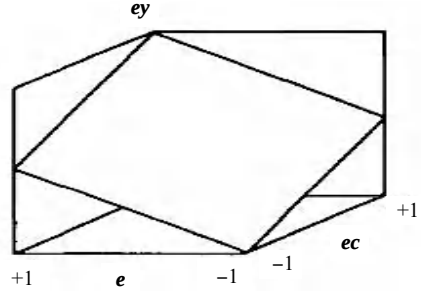
(1) Definition of dynamic signal. Here, the speed tracing error and its change are defined as

$$\begin{cases} e(k) = n^*(k) - n(k) \\ ec(k) = e(k) - e(k-1) \end{cases} \tag{4.11}$$

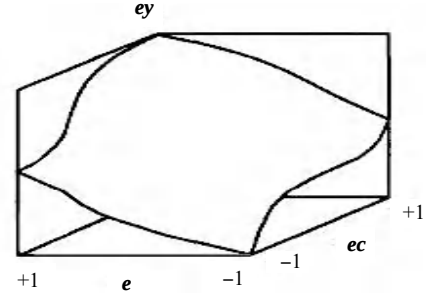
where $n^*(k)$ — reference speed of kth sample,
$n(k)$ — motor speed response of kth sample.

Let ey be the output of the fuzzy controller, i.e. $ey = f(e, ec)$, then the control surfaces corresponding to the traditional PID controller and fuzzy controller can be shown as Figure 4.13.

(2) Quantization factor and scale factor. In order to increase the sensitivity of the control and convenience for application of the fuzzy rule, the actual values of error e and its change ec are quantized by using the quantization factors K_{e1} and K_{ec}, then they are mapped to the fuzzy set domain $X = \{-m, -m+1, \ldots, 0, \ldots, m-1, m\}$. Generally, the system control



(a) PID controller



(b) Fuzzy controller

Figure 4.13 Control surface.

performance will be improved by increasing m. Note that too large a value for m would increase the difficulty in determination of fuzzy control rules. Commonly, in BLDC motor control systems, one can choose the fuzzy domain with 7 language variables including negative big (NB), negative middle (NM), negative small (NS), zero (ZE), positive small (PS), positive middle (PM) and positive big (PB). Further, the output of fuzzy decision cannot be applied into the control system directly. The output signal is required to be converted from the fuzzy domain to the basic domain of actual output by using the scale factor K_u, so that the output can be used to control the object.

(3) Member function. Different member functions such as the trapezoidal distributed function, the triangle distributed function and the Gaussian-distributed function can be chosen for various applications. Whether the selected member functions are proper or not needs to be verified by theory, simulation and experiment. In order to facilitate the implementation and ensure the reliable operation of the system, the triangle distributed functions, as shown in Figure 4.14, are generally selected as member functions of fuzzy controller for BLDC motor.

(4) Control rules for fuzzy controller. According to expert experience, a fuzzy-control decision table is obtained from the "IF-THEN" interference rules. Table 4.1 gives a fuzzy decision table.

In the table, FD represents the output of fuzzy decision. Hence, 49 fuzzy control rules are produced. Each of them can be expressed using the following form:

If e is NB and e_c is PM, then FD is ZE
If e is PM and e_c is NB, then FD is ZE
If e is NS and e_c is NM, then FD is NM
⋮
⋮

4.2.2 *Neural-Network Control*

Artificial neural networks (ANN) were originated in the period of Freud psychoanalysis in the early 19th century. Now they have been widely applied in the control of permanent magnet synchronous motors, switched reluctance motors, ultrasonic motors, BLDC motors and other new types of motors. The typical applications include position control, speed control, current control, parameter identification and state estimation of the motors. At present, neural

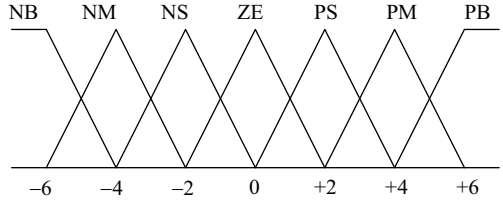


Figure 4.14 Member functions of fuzzy controller.

Table 4.1 Fuzzy decision table

FD (*ec* \ *e*)	NB	NM	NS	ZE	PS	PM	PB
*N*B	NB	NB	NM	NS	NS	ZE	ZE
NM	NB	NB	NM	NS	NS	ZE	ZE
NS	NM	NM	NS	NS	ZE	ZE	PS
ZE	NM	NS	NS	ZE	PS	PS	PM
PS	NS	ZE	ZE	PS	PS	PM	PM
PM	ZE	ZE	PS	PS	PM	PM	PB
PB	ZE	ZE	PS	PM	PM	PB	PB

networks used in the applications of BLDC motor speed control mainly include back-propagation (BP) neural networks, radial basis function (RBF) networks, wavelet networks, single neural networks and other types [9–17]. Here, an adaptive RBF network learning algorithm with simple structure and fast convergence is presented. Then, it is applied to the online estimation of power switch conducting signal of the BLDC motor for controlling the inverter directly. Finally, with the help of offline and online training for the network, the direct current control is obtained.

4.2.2.1 Adaptive RBF Network Learning Algorithm

An RBF network is not only biology based, but also consistent with the function approximation theory, which is proved to be suitable for multivariable function approximation. As long as the set of central points is chosen rightly, a good approximation with advantage of unique and best approximation point can be achieved with few neurons. The relation between the network connection weight and the output layer is linear, so that it can adopt the linear optimization algorithm guaranteeing global convergence. Based on these advantages of RBF networks, in recent years it has been paid more and more attention and used widely in areas of pattern recognition, function approximation, adaptive filtering and other fields.

The difficulty on applications of RBF networks is the proper selection of RBF hidden-layer units, which has a significant impact on the NN's approaching capacity and performance. Thus, it will affect the size of the network. If the hidden units are few, then it cannot complete the task of classification or function approximation; while if there are too many hidden units, the learning rate will be slowed down due to too many network parameters. Consequently, the initial network parameters, specificity of training samples and outer interferences will have a great influence on the network's connection weight. Moreover, when small distortion exists between the input pattern and training samples, the correct generalization results may not be attained, and the increase of the network size has an adverse effect on applications.

Fortunately, the possible phenomenon of slow convergent speed or even nonconvergence from the improper selection of the initial value of the hidden layer parameters was eliminated by using the adaptive algorithm with dynamically adjusting network structure and parameters [18–21]. Generally, the adaptive RBF network's initial numbers of hidden units can be set to zero, then added adaptively according to certain rules in the training process, and the hidden units with less effect on the output signal can be deleted. This can effectively realize

the nonlinear mapping by using the least hidden-layer units, so that a simple and compact network structure is obtained. For each new input sample($\boldsymbol{X}_i$, t_i), the adaptive algorithm consists of the following six steps:

(1) The hidden layer output $\varphi_{\mathrm{k}}(\boldsymbol{X}_i)$and the network output y_i are, respectively, calculated as

$$\varphi_k(\boldsymbol{X}_i) = \exp\left(-\frac{\|X_i - C_i\|^2}{2{\sigma_i}^2}\right) \tag{4.12}$$

and

$$y_i = f(\boldsymbol{X}_i) = \sum_{k=1}^{n} \omega_k \varphi_k(\boldsymbol{X}_i) \tag{4.13}$$

where X_i is the N-dimensional input, C_i is the center vector of Gaussian function at the ith hidden-layer unit, σ_{i} is the normalized constant of the ith hidden-layer unit, ω_k is the weighting coefficient from the hidden layer to the output layer.

(2) Calculate the network error between the expected output response t_i and the actual output y_i as

$$\|e_i\| = \|t_i - y_i\| \tag{4.14}$$

and the deviation between the samples and existed hidden-layer units as

$$d_j = \left\|\boldsymbol{X}_i - \boldsymbol{C}_j\right\| \quad j = 1, 2 \cdots u \tag{4.15}$$

where u is the number of existed hidden-layer units.
Let

$$d_{\min} = \min(d_j) \tag{4.16}$$

(3) If there exists

$$\|e_i\| > \varepsilon,\ d_{\min} > \lambda(i) \tag{4.17}$$

$$\lambda(i) = \max(\lambda_{\max}\gamma^i, \lambda_{\min}) \tag{4.18}$$

where ε is the desired accuracy of the network, $\lambda(i)$ is the network's approximation accuracy of the ith input, which is reduced from $\lambda_{\max}$ to $\lambda_{\min}$, and γ is the attenuation factor ($0 < \gamma < 1$).

Then a new hidden-layer unit is added, and the parameters of the new layer should satisfy

$$\boldsymbol{C}_k = \boldsymbol{X}_i \tag{4.19}$$

$$\sigma_{\mathrm{k}} = \frac{1}{q}\left(\sum_{j=1}^{q} \left\|\boldsymbol{X}_i - \boldsymbol{C}_j\right\|^2\right)^{1/2} \tag{4.20}$$

where $\boldsymbol{C}_j$ is the center of the qth hidden-layer unit that is the closest to the input sample.

(4) If Equations (4.17) and (4.18) are not satisfied, then adjust the connection weight by recursive least square method.

(5) If all the n continuous input samples satisfy

$$\left\| \frac{w_k \varphi_k(\boldsymbol{X}_i)}{y_i} \right\| \leq \delta \tag{4.21}$$

where δ is the predefined constant.
Then, the kth hidden-layer unit is deleted.
(6) Input new samples, and go to step (1).

4.2.2.2 Neural-Network Direct-Current Control for a BLDC Motor

In the BLDC motor speed-control system, the rotor position directly determines the ON/OFF states of the inverter power switches, which is the fundamental basis for the direct current neural-network control of BLDC motor. Through offline and online training for the RBF network, nonlinear mapping between the motor stator voltages, winding currents and the ON/OFF states of power switches are realized, so that the winding current can be controlled directly.

During offline training, the access of training samples is very important. A neural network's training samples could come from the simulating or experimental data. In order to make the network obtained from offline training more close to the actual motor operation, the samples used by offline training are generally the experimental data.

Note that only two of the three phases of the BLDC motor with Y-connected three-phase stator windings are conducted at any time. Moreover, the summing current of the three phase windings is equal to zero. So, the input sample vector can be taken as

$$\boldsymbol{X}_i = \{i_A(k), i_B(k), i_A(k-1), i_B(k-1), u_{AG}(k-1), u_{BG}(k-1)\}$$

where u_{AG} and u_{BG} are, respectively, the terminal to ground voltages of phases A and B.

Since the output sample are the ON/OFF states of the six power switches, it is difficult to detect the states of power switches directly. One method for solving this problem is to obtain switch states depending on different rotor positions with 1 representing state ON, while 0 represents state OFF according to the BLDC motor's commutation logic. So the output vectors of training sample can be represented as

$$\boldsymbol{Y}_i = \{S_1, S_2, S_3, S_4, S_5, S_6\}$$

where S_1, S_3 and S_5 are the conduction signals of upper power switches for the three-phase bridge inverter, while S_2, S_4 and S_6 are the conduction signals of lower power switches for the three-phase bridge inverter.

While the training sample is obtained, the offline training can be implemented according to the adaptive training algorithm presented above. The whole offline training algorithm can be realized through MATLAB software on a PC. With training of 3500 samples, the network achieves the predetermined precision. After the offline training, the number and center of the RBF network hidden-layer nodes, and the initial values of connection weights are consequently determined. The initial structure of network is shown in Figure 4.15. Because the offline training samples come from experimental data, the trained network could be considered approximately close to the motor's actual condition. Moreover, the parameters of the hidden layer need not be tuned online.

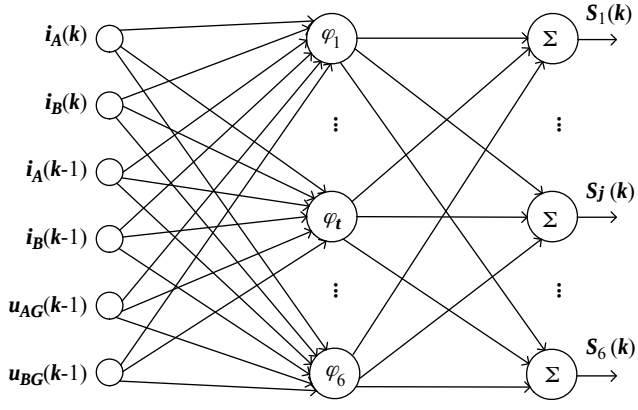


Figure 4.15 Offline trained RBF network.

The network connection weights are trained online by using recursive least square method in supervision mode. The teacher of the network comes from the network output signals after the logic process. The corresponding diagram of training is shown in Figure 4.16.

In order to avoid improper conduction of power switches, state signals need to be adjusted and processed logically. So, the corresponding network output signal is represented as

$$S_x(n) = \begin{cases} 0 & \hat{S}_x(n) \le 0.25 \\ 1 & \hat{S}_x(n) \geqslant 0.7 \\ S_x(n-1) & \text{Others} \end{cases} \tag{4.22}$$

In which, the rules for logic procession are formulated as:

(1) At any moment, only one state of S_1, S_3, and S_5 is equal to be 1, and so is the state of S_2, S_4 and S_6;
(2) S_1 and S_4, S_3 and S_6, S_5 and S_2 cannot be equal to 1 at the same time;
(3) If confliction happens to the above two laws, then the network output signal must be set to its closest state.

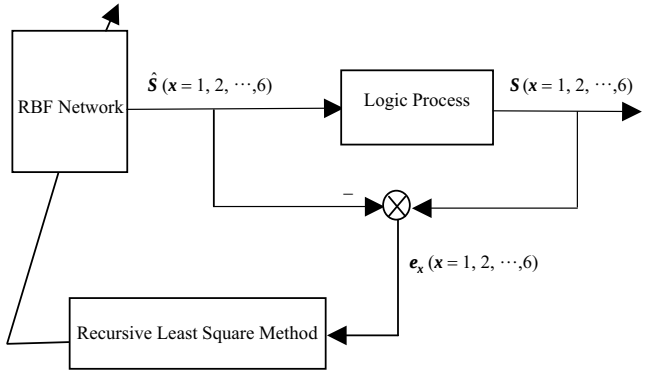


Figure 4.16 Online training diagram of RBF network.

The main procedures of the recursive least square learning rules are:

(1) As for the kth input, the network output function can be rewritten as

$$y(k) = \sum_{i=1}^{n} w_i \varphi_i(\boldsymbol{X}(k)) = \boldsymbol{w}^H(k)\boldsymbol{u}(k) \tag{4.23}$$

where $w(k)$ is the weight vector, $u(k)$ is the RBF vector, H represents the conjugate and transpose symbol.

(2) Let the initial values of the recursive matrix $\boldsymbol{P}$ and weight vector matrix $\boldsymbol{w}$ be

$$\boldsymbol{P}(0) = \delta_0^{-1}\boldsymbol{I}, \quad \boldsymbol{w}(0) = 0 \tag{4.24}$$

where δ_0 is a small and positive constant, and $\boldsymbol{I}$ is the identity matrix.

(3) Then, calculate $\boldsymbol{v}(k)$, $\zeta(k)$, $\boldsymbol{w}(k)$, and $\boldsymbol{P}(k)$ according to the following equations as

$$\boldsymbol{v}(k) = \frac{\lambda^{-1}\boldsymbol{P}(k-1)\boldsymbol{u}(k)}{1 + \lambda^{-1}\boldsymbol{u}^H(k)\boldsymbol{P}(k-1)\boldsymbol{u}(k)} \tag{4.25}$$

$$\zeta(k) = y(k) - \boldsymbol{w}^H(k-1)\boldsymbol{u}(k) \tag{4.26}$$

$$\boldsymbol{w}(k) = \boldsymbol{w}(k-1) + \boldsymbol{v}(k)\zeta^*(k) \tag{4.27}$$

$$\boldsymbol{P}(k) = \lambda^{-1}\boldsymbol{P}(k-1) - \lambda^{-1}\boldsymbol{v}(k)\boldsymbol{u}^H(k)\boldsymbol{P}(k-1) \tag{4.28}$$

where λ is the forgetting factor ($0 \leq \lambda \leq 1$), $*$ represents the complex conjugate symbol.

Note that the online training algorithm only needs to adjust the connection weights between the hidden-layer nodes and the output layer, which can be realized easily. Hence, the computation time of the proposed algorithm is greatly reduced, so that the system's dynamic response speed is improved.

Moreover, when the BLDC motor system works in position-sensorless control, a dual-RBF network control mode can be used, as shown in Figure 4.17.

In Figure 4.17, the motor voltage and current are mapped nonlinearly into the rotor position by the first RBF network. The inputs of the network are the motor phase currents and phase voltages (i.e. the voltages between the winding terminal and ground), while the output of network is the rotor's position angle. The network is trained offline by using the proposed adaptive RBF network algorithm. All training samples come from experimental data. Therefore, the trained network could estimate the rotor position online.

The other RBF network in Figure 4.17 also uses the same learning algorithm to guarantee the compactness of network structure. This network is used to achieve the nonlinear mapping from the rotor position and the reference torque to the reference current. For three-phase Y-connected BLDC motors with six states, only two of the three phase windings are conducted at any time. Under this condition, if the back-EMF of the motor is assumed to be an ideal trapezoidal wave, then the back-EMF can be determined by the rotor position angle and its rate of change (i.e. the speed). With the back-EMF known, when the torque is given and the

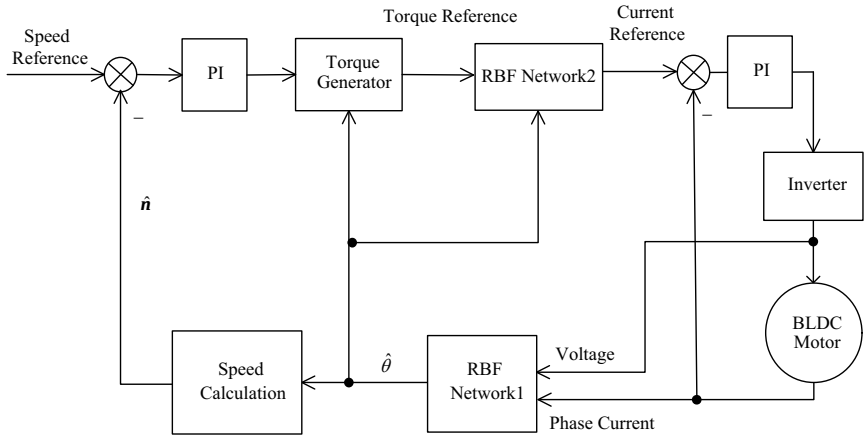


Figure 4.17 Dual-RBF network control without position sensors.

operation in maximum torque mode is guaranteed, the current reference value without torque ripple can be calculated. In other words, the reference current is the function of motor torque and rotor position, the function relation could be accomplished by RBF network 2. By comparing the estimated reference current with the actual current and regulating the current through a PI controller, the current injected into the winding is controlled, so that the torque ripple of the speed-control system is restrained.

When a BLDC motor speed-control system runs with position sensors, the mentioned dual-RBF network control above can be transformed into single neural-network direct control mode, so that the speed loop adopts PI control while the current loop uses RBF network control, as shown in Figure 4.18. The dual-closed-loop control strategy of a single RBF network with position sensors could also use the combination control mode where the speed loop is neural-network control while the current loop adopts PI control.

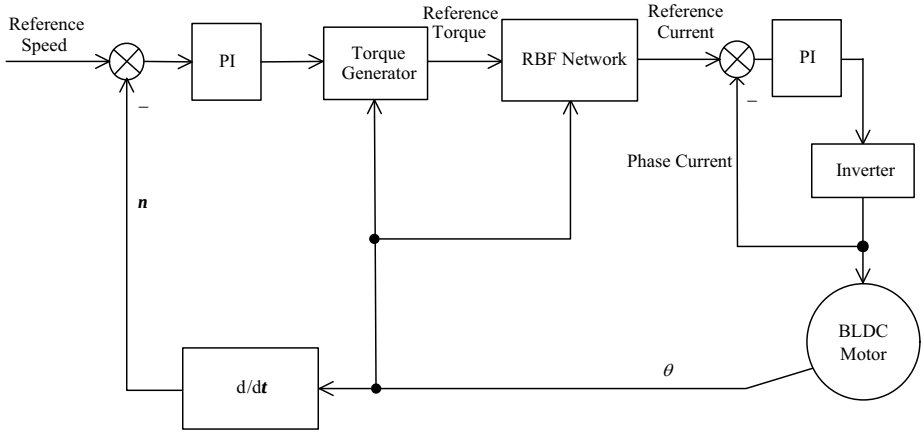


Figure 4.18 Single RBF network control with position sensors.

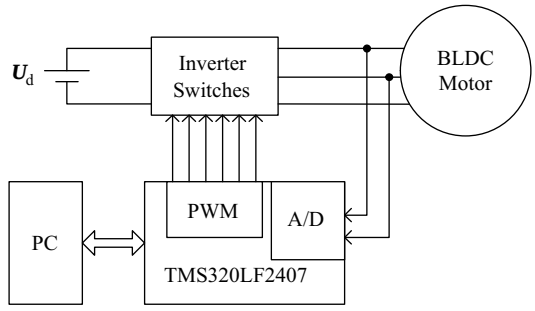


Figure 4.19 System control diagram.

The proposed dual-RBF network position sensorless speed control algorithm is implemented in TMS320LF2407 DSP, whose high-speed calculation capacity guarantees the reliable online control for BLDC motor. The system control diagram is shown in Figure 4.19, and the corresponding flowchart of software program is shown in Figure 4.20.

The experimental waveform is obtained through an Agilent 54622A oscilloscope. Figure 4.21(a) presents the current of phase A when the motor runs under rated speed

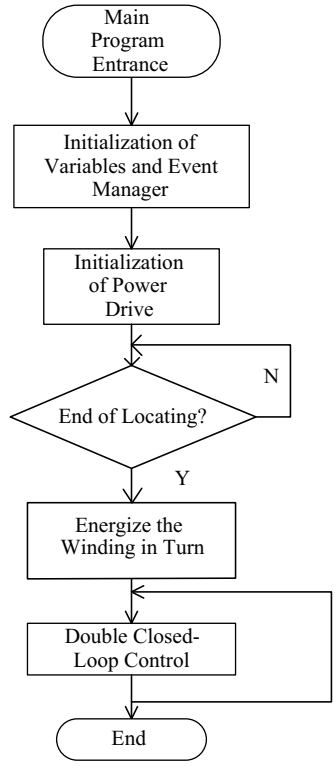
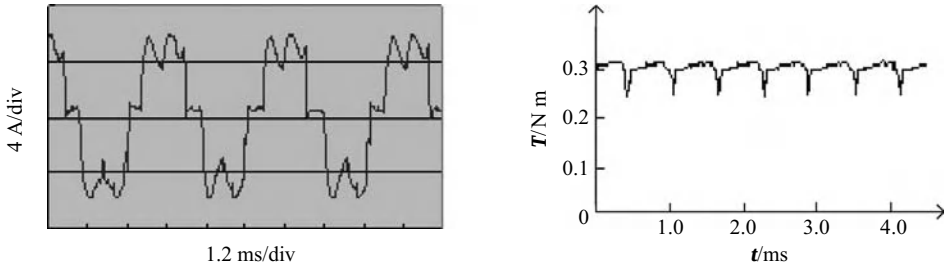


Figure 4.20 Flowchart of the main program.



(a) Current waveform of phase A (b) Torque waveform

Figure 4.21 Experimental results without reference-current estimation.

with only the rotor position online estimation network and a load torque equal to 0.3 N m. The corresponding output torque is shown in Figure 4.21(b).

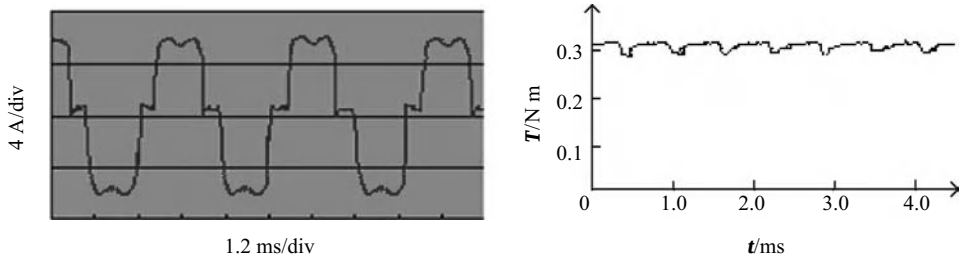
It can be seen from Figure 4.21 that if there are no rotor-position sensors, the current could still commutate correctly through position-sensorless speed control. However, there is a great difference between the actual current waveform and the ideal square wave. Figure 4.21 shows that the amplitude of the torque ripple is about 30 per cent of the average torque.

Figure 4.22 is the current waveform of phase A and its corresponding output torque when the real time reference current estimation is applied.

From Figure 4.22, we can see that the current waveform is clearly improved. In this case, the amplitude of torque ripple is reduced to 4 per cent of the average torque. Thus, the robustness and stability of the speed-control system are improved greatly. Therefore, the dual-BRF-based neural-network control could realize position-sensorless speed control with less torque ripple for BLDC motors.

4.2.3 Genetic Algorithm Optimization Control

In order to achieve precise speed control for BLDC motors, advanced algorithms such as genetic algorithms, ant-colony algorithms, and artificial immune algorithms could be used to optimize the control rules under different operating states, so that better optimized control rules could be obtained to improve the control performance of BLDC motors [22–26]. This section mainly focuses on the application of genetic algorithm on BLDC motors.



(a) Current waveform of phase A (b) Torque waveform

Figure 4.22 Experimental results with reference current estimation.

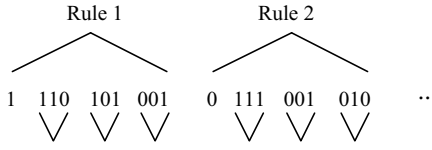


Figure 4.23 Encoding modes of genetic algorithm.

4.2.3.1 Optimization of Fuzzy Control Rules

Note that the nonlinearity of a controlled object usually increases the difficulty in determination of control rules for a BLDC motor fuzzy controller. Even the fuzzy control rules are already obtained in certain conditions, it is difficult for them to be used directly with system variation. Theoretical analysis and practical experiences have shown that the fuzzy control rules could be optimized by the genetic algorithm, so that the control performance of the controller could be improved with better stability and higher control accuracy. Figure 4.23 shows the encoded modes that are used for the fuzzy control rules optimized by the genetic algorithm. In Figure 4.23, 10-bit binary codes are used to express the fuzzy decision rules. The first bit is the flag, which indicates whether the rule is used or not. "1" indicates that the rule is preserved, while "0" indicates that the rule is abandoned. The codes of 2–4 bits, 5–7 bits, and 8–10 bits, respectively, represents the error e, the change of error ec, and the decision value FD. All the three variables use 001, 010, 011, 100, 101, 110 and 111 to represent NB, NM, NS, ZE, PS, PM and PB, respectively. For example, in Figure 4.23, rule 1 represents that if e is PM and ec is PS, then FD is NB, in which the first bit 1 indicates that the rule 1 is preserved after optimization. Rule 2 indicates that if e is PB and ec is NB, then FD is NM. The first bit 0 indicates that the rule 2 will be abandoned after optimization. Table 4.2 presents the fuzzy control rules after genetic algorithm optimization.

Table 4.2 shows that 6 fuzzy control rules are abandoned and 4 rules are changed after genetic algorithm optimization. Since the optimization procedure of fuzzy control rules using a genetic algorithm is relatively complex, the high-speed performance DSP is also difficult to fulfill the optimization algorithm online when the BLDC motor runs at high speed. Therefore, the optimization of fuzzy control rules is generally performed offline according to the experimental data and then embedded into DSP.

Table 4.2 Fuzzy decision rules optimized by genetic algorithm

FD (*e* / *ec*)	NB	NM	NS	ZE	PS	PM	PB
NB	NB	NB	NM		NS	ZE	ZE
NM		NM	NS	NS	NS	ZE	ZE
NS	NM	NM	NS	NS	ZE	ZE	PS
ZE	NM	NS	NS	ZE	PS	PS	PM
PS		ZE	ZE	PS	PS	PM	
PM	ZE	ZE	ZE	PS	PM	PB	PB
PB	ZE		PS		PM	PB	PB

4.2.3.2 Parameter Optimization of the Fuzzy Controller

The design of the fuzzy controller determines the performance of the fuzzy-control system, while the performance of fuzzy controller is determined by the fuzzy rules or fuzzy inference. In general, after the fuzzy controller design is finished, its fuzzy rules or fuzzy inference are usually determined and cannot be adjusted. A large number of simulation and experimental results suggest that the quantization factor and the scaling factor of the fuzzy controller have a great influence on its performance. Occasionally, the output characteristics of the fuzzy controller may be changed. When the system characteristics are changed, the parameters of the fuzzy controller need to be adjusted in real time so that good dynamic and static characteristics of the system can be achieved. Hence, a fuzzy controller with fixed parameters lacks good generality and adaptability. In this case, control rules with simple analytic expressions can be adopted to design the BLDC motor fuzzy controller with adjustable weight coefficients.

In the design of a fuzzy controller for a BLDC motor, the input variable is required to be converted from the basic discourse domain to the fuzzy set discourse domain. The error quantization factor K_{e1} and the error change quantization factor K_{ec} are used to achieve this goal. Besides, the control value of each sampling from the fuzzy controller cannot be used on the controlled object directly. It should be converted into the basic domain by using the scaling factor K_u.

As for the influences of the parameters K_{e1}, K_{ec} and K_u on the system response, we can fix any two of the three parameters and change the third parameter to analyze the control laws. The corresponding control laws are concluded as follows.

(1) The larger the K_{e1}, the faster the system response. Note that a large K_{e1} may cause big overshoot and long adjusting time for the system. Moreover, an oscillating phenomenon would appear in serious cases. While if the K_{e1} is too small, the system convergence rate will be slower. Generally, the system static error will be reduced by increasing K_{e1}.
(2) The larger the K_{ec}, the slower the system response. Usually, the smaller the K_{ec}, the more sensitive the system response. Hence, a faster rising rate is achieved. But too small a K_{ec} may cause oscillation in the system. Similarly, the static error will be reduced by increasing K_{ec} too.
(3) K_u is equivalent to the proportional gain in a normal control system. Generally, the larger the K_u, the faster the response rate. Note that large K_u may cause serious response oscillation, while a small K_u may lead to a slower convergence rate. In the three quantization factors, K_u is the most influential factor for system response.

So, it can be concluded that proper adjustment of the three parameters could increase the system response speed, reduce the overshoot, and improve the static and dynamic performance of the fuzzy controller. In addition, good dynamic performance and reliable stability performance cannot be easily obtained by using fuzzy controller with fixed parameters. Therefore, it is necessary to adjust these parameters online according to the system dynamic error e as the following equations:

$$K_{e1} = \begin{cases} K_{e10} + K_1 \times e, & |e| \le \dfrac{e_{max}}{2} \\ K_{e10} + K_1 \times \dfrac{e_{max}}{2}, & |e| > \dfrac{e_{max}}{2} \end{cases} \tag{4.29}$$

$$K_{ec} = \begin{cases} K_{ec0} + K_2 \times e, & |e| \le \dfrac{e_{max}}{2} \\ K_{ec0} + K_2 \times \dfrac{e_{max}}{2}, & |e| > \dfrac{e_{max}}{2} \end{cases} \tag{4.30}$$

$$K_u = \begin{cases} K_{u0} + K_3 \times e, & |e| \le \dfrac{e_{max}}{2} \\ K_{u0} + K_3 \times \dfrac{e_{max}}{2}, & |e| > \dfrac{e_{max}}{2} \end{cases} \tag{4.31}$$

where K_{e10}, K_{ec0} and K_{u0} are the base values, K_1, K_2 and K_3 are fine-tuning parameters (all are non-negative), and e_{max} is the largest positive error value in the basic domain.

From the above, we can see that increasing K_{e1} is equivalent to decreasing the basic domain of error. Hence, the control effect of error variables is increased. In addition, it can be seen from Equation (4.29) that when $|e| \le e_{max}/2$ is satisfied, the control effect will be increased by increasing $K_{e1}$with the error increasing. When the error decreases gradually, in order to reduce the overshoot, the control effect of error change should be increased, i.e. K_{ec} should be increased. From Equation (4.31) we can see that K_u increases with the error increasing, so that faster convergence rate can be obtained.

The main procedures of how to use the genetic algorithm to optimize the fuzzy controller's parameters are shown in the following three steps:

(1) Determine the decision variables with their constraining conditions and the corresponding encoding and decoding methods. In the optimization of parameters, base values K_{e10}, K_{ec0}, K_{u0} and fine adjusting parameters K_1, K_2, K_3 are chosen to be decision variables. The restraining conditions of decision variables are usually determined by the system stability performance index. If the stable error is required to be less than δ_1, then

$$K_{e1} \geqslant \frac{1}{2\delta_1} \tag{4.32}$$

Hence, according to experience, the range of base values are determined as K_{e10}: 0–120, K_{ec0}: 0–120, K_{u0}: 0–7. The restraining conditions of K_1, K_2 and K_3 are the current predetermined base values obtained by genetic algorithm optimization.

Construct the optimized model and determine the individual evaluation methodology. One of the characters of a genetic algorithm is to use the objective function of the solved problem to obtain the next step's searching information, where the usage of objective function is reflected through evaluation of individual fitness. Therefore, the fitness function is the key of genetic algorithm. The fitness function is generally transformed from the objective function. Here, the fitness function is designed by using the weight coefficients combination method based on the system's maximum overshoot M_p, adjusting time t_s and stable error e_{sr}, which is shown as

$$f = \alpha \exp[-(M_p/M_{p0})^2] + \beta \exp[-(t_s/t_{s0})^2] + \gamma \exp[-(e_{sr}/e_{sr0})^2] \tag{4.33}$$

where M_{p0}, t_{s0}, e_{sr0} are the corresponding expected index values; α, β, γ are the weight coefficients, which satisfy the condition $\alpha + \beta + \gamma = 1$.

Equation (4.33) shows that the larger the value of the fitness function, the better the system performance.

(2) Genetic operations. Genetic operation is a simulating control of biology genetic inheritance, including the design of three genetic operators (selection operator, crossover operator and mutation operator) and the determination of other operating parameters in the genetic algorithm.

The selection operator, which indicates the chance for each individual to be selected is proportional to its fitness, can be represented as

$$P_{s_i} = f_i / \sum_{j=1}^{n} f_j \tag{4.34}$$

where P_{s_i} is the selected probability of ith individual, f_i is the fitness of ith individual, and n is the population size.

The crossover operator is the main approach to produce new individuals in the genetic algorithm. It is regarded as the major operator for its global searching capability. Here, the single-point crossover operator is used. However, the mutation operator is just the auxiliary method to produce new individuals because of its local searching capability. Here, the basic bit mutation operator is adopted.

As for the determination of operation parameters, the parameters that need to be determined mainly include population size M, termination algebra T, crossover probability P_c and mutation probability P_m. Here, M is set to be 60 while T is equal to 160. Hence, by using the adaptive genetic algorithm proposed by Srinvivas, the parameters P_c and P_m are, respectively, calculated as

$$P_c = \begin{cases} \dfrac{P_{c1}(f_{max} - f')}{f_{max} - f_{avg}}, & f' \geqslant f_{avg} \\ P_{c2}, & f' < f_{avg} \end{cases} \tag{4.35}$$

and

$$P_m = \begin{cases} \dfrac{P_{m1}(f_{max} - f')}{f_{max} - f_{avg}}, & f \geqslant f_{avg} \\ P_{m2}, & f < f_{avg} \end{cases} \tag{4.36}$$

where f_{max} is the maximum population fitness, f_{avg} is the average fitness for per generation population, $f'$is the larger fitness in two crossover individuals, and f is the fitness of the mutation individuals.

Figure 4.24 gives the block diagram of the BLDC motor fuzzy-control system based on optimization of a genetic algorithm. The corresponding flowchart of optimized design for fuzzy controller parameters is shown in Figure 4.25.

Figures 4.26 and 4.27 present the simulation and experimental results of the BLDC motor system controlled by traditional PID and the genetic optimized fuzzy controller. From the figures, we can see that the genetic optimized fuzzy controller has better speed-regulation performance.

In the intelligent control systems for BLDC motor, the genetic algorithm can be combined not only with fuzzy control strategy, but also with the neural network. For example, the

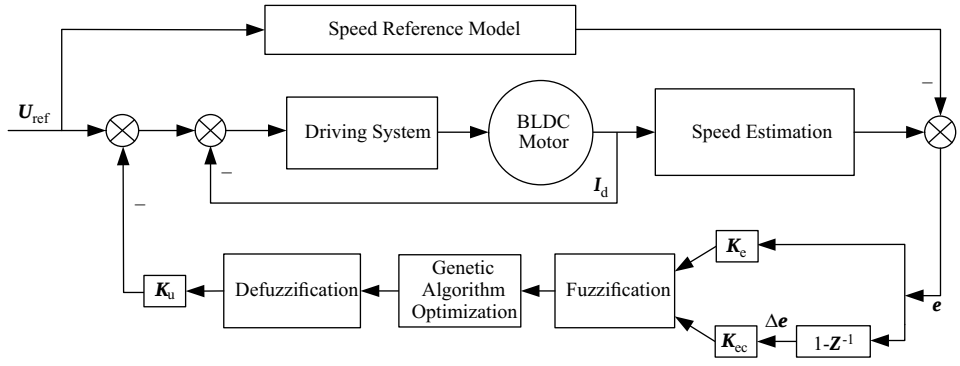


Figure 4.24 The block diagram of a fuzzy-control system based on optimization of genetic algorithm.

structure and learning rules of a neural network can be optimized by a genetic algorithm, so that the corresponding performance of the intelligent controller is improved. In Figure 4.28, the speed loop adopts RBF network control optimized by a genetic algorithm, while the current loop adopts traditional PID control. The RBF network structure in a speed loop is optimized by the genetic algorithm, which can guarantee good stability and better antidisturbance ability of the system.

4.2.4 Sliding-Mode Variable Structure Control

Sliding-mode control is usually used for motor drive. One of the advantages of sliding-mode variable structure control is that its sliding mode has good adaptive ability against the system disturbance and perturbation. In particular, its high-speed switching characteristic has better control on the current ripple caused by load variation and winding commutation [27,28]. The block diagram of a single closed-loop sliding mode speed-control system based on the extended state observer is shown in Figure 4.29. The part outside the dotted line is the motor model, while the part inside the dotted line is the controller. The extended state observer estimates the load torque through the electromagnetic torque and speed of the motor. K_1, K_2, K_3, K_4 and K_5 are parameters of the variable structure control systems.

4.2.4.1 Controller Design

From the principle of BLDC motor, the second-order model for BLDC motor can be described by state equations as

$$\begin{cases} \dot{x}_1 = x_2 \\ \dot{x}_2 = -\dfrac{(r_a J + B_v L_a)}{L_a J} x_2 - \dfrac{(B_v r_a + k_e K_T)}{L_a J} x_1 + \dfrac{K_T}{L_a J} u - \dfrac{r_a T_L}{L_a J} \end{cases} \tag{4.37}$$

where x_1 is the motor's angular speed, T_L is the motor load, which is regarded as the motor disturbance to be estimated by the extended state observer.

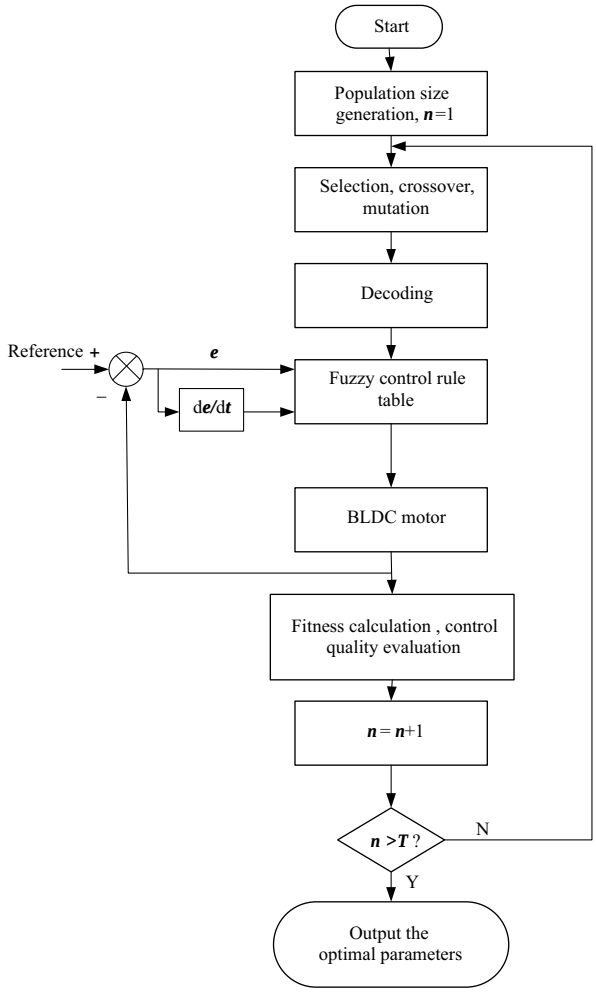
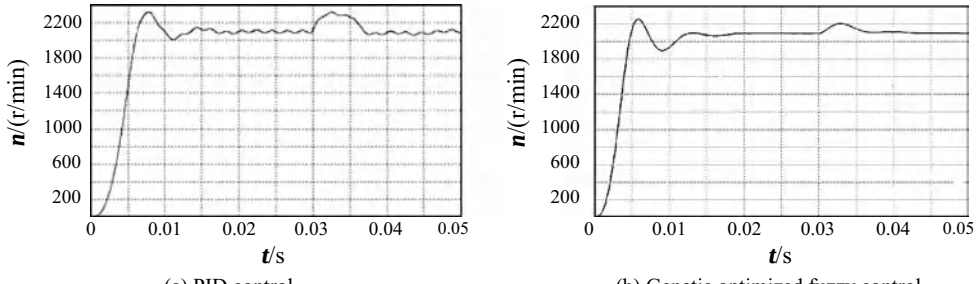


Figure 4.25 The flowchart of optimized design for a fuzzy controller's parameters based on a genetic algorithm.



(a) PID control (b) Genetic optimized fuzzy control

Figure 4.26 Simulation speed curves with load variation.

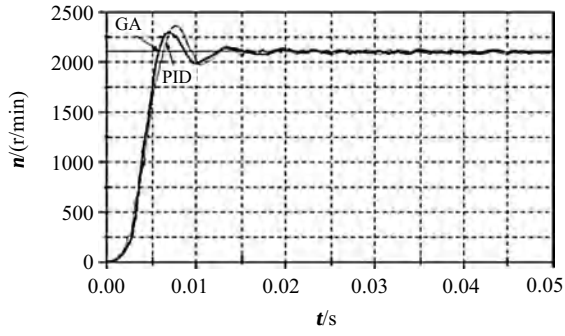


Figure 4.27 Experimental speed curves with load variation.

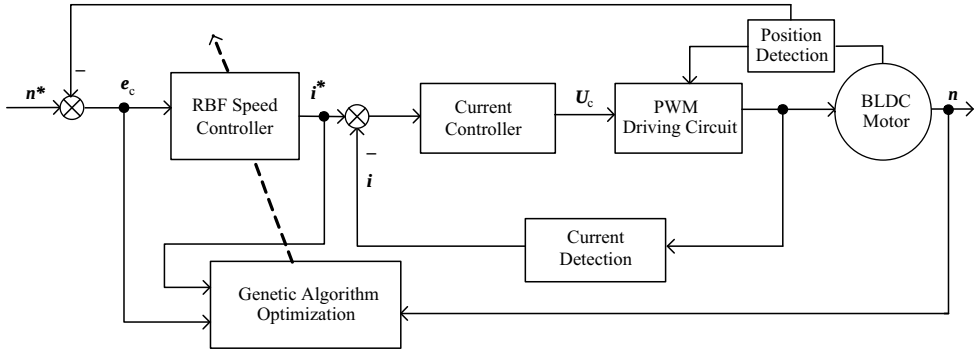


Figure 4.28 Block diagram of a BLDC motor speed-control system based on a genetic neural network.

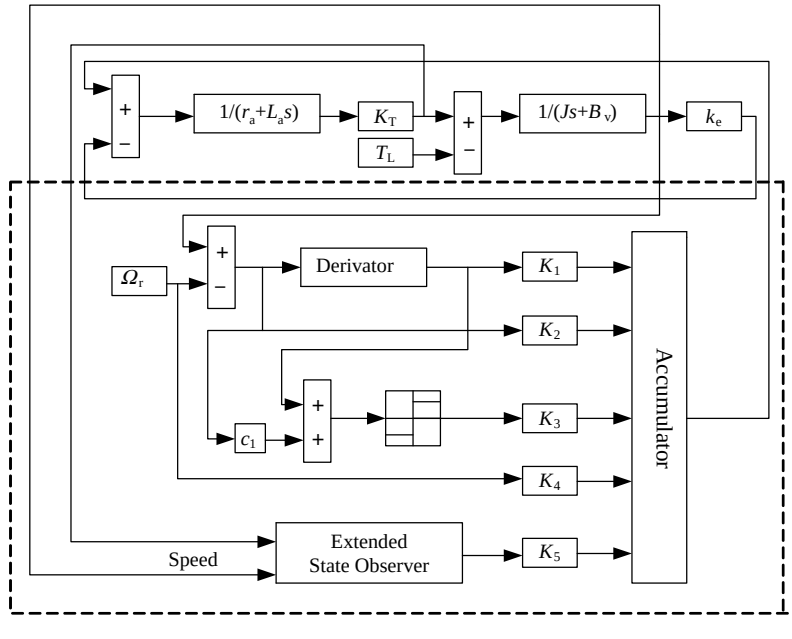


Figure 4.29 Variable structure control based on an extended state observer.

Let

$$e = \Omega_r - \Omega \tag{4.38}$$

where Ω_r is the reference angular speed.

Substituting Equation (4.38) into Equation (4.37), we get

$$\begin{cases} \dot{x}_1 = x_2 \\ \dot{x}_2 = -\dfrac{(r_a J + B_v L_a)}{L_a J} x_2 - \dfrac{(B_v r_a + k_e K_T)}{L_a J} x_1 + \dfrac{(B_v r_a + k_e K_T)}{L_a J} \Omega_r - \dfrac{K_T}{L_a J} u + \dfrac{r_a T_L}{L_a J} \end{cases} \tag{4.39}$$

where $x_1 = e$, $x_2 = \dot{e}$.

So, the parameters of $\boldsymbol{A}$ and $\boldsymbol{B}$ in $\dot{\boldsymbol{x}} = \boldsymbol{A}\boldsymbol{x} + \boldsymbol{B}\boldsymbol{u} + \boldsymbol{F}(t)$ are, respectively, given as

$$\boldsymbol{A} = \begin{bmatrix} 0 & 1 \\ -\dfrac{(B_v r_a + k_e K_T)}{L_a J} & -\dfrac{(r_a J + B_v L_a)}{L_a J} \end{bmatrix} \tag{4.40}$$

$$\boldsymbol{B} = \begin{bmatrix} 0 & -\dfrac{K_T}{L_a J} \end{bmatrix} \tag{4.41}$$

Let $C^T = [c_1\ 1]$ and $\boldsymbol{F}(t)=[0\ f(t)]^T$, then

$$f(t) = \frac{(B_v r_a + k_e K_T)}{L_a J} \Omega_r + \frac{r_a T_L}{L_a J} \tag{4.42}$$

Further, considering the sliding-mode switching surface as

$$s = \boldsymbol{C}^T \boldsymbol{x} = 0 \tag{4.43}$$

Then, the sliding mode switching surface divides the whole state space into two parts: $s>0$ and $s<0$. So the controlling value $u(x)$ of variable structure control can be defined as

$$u(x) = \begin{cases} u^+(x) & s(x) > 0 \\ u^-(x) & s(x) < 0 \end{cases} \tag{4.44}$$

where $u^+(x) \neq u^-(x)$.

Note that the existing condition of the sliding mode is

$$\lim_{s \to +0} \dot{s} < 0, \ \lim_{s \to -0} \dot{s} > 0$$

Besides the existence of the sliding mode, the ability of the motion going into sliding mode and its stability should be guaranteed too. Generally, different parameters can be used to achieve different variable structure control strategies.

Moreover, by using the equivalent control law, the sliding mode equation can be obtained directly without limit calculation.

Let $\dot{s} = 0$, then

$$\boldsymbol{CAx} + \boldsymbol{CBu} + \boldsymbol{CF}(t) = 0 \tag{4.45}$$

The solution of Equation (4.45) is

$$\boldsymbol{u}_{\text{eq}} = -(\boldsymbol{CB})^{-1}[\boldsymbol{CAx} + \boldsymbol{CF}(t)] \tag{4.46}$$

Hence, the ideal sliding mode equation is obtained as

$$\dot{\boldsymbol{x}} = [\boldsymbol{I} - \boldsymbol{B}(\boldsymbol{CB})^{-1}\boldsymbol{C}]\boldsymbol{Ax} + [\boldsymbol{I} - \boldsymbol{B}(\boldsymbol{CB})^{-1}\boldsymbol{C}]\boldsymbol{F}(t) \tag{4.47}$$

and the control input is rewritten as

$$\boldsymbol{u} = \boldsymbol{u}_{\text{eq}} - \alpha \text{sgn}(s)\boldsymbol{I} \tag{4.48}$$

Note that if the initial state of system is not near the area of $s = 0$, the state trajectory is required to move towards the switching surface $s = 0$. This means that the reaching condition of the sliding mode must be satisfied.

Further, if the Lyapunov function is chosen as $V = s^2/2$, by using Lyapunov stability theorem, we get

$$\frac{1}{2}\frac{\text{d}}{\text{d}t}(s^2) = s\dot{s} < 0 \tag{4.49}$$

This is exactly the condition of global sliding control mode, which indicates that any motion point in state space has the approaching tendency to the switching surface $s = 0$. Obviously, if the system satisfies the condition of global sliding control mode, it will satisfy the existing condition and the reaching condition of sliding mode simultaneously.

From Equations (4.43) and (4.49), we obtain

$$s(c_1\dot{x}_1 + \dot{x}_2) < 0 \tag{4.50}$$

Then, substituting Equations (4.39), (4.46) and (4.48) into Equation (4.50) gives

$$s[-b\alpha \,\text{sgn}(s) + f(t)] < 0 \tag{4.51}$$

So, $\text{sgn}(b)\alpha > |f(t)/b|$. Hence, the value of α is determined. Then, by substituting α and u_{eq} into Equation (4.48), the control value u can be obtained.

Now, the torque equation of BLDC motor is recalled as

$$\dot{\Omega} = -\frac{B_{\text{v}}}{J}\Omega - \frac{1}{J}T_{\text{L}} + \frac{1}{J}T_{\text{e}} \tag{4.52}$$

Let

$$\begin{cases} z_1 = \Omega \\ z_2 = T_{\text{L}} \\ u = T_{\text{e}} \end{cases} \tag{4.53}$$

Table 4.3 Parameters for variable structure control

K_1	K_2	K_3	K_4	K_5
0.0001637	0.06710	0.0006	0.06710	18.08

Then, the second-order extended state observer of the system can be represented as

$$\begin{cases} \dot{z}_1 = z_2 - \beta_{01}\text{fal}(z_1 - x(t), \alpha_1, \delta) + b_0 u \\ \dot{z}_2 = -\beta_{02}\text{fal}(z_1 - x(t), \alpha_2, \delta) \end{cases} \tag{4.54}$$

where β_{01}, β_{02} — coefficients of observer;
b_0 — estimated value of b;

$$\text{fal}(z, \alpha, \delta) = \begin{cases} |z|^{\alpha}\text{sgn}(z), & |z| > \delta \\ z/\delta^{1-\alpha}, & |z| \le \delta. \end{cases}$$

$0 < \alpha_2 < \alpha_1 \le 1$, and usually α_1 and α_2 are set to 1 and 0.5, respectively.

Thus, the load torque T_L will be estimated by the observer designed from Equation (4.54).

The corresponding variable structure parameters such as K_1, K_2, K_3, K_4 and K_5 are shown in Table 4.3. Table 4.4 shows the related parameters of the extended state observer.

4.2.4.2 Simulation and Experimental Results

The simulation curves in Figure 4.30 are the speed responses of the BLDC motor under the control of the PID controller and the variable structure controller based on an extended state observer, respectively, in which, the load torque changes from 0.1 N m to 0.2 N m at 0.05 s. Comparing the proposed variable structure control with PID control, less speed ripple and a shorter recovery time are achieved by the variable control method. Hence, the variable structure controller has less overshoot, a faster response speed and is not sensitive to the load variation.

In Figures 4.31 and 4.32, the experimental speed-tracing curves under PID control and VSC are shown, respectively. In the experiment, the input of the reference signal is the sinusoidal waveform.

Figures 4.31 and 4.32 show that faster response speed and better trace ability of the system can be obtained under the control of VSC with the extended state observer.

For the purpose of getting better control performance, the sliding-mode control combined with other filtering and estimation methods can be used [29]. If the Kalman filter is added to the

Table 4.4 Parameters of extended state observer

α_1	α_2	β_{01}	β_{02}	δ_1	δ_2
0.75	0.25	7000	2000	0.1	0.01

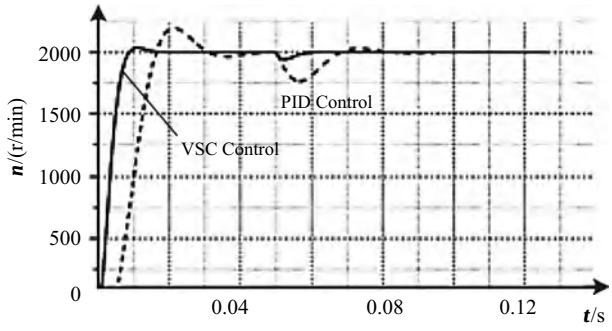


Figure 4.30 Speed response curves under the control of PID and VSC.

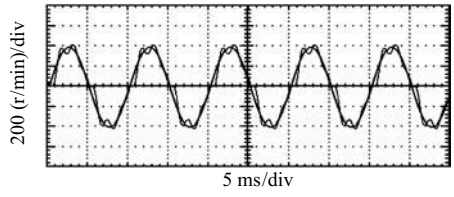


Figure 4.31 Speed-tracing curve under PID control.

sliding-mode control, the sliding-mode chattering can be reduced to some degree. Figure 4.33(a) shows the block diagram of the BLDC motor driving system controlled by VSC with a Kalman filter. The corresponding simulation model in MATLAB is shown in Figure 4.33(b).

Since the system phase trajectory can reflect the chattering of sliding-mode variable structure control, Figure 4.34(a) shows the system phase trajectory without Kalman filter, while Figure 4.34(b) is the system phase trajectory with a Kalman filter.

It is obvious from Figure 4.34 that a Kalman filter has a certain influence on reducing the chattering in the sliding-mode variable structure control for BLDC motors. Hence, the Kalman filter can improve the control precision.

4.2.5 Grey Control

Grey control, a novel method solving indefinite problems with little statistical information, is used to study uncertain systems together with theories like fuzzy mathematics, rough set theory and unascertained mathematics. Within the last 30 years, grey control theory has been

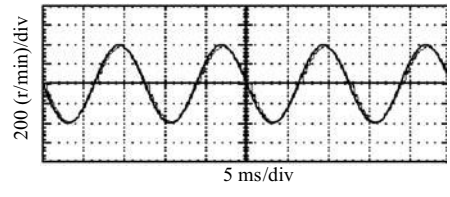
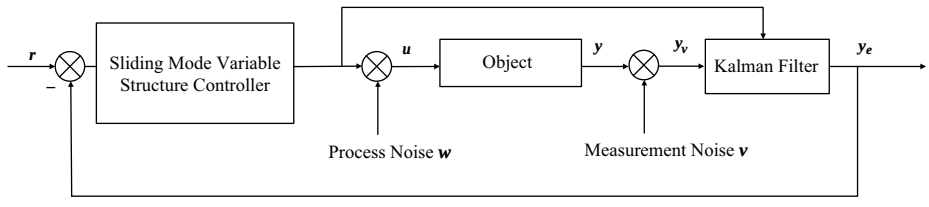
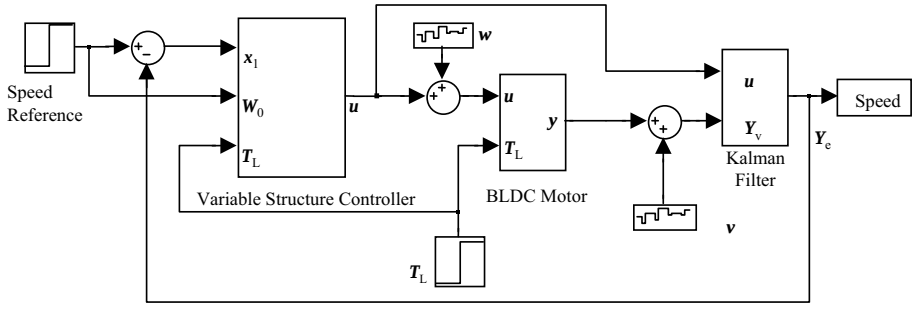


Figure 4.32 Speed-tracing curve under VSC.

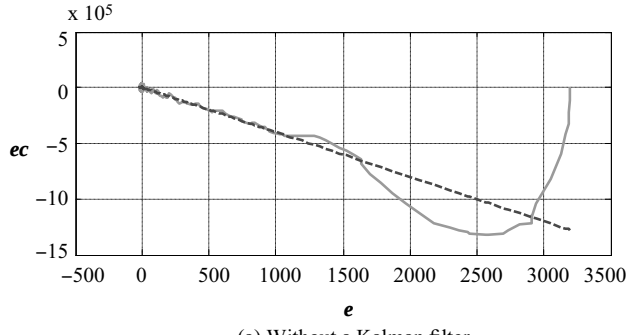


(a) Block diagram of control system

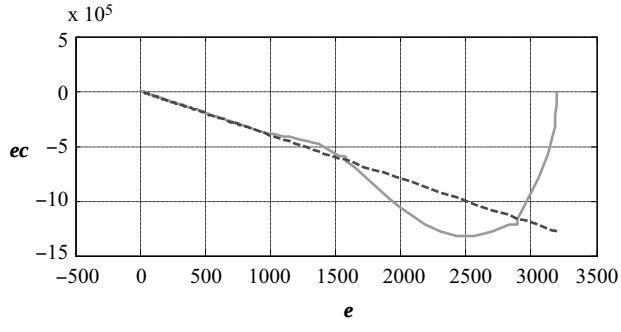


(b) Simulation model in MATLAB

Figure 4.33 Sliding-mode variable structure control for a BLDC motor based on a Kalman filter.



(a) Without a Kalman filter



(b) With a Kalman filter

Figure 4.34 System phase trajectory (— Phase trajectory, ---- Sliding surface).

much developed and has been applied in many fields [30,31]. Grey control mainly consists of eigengrey system control and grey system method-based control, such as grey-related control and GM (1, 1) predictive control.

Grey theory doesn't need distribution rules of membership functions, which makes it superior in solving problems with inaccurate or incomplete information and small samples. A motor control system is a typical grey system since the disturbances of internal parameters and motor load can be considered as uncertainties. It can obtain expected control performances for the induction motor, BLDC motor and reluctance synchronous motor by building a grey control model with grey system theory [32–34]. Therefore, grey control is feasible when applied to BLDC motors.

4.2.5.1 Controller Design

Currently, a BLDC motor control system is becoming more complex with novel control algorithms implemented. In practice, it is difficult for a motor control system to give definite values to control inputs due to the complexity of problems, incompleteness of information and inaccuracy of data. Consequently, it is not easy for the speed of the BLDC motor to be controlled accurately. In this condition, the system could be seen as a grey system where grey predictive control is utilized to improve the performance of the system.

A typical speed-control model of the BLDC motor can be simplified as

$$\begin{cases} \dfrac{\mathrm{d}i}{\mathrm{d}t} = -\dfrac{r_\mathrm{a}}{L_\mathrm{a}} i - \dfrac{k_\mathrm{e}}{L_\mathrm{a}} \Omega + \dfrac{u}{L_\mathrm{a}} \\ \dfrac{\mathrm{d}\Omega}{\mathrm{d}t} = -\dfrac{B_\mathrm{v}}{J} \Omega - \dfrac{k_\mathrm{T}}{J} i - \dfrac{T_\mathrm{L}}{J} \end{cases} \tag{4.55}$$

And its corresponding state equation is

$$\dot{\boldsymbol{x}} = \boldsymbol{A}\boldsymbol{x} + \boldsymbol{B}u + \boldsymbol{F}w_1 \quad = \begin{bmatrix} -\dfrac{r_\mathrm{a}}{L_\mathrm{a}} & -\dfrac{k_\mathrm{e}}{L_\mathrm{a}} \\ \dfrac{K_\mathrm{T}}{J} & -\dfrac{B_\mathrm{v}}{J} \end{bmatrix} \begin{bmatrix} i \\ \Omega \end{bmatrix} + \begin{bmatrix} \dfrac{1}{L_\mathrm{a}} \\ 0 \end{bmatrix} u - \begin{bmatrix} 0 \\ \dfrac{1}{J} \end{bmatrix} T_\mathrm{L} \tag{4.56}$$

Considering the uncertainty of state parameters, it can be expressed as

$$\dot{\boldsymbol{x}} = \boldsymbol{A}\boldsymbol{x} + \boldsymbol{B}u + \boldsymbol{F}w \tag{4.57}$$

where $w = w_1 + w_2$, and $w_2 = V_1 x_1 + V_2 x_2$ represent the disturbances caused by the uncertainty of state parameters.

Generally, the unknown variable w that cannot be measured directly can be estimated from the measured data as

$$w(x,k) = \boldsymbol{F}^{-1}(\dot{\boldsymbol{x}}(t) - \boldsymbol{A}\boldsymbol{x}(t) - \boldsymbol{B}u(t)) \tag{4.58}$$

where $t = kT$, T is the sampling period, and $k = 1, 2, \cdots, N$.

In order to reduce the influence of uncertain parts on the system, improve control performance of the system and increase its disturbance rejection ability, a grey estimator is adopted to estimate the uncertain model parameter $\boldsymbol{V} = [V_1, V_2, \omega_1]$ and then $w(x,k)$ is compensated properly. Such grey estimation doesn't demand a continuous and real-time operation, implying that data divergence in traditional real-time identification will not happen.

The grey estimator algorithm when GM (1, 2) control is used to predict and compensate the speed-control system of BLDC motor is given as:

(1) Establish an initial discrete state sequence $x_i^{(0)}(k)$, and compute the summation of the discrete sequence $x_i^{(1)}(k)$, where $i = 1, 2, \cdots, n$. The equal dimension new information can be used for the modeling of $x_i^{(0)}(k)$, meaning that at every sampling instant the most initial information is eliminated and the latest information is added, which guarantees that the GM (1, 2) model always reflects the latest actions of the system without extra calculation. It is expressed as

$$\boldsymbol{X}^{(0)} = \left(x^{(0)}(1), x^{(0)}(2), \cdots x^{(0)}(n)\right) \overset{\text{NEXT}}{\longrightarrow} \boldsymbol{X}^{(0)} = \left(x^{(0)}(2), x^{(0)}(3), \cdots x^{(0)}(n+1)\right)$$

(2) Calculate the vector $\boldsymbol{D} = \left[x_1^{(0)}(2), \quad x_1^{(0)}(3), \ \cdots, x_1^{(0)}(n)\right]^{\mathrm{T}}$ and the corresponding sequence $x^{(1)}(k) = \sum_{i=1}^{k} x^{(0)}(i)$ produced by the accumulated generating operation (AGO);

(3) Calculate the matrix $\boldsymbol{B}_1 = \begin{bmatrix} -[x_1^{(1)}(1) + x_1^{(1)}(2)]/2 & x_2^{(1)}(2) & 1 \\ -[x_1^{(1)}(2) + x_1^{(1)}(3)]/2 & x_2^{(1)}(3) & 1 \\ \vdots & \vdots & \vdots \\ -[x_1^{(1)}(n-1) + x_1^{(1)}(n)]/2 & x_2^{(1)}(n) & 1 \end{bmatrix}$;

(4) Estimate the unknown parameters by using the least squares method as

$$\hat{\boldsymbol{V}}^{\mathrm{T}} = (\boldsymbol{B}_1^T \boldsymbol{B}_1)^{-1} \boldsymbol{B}_1^T \boldsymbol{D} = [\hat{V}_1, \hat{V}_2, \hat{w}_1]^{\mathrm{T}}.$$

Based on the above control law, the compensation control u_{c} is introduced according to the estimated $\hat{\boldsymbol{V}}$, where

$$u = u_{\mathrm{p}} + u_{\mathrm{c}} \tag{4.59}$$

$$u_{\mathrm{c}} = -\boldsymbol{B}^{-1}\boldsymbol{F}\left[\sum_{i=1}^{n} \hat{V}_i x_i + \hat{w}_1\right] \tag{4.60}$$

Figure 4.35 shows the diagram of the speed-control system of a BLDC motor, in which dual closed-loop control is applied. In addition, a PI controller is used in both loops.

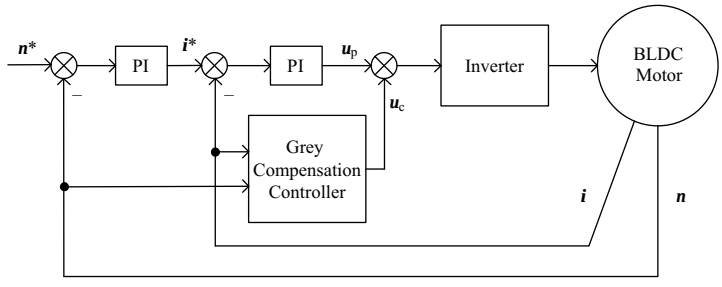


Figure 4.35 Diagram of BLDC motor speed-control system.

4.2.5.2 Simulation Results

Figure 4.36 shows the simulation results of the BLDC motor under GM (1, 2) control with no load and when the load is applied at 0.1 s, respectively.

It is seen from Figure 4.36 that grey GM (1, 2) speed control is better than simple PID control for its smaller overshoot and faster dynamic response whether the motor is operating with no load or varied load.

Meanwhile, the grey control model GM (1, 2) can be used for the predictive compensation control of external load disturbance and internal parameter perturbation comprehensively. Figure 4.37 shows the speed response of the BLDC motor under the predictive compensation control of GM (1, 2) when both phase resistance and moment of inertia of the motor are increased by 50% and the load variation is the same as that in Figure 4.36(b).

It is seen from Figure 4.37 that the internal parameter variation has little influence on speed output, which is still able to follow the reference value of the system.

4.2.6 Other Intelligent Control Strategies

There are many good intelligent speed-control methods for BLDC motors, of which some commonly used ones have been analyzed above. Meanwhile, there are some other intelligent speed-control methods, such as fuzzy-control methods based on ant-colony optimization,

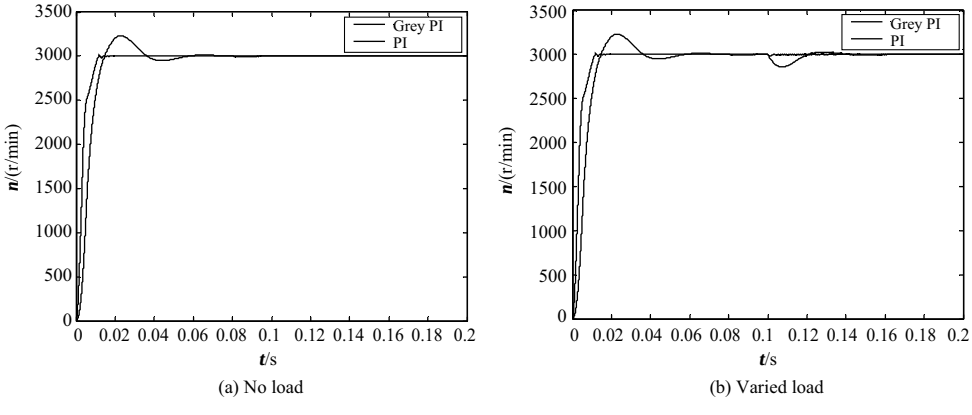


Figure 4.36 Simulation results of BLDC motor under GM (1, 2) control.

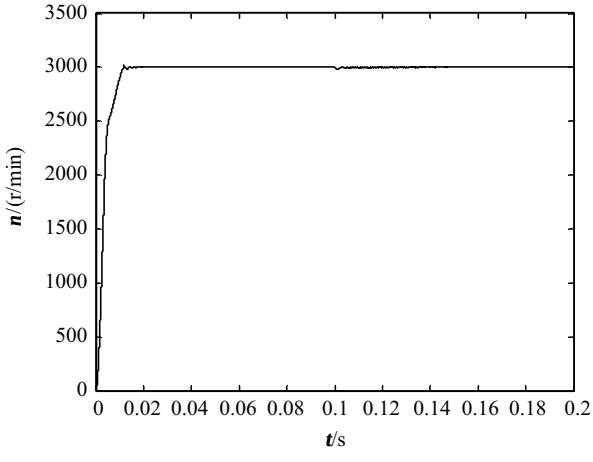


Figure 4.37 Speed response with parameter perturbation.

adaptive-learning neural-network control based on artificial immune feedback, and so on [24,26,35].

The ant-colony algorithm is inspired by the fact that ants search for food by the shortest path, as shown in Figure 4.38. Compared with genetic algorithms and simulated annealing algorithms, the ant-colony algorithm is outstanding since its combination of distributed computing, mechanism of positive feedback and greedy searching ability, which increases its parallelism and extensibility. On the other hand, the deficiency of the ant-colony algorithm is that it usually takes a long time to search and it is likely to fall into stagnation. It is demonstrated both theoretically and practically that in some conditions the optimal fuzzy control rules generated by the ant-colony optimization algorithm functions better than the rules generated by other algorithms such as genetic algorithms, which will improve the control performance.

The immune system is considered as "the second brain system" next to the nervous system, which establishes self- and nonself-nonlinear adaptive networks from different kinds of antibodies and identifies foreign objects adaptively. Also, the immune system can control and eliminate the invading foreign antigens, playing an important role in handling dynamic changing environment [26,36]. Figure 4.39 shows the simplified schematic diagram of the biological immune system, in which the real lines represent positive effect and the imaginary lines negative effect. Using the immune feedback law as the adaptive learning algorithm of

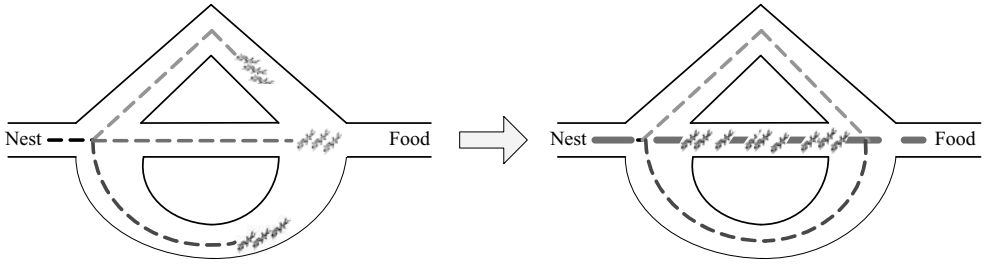


Figure 4.38 The shortest path of ants' searching for food.

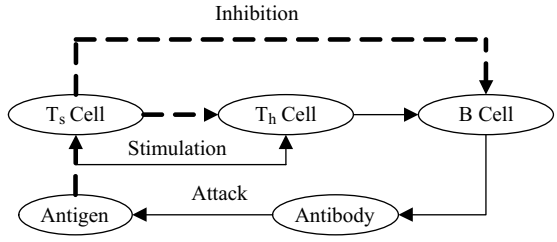


Figure 4.39 Simplified schematic diagram of biological immune system.

artificial neural network increases the downward gradient of the neural network learning algorithm, so as to reduce the deviation to a minimum faster for the neural network and increase the learning step as much as possible. Therefore, the dynamic and static performance and the control precision of the BLDC motor are improved. The problem of tracking characteristics for speed control that is poor when interfered strongly and influenced by intense nonlinear and uncertainties for a typical PID controller is solved.

4.3 Influences of Machine Parameters on Dynamic Response and Speed Range

Similar to other types of motors, the parameters of a BLDC motor, such as resistance, inductance and moment of inertia, will change under different operating conditions, affecting the speed performance of the BLDC motor. There exists a complex nonlinear relation among resistance, inductance and moment of inertia, and the speed and torque of the motor, for which a digital simulation method can be used here to analyze the effect of relative parameters on speed control of the motor. The following simulation analysis is performed on a 220-V, 8-pole and 3-phase BLDC motor. The controller and motor parameters are shown in Table 4.5, and the double closed-loop PI control is used in the operation.

4.3.1 Armature Resistance

The transition of the stator current is determined mainly by the electrical time constant of the stator. It is obvious from the characteristic of the RL circuit that either increasing the

Table 4.5 Parameters of the controller and motor

Controller parameters		K_{p1}	T_{I1}	K_{p2}	T_{I2}
		0.015	1	100	0.1
Motor parameters	Rated Voltage (V)	Rated speed (r/min)	Rated torque (N m)	Phase resistance (Ω)	Back-EMF coefficient (V/(rad/s))
	220	3000	3	2.875	0.7
	Phase inductance (mH)	Moment of inertia (kg m^2)	Damping coefficient (N m s)	Pole pairs	Torque coefficient (N m/A)
	8.5	0.8×10^{-3}	1×10^{-3}	4	1.2

inductance or decreasing the resistance would result in the increase of stator electrical time constant, which consequently extends the process of currents reaching the steady-state value. However, a decrease of resistance would lead to an increase of the steady-state value of current, for which it cannot be considered simply that decreasing the resistance will certainly retard the establishment of the commutating currents of a BLDC motor control system. Meanwhile, the increase of BLDC motor stator resistance usually indicates that the number of its winding turns also increase, which decreases the efficiency and the average output torque. When the stator resistance is decreased, the results are opposite. This is why such factors should be considered comprehensively when a BLDC motor is designed and chosen to establish a speed-control system.

Figure 4.40 shows the speed response of the motor under control of the given parameters shown in Table 4.5 when the phase resistance is 2 Ω, 2.875 Ω and 4 Ω, respectively. It can be seen that the speed response has not been affected largely by the resistance when the speed is controlled by a double closed-loop mode. Therefore, the temperature effect of resistance can be neglected in real closed-loop control. Figure 4.41 shows the dynamic response of the electromagnetic torque when the phase resistance changes from 2.875 Ω to 4 Ω at 0.5 s. It can be seen from Figure 4.41 that when the resistance increases, the average torque falls, i.e. the output capacity of the motor decreases. Indeed, if open-loop control is adopted, the increase of resistance would result in a remarkable fall in speed where the effect of resistance variation on the system should be taken into account adequately.

Figure 4.42 shows the curve of maximum speed that the motor can reach when the stator resistance is altered. It is seen that decreasing the resistance can expand the speed range to some degree.

4.3.2 Armature Inductance

It should be noted that the inductance can hinder the change of current. The smaller the inductance, the faster the current changes. Figure 4.43 shows the dynamic speed response of

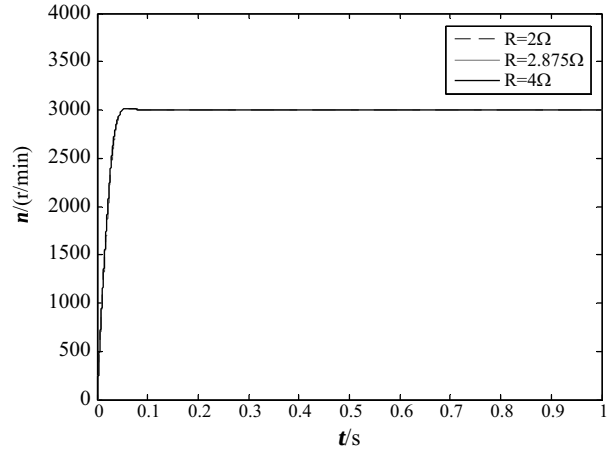


Figure 4.40 Speed response with resistance variation.

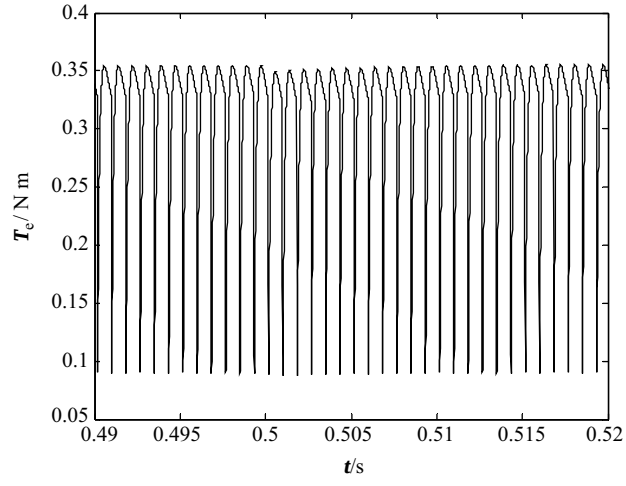


Figure 4.41 Torque response with resistance variation.

BLDC motor control system under double closed-loop PI control when the inductance is varied from 8.5 mH to 5.5 mH at 0.5 s.

As seen from Figure 4.43, the decrease of inductance will slightly increase the steady-state value of speed when the motor is under double closed-loop control. Instead, if the motor is under open-loop control, the speed will increase much more, and such qualitative results can be similarly obtained from the mathematical equations of a BLDC motor. Therefore, the decrease of inductance, as for the decrease of resistance, can also expand the speed range. However, a large inductance can lessen the current rush, and the resistance and inductance will also affect the efficiency and torque ripple of the motor. So, it is important to take the above factors into consideration comprehensively when it comes to the optimization of a motor control system.

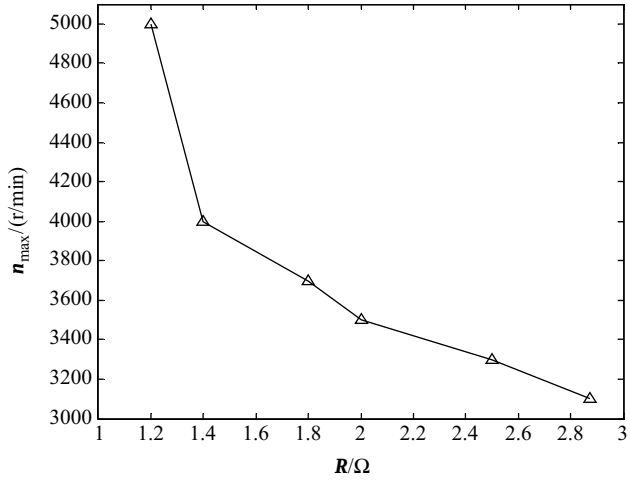


Figure 4.42 Relationship between motor resistance and maximum speed.

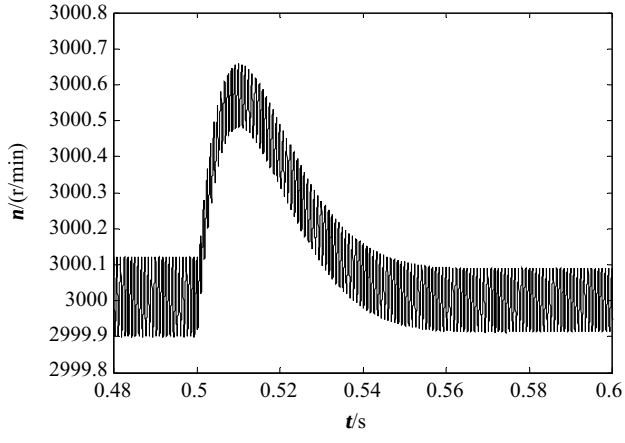


Figure 4.43 Speed response when stator inductance decreases.

4.3.3 Rotor Inertia

Figure 4.44 shows the dynamic speed response when the moment of inertia of the motor is changed from $0.8 \times 10^{-3}\,\mathrm{kg\,m^2}$ to $0.4 \times 10^{-3}\,\mathrm{kg\,m^2}$ at 0.5 s.

It is seen from Figure 4.44 that decreasing the moment of inertia deteriorates the speed stability, which will be more conspicuous in open-loop control. Therefore, a large moment of inertia is usually demanded in motor design to enhance the speed stability of the operation. If varied speed control is required frequently, what the motor should follow is that its moment of inertia is small to satisfy the dynamic speed-response requirement, which complies with the general criteria of motor control systems.

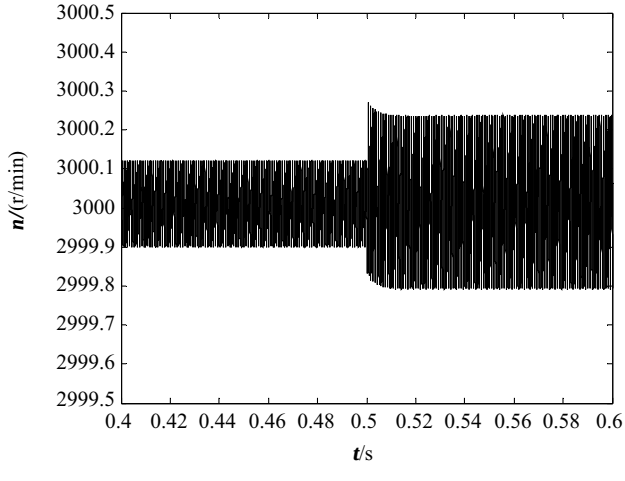


Figure 4.44 Speed response when moment of inertia decreases.

4.4 Practical Issues on Implementation

In the previous sections of this chapter, the influences of speed-control strategy and motor parameters on the speed-control performance of a BLDC motor are analyzed. In practice, the circumstances of the speed-control system, the type of load torque and the demands of the system vary greatly, thus it is necessary to take the following factors into consideration.

4.4.1 Type of Power Switches and Circuit Forms

The circuit of speed-control system is broadly comprised of the main circuit, driving circuit and control circuit, of which the devices should be selected according to their different demands. For the main circuit, the main factor to be considered is the type of power switches, which includes diode, thyristor, MOSFET, IGBT, IPM, IGCT, etc. Different types of power switches have different switching characters and power grades. When the topology of the main circuit is decided, the operating mode of each power device will be determined too and the switching frequency, the voltage and current grade can be calculated, consequently the type of power switch will be determined. The driving circuit can be constructed with separated devices, which are easy to reorganize, while it can also be highly integrated with a driving chip with small size, low loss and high reliability. As for the control circuit, the core microprocessor should be selected carefully. The MCU can meet the needs of the conventional PI double closed-loop system, while DSP will be more appropriate for advanced control of the BLDC motor, which involves complex calculations of multiplication, division and matrix operations.

4.4.2 Detection of Rotor Position

Note that when space is limited and high reliability is demanded for the BLDC motor, rotor position is usually detected by using a sensorless method, which has strong antidisturbance ability and high reliability. To date, there are various types of sensorless control methods for BLDC motors. The corresponding techniques will be discussed in detail in Chapter 6.

4.4.3 Braking Circuit and Protection Circuit

In practice, rapid deceleration or shutdown of the motor is needed, which will produce braking energy, so that the motor is operating in the second or the fourth quadrant. If the energy-regeneration unit is designed in the circuit, the energy generated during the deceleration of the motor can be fed back to the DC bus, which will quicken the braking of the motor. If the rectifier circuit is uncontrollable, the braking energy is not able to be fed back, and unless an extra braking unit is introduced, the DC voltage will keep increasing until the main circuit devices are damaged. A simple braking unit usually contains a braking resistance, on which the braking energy is consumed and transformed into heat energy. Note that when this simple type of braking unit is used, the system efficiency will be reduced. Thus, various regenerative braking approaches should be considered in practice.

Meanwhile, during the practical operation of the BLDC motor control circuit, abnormal events may occur to produce overvoltage and overcurrent phenomena, so corresponding protection circuits are required to ensure the safety of power switches.

4.4.4 Antidisturbance Measures of Software and Hardware

In practical industrial control system, electromagnetic disturbance problems are more and more severe with the wide application of various nonlinear power electronic devices, which make antidisturbance techniques much more important. Electromagnetic disturbances may directly damage the hardware of speed-control system, or cause the program in microprocessor out of control. Therefore antidisturbance measures of hardware and software play a significant role in the design of a speed-control system.

The common hardware antidisturbance methods include increasing the internal impedance of the power supply, adding smoothing reactors and filters, adopting a multipulse rectifier circuit, and proper topology design of the main circuit, and so on.

Besides the above hardware methods, software antidisturbance approaches, such as digital filtering, instruction redundancy, delayed confirmation, and software reset, can be applied for the control of BLDC motor too.

Questions

1. Compared with the continuous control system, what are the advantages of the digital control system?
2. Why is antiwindup control usually required in the design of BLDC motor controller?
3. What are the main characteristics of an intelligent controller?
4. List some types of fuzzy controller, and give the general procedures of fuzzy controller design.
5. Show how the fuzzy controller of a BLDC motor is optimized through genetic algorithm.
6. What are the advantages and disadvantages of the sliding-mode controller?
7. What is the principle of grey control? Try to explain it in your own words.
8. What are the advantages of grey control and where does the main idea of the ant-colony algorithm come from?
9. Summarize the influences of motor parameters on dynamic response and speed range.

References

1. Hodel, A. S., Hall, C. E. (2001) Variable-structure PID control to prevent integrator windup. *IEEE Transaction on Industrial Electronics*, **48**(2), 442–451.
2. Zhang, D., Li, H., Collins, E. G. (2006) Digital anti-windup PI controllers for variable-speed motor drives using FPGA and stochastic theory. *IEEE Transactions on Power Electronics*, **21**(5), 1496–1501.
3. Kwon, T. S., Sul, S. K. (2005) Novel anti-windup of a current regulator of a surface-mounted permanent-magnet motor for flux-weakening control. *Industry Applications Conference,* Hong Kong, **3**:1813–1819.
4. http://www.isep.pw.edu.pl/ZakladNapedu/lab-ane/anti-windup.pdf
5. Xia, C. L., Liu, D., Wang, Y. F., *et al.* (2007) Control of brushless DC motors using fuzzy set based immune feedback PID controller. *Transactions of China Electrotechnical Society*, **22**(9), 68–73 (in Chinese).
6. Chen, W., Xia, C. L., (2006) Sensorless control of brushless DC motor based on fuzzy logic. *IEEE Proceedings of the World Congress on Intelligent Control and Automation*, China, 6298–6302.

7. Xia, C. L., Xiu, J. (2006) Sensorless control of switched reluctance motor based on ANFIS. *Lecture Notes in Computer Science*, **4234**:645–653.
8. Rubaai, A., Ricketts, D., Kankam, M. D. (2001) Experimental verification of a hybrid fuzzy control strategy for a high-performance brushless DC drive system. *IEEE Transactions on Industry Applications*, **37**(2), 503–512.
9. Cao, J. B., Cao, B. G., Xu, P., (2008) Torque ripple control of position-sensorless brushless DC motor based on neural network identification. *IEEE International Conference on Industrial Electronics and Applications*, Singapore, 752–757.
10. Xia, C. L., Li, Z. Q., Wang, Y. F. (2008) Compound control for brushless DC motors using cerebellar model controller and PID controller. *Electric Machines and Control*, **12**(3), 254–259 (in Chinese).
11. Shi, T. N., Tian, Y., Xia, C. L. (2007) Direct control of voltage based on adaptive wavelet neural network for PM brushless DC motors. *Transactions of China Electrotechnical Society*, **22**(9), 74–79 (in Chinese).
12. Shi, T. N., Tian, Y., Xia, C. L. (2007) Position sensorless control based on wavelet neural network for PM brushless DC motors. *Journal of Tianjin University*, **40**(2), 190–194 (in Chinese).
13. Wang, Y. F.Control for brushless DC motors based on genetic algorithm and RBF neural network. Tianjin: Tianjin University Master Thesis, 2007 (in Chinese).
14. Xia, C.L., Li, Z.Q. Wang, M.C. *et al.* (2005) Single neuron PID model reference adaptive control for PM brushless DC motors based on RBF neural network on-line identification. *Transactions of China Electrotechnical Society*, **20**(11), 65–69 (in Chinese).
15. Xia, C.L., Wen, D., Fan, J. *et al.* (2002) Based on RBF neural network position sensorless control for brushless DC motors. *Transactions of China Electrotechnical Society*, **17**(3), 26–29 76 (in Chinese).
16. Tian, Y.Position sensorless control for PM brushless DC motor based on wavelet neural network. Tianjin: Tianjin University Master Thesis (2007) (in Chinese).
17. Zhang, M. H., Xia, C. L., Tian, Y., *et al.* (2007) Speed control of brushless DC motor based on single neuron PID and wavelet neural network. *IEEE International Conference on Control and Automation*, China, 621–624.
18. Wang, J.Direct control of current and torque analysis based on neural network for brushless DC motors. Tianjin: Tianjin University Master Thesis (2003) (in Chinese).
19. Xia, C. L., Wang, J., Shi, T. N. *et al.* (2003) Direct control of currents based on adaptive RBF neural network for brushless DC motors. *Proceeding of the CSEE*, **23**(6), 123–127 (in Chinese).
20. Wu, S. Q., Meng, J. E. (2000) Dynamic fuzzy networks-a novel approach to function approximation. *IEEE Transactions on System*, **30**(2), 358–364.
21. Xia, C. L., Wen, D., Wang, J. (2002) A new approach of minimizing commutation torque ripple for brushless DC motor based on adaptive ANN. *Proceeding of the CSEE*, **22**(1), 54–58 (in Chinese).
22. Lin, C. L., Jan, H. Y., Shieh, N.C. (2003) GA-Based multi-objective PID control for a linear brushless DC motor. *IEEE Transactions on Mechatronics*, **8**(1), 56–65.
23. Xia, C. L., Liu, D., Wang, Y. F. (2007) Artificial neural network control of brushless DC motor based on immune feedback adaptive learning. *Journal of Tianjin University*, **40**(10), 1235–1240 (in Chinese).
24. Xia, C. L., Fang, H. W., Chen, W., *et al.* (2006) Ant colony algorithm based fuzzy control for a brushless DC motor. *IEEE Proceedings of the World Congress on Intelligent Control and Automation* China, 6498–6502.
25. Wang, Y. F., Xia, C. L., Zhang, M. H., *et al.* (2007) Adaptive speed control for brushless DC motors based on genetic algorithm and RBF neural network. *IEEE International Conference on Control and Automation*, China, 1219–1222.
26. Liu, D., Xia, C. L., (2007) Control of brushless DC motor using fuzzy set based immune feedback PID controller. *IEEE International Symposium on Industrial Electronics*, Spain, 1045–1049.
27. Xia, C. L., Liu, J. H., Yu, W., *et al.* (2005) Variable structure control of BLDCM based on extended state observer. *IEEE International Conference on Mechatronics and Automation*, Canada, 568–571.
28. Lim, K. W., Low, T. S., Rahman, M. F. *et al.* (1991) A discrete time variable structure controller for a brushless DC motor drive. *IEEE Transactions on Industrial Electronics*, **38**(2), 102–107.
29. Shi, T. N., Zhang, Q., Xia, C.L. *et al.* (2008) Estimates of rotor position and velocity of brushless DC motor with UKF algorithm. *Journal of Tianjin University*, **41**(3), 338–343 (in Chinese).
30. Deng, J. L. (1993) *Grey Control System*. Huazhong Institute of Technology Press, Wuhan (in Chinese).
31. Luo, Y. X., Zhang, L. T., Li, M., *et al.* (2001) *Grey System Theory and Its Application in Mechanical Engineering*. National University of Defense Technology Press, Changsha (in Chinese).
32. Chiang, H. K., Tseng, C. H. (2003) The grey integral variable structure speed control of synchronous reluctance motor drives. *The Journal of Grey System*, **15**(2), 115–124.

33. Wai, R. J., Duan, R. Y., Chang, L. J., (2001) Grey feedback linearization speed control for induction servo motor drive. *The 27th Annual Conference of the IEEE Industrial Electronics Society*, Denver, **3**:580–585.
34. Xia, C. L., Cao, W. L., Song, P., (2008) The speed-adjustment system of brushless DC motor based on grey PID. *IEEE International Conference on Automation and Logistics*, China, 35–38.
35. Chen, W., Xia, C. L., Xue, M., (2008) A torque ripple suppression circuit for brushless DC motors based on power DC/DC converters. *IEEE International Conference on Industrial Electronics and Applications*, Singapore, 1453–1457.
36. Farmer, J. D., Packard, N. H., Perelson, A. S. (1986) The immune system, adaptation, and machine learning. *Physica D*, **22**, 187–204.

5

Analysis and Reduction of Torque Ripple

Torque ripples reflected as periodic oscillations in torque will degrade the servo performance of permanent magnet motors. Compared with PMSM, the torque ripples in BLDC motor are much more serious. The pulsation will not only cause acoustics and vibration, but severely limit the performance of the system, especially in high-precision and high-stabilization applications. Minimization of the torque ripples in a BLDC motor drive system has been an important and difficult problem. Generally speaking, the pulsation in a BLDC motor can be divided into two categories: cogging torque and commutation torque. The cogging torque is produced by the different reluctance in the air gap caused by the existing of a stator slot. The back-EMF pulsation caused by cogging torque is a periodic function of rotor position, which will lead to torque ripples. It is a great challenge to reduce cogging torque during machine design. However, researchers have developed various methods based on motor design that can minimize cogging torque by changing the structure of the motor. The existing methods mainly contain skewing poles or slots, embedding a magnetic slots wedge, placing auxiliary slots and teeth, designing fractional slots, and so on [1–5]. The commutation torque ripple in a BLDC motor, due to current variation during commutation interval, also limits its application in high-performance servo system. The commutation torque ripple and its minimization methods will be investigated in this chapter. First, the cogging torque ripple and its minimization methods are analyzed. Then, the principle of the commutation torque ripple is presented. After that, the influences of back-EMF, commutation modes and PWM control on the commutation torque will be analyzed. Further, torque-ripple-reduction methods based on time-division commutation, active disturbance rejection control technology, BP neural networks, and fuzzy niching genetic algorithms will be discussed.

5.1 Cogging Torque-Ripple-Minimization Techniques Analysis

Cogging torque in BLDC motor can be defined as the periodic electrical torque when the armature winding is open. The presence of the stator slot will cause reluctance variation in the

Permanent Magnet Brushless DC Motor Drives and Controls, First Edition. Chang-liang Xia.
© 2012 Science Press. Published 2012 by John Wiley & Sons Singapore Pte. Ltd.

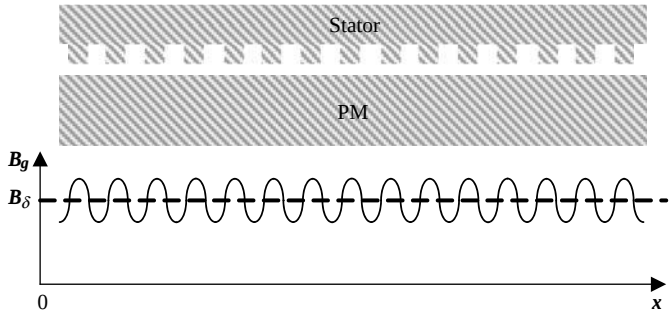


Figure 5.1 Schematic diagram of cogging torque.

air gap, thus the air-gap magnetic-field distribution in space produces pulsations of back-EMF, which will lead to torque ripple. Therefore, the cogging torque is also called the reluctance torque [3]. In addition, this torque is caused by the interaction between the slot and the tooth of the armature core and the magnetic field of permanent magnet along with the direction of rotor circumference, which make the rotor of the BLDC motor align with the stator in a particular direction, so cogging torque can be named location torque too. Figure 5.1 shows the schematic diagram of cogging torque.

The energy stored in the air gap varies with the relative position of rotor and stator between its maximum and minimum. The relationship between the frequency of the electromagnetic field energy and the slots of the armature core is shown as

$$f = nZ/60 \tag{5.1}$$

where n — motor speed (r/min);
Z — slots of the armature core.

Thus, the cogging torque can be expressed as

$$T_c = -\frac{\partial W_m}{\partial \theta} \tag{5.2}$$

where W_m — energy of air-gap electromagnetic field;
θ — relative angular displacement between rotor and stator.

Further, it can be illustrated as in Figure 5.2.

The cogging torque is a direct expression of magnetostatic energy when the motor rotates. The magnetostatic energy in a motor is approximately equal to that stored in the air gap, because the magnetostatic energy in the permanent magnet and the core, which can be ignored, is very small with respect to the variance of the magnetostatic energy in air gap. Magnetic field energy varies with the rotor angle as slots are present in the stator core. Meanwhile, it will produce torque in the decreasing direction of magnetic-energy product. Cogging torque can be expressed as a spectrum function whose fundamental frequency is equal to the least common

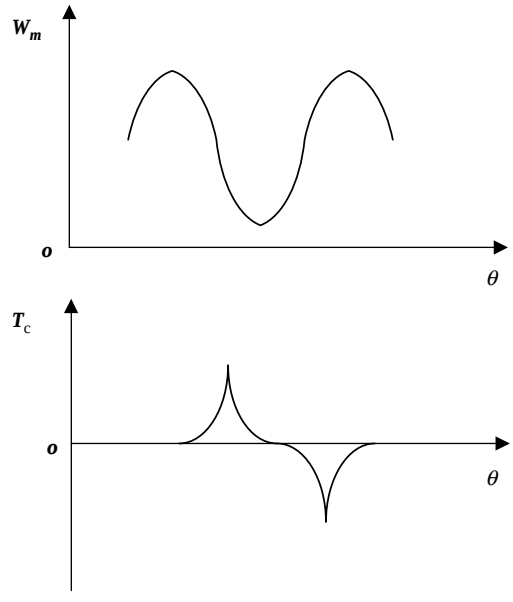


Figure 5.2 The energy stored in the air gap and the motor cogging torque.

multiple (LCM) of the poles number and the slot number. The other higher-order harmonics are in inverse proportion to the square of frequency. So the higher the fundamental frequency, the lower its amplitude.

During variable-speed drive, vibration and noise produced by the cogging torque will be amplified when the torque ripple frequency is equal to the mechanical resonance frequency of the rotor or stator. Moreover, the existence of cogging torque will affect the servoperformance of low-speed control and high-accuracy position control for a BLDC motor system.

Cogging-torque minimization is a challenge during the design procedure of a BLDC motor. Optimization of the structure of a BLDC motor can reduce the cogging torque. To date, numerous methods, such as skewing slots and magnets, embedding magnetic slot wedge, auxiliary slots or teeth and a fractional number of slots per pole, have been proposed for reducing the cogging torque [2].

5.1.1 Skewing Slots and Magnets

Stator laminations having one slot pitch shift along the axial direction is one of the skewing methods, which can eliminate cogging torques obviously and improve the stator wingding distribution of BLDC motor. Skewing the magnet on the rotor by one tooth pitch is another alternative. The proper skew angle is significant for reducing cogging torque. In theory, skewing one slot pitch will eliminate cogging torque altogether. But in fact, this cannot be achieved because of the edge effect and rotor asymmetry. Note that both magnet and stator skewing will make the corresponding stator design of BLDC motor more complex. Consequently, the mutual inductance and stray loss will be increased, while the shape of the

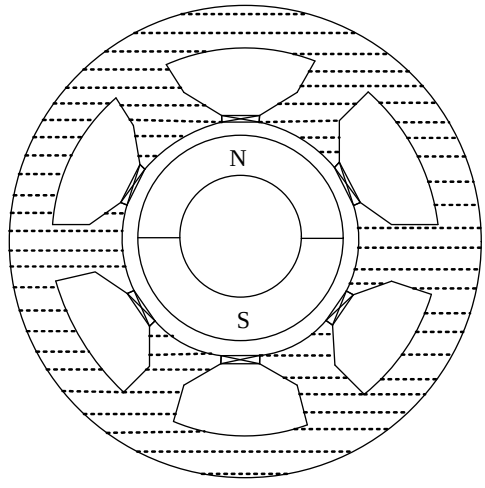


Figure 5.3 Magnetic slot wedges.

back-EMF of the winding is more sinusoidal than rectangular. From this viewpoint, the torque ripple will be increased with the average output torque reduced.

5.1.2 Embedding Magnetic Slot Wedges

Filling the open part of slots with magnetic wedges can also minimize the cogging torque because it has a more uniform air-gap permeability, which makes the coenergy variation of magnets decrease. The structure of a BLDC motor with magnetic wedges filled is illustrated in Figure 5.3.

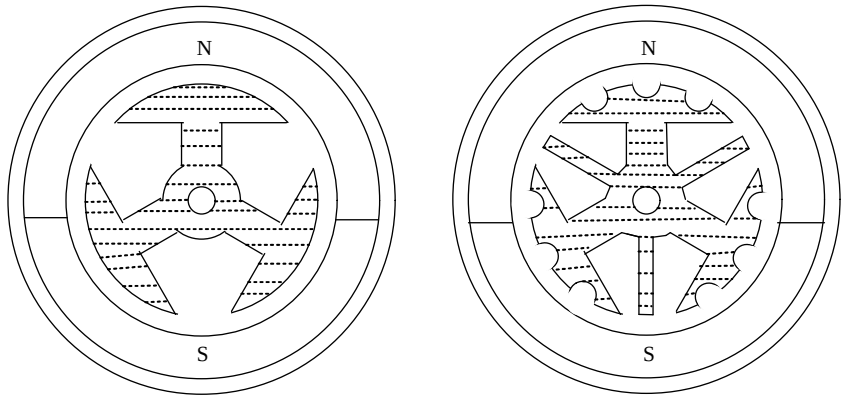
5.1.3 Auxiliary Slots and Teeth

This method can reduce the fundamental component of cogging torque by placing some auxiliary grooves on the PM surface or armature core [3] (see Figure 5.4), with a more uniform distribution of the magnetic flux density.

5.1.4 Fractional Number of Slots Per Pole

Another cogging-torque-reduction method employs the fractional stator slots in a BLDC motor. It will increase the least common multiple of the poles number and the slot number, so that the fundamental frequency of the cogging torque is increased [4]. Hence, the cogging torque is reduced. In general, the higher the frequency of the cogging torque, the lower the amplitude of the cogging torque. A BLDC motor with fractional number of slots per pole is shown in Figure 5.5.

One or more of the techniques discussed above should be used during the design procedure of electrical machines. In this manner, the cogging torque of a BLDC motor can be reduced substantially with the performance enhanced.



(a) Without auxiliary slots (b) With auxiliary slots

Figure 5.4 Schematic diagram of a BLDC motor with auxiliary slots.

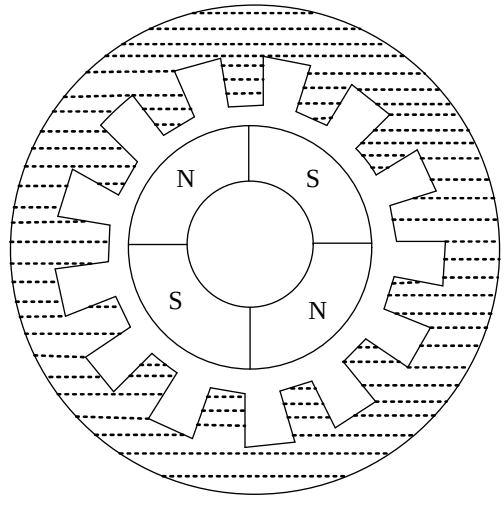


Figure 5.5 BLDC motor with fractional number of slots per pole.

5.2 Torque-Ripple Reduction with Time-Sharing Commutation Strategy

5.2.1 Time-Sharing Commutation Strategy

Three-phase BLDC motor with full-bridge driving mode as an example is taken in this section. In normal operation condition, there are two states (steady state and transient state) of a BLDC motor under two-phase conduction mode. Generally speaking, the longer steady state of the two-phase conduction determines the amplitude of the electromagnetic torque. However, the transient state of the commutation will affect the performance of the motor too. In the condition that load torque and rotor speed are invariant, meanwhile, two-phase conduction is

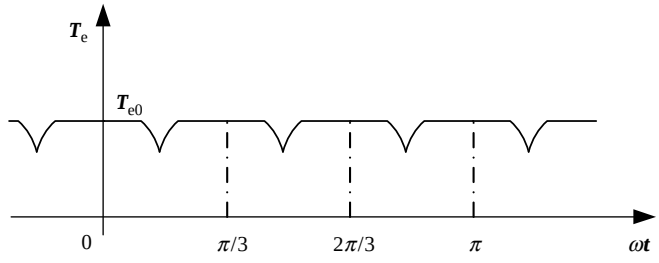


Figure 5.6 Waveform of electromagnetic torque in three phase BLDC motor with full-bridge driving.

adopted in the three phase BLDC motor with full-bridge driving, we can obtain the waveform of the electromagnetic torque as shown in Figure 5.6.

As illustrated in Figure 5.6 the electromagnetic torque of the motor is T_{e0} when a two-phase conduction mode is adopted. Electromagnetic torque, which is a periodic function, can be expressed as

$$T_e(\theta) = T_e\left(\theta + \frac{\pi}{3}\right) \tag{5.3}$$

Let $t_1 = \pi/3\omega$, in which ω is the electrical angle of the motor. Suppose that two-phase conduction is adopted in the motor between 0 and t_1, then analysis of the commutation can be obtained in the interval $[0,t_1]$, since the electromagnetic torque is a periodic function.

The mean value of the torque ripple in the interval $[0,t_1]$ can be defined as a criterion for the commutation torque ripple, which can be expressed as

$$\overline{T}_{e\sigma} = \frac{\int_0^{t_1} |T_e - T_{e0}| \mathrm{d}t}{t_1} \tag{5.4}$$

where

$$T_{e0} = \frac{2EI}{\Omega} \tag{5.5}$$

where E — phase back-EMF under two-phase conduction in the interval $[0,t_1]$;
I — current amplitude under two-phase conduction in the interval $[0,t_1]$;
Ω — mechanical angular velocity in the interval $[0,t_1]$.

Suppose that the rotor speed of the motor is invariant during the interval $[0,t_1]$, then

$$E = K_e\Omega \tag{5.6}$$

where K_e — coefficient of back-EMF.

It can be seen from the equation of the electromagnetic torque of BLDC motor that phase current and phase back-EMF play an important role on the electromagnetic torque. Meanwhile, during the commutation intervals, back-EMF influenced by flux leakage affects the

phase current. Therefore, it is difficult to analyze the torque ripple generated by phase current and back-EMF simultaneously [1].

5.2.1.1 Effect of the Back-EMF

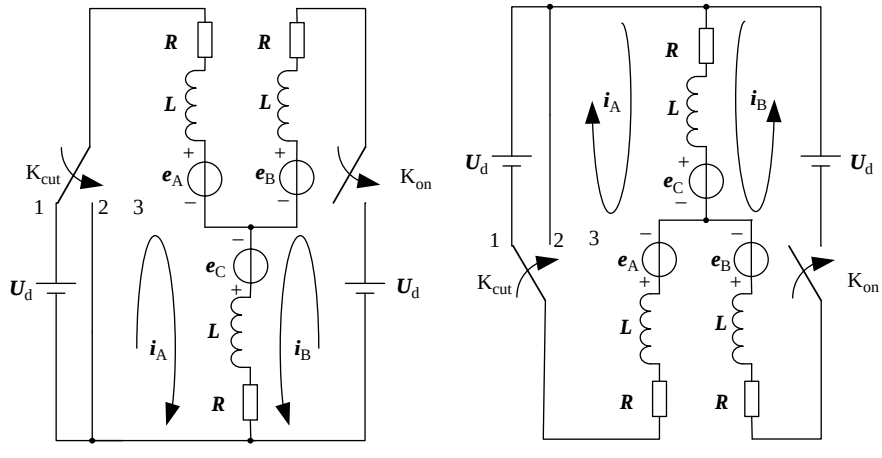
Commutation of a BLDC motor can be achieved by turning on or off the corresponding power switches. If the turn-on and the turn-off power switches all belong to the upper half-bridge, it is defined as upper half-bridge commutation. Similarly, lower half-bridge commutation denotes the turn-on and the turn-off power switches all belong to the lower half-bridge. Neglecting the voltage of the power switches and freewheel diodes when they are conducted, the equivalent circuit in the commutation can be obtained as Figure 5.7.

As illustrated in Figure 5.7, the equivalent circuits of the upper half-bridge and lower half-bridge have no differences except that the current is reverse. In order to analyze the principle of commutation torque ripple, conduction switches from phase AC to BC in the upper half-bridge is taken as an example.

How the back-EMF affects the commutation torque ripple separately is developed under the assumptions stated below.

(1) Commutation transient process is neglected.
(2) Two phase windings are conducted at any time.
(3) Ideal square waveform of the current is supposed.

The ideal waveform of back-EMF is 120° trapezoidal, while the width of the flat is less than 120° practically. The waveform of back-EMF is shown in Figure 5.8, where the dotted line is the ideal 120° waveform of the back-EMF, and the solid line curve is the actual waveform of



(a) Upper half-bridge commutation (b) Lower half-bridge commutation

Figure 5.7 Equivalent circuit in commutation of a BLDC motor.

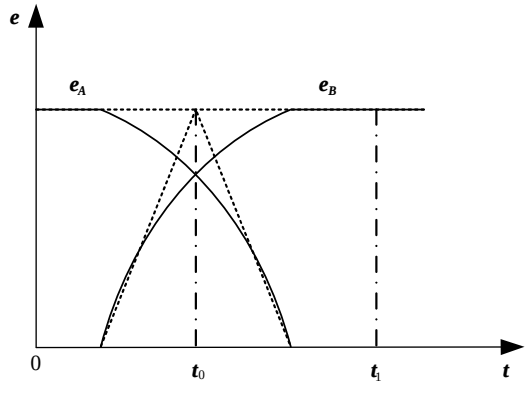


Figure 5.8 Schematic diagram of back-EMF waveform.

the back-EMF. In addition, suppose the back-EMF varies from the positive flat to the negative flat monotonously.

Hence, if the current commutation starts at t_0, then the current of the turn-off phase will change into 0 from I and the current of the turn-on phase will change from 0 to I at the same time. Also, currents between $[0,t_1]$ satisfy

$$\begin{cases} i_{\mathrm{A}} = I(1 - u(t_0)) \\ i_{\mathrm{B}} = Iu(t_0) \\ i_{\mathrm{C}} = -I \end{cases} \tag{5.7}$$

where $u(\mathrm{t}_0)$ — the step function.

In the interval $[0,t_1]$, the electromagnetic torque will be

$$T_{\mathrm{e}} = \frac{e_{\mathrm{A}} i_{\mathrm{A}} + e_{\mathrm{B}} i_{\mathrm{B}} + e_{\mathrm{C}} i_{\mathrm{C}}}{\Omega} \leq T_{\mathrm{e0}} \tag{5.8}$$

Thus, the mean value of the electromagnetic torque between $[0,t_1]$ is given by

$$\bar{T}_{\mathrm{e}} = \frac{\int_0^{t_1} T_{\mathrm{e}} \mathrm{d}t}{t_1} \tag{5.9}$$

Substituting Equation (5.8) into Equation (5.9), yields

$$\bar{T}_{\mathrm{e}} = \frac{\int_0^{t_1} \frac{e_{\mathrm{A}} i_{\mathrm{A}} + e_{\mathrm{B}} i_{\mathrm{B}} + e_{\mathrm{C}} i_{\mathrm{C}}}{\Omega} \mathrm{d}t}{t_1} \tag{5.10}$$

Further, substituting Equation (5.7) into Equation (5.10), the average electromagnetic can be expressed as

$$\bar{T}_{\mathrm{e}} = \frac{I}{\Omega t_1}\left(\int_0^{t_0} e_{\mathrm{A}}\mathrm{d}t + \int_{t_0}^{t_1} e_{\mathrm{B}}\mathrm{d}t - \int_0^{t_1} e_{\mathrm{C}}\mathrm{d}t\right) \tag{5.11}$$

Therefore, the average electromagnetic torque ripple between $[0,t_1]$ is

$$\overline{T}_{\mathrm{e}\sigma} = T_{\mathrm{e}0} - \overline{T}_{\mathrm{e}} \tag{5.12}$$

If commutation of the motor happens at t_0, then solving the best commutation moment can be transformed to an optimization issue as

$$\min_{t_0\in[0,t_1]} \overline{T}_{\mathrm{e}\sigma} = \min_{t_0\in[0,t_1]} (T_{\mathrm{e}0} - \overline{T}_{\mathrm{e}}) \tag{5.13}$$

The derivative of the average electromagnetic torque ripple at t_0 is

$$\frac{\mathrm{d}\bar{T}_{\mathrm{e}\sigma}}{\mathrm{d}t_0} = \frac{-I}{\Omega t_1}(e_{\mathrm{A}} - e_{\mathrm{B}}) \tag{5.14}$$

Thus, the second derivative of the average electromagnetic torque ripple at t_0 is

$$\frac{\mathrm{d}^2\bar{T}_{\mathrm{e}\sigma}}{\mathrm{d}t_0^2} = \frac{-I}{\Omega t_1}\left(\frac{\mathrm{d}e_{\mathrm{A}}}{\mathrm{d}t_0} - \frac{\mathrm{d}e_{\mathrm{B}}}{\mathrm{d}t_0}\right) \tag{5.15}$$

Notice that both e_{A} and e_{B} are functions of t_0. Therefore, if appropriate t_0 is chosen so that e_{A}–$e_{\mathrm{B}} = 0$ holds, the derivative of average electromagnetic torque ripple is 0 with the second derivative greater than 0. Thus, the torque ripple has its minimum value. Further, e_{A} is monotone decreasing, while e_{B} is monotone increasing around the commutation moment, and the derivative of average electromagnetic torque ripple is greater than 0, consequently, there is only one minimum value of the average torque ripple. If so, the minimum value of torque ripple will be achieved at t_0 for e_{A}–$e_{\mathrm{B}} = 0$. This means that if and only if the commutation happens at t_0 corresponding to e_{A}–$e_{\mathrm{B}} = 0$, the least value of average torque ripple will be obtained. Similarly, define e_{A}–$e_{\mathrm{B}} = e_{\mathrm{AB}}$ as the line back-EMF of phase A and B, commutation torque ripple will achieve the least value if the commutation happens at the zero-crossing point of the line back-EMF. It must be emphasized that the best moment of commutation happens at the time lag 30° behind the zero-crossing point of phase back-EMF, which is a special case of the phenomenon that the phase back-EMF is a 120° trapezoidal waveform and the rotor speed is invariant.

The waveforms of back-EMF and electromagnetic torque at the best moment of commutation t_0 are shown in Figure 5.9.

The higher the rotor speed, the greater the steady state value of the back-EMF. Therefore, the torque will decrease faster as the steady state value of back-EMF becomes greater. But the period of torque ripple will be smaller and the average torque ripple does not varied with rotor speed.

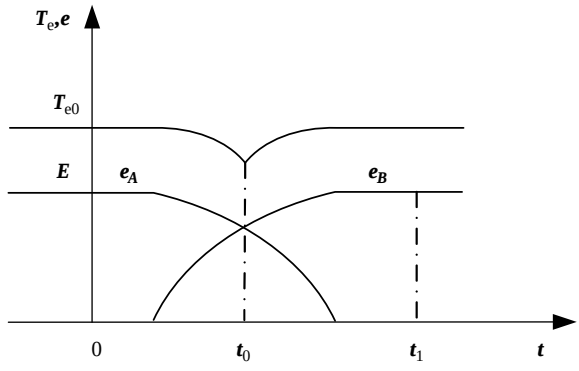


Figure 5.9 Waveforms of back-EMF and electromagnetic torque.

5.2.1.2 Effect of the Commutation Transient Process

Neglect the variance of the back-EMF waveform and the PWM effect, and suppose the phase back-EMF is equal to E or $-E$ during the transient process of commutation, then the steady-state value of the phase current I is

$$I = \frac{U_d - 2E}{2R} \tag{5.16}$$

where U_d — DC voltage of the bridge inverter.

The current cannot be changed suddenly especially when the voltage source converter is adopted because of the inductance of the windings. During the commutation switching from phase A and C conduction to phase B and C conduction, the electromagnetic torque in $[0,t_1]$ can be obtained as

$$T_e = \frac{e_A i_A + e_B i_B + e_C i_C}{\Omega} = \frac{-2Ei_C}{\Omega} \tag{5.17}$$

Therefore, torque ripple is mainly determined by the current of the nonenergized phase if the variance of back-EMF is neglected. Taking current of phase C as an example, the variation tendency of electromagnetic torque during the transient process of commutation is analyzed as follows.

Usually, turning off and turning on certain phases in a BLDC motor happens synchronously. Suppose the commutation happens at $t = 0$, then the voltage between phase A and phase C will change from U_d to 0 while the voltage will be U_d between phase B and phase C. If i_A is assumed to be 0 at $t = t_{off}$, the current of phase B will change from $i_B(t_{off}-)$, which is the value of the current before t_{off}, into the steady-state value I. Since the motor is running in steady state before commutation, i.e. $i_A(0–) = I$, $i_B(0–) = 0$, $i_C(0–) = -I$, thus with the Laplace transform the current equations in $[0,t_{off}]$ will be obtained as

$$\begin{cases} 2(R + sL)i_A(s) + (R + sL)i_B(s) = 2LI - 2E/s \\ (R + sL)i_A(s) + 2(R + sL)i_B(s) = LI - 2E/s + U_d/s \\ i_C(s) = -(i_A(s) + i_B(s)) \end{cases} \tag{5.18}$$

If $t > t_{\text{off}}$, the current equations will be

$$\begin{cases} i_{\text{A}}(s) = 0 \\ 2(R + sL)i_{\text{B}}(s) = 2Li_{\text{B}}(t_{\text{off}-}) - 2E/s + U_{\text{d}}/s \\ i_{\text{C}}(s) = -i_{\text{B}}(s) \end{cases} \tag{5.19}$$

So, the time domain solutions of Equations (5.18) and (5.19) are given by

$$i_{\text{A}} = \begin{cases} I\mathrm{e}^{-\frac{R}{L}t} - \dfrac{U_{\text{d}} + 2E}{3R}\left(1 - \mathrm{e}^{-\frac{R}{L}t}\right), & 0 < t \le t_{\text{off}} \\ 0, & t > t_{\text{off}} \end{cases} \tag{5.20}$$

$$i_{\text{B}} = \begin{cases} \dfrac{2U_{\text{d}} - 2E}{3R}(1 - \mathrm{e}^{-\frac{R}{L}t}), & 0 < t \le t_{\text{off}} \\ i_{\text{B}}(t_{\text{off}-})\mathrm{e}^{-\frac{R}{L}(t - t_{\text{off}})} + \dfrac{U_{\text{d}} - 2E}{2R}(1 - \mathrm{e}^{-\frac{R}{L}(t - t_{\text{off}})}), & t > t_{\text{off}} \end{cases} \tag{5.21}$$

$$i_{\text{C}} = \begin{cases} -I\mathrm{e}^{-\frac{R}{L}t} - \dfrac{U_{\text{d}} - 4E}{3R}(1 - \mathrm{e}^{-\frac{R}{L}t}), & 0 < t \le t_{\text{off}} \\ -i_{\text{B}}(t_{\text{off}-})\mathrm{e}^{-\frac{R}{L}(t - t_{\text{off}})} - \dfrac{U_{\text{d}} - 2E}{2R}(1 - \mathrm{e}^{-\frac{R}{L}(t - t_{\text{off}})}), & t > t_{\text{off}} \end{cases} \tag{5.22}$$

Substituting Equation (5.16) into Equation (5.22), i_{C} can be simplified as

$$i_{\text{C}} = \begin{cases} -I + \dfrac{U_{\text{d}} + 2E}{6R}(1 - \mathrm{e}^{-\frac{R}{L}t}), & 0 < t \le t_{\text{off}} \\ -I + [I - i_{\text{B}}(t_{\text{off}-})]\mathrm{e}^{-\frac{R}{L}(t - t_{\text{off}})}, & t > t_{\text{off}} \end{cases} \tag{5.23}$$

As shown in Equation (5.23), i_{C} is monotone decreasing during [0,t_{off}]. When $t > t_{\text{off}}$, the amplitude of i_{C} increases monotonically to the steady-state value I from $-i_{\text{C}}(t_{\text{off}-})$, which is the value at the moment before t_{off}. Thus, the electromagnetic torque during the transient process of commutation is always lower than that in steady state, and the difference between them may achieve its maximum at t_{off}. The corresponding current and electromagnetic torque waveforms are shown in Figure 5.10.

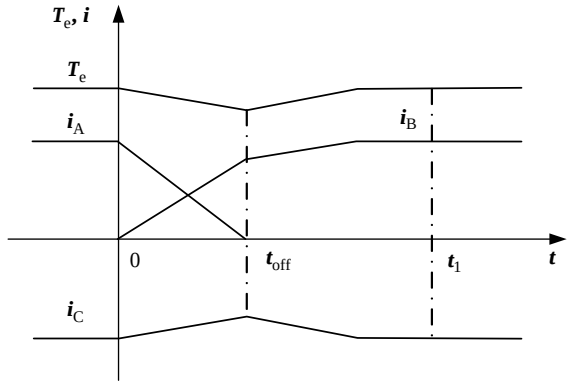


Figure 5.10 Waveforms of current and torque ripple during commutation.

So, the average electromagnetic torque ripple in $[0,t_1]$ is

$$\begin{aligned}\overline{T}_{e\sigma} &= \frac{2E\left\{\int_0^{t_{off}} \frac{U_d + 2E}{6R}(1 - e^{-\frac{R}{L}t})dt + \int_{t_{off}}^{t_1} [I - i_B(t_{off-})]e^{-\frac{R}{L}(t-t_{off})}dt\right\}}{\Omega t_1} \\ &= \frac{2E\left\{\frac{U_d + 2E}{6R}\left[t_{off} + \frac{L}{R}(e^{-\frac{R}{L}t_{off}} - 1)\right] + \frac{L}{R}[I - i_B(t_{off-})](1 - e^{-\frac{R}{L}(t_1 - t_{off})})\right\}}{\Omega t_1}\end{aligned} \tag{5.24}$$

As Equation (5.24) states, electromagnetic torque ripple that is caused by the variance of the current could be affected by the rotor speed and the load torque. In the case that the load torque of the motor is invariant, torque ripple will be much more serious when the amplitude of back-EMF is large since the rotor speed is at a high level. If the rotor speed is invariant and the load torque of the motor is larger, the steady-state current I will become bigger. In other words, the electromagnetic torque ripple will become larger as the rotor speed or the load torque increases.

5.2.1.3 Effect of Both Back-EMF and the Commutation Transient Process

The variance of back-EMF in $[0,t_1]$ can bring about a change of the commutation current. Suppose that the waveform of the back-EMF is an ideal 120° trapezoidal wave and the commutation happens when $e_A - e_B = 0$ holds. Then, the back-EMF of phase A after conducted can be obtained as

$$e_A = E - \frac{6\omega E}{\pi}t, \quad 0 < t < \frac{\pi}{3\omega} \tag{5.25}$$

where ω — electrical angular velocity of the motor.

The Laplace transform of Equation (5.25) is

$$e_{\mathrm{A}}(s) = \frac{E}{s} - \frac{6\omega E}{\pi s^2} \tag{5.26}$$

Hence, the current equations in [0,t_{off}] are

$$\begin{cases} 2(R+Ls)i_{\mathrm{A}}(s) + (R+Ls)i_{\mathrm{B}}(s) = 2LI - \dfrac{2E}{s} + \dfrac{6\omega E}{\pi s^2} \\ (R+Ls)i_{\mathrm{A}}(s) + 2(R+Ls)i_{\mathrm{B}}(s) = LI + \dfrac{U_{\mathrm{d}} - 2E}{s} \\ i_{\mathrm{C}}(s) = -(i_{\mathrm{A}}(s) + i_{\mathrm{B}}(s)) \end{cases} \tag{5.27}$$

When $t > t_{\mathrm{off}}$, the current equations will be

$$\begin{cases} i_{\mathrm{A}}(s) = 0 \\ 2(R+Ls)i_{\mathrm{B}}(s) = 2Li_{\mathrm{B}}(t_{\mathrm{off}-}) + \dfrac{U_{\mathrm{d}} - 2E}{s} \\ i_{\mathrm{C}}(s) = -i_{\mathrm{B}}(s) \end{cases} \tag{5.28}$$

So, the time solutions of the phase currents are

$$i_{\mathrm{A}} = \begin{cases} I\mathrm{e}^{-\frac{R}{L}t} - \dfrac{U_{\mathrm{d}} + 2E}{3R}(1 - \mathrm{e}^{-\frac{R}{L}t}) + \dfrac{4\omega E}{\pi R}t - \dfrac{4\omega LE}{\pi R^2}(1 - \mathrm{e}^{-\frac{R}{L}t}), & 0 < t \le t_{\mathrm{off}} \\ 0, & t > t_{\mathrm{off}} \end{cases} \tag{5.29}$$

$$i_{\mathrm{B}} = \begin{cases} \dfrac{2U_{\mathrm{d}} - 2E}{3R}(1 - \mathrm{e}^{-\frac{R}{L}t}) - \dfrac{2\omega E}{\pi R}t + \dfrac{2\omega LE}{\pi R^2}(1 - \mathrm{e}^{-\frac{R}{L}t}), & 0 < t \le t_{\mathrm{off}} \\ i_{\mathrm{B}}(t_{\mathrm{off}-})\mathrm{e}^{-\frac{R}{L}(t-t_{\mathrm{off}})} + \dfrac{U_{\mathrm{d}} - 2E}{2R}(1 - \mathrm{e}^{-\frac{R}{L}(t-t_{\mathrm{off}})}), & t > t_{\mathrm{off}} \end{cases} \tag{5.30}$$

$$i_{\mathrm{C}} = \begin{cases} -I\mathrm{e}^{-\frac{R}{L}t} - \dfrac{U_{\mathrm{d}} - 4E}{3R}(1 - \mathrm{e}^{-\frac{R}{L}t}) - \dfrac{2\omega E}{\pi R}t + \dfrac{2\omega LE}{\pi R^2}(1 - \mathrm{e}^{-\frac{R}{L}t}), & 0 < t \le t_{\mathrm{off}} \\ -i_{\mathrm{B}}(t_{\mathrm{off}-})\mathrm{e}^{-\frac{R}{L}(t-t_{\mathrm{off}})} - \dfrac{U_{\mathrm{d}} - 2E}{2R}(1 - \mathrm{e}^{-\frac{R}{L}(t-t_{\mathrm{off}})}), & t > t_{\mathrm{off}} \end{cases} \tag{5.31}$$

Compared with the effect of the commutation transient process on torque the current amplitudes of phase A and phase C become bigger, while phase B will be smaller as stated in

Equations (5.29)–(5.31). In practice, this phenomenon will be more apparent as the waveform of the back-EMF is not an ideal 120° flat wave.

Generally speaking, the variance of back-EMF will give rise to electromagnetic torque ripple. Commutation torque ripple can be suppressed to its minimum value when the line back-EMF is zero. If the effects of PWM are neglected, the minimum electromagnetic torque can be achieved at t_{off} because the current variance in the commutation transient process will cause the electromagnetic torque to decrease. In addition, the amplitude of torque ripple will increase as the rotor speed and load torque become higher. Torque ripple can be reduced if the proper commutation moment is chosen and this effect is related to the characteristic of the ripple. If the torque ripple is increasing, the proper commutation moment will suppress the torque ripple effectively. However, if the torque ripple is decreasing, this method can only reduce the torque ripple partly. Note that the effects of rotor speed and load torque on torque ripple cannot be changed in the reverse direction although proper commutation moment is chosen.

5.2.2 *Analysis of Time-Sharing Commutation Strategy*

Transient process of BLDC motor commutation is complex and of short duration. In addition, the commutation torque ripples become more obvious as the rotor speed and load torque become higher. In many cases, torque ripples can only be reduced partly in spite of the fact that a proper commutation moment is chosen to fire the conduction phase and cut off the unenergized phase at the same time.

The moment of phase conduction or turn off can be controlled separately by the time-sharing commutation strategy. The conduction of phases A and C switching to phase B and C will be discussed as an example as follows. The line voltage between phases B and C is equal to U_{d} when phase B is conducted at t_{on}, while the line voltage between phases A and C will be 0 as phase A turned off at t_{cut} ($t_{\text{on}} \neq t_{\text{cut}}$). Meanwhile, the current of phase A will become 0 at t_{off}. Thus, three switch modes can be chosen, which could be expressed as conduction after cut off entirely, conduction after cut off and cut off after conduction. Different modes can produce varied effects on the commutation torque ripple, which will be discussed in the following sections. Similarly, to analyze how the time-sharing commutation strategy affects commutation torque ripple separately, we suppose that phase back-EMFs are equal to E or $-E$ during the commutation process.

5.2.2.1 Commutation Mode of Conduction After Cut Off Entirely

When this mode is adopted, we must cut off phase A first, then conduct phase B until the current of phase A is 0. In this condition, there exists $t_{\text{cut}} < t_{\text{off}} < t_{\text{on}}$.

Suppose $t_{\text{cut}} = 0$, then the current of phase C can be obtained during [0,t_1] as

$$i_{\text{C}} = \begin{cases} -I\mathrm{e}^{-\frac{R}{L}t} + \dfrac{E}{R}\left(1 - \mathrm{e}^{-\frac{R}{L}t}\right), & 0 < t < t_{\text{off}} \\ 0, & t_{\text{off}} \leq t < t_{\text{on}} \\ \dfrac{2E - U_{\text{d}}}{2R}\left(1 - \mathrm{e}^{-\frac{R}{L}(t - t_{\text{on}})}\right), & t \geqslant t_{\text{on}} \end{cases} \tag{5.32}$$

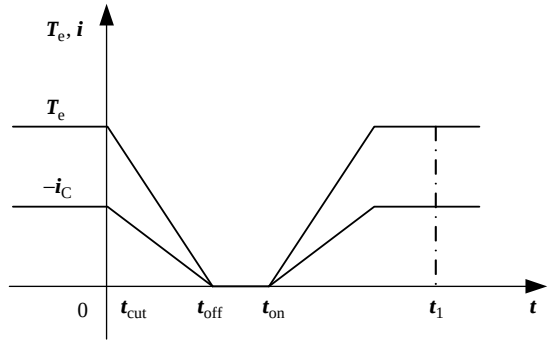


Figure 5.11 Current and torque ripple under commutation mode of conduction after cut off entirely.

Substituting Equation (5.16) into Equation (5.32), then i_C can be simplified as

$$i_C = \begin{cases} -I + \dfrac{U_d}{2R}(1 - e^{-\frac{R}{L}t}), & 0 < t < t_{off} \\ 0, & t_{off} \le t < t_{on} \\ -I + Ie^{-\frac{R}{L}(t - t_{on})}, & t \geqslant t_{on} \end{cases} \tag{5.33}$$

As Equation (5.31) states, the amplitude of i_C will drop dramatically during $[0, t_{off}]$ and will be 0 during $[t_{off}, t_{on}]$. But it will increase to I when $t > t_{on}$. Thus, current variation will cause an electromagnetic torque decrease during the transient process of commutation and the torque will achieve its minimum value at t_{off}. The corresponding current and torque waveforms are shown in Figure 5.11.

So, during $[0, t_1]$, the average torque ripple can be expressed as

$$\begin{aligned} \overline{T}_{e\sigma} &= \frac{2E\int_0^{t_1}(I + i_C)\mathrm{d}t}{\Omega t_1} = \frac{2E\left\{\int_0^{t_{off}}\frac{U_d}{2R}(1 - e^{-\frac{R}{L}t})\mathrm{d}t + \int_{t_{on}}^{t_1} Ie^{-\frac{R}{L}(t - t_{on})}\mathrm{d}t\right\}}{\Omega t_1} \\ &= \frac{2E\left\{\dfrac{U_d}{2R}\left[t_{off} + \dfrac{L}{R}(e^{-\frac{R}{L}t_{off}} - 1)\right] + \dfrac{L}{R}I(1 - e^{-\frac{R}{L}(t_1 - t_{on})})\right\}}{\Omega t_1} \end{aligned} \tag{5.34}$$

Compare Equation (5.34) to Equation (5.24), it is worth noting that torque ripples, which are caused by current variation, are more serious in the commutation mode of conduction after cut off entirely than that in switching at the same time. Therefore, this method is not good to reduce torque ripple since it will decrease the output electromagnetic torque.

5.2.2.2 Commutation Method of Conduction After Cut Off

In this method, phase A is cut off first, then conduct phase B before the current of phase A becomes zero. In this condition, there exists $t_{cut} < t_{on} < t_{off}$.

If $t_{cut} = 0$, the current of phase C during interval $[0,t_1]$ can be expressed as

$$i_C = \begin{cases} -Ie^{-\frac{R}{L}t} + \dfrac{E}{R}(1 - e^{-\frac{R}{L}t}), & 0 < t < t_{on} \\ i_C(t_{on-})e^{-\frac{R}{L}(t-t_{on})} - \dfrac{U_d - 4E}{3R}(1 - e^{-\frac{R}{L}(t-t_{on})}), & t_{on} \le t < t_{off} \\ i_C(t_{off-})e^{-\frac{R}{L}(t-t_{off})} + \dfrac{2E - U_d}{2R}(1 - e^{-\frac{R}{L}(t-t_{off})}), & t \geqslant t_{off} \end{cases} \tag{5.35}$$

By substituting Equation (5.14) into Equation (5.35), i_C can be simplified as

$$i_C = \begin{cases} -I + \dfrac{U_d}{2R}(1 - e^{-\frac{R}{L}t}), & 0 < t < t_{on} \\ -I + \dfrac{U_d + 2E}{6R} + \left[i_C(t_{on-}) + \dfrac{U_d - 4E}{3R} \right] e^{-\frac{R}{L}(t-t_{on})}, & t_{on} \le t < t_{off} \\ -I + [i_C(t_{off-}) + I]e^{-\frac{R}{L}(t-t_{off})}, & t \geqslant t_{off} \end{cases} \tag{5.36}$$

It can be seen from Equation (5.36) that the amplitude of i_C decreases dramatically during $[0,t_{on}]$ and i_C changes monotonically during $[t_{on}, t_{off}]$ with its amplitude less than the steady-state value I. However, when $t > t_{off}$, i_C increases gradually with its initial amplitude of i_C less than I and the steady-state value equal to I. The corresponding current and torque waveforms are shown in Figure 5.12.

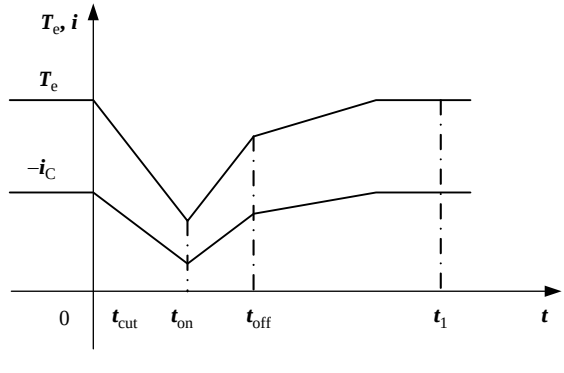


Figure 5.12 Waveforms of current and torque ripple under commutation method of conduction after cut off.

Compared with the traditional simultaneous switching method, electromagnetic torque ripple caused by current variation is much more serious by using this method. Thus, it has no obvious advantage.

5.2.2.3 Commutation Method of Cut Off After Conduction

In this method, conduct phase B first and then cut off phase A with $t_{on} < t_{cut} < t_{off}$.

Suppose $t_{on} = 0$, then the current of phase C during interval $[0,t_1]$ can be obtained as

$$i_C = \begin{cases} -Ie^{-\frac{R}{L}t} - \dfrac{2(U_d - 2E)}{3R}(1 - e^{-\frac{R}{L}t}), & 0 < t < t_{cut} \\ -i_C(t_{cut-})e^{-\frac{R}{L}(t-t_{cut})} - \dfrac{U_d - 4E}{3R}(1 - e^{-\frac{R}{L}(t-t_{cut})}), & t_{cut} \le t < t_{off} \\ -i_C(t_{off-})e^{-\frac{R}{L}(t-t_{off})} - I(1 - e^{-\frac{R}{L}(t-t_{off})}), & t \geqslant t_{off} \end{cases} \tag{5.37}$$

Similarly, by substituting Equation (5.16) into Equation (5.37), i_C can be simplified as

$$i_C = \begin{cases} -I - \dfrac{U_d - 2E}{6R}(1 - e^{-\frac{R}{L}t}), & 0 < t < t_{cut} \\ -I + \dfrac{U_d + 2E}{6R} + \left[\dfrac{U_d - 4E}{3R} - i_C(t_{cut-})\right]e^{-\frac{R}{L}(t-t_{cut})}, & t_{cut} \le t < t_{off} \\ -I + [I - i_C(t_{off-})]e^{-\frac{R}{L}(t-t_{off})}, & t \geqslant t_{off} \end{cases} \tag{5.38}$$

As stated in Equation (5.38), the amplitude of i_C increases gradually from I during $[0,t_{cut}]$ and it will increase faster as the back-EMF decreases more marked. During interval $[t_{cut}, t_{off}]$, i_C decreases monotonously with its initial value greater than I. The smaller E and I are, the faster the amplitude of i_C decreases. When $t > t_{off}$, i_C varies monotonously with its steady-state value equal to I. Note that the variation tendency of i_C depends on the value of i_C at the last moment. Current variation during the transient process of commutation may cause electromagnetic torque ripple, which will achieve its maximum at t_{cut}.

The waveforms of current and electromagnetic torque are shown in Figure 5.13. Torque ripple during the transient process of commutation will increase in this mode.

As discussed above, only the commutation mode of cut off after conduction will make the commutation torque increase among the three modes. Variation of the back-EMF during transient process of commutation may decrease the electromagnetic torque. Therefore, the influence of back-EMF can be suppressed by the commutation mode of cut off after conduction so that the commutation torque ripple is reduced.

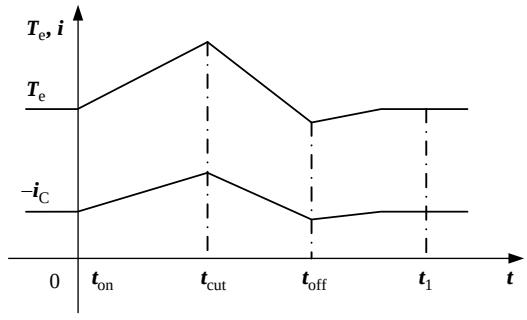


Figure 5.13 Waveforms of current and torque ripple under commutation method of cut off after conduction.

5.2.3 Optimal Time-Sharing Commutation

5.2.3.1 Optimum Time-Sharing Commutation Moment

Since the commutation method of cut off after conduction can increase the current of the nonenergized phase, proper selection of t_{on} and t_{cut} can offset the influence of the back-EMF waveform on electromagnetic torque, so as to reduce the commutation torque ripple to a certain extent.

At the best moment for time-sharing commutation, the commutation torque ripple minimum average torque ripple can be obtained by the optimization problem as

$$\min_{t_{on},t_{cut}\in[0,t_1]} \overline{T}_{e\sigma} = \min_{t_{on},t_{cut}\in[0,t_1]} \frac{\int_0^{t_1} |T_e - T_{e0}| dt}{t_1} \tag{5.39}$$

The best moment of time-sharing commutation is related with the rotor speed, motor load, etc. If the optimal time-sharing commutation moment can be identified according to the operation states of the motor, torque ripple can be reduced effectively. The practical waveform of back-EMF may cause a decrease of commutation electromagnetic torque. If commutation happens at the moment that the line back-EMF is zero, the electromagnetic torque ripple achieves its minimum with the maximum average electromagnetic torque achieved.

Time-sharing commutation can make the commutation torque first increase and then decrease. And the electromagnetic torque will achieve its maximum at t_{cut}. Therefore, by taking t_{cut} as the zero-crossing point of line back-EMF, the effect of the transient process of current commutation and the back-EMF on electromagnetic torque can be compensated. Define "t_{cut}–t_{on}" as the advanced conduction time, and then the electrical angle for the motor running during this period is exactly the advanced electrical angle. After t_{cut} is defined, the only need to know is the best advanced electric angle, so that the time-sharing commutation strategy is achieved.

Note that the best advanced electrical angle is related to many factors. When the rotor speed is high, the torque ripple that is caused by back-EMF is more serious, so that the advanced electrical angle should be appropriately increased. In addition, while the motor load is heavy, the amplitude of the steady current is big with a longer transient process of current commutation, so the advanced electrical angle should also be appropriately increased.

Table 5.1 Fuzzy rules for conduction moment

E \ *I*	NB	NS	ZE	PS	PB
NB	NB	NB	NS	NS	ZE
NS	NS	NS	NS	NS	PS
ZE	ZE	ZE	ZE	ZE	PS
PS	PS	PS	PS	PS	PB
PB	PS	PS	PB	PB	PB

5.2.3.2 Fuzzy-Controller Design

In different motor operation modes, the relationship between advanced conduction angle and the steady variables (i.e. the amplitude of back-EMF and current) cannot be described in the traditional mathematical method. A fuzzy controller is free of accurate mathematical model. Its output is usually determined according to the input signal and control rules with fuzzy reasoning [6–12]. Therefore, a two-dimensional fuzzy controller can be adopted to determine the advanced conduction time, where the controller inputs are the per-unit value of the amplitude of the current and back-EMF, and the output is the advanced conduction angle.

First, per-unit values of E and I are mapped to $[-1, 1]$, 5 fuzzy subsets can be defined as PB, PS, ZE, NS and NB, respectively. Suppose the detected E and I are of normal distribution, then the membership of different fuzzy subsets can be gained. The fuzzy control rules of BLDC motor by using the Mamdani minimum operation is shown in Table 5.1.

5.2.3.3 The Realization of Time-Sharing Commutation Strategy

Since the conduction moment precedes the zero-crossing point of back-EMF, it is difficult to give a commutation command according to the zero-crossing point of the line back-EMF during the control process. In order to solve this problem, by using the approximate linear characteristics of the line back-EMF near the commutation moment, we can obtain the line back-EMF corresponding to the advanced electrical angle. Hence, the commutation command can be determined by the line back-EMF.

The relationship between the line back-EMF and electrical angle θ is shown in Figure 5.14, in which the line back-EMF near the commutation moment remains approximately linear.

The line back-EMF e_{L} and electric angle θ will meet

$$\frac{e_{\mathrm{L}}}{\theta - \theta^*} = \frac{2E}{\theta_{\mathrm{E}} - \theta^*} = k \tag{5.40}$$

where $\theta*$ — electrical angle at the crossing point of the line back-EMF.
θ_{E} — electrical angle at the decreasing moment of the line back-EMF.
θ — electrical angle corresponding to e_{L}.
k — the slope.

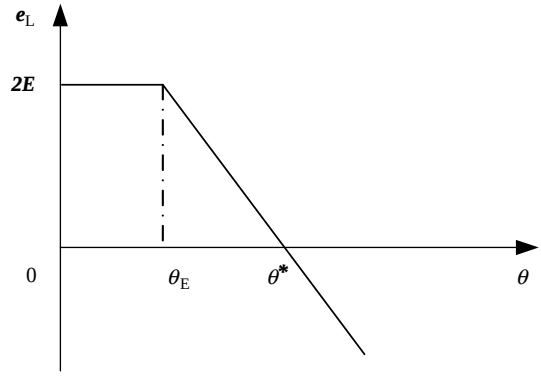


Figure 5.14 The relationship between line back-EMF and θ.

As stated in Equation (5.40), we can calculate the line back-EMF e_{on} corresponding to the advanced electrical angle, then get the e_{cut} with the time of sampling, calculation, and operation being taken into consideration. Thus, the time-commutation strategy is achieved so that the commutation torque ripple of the BLDC motor can be reduced.

5.3 Torque-Ripple Reduction with Active Disturbance Rejection Control

5.3.1 Principles of ADRC

An active disturbance rejection nonlinear controller is based on the state observer and disturbance compensation, which is composed of a tracking differentiator, an extended state observer and a nonlinear state feedback control law. Among them, the tracking differentiator can filter the reference input signal and then achieve fast tracking without overshoot, and extract the differential signal based on the generalized differential theory. The extended state observer can estimate the system status, model uncertainties and the external disturbances well. The nonlinear state feedback control law can generate control signals by a nonlinear structure configuration. In other words, the active disturbance rejection controller deals with the system input and output by using a tracking differentiator and an extended state observer, respectively. Also, the control input of system can be obtained through the combination of nonlinear state error and the feedforward compensation [13–18].

Compared with the traditional PID control, an active disturbance rejection controller has much significant superiorities. First, it can provide reasonable arrangement of transition process according to the tracking differentiator. Secondly, the nondifferentiable and discontinuous problem of error signal, and the noise of the differential signal can be solved with the generalized differential method. Meanwhile, the unmodeled dynamics and unknown external disturbance are all resolved into a total disturbance of the system to be estimated by the extended state observer. Therefore, an accurate model of the controlled object is not necessary

in practice, but the system is still robust. In addition, the ADRC nonlinear structure instead of using a classical control configuration in the form of linear weighted sum forms the nonlinear state error feedback control law, which greatly improves the processing efficiency of the error signal and the performance of the closed-loop control system.

5.3.2 ADRC Controller Design

5.3.2.1 Model of BLDC Motor

The main circuit of the three-phase BLDC motor is shown in Figure 5.15.

Using lumped parameters and ignore the armature reaction, the voltage balance equation of the motor will be

$$u_x = Ri_x + (L - M)\frac{\mathrm{d}i_x}{\mathrm{d}t} + e_x \tag{5.41}$$

where u_x — phase voltage;
i_x — phase current;
e_x — phase back-EMF.

The electromagnetic torque equation of the motor is

$$T_\mathrm{e} = (e_\mathrm{A}i_\mathrm{A} + e_\mathrm{B}i_\mathrm{B} + e_\mathrm{C}i_\mathrm{C})/\Omega \tag{5.42}$$

Moreover, the mechanical motion equation is

$$T_\mathrm{e} = T_\mathrm{L} + B_\mathrm{v}\Omega + J\frac{\mathrm{d}\Omega}{\mathrm{d}t} \tag{5.43}$$

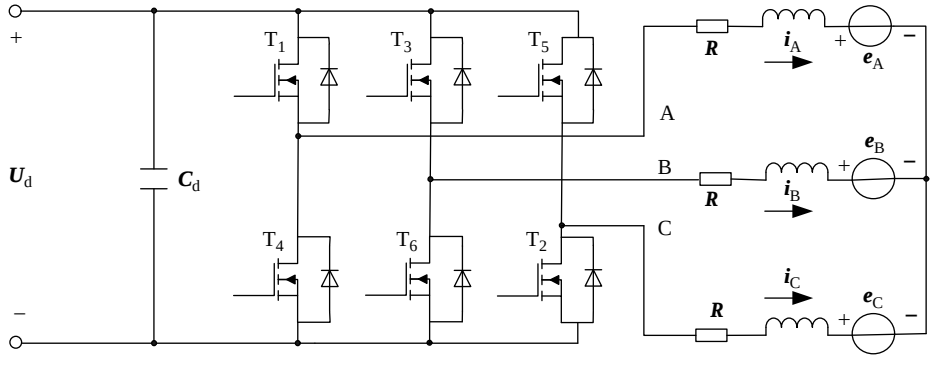


Figure 5.15 Main circuit of a BLDC motor.

5.3.2.2 Torque Subsystem Design of ADRC

Let

$$\begin{cases} T_{\mathrm{ex}} = e_x i_x / \Omega \\ E = K_{\mathrm{e}} \Omega \end{cases} \tag{5.44}$$

where E — amplitude of e_x;
K_{e} — coefficient of back-EMF.

Then, T_{ex} can be approximately taken as

$$T_{\mathrm{ex}} = s K_{\mathrm{e}} i_x \tag{5.45}$$

where $s = \begin{cases} 1 & i_x \geqslant 0 \\ -1 & i_x < 0 \end{cases}$.

As stated in Equation (5.41), one can obtain

$$\dot{T}_{\mathrm{ex}} = -\frac{R}{L-M} T_{\mathrm{ex}} + \frac{K_{\mathrm{e}}}{L-M} s u_x - \frac{K_{\mathrm{e}}}{L-M} s e_x \tag{5.46}$$

Thus, we can define the disturbance of the torque subsystem as

$$\begin{cases} w_{1x} = -\dfrac{K_{\mathrm{e}}}{L-M} s e_x \\ u'_x = s u_x \end{cases} \tag{5.47}$$

Then, three extended state observers of phase A, B and C are built to observe the electromagnetic torque of the motor as

$$\begin{cases} \dot{z}_{1x} = z_{2x} - \beta_1 fal(z_{1x} - T_{\mathrm{ex}}(t), \alpha_1, \delta_1) + b_0 u'_x \\ \dot{z}_{2x} = -\beta_2 fal(z_{1x} - T_{\mathrm{ex}}(t), \alpha_1, \delta_1) \end{cases} \tag{5.48}$$

where $b_0 = K_{\mathrm{e}}/(L-M)$.
Hence,

$$\begin{cases} \hat{T}_{\mathrm{e}} = z_{1\mathrm{a}} + z_{1\mathrm{b}} + z_{1\mathrm{c}} \\ a = z_{2\mathrm{a}} + z_{2\mathrm{b}} + z_{2\mathrm{c}} \end{cases} \tag{5.49}$$

where $\hat{T}_e$ — tracking value of the electromagnetic torque;
a — real-time value of the torque subsystem during its operation.

The greatest advantage of ADRC is that it does not rely on its object model. The tracking value and real-time value of the torque subsystem are obtained by the extended state observer to construct a first-order ADRC controller that takes the bridge inverter output

voltage as control input, the electromagnetic torque as the measurement input in order to reduce the torque ripple of BLDC motor. Here, the control input parameter b is chosen to be $1/(2L–2M)$.

Note that the torque observed by the extended state observer of torque subsystem is not the actual motor torque, but the error between them is not significant. Simulation and experimental results show that the torque observer can meet the system requirements of torque-ripple suppression.

5.3.2.3 Design of ADRC in Speed Subsystem

From the mechanical motion Equation (5.43), we further get

$$\frac{\mathrm{d}\Omega}{\mathrm{d}t} = -\frac{B_\mathrm{v}\Omega}{J} + \frac{T_\mathrm{e}}{J} - \frac{T_\mathrm{L}}{J} \tag{5.50}$$

with the disturbance of the speed subsystem be defined as

$$w_2 = -\frac{T_\mathrm{L}}{J} \tag{5.51}$$

Thus, the first-order ADRC of the speed subsystem can be designed, where T_e is the control input and Ω is the measurement output.

So, two first-order ADRCs can be designed by considering the motor equivalent to an integral series model composed of two nonlinear subsystems to realize the double loop control of a BLDC motor driving system. The outer loop is taken as speed control that provides the reference torque for the inner control loop. The inner loop is taken as torque control to reduce the torque ripple of the motor. The corresponding ADRC is obtained as shown in Figure 5.16, where the DC side voltage of the inverter is taken as the control input and the mechanical velocity as the measurement input.

In the ADRC, the external disturbance and internal disturbances of the system are in the equivalent status. The extended state observer can track the output electromagnetic torque quickly, so that the online control of the torque subsystem is ensured. For a given reference torque, the torque fluctuations as disturbance can be estimated in real time by the extended state observer and compensated by adjusting the inverter output voltage. This can also keep the torque steady.

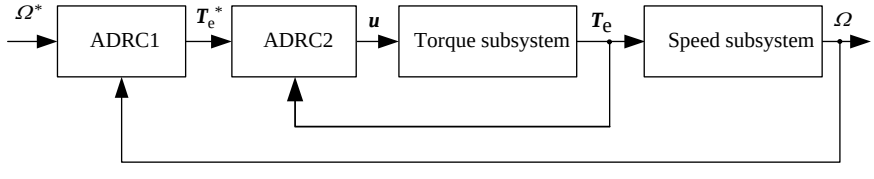


Figure 5.16 Scheme of the ADRC to reduce torque ripple.

5.3.3 Experimental Results

Here, the experimental test system is designed based on the DSP chip TMS320LF2407A of TI Company to design and verify the active disturbance rejection control scheme for torque fluctuations reduction in BLDC motor. The corresponding hardware block diagram is shown in Figure 5.17. The parameters of the ADRC are defined in the MATLAB environment initially, and then certain adjustments are made during the experiment. The active disturbance rejection control algorithm is implemented in TMS320LF2407A.

During the experiment, a 4-pole-pair Y-connected BLDC motor is used as a prototype, which is controlled in the two-phase 120° conduction mode. The rotor position is detected by position sensors. DSP changes the position signal into the speed signal. Then the speed signal, as the output of the speed subsystem, is put into ADRC1. The control variable calculated by the nonlinear feedback control law is taken as the given input of ADRC2. The output of the torque subsystem can be calculated by three phase currents, and the control variable of ADRC2 will be changed into the corresponding duty cycle square wave by the EVA of DSP to achieve the PWM control for the motor. The torque is detected by a noncontact rotary torque sensor (range: 1 N m, accuracy class: 0.5%).

Figure 5.18 shows the torque waveform of open-loop operation. As can be seen from the figure, the torque ripple can reach about 25% of the average torque.

Then, the motor is controlled by the active disturbance rejection control scheme with the rated load ($T_L = 0.4$ N m). Figure 5.19 shows the detected torques with the given speed being equal to 300 r/min, 1000 r/min, and 1500 r/min, respectively.

As can be seen from Figure 5.19, the inhibitory effect of torque ripple is more feasible at low speed. In this condition, the torque is more stable and the fluctuations can be controlled within 1%.

Figure 5.20 shows the torque waveform of the motor with light load ($T_L = 0.05$ N m) at the rated speed condition. It can be seen from Figure 5.20 that the torque ripple has also been well suppressed when the motor runs with light load at high speed.

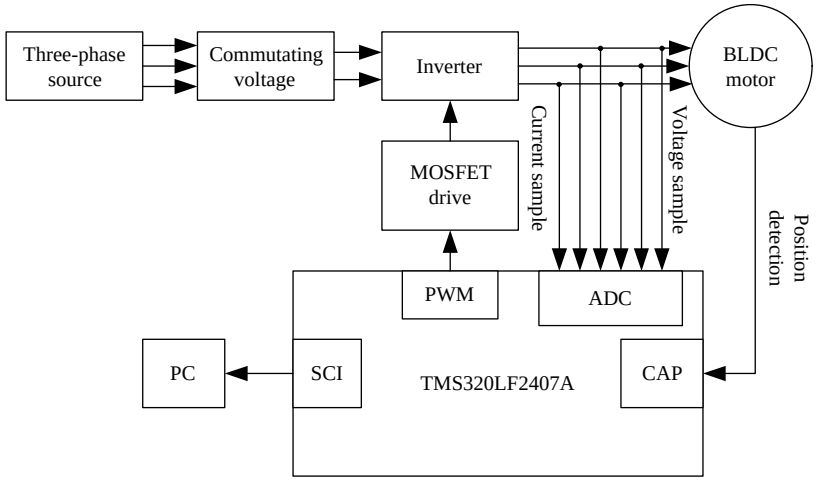


Figure 5.17 Hardware control scheme.

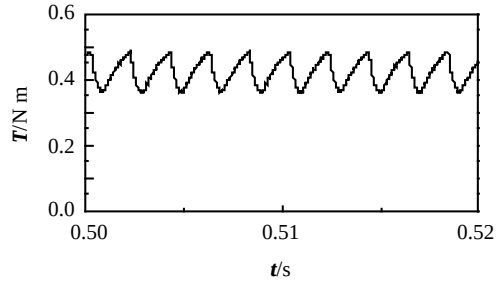
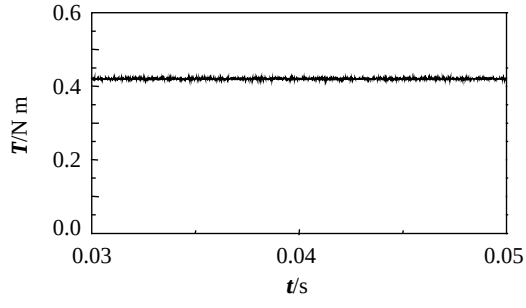
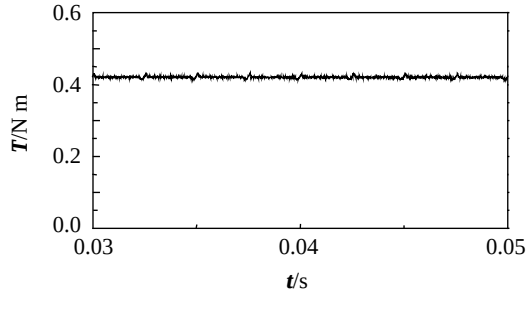


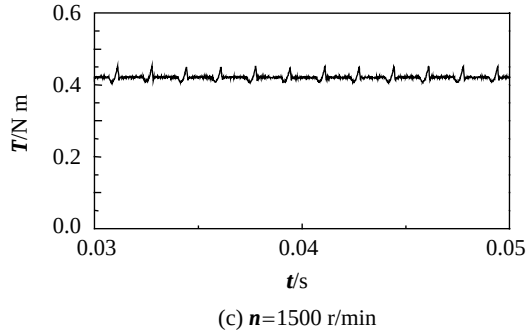
Figure 5.18 Torque waveform of open-loop operation.



(a) n=300 r/min



(b) n=1000 r/min



(c) n=1500 r/min

Figure 5.19 Torque waveforms for the motor running at different speeds.

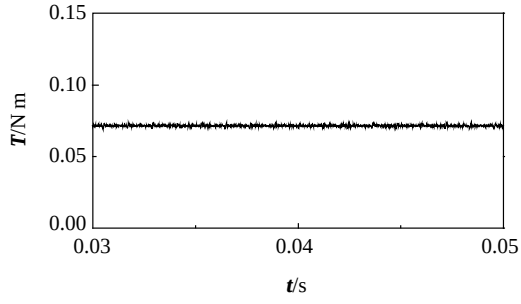


Figure 5.20 Torque waveform for the motor running with light load at the rated speed.

Comparing Figure 5.19 with Figure 5.20, it can be seen that the torque-ripple-reduction effect of ADRC is independent with respect to the motor speed. At the rated torque or high torque level, the torque ripple cannot be effectively suppressed mainly due to the limitation of the inverter voltage output. The DC voltage of the bridge inverter is limited to 40 V in experiments. So, in high-speed operation and high-torque conditions, the torque ripple cannot achieve full compensation due to this voltage limitation. Since the torque ripple observation is accurate, a sufficient voltage output level of the inverter will suppress the torque ripple at high speed too.

Generally speaking, by using ADRC, not only will better speed response of the motor be achieved, but also the torque ripple and motor noise will be significantly reduced. The ADRC-based closed-loop torque control can suppress the torque ripple caused by various factors obviously, especially for motor commutation torque ripple.

5.4 Torque-Ripple Reduction with BP Neutral Network

5.4.1 BP Neural Network

5.4.1.1 Topology of BP Neural Network

A BP neural network is a kind of one-way transmission multilayer feedforward neural network. It has a flexible network structure with strong nonlinear mapping and adaptive capabilities. Except for the input and output layer nodes, there are one or more layers of hidden nodes in the network. Nodes of the same layer have no connection. Therefore, the output of each node only affects the nodes of the next layer. A BP neural network can be seen as a complex nonlinear mapping from input to output. It can approximate to an arbitrarily complex function by compounding simple nonlinear functions. In theory, a continuous L_2-function can be approximated by the BP neural network with only three layers to any desired degree of accuracy [19]. In addition, the learning of a BP neural network is essentially an unconstrained nonlinear optimization problem.

The commutation moment of a BLDC motor is determined mainly by the voltage and back-EMF, whereas the back-EMF is related to the speed of the motor. Therefore, there is a certain relation among the commutation moment t, speed n, and the terminal voltage u. A three-layer BP neural network used in BLDC motor control system, with one input layer, one hidden layer, and an output layer, is shown in Figure 5.21.

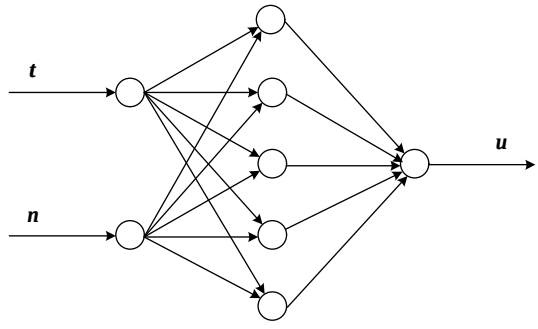


Figure 5.21 Topology of the BP neural network.

In the network, there are two input nodes (t and n), five hidden layer nodes and an output node u. The network is mainly used to identify the relationship between u and t, n. The logsigmoid function of the hidden layer and the tansigmoid function of the output layer are, respectively, represented as

$$\log \mathrm{sig}(x) = \frac{1}{1 + \mathrm{e}^{-x}} \tag{5.52}$$

and

$$\tan \mathrm{sig}(x) = \frac{1 - \mathrm{e}^{-2x}}{1 + \mathrm{e}^{2x}} \tag{5.53}$$

Note that it is better to choose different output functions with varied running conditions to enhance the network's mapping function ability and improve its convergence speed.

5.4.1.2 Network Training

As is well known, network training is divided into online training and offline training. If the offline trained network is used to the actual control system directly, it may not adapt to environmental changes. On the other hand, online training can immediately update the model with environmental changes, but it will lose accuracy for initial training. Therefore, a combination of online training and offline training can be used to enhance the training performance. Usually, the offline trained network is adopted first, and then the online training of network is applied when the motor is running.

The samples for offline training can be derived from simulations or experiments by recording the time t of current rising from zero to the maximum, the corresponding speed n and the terminal voltage u. If the motor parameters are determined, a series of different samples of $t(k)$, $n(k)$ and $u(k)$ can be obtained by changing the power supply voltage or the motor load.

Here, 5000 simulation samples are used to train the network by modifying the voltage and load 50 times. In this condition, the network will converge to the sample data in the second period. As discussed above, the disadvantages the offline training can be compensated by the

online training with real-time identification of model parameters. The samples of online training include the current, speed and power-supply voltage. The commutation moment t can be derived from the detected current. Then, taking t and n as the network inputs to obtain u, the error between u and its expected value is thus used to correct the weights of the network so that the merits of online training are obtained.

In the network-training process, it is necessary to modify the network weights between neurons constantly, so that the error of the performance function is reduced to the required precision gradually. Therefore, the mapping of the network is approximated to the true model.

The main disadvantages of a BP neural network include its slow learning speed and the existence of a local minimum point. To solve these problems, many scholars have carried out extensive research and exploration, and have made many valuable achievements. The results show that a BP neural network learning speed is related to the optimization of learning algorithm, the choice of learning rate, and many other factors. So, in different learning environments, we can select different learning methods.

If appropriate learning methods are adopted, the local optimization problem of the network can be solved. The control strategy of adding inertia terms with its inertia factor equal to 0.92 is used in this section, so that only small oscillations occur in the BP neural network training process. The training results show that fast convergence of network is obtained [20].

The formula for weight correction is

$$\Delta w_{ij}(k+1) = \gamma \delta_i(k) y_i(k) + \alpha \Delta w_{ij}(k) \tag{5.54}$$

where w_{ij} — weight between network layers;
y_i — actual output of the ith neuron;
δ_i — local gradient for weight correction of ith neuron;
γ — learning rate;
α — momentum factor.

For the output layer

$$\delta_i^k = (d_i(k) - y_i(k))\varphi'(v_i(k)) \tag{5.55}$$

For the hidden layer

$$\delta_i^k = \varphi'(v_i(k)) \sum_o \delta_o(k) w_{oi}(k) \tag{5.56}$$

where φ — output function;
$d_i(k)$ — teacher output of the ith neuron;
v_i — input of the ith neuron.

5.4.2 Self-Tuning Regulator

Since the 1970s, due to the needs of space technology and process control, especially with the development of microelectronics and computer technology, the adaptive control theory and design has made great progress. It has become an important branch of modern control theory. In contrast to traditional regulation principles and optimal control theory, adaptive control can give good quality of control in the condition that the knowledge of the object model or environment is less sufficient.

A large number of engineering practices show that the adaptive control for complex controlled object can often reduce costs, and improve the existing productivity and the quality of products [21–23]. Currently, the most commonly used adaptive control contains the model reference adaptive system (MRAS) and self-tuning regulator (STR).

Here, the self-tuning regulator is used for the BLDC motor control. The self-tuning regulator separates the unknown parameters estimation and controller design. The unknown parameters are estimated online with a recursive estimation method, so that the estimated parameters can be seen as the real parameters for system control. Moreover, the self-tuning regulator is designed based on a BP neural network as shown in Figure 5.22.

In Figure 5.22, the network ANN2 is used to estimate parameters, while the network ANN1 for regulating the voltage. ANN1 and ANN2 have the same structure and weight. With ANN2 online training, the updated weights are used for ANN2 and ANN1 together. The inputs of the network ANN2 are t_2 and n. The parameters (the weights between neurons) estimated by ANN2 are taken as the true parameters to model ANN1. Since the inputs of ANN1 are t_1 and n, we get $t_2 = t_1$. Thus, the voltage U_{n1} under the ideal state is obtained by ANN1 to regulate the power-supply voltage. Meanwhile, U_{n1} is used as the teacher of network ANN2. The error between U_{n1} and the output of ANN2 U_{n2} are used to correct the corresponding weights. Finally, while the input and output of the network ANN1 and ANN2 have no significant differences, the commutation torque ripple can be reduced. Note that ANN2 can correct the parameters of the system and update the weights of ANN1 online, so that the network model will always approach its actual model.

5.4.3 Experimental Results

The network training and adaptive control algorithm are achieved by VC + + 6.0. The current signals of the last period are used to calculate the corresponding t_1 and t_2 by simple fitting.

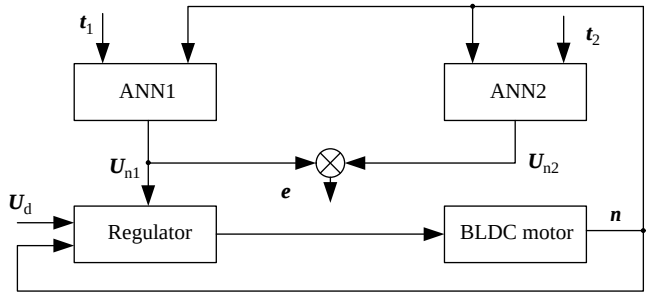


Figure 5.22 Self-tuning regulator.

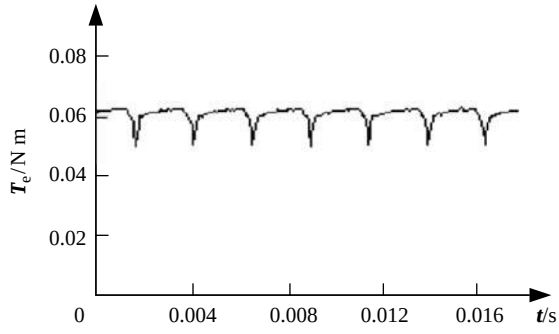


Figure 5.23 Torque waveform without adding a commutation torque-ripple-reduction control strategy.

Values of t_1 and t_2 are applied for the training of network ANN2 and the updating of network ANN1. Meanwhile, t_1 and t_2 of the current period are recorded for network training and adaptive voltage regulation of the next period.

Figure 5.23 is a record of the detected torque without adding the commutation torque-ripple-reduction control strategy. As is seen from Figure 5.23, the torque ripple is more obvious. It reaches about 25% of the average torque.

Figure 5.24 shows that the measured torque after the commutation torque-ripple reduction control is implemented. It can be seen from Figure 5.24 that the ripple is dramatically reduced. Note that the commutation current is simplified to linear during the transient process, which is not fully consistent with the actual situation. Thus, the output torque still has small fluctuations and its value is about 1.2% of the average torque, as shown in Figure 5.24.

Figure 5.25 illustrates the effect of the adaptive control. As load increases suddenly, the previous control model is no longer adaptive to the new environment. The online learning, parameters re-estimation and model correction will make the system reach a new equilibrium in a short time. Thus, there is a transition between the new equilibrium and the former one. The transition duration is related to the convergence speed of network learning. The faster the convergence, the shorter the transition time. Here, the system transition time is equal to 5–6 cycles (about 14 ms).

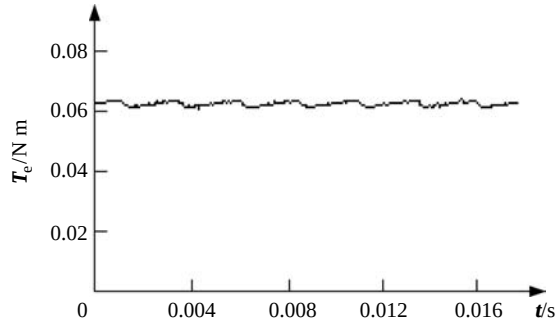


Figure 5.24 Torque waveform with a commutation torque-ripple-reduction control strategy.

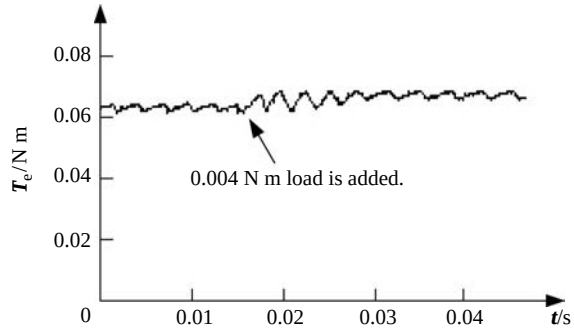


Figure 5.25 Torque waveform with a sudden load increase.

Torque ripple in a BLDC motor is mostly generated in the transient process of commutation, while the commutation torque ripple is caused by the amplitude variation of the DC bus current during the transient process of commutation. Controlling the winding voltage during the transient process of commutation, so that the rise and fall rates of the corresponding phase currents are equal, can compensate the amplitude variation of the DC bus current and reduce the torque ripple. So, it can be concluded that in the control strategy described in this section based on a BP neural network and self-tuning regulator, the exact parameters of the motor need not be predicted, and the system can respond quickly to changes of the environment. The results show that the proposed method can greatly reduce the commutation torque ripple with high control accuracy and robustness.

5.5 Motor Optimization and Torque-Ripple Minimization with Fuzzy Niche Genetic Algorithm

The platform width of the back-EMF waveform of a BLDC motor is 120° electrical angle ideally, which is greater than that in actual operation. Also, the amplitude of the torque ripple will increase as the platform width decreases. It is clearly seen that the platform width of the back-EMF affects motor torque ripple. Therefore, whether it is computed accurately plays an important role in related optimization of motor torque ripple.

The structural parameters of BLDC motor, which have essential connection with the motor torque ripple, have an effect on winding inductance and the platform width of the back-EMF waveform. In this section, the calculation of platform width based on the structural parameters is presented, by which the theoretical basis for minimizing torque ripple is provided. Also, the principle of niche genetic algorithm for multiobjective optimization is given and a niche genetic algorithm based on fuzzy control is proposed while taking the calculation complexity of motor design into account. The novel genetic algorithm makes adaptive control of parameters possible and accelerates its rate of convergence. The validity of the novel algorithm is proved practically. Then it is applied in the optimization of a BLDC motor, which improves the motor efficiency and minimizes torque ripple effectively.

5.5.1 Platform-Width Calculation of Back-EMF Waveform

5.5.1.1 The Platform Width of Back-EMF Waveform of Concentrated and Full-Pitch Windings

Figure 5.26 shows the spatial distribution of the air-gap flux density of a BLDC motor, where b_p represents the length of pole arc, τ represents the polar distance and B_δ represents the amplitude of air-gap flux density, respectively.

If the edge effect is neglected, the platform width of the air-gap flux density waveform is

$$\theta_B = \frac{180 \times b_p}{\tau} \tag{5.57}$$

The back-EMF waveform of phase A is analyzed as an example in this section. The back-EMF equation of phase A based on basic electromagnetic relation is given by

$$e_A = L_{af} v \sum_{n=1}^{N_a/p} B_\delta(n) \times 10^{-3} \tag{5.58}$$

where B_δ (n), L_{af}, v, N_a and p represent the air-gap flux density of the nth conductor, the armature effective length, the peripheral speed, the number of conductors in series per phase and the number of pole pairs, respectively.

The conductor peripheral speed is

$$v = \frac{n}{60} \times \pi D_1 \times 10^{-3} \tag{5.59}$$

where D_1 represents the diameter of the armature.

It is obtained from Equations (5.58) and (5.59) that

$$e_A = K_e \Omega \frac{p \sum_{n=1}^{N_a/p} B_\delta(n)}{N_a B_\delta} = E \frac{p \sum_{n=1}^{N_a/p} B_\delta(n)}{N_a B_\delta} \tag{5.60}$$

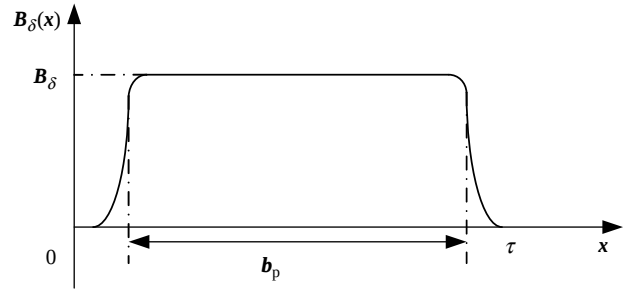


Figure 5.26 Spatial distribution of air-gap flux density.

where the back-EMF coefficient is

$$K_{\mathrm{e}} = \frac{N\mathrm{a}D_1 L_{\mathrm{af}} B_\delta \times 10^{-6}}{2p} \tag{5.61}$$

For concentrated and full-pitch windings, conductors of the same winding lie in the same position x, which indicates that the air-gap flux density remains unchanged. The overall back-EMF waveform is obtained by synthesizing the back-EMF waveforms of all the conductors of phase A, which looks like the waveform of the air-gap flux density and whose platform width θ_{e} equals that of the spatial distribution of air-gap flux density, θ_{B}.

5.5.1.2 The Platform Width of Back-EMF Waveform of Distributed and Full-Pitch Windings

In order to utilize the inner surface of the stator effectively and facilitate winding cooling, the coils are dispersed evenly around the surface of the stator. Assume that the phase belt of phase A winding is 60° and the number of slots per phase and per pole is q. In this way, the difference of back-EMFs generated by two adjacent conductors is $60°/q$ electrical angle, and the platform width of the overall back-EMF waveform is obtained from superposition as

$$\theta_{\mathrm{e}} = \theta_{\mathrm{B}} - 60\left(1 - \frac{1}{q}\right) \tag{5.62}$$

Now assume that the winding has infinite conducts that are dispersed evenly around the inner surface of the stator, then the summation can be expressed as integration. Therefore, the back-EMF is given by

$$e_{\mathrm{A}} = K_{\mathrm{e}}\Omega \frac{3\int_{\theta}^{\theta+\pi/3} B_\delta(x)\mathrm{d}x}{B_\delta \pi} = E\frac{3\int_{\theta}^{\theta+\pi/3} B_\delta(x)\mathrm{d}x}{B_\delta \pi} \tag{5.63}$$

Assume that the distribution of the air-gap flux density is square wave whose ideal amplitude is B_δ, which means

$$B_\delta(x) = \begin{cases} B_\delta, & 2k\pi < x < 2k\pi + \pi \\ -B_\delta, & 2k\pi + \pi < x < 2(k+1)\pi \end{cases} \tag{5.64}$$

and its waveform is as shown in Figure 5.27.

Substituting Equation (5.64) into Equation (5.63) gives the back-EMF waveform of phase A, which is relatively ideal and is a trapezoid with a 120° platform width, as shown in Figure 5.28.

Usually, it is difficult to attain ideal waveforms by using distributed windings since the distribution of the air-gap flux density is not a perfect square wave.

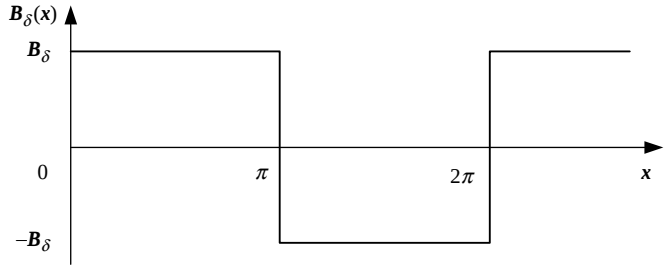


Figure 5.27 Schematic diagram of ideal air-gap magnetic field.

5.5.1.3 The Platform Width of Back-EMF Waveform of Distributed and Short-Pitch Windings

The advantage of short-pitch windings lies in the shortening of terminal parts of conductors. Assume that the phase belt of phase A is 60° and distributed and short-pitch windings are employed, the number of slots per pole and per phase, the polar distance and the pitch are q, τ, and y_1, respectively. Therefore, the platform width of the overall back-EMF waveform from superposition as

$$\theta_e = \theta_B - 180\left(1 - \frac{y_1}{\tau}\right) - 60\left(1 - \frac{1}{q}\right) \tag{5.65}$$

5.5.1.4 The Platform Width of Back-EMF Waveform using a Skewed Slot or a Skewed Pole

The utilization of a skewed slot or a skewed pole can reduce the cogging torque ripple of the motor. However, it also reduces the higher harmonics of the back-EMF waveform, which narrows the platform width of the back-EMF and increases torque ripple. The platform width of the back-EMF waveform when the skewed slot coefficient is α_{sk} can be expressed approximately as

$$\theta_e = \theta_B - 2\alpha_{sk} \tag{5.66}$$

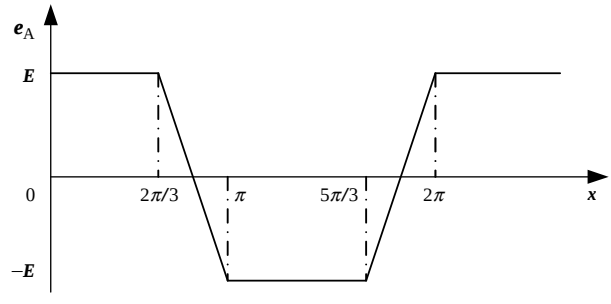


Figure 5.28 Back-EMF waveform in ideal conditions.

From what has been learned above it is evident that the shape of the back-EMF waveform depends on the structure of windings, which will further have an effect on the commutation torque ripple of the motor, therefore what should be considered synthetically in motor design is the motor performance and applications with various winding structures.

5.5.2 Fuzzy Niche Genetic Algorithm

5.5.2.1 Multiobjective Optimization

Minimizing the torque ripple is just one of the objectives in motor optimization, and usually the efficiency and cost of the motor should be covered. The optimization of motor design can be concluded as nonlinear programming of multiobjective functions, each of them is usually a nonconvex function that has more than one extreme point.

In multiobjective programming, sometimes several objective functions contradict with each other, such as the efficiency, the speed and the platform width of the air-gap flux density waveform of the BLDC motor, and so on. Therefore, solving a minimization problem is to search for the optimal solution, or a Pareto optimal solution, when all objective functions are taken into account synthetically. Although not each objective function is optimized to its own optimal solution when they are considered individually, it is not allowed for any objective function to compromise in order to cater to other objective functions, by which multi-objective optimization is distinguished from single-objective optimization. Meanwhile, this is just the difficulty of multiobjective optimization. Usually, a Pareto solution is not confined to one optimal solution. Instead, it is a set of solutions (Pareto optimal set). Figure 5.29 shows the Pareto optimal set of a BLDC motor whose objective functions consist of the platform width of the air-gap flux density waveform θ_B, and the efficiency of the motor η.

The complexity of multiobjective optimization is exponential with its scale, which consists of the number of optimization variables and the number of values that each variable may take. Applying exhaustive method to the above problem belongs to an NP-complete problem, which cannot be solved in finite time. Some conventional multiobjective optimization methods are

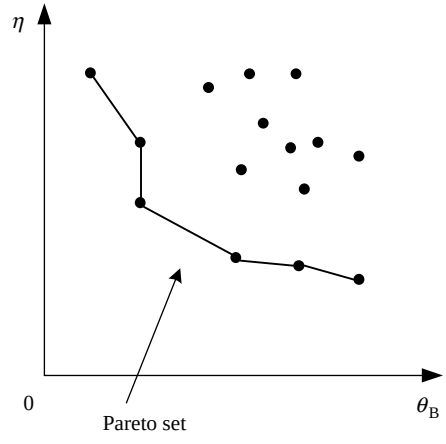


Figure 5.29 Schematic diagram of Pareto set of θ_B and η.

directional search based and converge fast, such as the weighted sum method, the goal programming method and the game theory method. However, they often need derivative information in calculations, which tend to converge at local optimal points caused by the impact of objective functions′ performance. The simulated annealing algorithm belonging to random search methods is immune to the behavior of objective functions, but only one optimal point can be converged to. The randomness and implicit parallelism of a niche genetic algorithm makes it possible to find more than one local optimal point and obtain Pareto optimal sets, from which the best solution can be obtained according to certain preferences. Currently the niche genetic algorithm is known as one of the most effective methods to achieve multiobjective optimization. The following is the optimization of the motor based on a niche genetic algorithm.

5.5.2.2 Niche Genetic Algorithm

Niche is a kind of survival environment. The niche genetic algorithm groups every generation into categories, in which individuals having larger fitness values are chosen as the excellent representatives, or a population. Then, a new generation is produced through hybridization and mutation within a population or between populations, and then excellent representatives are kept through certain mechanism. In this way, new populations are produced continually through clustering in the evolution, and populations are continually updated by newly obtained excellent individuals, through which populations are continually optimized.

The diversity of the solution remains in the niche genetic algorithm in evolution. Also, global optimization is guaranteed, which is superior in optimizing multipeak functions that are common in mathematics and engineering. Compared to the conventional genetic algorithm, the niche genetic algorithm performs immensely well in increasing the convergence rate, enhancing global search ability and improving the quality of solutions. The niche genetic algorithm is primarily implemented through the mechanism of preselection, crowding and sharing.

Among them, the limited competitive niche genetic algorithm based on the mechanism of sharing limits the competition among design plans having different shape, structure and characteristics, which is suitable for the optimization of the shape or structure of electromagnetic equipments.

5.5.2.3 Fuzzy Niche Genetic Algorithm

It is known that both the crossover probability P_c and the mutation probability P_m affect the convergence rate and the quality of the optimal solution for the niche genetic algorithm. Generally, P_c and P_m are fixed, and cannot adapt to the varied actual situation, which results in the low efficiency of solving such computationally complex multivariable optimization problems as motor optimization for niche genetic algorithm. If P_c and P_m are adaptive, then the convergence rate can be improved. It is complex to determine the optimal values of P_c and P_m online since many factors should be considered and the exact expression is difficult to acquire. In order to handle the fuzzy information of the rules better, fuzzy control is utilized to determine P_c and P_m. Making use of previous knowledge and experience, utilizing fuzzy reasoning method, and considering the actual situation in evolution, a fuzzy controller refines

the crossover probability and mutation probability dynamically, then a fuzzy control table containing the variation of crossover probability and mutation probability is produced. Finally, the defuzzification is implemented based on the maximum membership degree method and the crossover probability and mutation probability can be determined.

Fuzzy reasoning improves the optimization effect of the niche genetic algorithm greatly, which endows the novel algorithm with better robustness, global optimality and convergence rate.

5.5.3 Optimization Design of BLDC Motors

5.5.3.1 Optimization Model

The optimization of the motor can significantly improve the operating performance of the motor, reduce material consumption, shorten the design cycle and enhance the product quality, which plays an important role in increasing the ratio of performance to price of the motor. After a proper multiobjective optimal algorithm and related performance evaluation criteria are selected, the optimization model of the BLDC motor, including objective function, optimization variable and constraint condition, should also be determined.

In general, the cost and efficiency of BLDC motor or other performance indices are selected as objective functions. In this section, the optimization of the motor based on a fuzzy niche genetic algorithm is presented, which solves multiobjective optimization problems effectively. Therefore, besides the cost and efficiency of the motor, the optimization of the motor commutation torque ripple is considered.

A lot of parameters are involved in motor design, of which the ones that have great influence on objective functions are generally chosen as optimization variables, such as air gap δ, wire diameter of the winding d_l, winding turns per phase N_a, stator outer diameter D_1, stator inner diameter D_{i1}, stator iron core length L_1, alnico thickness h_m, pole arc coefficient α_p and stator tooth width b_t, etc.

And the optimization variables are given by

$$X = \left[\delta, d_l, N_a, D_1, D_{i1}, L_1, h_m, \alpha_p, b_t\right]^T \tag{5.67}$$

Inequality is the main form of the constraint condition in motor optimization, which can be categorized into performance constraint and general constraint. The former is decided by the technical performance indices, of which the power factor, efficiency, the starting current, the starting torque, maximum torque and heat load are commonly used, and plays the role of controlling those indices within the range that motor design requires. The latter consists of constraints apart from technical performance indices, including primarily constraints about slot space-factor, stator current density, stator tooth flux density, stator yoke flux density, rotor current density, rotor tooth flux density and rotor yoke flux density, and so on. The commonly used inequality constraints for the BLDC motor optimization are shown in Table 5.2.

In motor optimization, the constraint values should be determined properly according to different types of motor. The optimization will be encumbered with too strict constraint values and the limit function will fail likewise when confronted with too arbitrary constraint values.

Table 5.2 Constraint conditions

Indices	Constraint conditions	Indices	Constraint conditions
Stator tooth flux density	$B_{t1min} \leq B_{t1} \leq B_{t1max}$	Rated torque	$T_N \geqslant T_{Nmin}$
Stator yoke flux density	$B_{j1min} \leq B_{j1} \leq B_{j1max}$	Starting torque	$T_{st} \geqslant T_{stmin}$
Winding current density	$J_m \leq J_{mmax}$	Maximum torque	$T_m \geqslant T_{mmin}$
Starting current	$I_{st} \leq I_{stmax}$	Efficiency	$\eta \geqslant \eta_{min}$

Table 5.3 Optimization plans

Criteria	Plan I	Plan II	Plan III	Plan IV
Voltage (V)	36	36	36	36
Power (W)	150	150	150	150
Speed (r/min)	3620	3615	3618	3619
Efficiency (%)	79	78.1	80	77.3
Platform width of back-EMF (°)	96	115	110	105

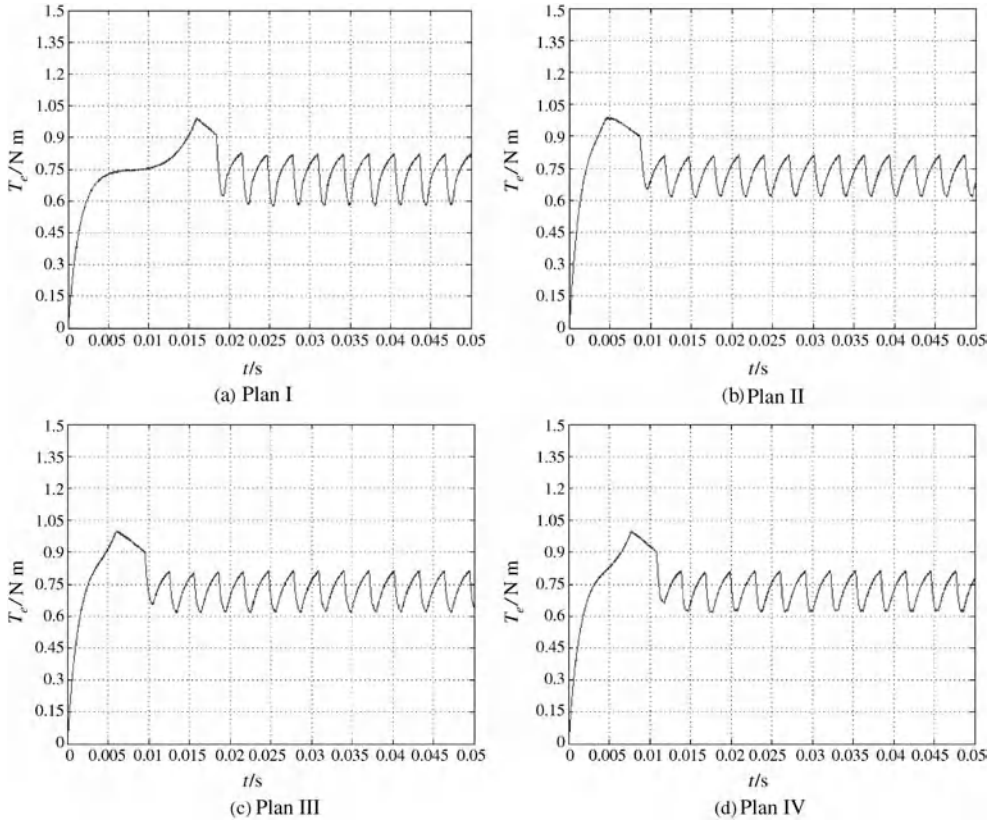


Figure 5.30 Simulation results of electromagnetic torque for all the optimization plans.

Note that the difference among constraint functions in the magnitude order is fairly large. In order to guarantee the same accuracy, normalization about the constraint conditions is required to achieve the same or similar magnitude order.

5.5.3.2 Design Cases

In this section, the optimization is implemented by using fuzzy niche genetic algorithm for a three-phase, Y-connected BLDC motor, and the parameters are given as: rated voltage: $U_N = 36$ V; rated power: $P_N = 150$ W; rated speed: $n_N = 3600$ r/min; efficiency: $\eta > 75\%$.

In accordance with the above parameters the optimization of the BLDC motor based on a fuzzy niche genetic algorithm is implemented, where the efficiency and torque ripple are chosen as the optimization objectives. The optimization schemes are shown in Table 5.3.

Figure 5.30 shows the simulated electromagnetic torque waveforms of the motor starting process corresponding to the four motor design schemes.

It is seen from the simulation results that at rated conditions, the four proposed schemes conform to the requirements of indices with different dynamic responses of torque during the starting process. Among those schemes, plan II (see Figure 5.30(b)) surpasses the others in torque performance for its faster rising speed of electromagnetic torque and smaller commutation torque ripple.

Questions

1. How many types of torque ripples are there in the BLDC motor and what are they?
2. How to minimize the cogging torque of the BLDC motor by using the methods of motor design?
3. What is the commutation torque ripple and how to reduce it?
4. What can affect the commutation torque ripple and how can they do this?
5. Give the principle of ADRC.
6. Draw the typical structure of a BP network.
7. How to calculate the platform width of the back-EMF waveform with different winding configurations?
8. Describe the principle and the characteristics of a fuzzy niche genetic algorithm.
9. List the main constraint conditions in motor optimization, including the performance constraint and the general constraint.

References

1. Jahans, T. M., Soong W. L. (1996) Pulsating torque minimization techniques for permanent magnet AC motor drives-a review. *IEEE Transactions on Industrial Electronics*, **43**(2), 321–330.
2. Islam R., Husain I., Fardoun A., McLaughlin K. (2009) Permanent-magnet synchronous motor magnet designs with skewing for torque ripple and cogging torque reduction. *IEEE Transactions on Industry Application*, **45**(1), 152–160.
3. Wu L. J., Jin W. B., Ni J., Ying J. P. (2007) A cogging torque reduction method for surface mounted permanent magnet motor. *Proceeding of International Conference on Electrical Machines and Systems*, *Seoul*, 769–773.

4. Ishikawa T., Slemon G. R. (1993) A method of reducing ripple torque in permanent magnet motors without skewing. *IEEE Transactions on Magnetics*, **29**(2), 2028–2031.
5. Zhu Z. Q. and Howe D. (2000) Influence of design parameters on cogging torque in permanent magnet motors. *IEEE Transaction on Energy Conversion*, **15**(4), 407–412.
6. Chen W.Study on torque ripple suppression technique of PM brushless DC motor. *Tianjin: Tianjin University PhD Thesis*, 2006 (in Chinese).
7. Xia C. L., Guo P. J., Shi T. N., *et al.* (2005) Control of brushless DC motor using genetic algorithm based fuzzy controller. *Proceedings of the CSEE*. **25**(11), 129–133 (in Chinese).
8. Xia C. L., Liu D., Wang Y. F., *et al.* (2007) Control of brushless DC motors using fuzzy set based immune feedback PID controller. *Transactions of China Electrotechnical Society*. **22**(9), 68–73 (in Chinese).
9. Shi T. N., Xu S. H., Xia C. L., *et al.* (2003) Fuzzy-PI dual-mode adaptive speed control for ultrasonic motors. *Transactions of China Electrotechnical Society*. **18**(3), 1–4 (in Chinese).
10. Guo P. J.Speed control of brushless DC motor using genetic algorithm based fuzzy controller. *Tianjin: Tianjin University Master Thesis*, 2005 (in Chinese).
11. Xia C. L., Fang H. W., Chen W., *et al.* (2006) Ant colony algorithm based fuzzy control for a brushless DC motor. *IEEE Proceedings of the World Congress on Intelligent Control and Automation*, China, 6498–6502.
12. Chen W., Xia C. L. (2006) Sensorless control of brushless DC motor based on fuzzy logic. *IEEE Proceedings of the World Congress on Intelligent Control and Automation*, China, 6298–6302.
13. Xia C. L., Li Z. J. (2005) Control system of brushless DC motor based on active-disturbance rejection controller. *Proceedings of the CSEE*. **25**(2), 82–86 (in Chinese).
14. Xia C. L., Song Z. F. (2007) Pitch control of variable speed constant frequency wind turbines based on active-disturbance-rejection controller. *Proceedings of the CSEE*. **27**(14), 91–95 (in Chinese).
15. Li Z. J.Control of brushless DC motor based on active-disturbance rejection controller. *Tianjin: Tianjin University Master Thesis*, 2004.
16. Xia C. L., Song Z. F. (2007) Rotor current control of doubly-fed induction generator based on active-disturbance-rejection controller. *Advanced Technology of Electrical Engineering and Energy*. **26**(3), 11–14, 19 (in Chinese).
17. Song Z. F.Active-disturbance-rejection control of variable speed constant frequency wind turbines using doubly-fed induction generator. *Tianjin: Tianjin University Master Thesis*, 2006 (in Chinese).
18. Xia C. L., Yu W., Li Z. Q. (2006) Torque ripple reduction of PM brushless DC motors based on auto-disturbance-rejection controller. *Proceedings of the CSEE*. **26**(24), 137–142 (in Chinese).
19. Yan P. F., Zhang C. S. (2000) *Artificial Neural Network and Simulated Evolutionary Computation*. Tsinghua University Press, Beijing (in Chinese).
20. Xia C. L., Wen D., Wang J. (2002) A new approach of minimizing commutation torque ripple for brushless DC motor based on adaptive ANN. *Proceedings of the CSEE*. **22**(1), 54–58 (in Chinese).
21. Xiu J., Xia C. L. (2007) GA-based adaptive fuzzy logic controller for switched reluctance motor. *Transactions of China Electrotechnical Society*. **22**(11), 69–73 (in Chinese).
22. Chen W.Rotor Position detection and model reference adaptive control based on Kalman method for brushless DC motor. *Tianjin: Tianjin University Master Thesis*, 2003 (in Chinese).
23. Xia C. L., Li Z. Q., Wang M. C., *et al.* (2005) Single neuron PID model reference adaptive control for PM brushless DC motors based on RBF neural network on-line identification. *Transactions of China Electrotechnical Society*. **20**(11), 65–69 (in Chinese).

6

Sensorless Control for BLDC Motor Drives

Many researches and preliminary achievements have been made for position-sensorless control, which is always an important issue of BLDC motor drives. When operating under sensorless conditions, BLDC motors have some advantages like high reliability and anti-disturbance capability. Meanwhile, to some extent, they can overcome the commutation torque ripples caused by inaccurate installation of position sensors. In this chapter, various rotor-position-detection methods for BLDC motor are presented. Taking the three-phase Y-connected BLDC motor with 120° electrical angle between each phase for example, position-sensorless controls based on modern control theories and artificial intelligence algorithms are investigated. Different means of the starting operation and ways to widen the speed range are proposed.

6.1 Principle of Sensorless Position Detection

Nowadays, position sensors used in BLDC motor drives are mainly electromagnetic types, photoelectric types and magnetic-sensing types. However, in some specific occasions, the applications of a BLDC motor are limited by the existence of position sensors. This can be mainly reflected in the following aspects:

(1) Position sensors may increase the volume of the system.
(2) Extra wiring between motor and control unit would be required, which causes the system to be easily interfered with.
(3) Under certain conditions, such as high temperature, high pressure, high humidity, and so on, position sensors work with poor sensitivity so that the system operates with low reliability.
(4) Position sensors have a high precision demand for installation, as inaccurate commutation caused by deviation of mechanical mounting will directly affect the operating performance of the motor.

Permanent Magnet Brushless DC Motor Drives and Controls, First Edition. Chang-liang Xia.
© 2012 Science Press. Published 2012 by John Wiley & Sons Singapore Pte. Ltd.

Therefore, sensorless control technology has received more and more attention. Furthermore, with the improvement of microcontrollers and the development of detection means and control technologies, sensorless control technology has been rapidly developed. Some of these technologies have been put into practice. According to different detection principles, the sensorless control methods for BLDC motor drives mainly include the back electromotive force (back-EMF)-based method, the flux-linkage-based method, the inductance-based method, and the artificial-intelligence-based method, etc.

6.1.1 Back-EMF-Based Method

Among all of the sensorless control methods, the back-EMF-based method is the most mature and widely used one at present. In this method, the zero-crossing points of back-EMFs are detected and made 30° electrical angle lag to get six discrete rotor-position signals in each electrical cycle, from which commutation information is obtained by the logical switch circuit, and then the sensorless operation is implemented.

The relationship between zero-crossing points of the back-EMF and the commutation instants is shown as Figure 6.1. In the figure, e_A, e_B, e_C are trapezoidal waves of three-phase back-EMFs. They are phase-separated by 120° as shown in Figure 6.1. Q_1, Q_2, ... and Q_6 are the commutation instants lagging the corresponding zero-crossing points of the back-EMF 30° electrical angle in the same period.

Nowadays, the challenge to the back-EMF-based estimation method is how to detect its zero-crossing point accurately. Many scholars have made a thorough study and various detection methods such as the terminal voltage sensing method, the back-EMF integration

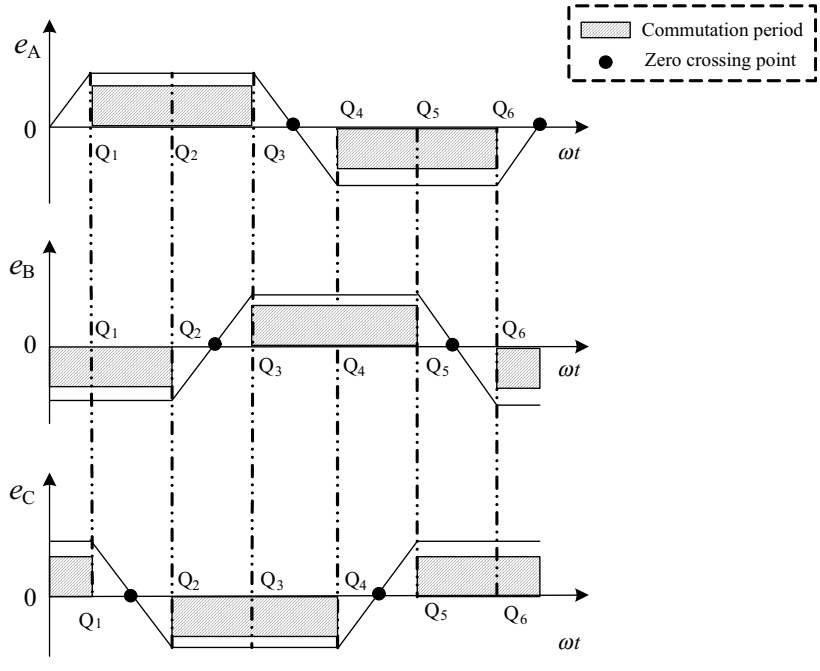


Figure 6.1 Relationship between zero-crossing points and commutation instants.

method, the third-harmonic back-EMF method, the freewheeling diode method and the line back-EMF method have been proposed.

6.1.1.1 Terminal Voltage Sensing

By detecting the terminal voltage of nonexcited phase winding, the zero crossings of the back-EMFs can be obtained with software programming or hardware circuit. Then this method can control the BLDC motor commutate properly. The means of how to get zero crossings of back-EMFs by using software programming is described as follows.

The mathematic model of BLDCM can be written as

$$\begin{cases} u_{AG} = Ri_A + (L-M)\dfrac{di_A}{dt} + e_A + U_N \\ u_{BG} = Ri_B + (L-M)\dfrac{di_B}{dt} + e_B + U_N \\ u_{CG} = Ri_C + (L-M)\dfrac{di_C}{dt} + e_C + U_N \end{cases} \tag{6.1}$$

where u_{AG}, u_{BG}, u_{CG} are terminal voltages, U_N is the neutral point voltage, and L–M is the equivalent inductance of each winding.

To illustrate the principle of terminal voltage sensing, we can suppose that phases A and B are conducted while phase C is inactive, as shown in Figure 6.2. At this time, the back-EMFs of phase A and B are on the opposite flat parts of the trapezoidal wave, while that related to phase C is on the sloping part. Clearly, the latter will change with the rotor position. Then, the back-EMF and current relationships of phases A and B in the BLDC motor can be, respectively, represented as

$$e_A + e_B = 0 \tag{6.2}$$

and

$$i_A + i_B = 0 \tag{6.3}$$

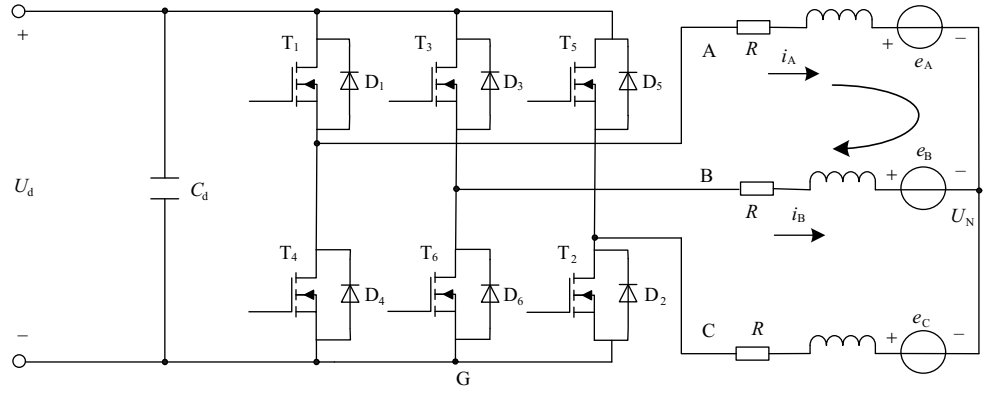


Figure 6.2 Current loop while phases A and B are conducted.

Adding the terminal voltages of phases A and B together, we can get

$$u_{AG} + u_{BG} = R(i_A + i_B) + (L - M)\left(\frac{di_A}{dt} + \frac{di_B}{dt}\right) + (e_A + e_B) + 2U_N \tag{6.4}$$

Then, substituting Equations (6.2) and (6.3) into Equation (6.4) yields

$$U_N = \frac{u_{AG} + u_{BG}}{2} \tag{6.5}$$

Since phase C is inactive, then $i_C = 0$ and $\frac{di_C}{dt} = 0$.
Thus, from Equation (6.1), we can get

$$e_C = u_{CG} - U_N = u_{CG} - \frac{u_{AG} + u_{BG}}{2} \tag{6.6}$$

Similarly, when phases A and C are conducted and phase B is inactive, we have

$$e_B = u_{BG} - \frac{u_{AG} + u_{CG}}{2} \tag{6.7}$$

and when phases B and C are conducted and phase A is inactive, we obtain

$$e_A = u_{AG} - \frac{u_{BG} + u_{CG}}{2} \tag{6.8}$$

It can be seen from Equations (6.6)–(6.8), six back-EMF zero-crossing signals in each cycle will be obtained from terminal voltages, where a 60° electrical angle exists in each two abutting signals. Hence, they can correctly provide commutation signals for the motor.

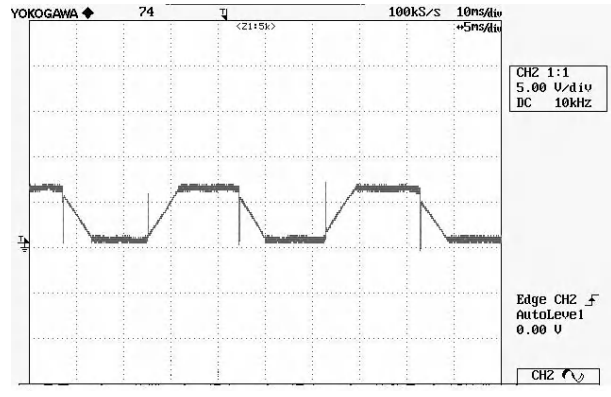
Commutation instants are decided by the electrical angles of back-EMF zero-crossing points delayed 30°. The angles can be achieved based on the interval of the previous two zero-crossing points as

$$\begin{cases} T(k-1) = Z(k-1) + \dfrac{1}{2}\Delta T \\ \Delta T = Z(k-1) - Z(k-2) \end{cases} \tag{6.9}$$

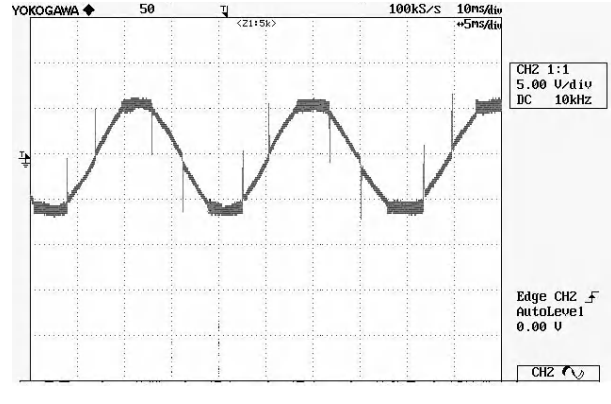
where $T(k-1)$ is the $(k-1)$th commutation instant, $Z(k-1)$ is the moment of the $(k-1)$th zero-crossing point, and $Z(k-2)$ is the moment of the $(k-2)$th zero-crossing point. (Note that the change of speed in the interval is neglected here.)

It is worth noting that each phase winding has two back-EMF zero-crossing points in an electrical cycle. Therefore, we must distinguish them according to the reversals in polarity after the back-EMF zero-crossing point or the conducting state of the windings. In addition, the capacitor used in the terminal voltage detection circuit for voltage regulating and filtering will cause the terminal voltage phase to shift. Thus, phase compensation should be performed in a software algorithm according to the parameters of the hardware circuit.

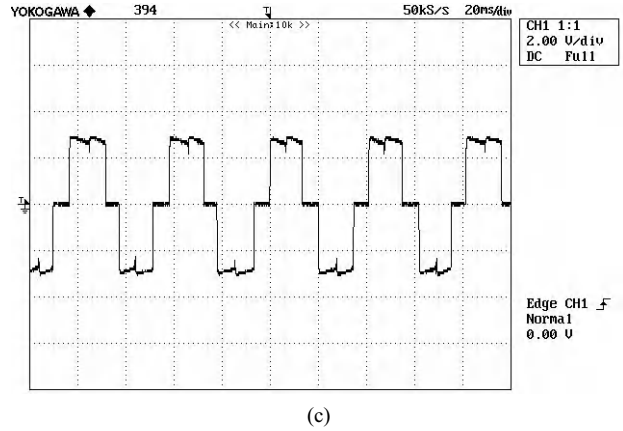
BLDC motors will run reliably within a certain speed range when the terminal voltage sensing method is adopted. Figure 6.3 shows the experimental waveforms of phase voltage, line voltage and phase current.



(a)



(b)



(c)

Figure 6.3 Experimental waveforms with the terminal voltage detection method: (a) the phase voltage waveform, (b) the line voltage waveform, (c) the phase current waveform.

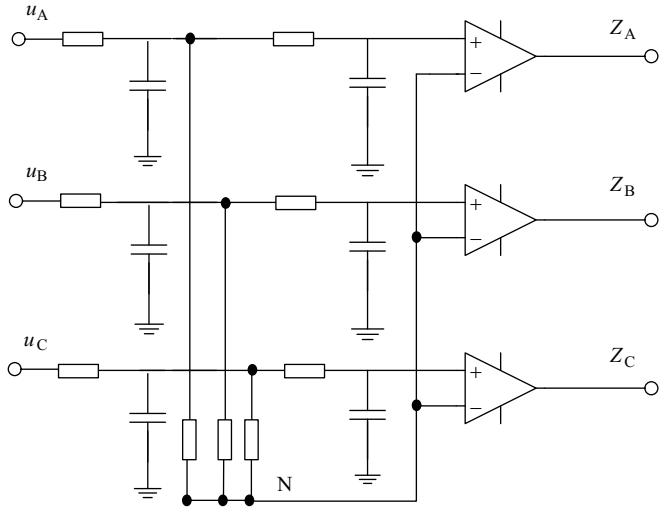


Figure 6.4 Back-EMF zero-crossing point detector.

The back-EMF zero crossing signals in the terminal voltage sensing method can be calculated not only by software but also from a hardware circuit. Figure 6.4 shows a typical hardware for terminal voltage sensing.

As depicted in Figure 6.4, the filtered terminal voltage signals are input into the comparators. Meanwhile, a virtual neutral point is constructed by using a symmetrical Y-connection resistive load. If the back-EMF of the nonexcited phase is equal to zero, the corresponding terminal voltage for this phase will be equal to the neutral voltage. That is, if phase C is inactive, u_{CG} will be equal to U_N while $e_C = 0$. Therefore, back-EMF zero crossing signals will be gained if we compare the output signals of filters with virtual neutral point signals as shown in Figure 6.4.

6.1.1.2 The Back-EMF Integration Method

The back-EMF integration method compares the integration of the inactive phase back-EMF with the threshold. It is the commutation instant of this phase when the integration of the back-EMF reaches the threshold. The relationship between the signals of back-EMF integration and the commutation instants is shown in Figure 6.5.

In Figure 6.5, the back-EMF varies approximately linearly. Then, the function of the sloping part can be represented as

$$e(t) = \pm E_0 t \tag{6.10}$$

When the back-EMF in the nonexcited phase crosses zero, the integrator begins to work. In this case we have

$$U_{out} = \left| \int_0^t \frac{e(t)}{k} \mathrm{d}t \right| = \left| \frac{E_0 t^2}{2k} \right| \tag{6.11}$$

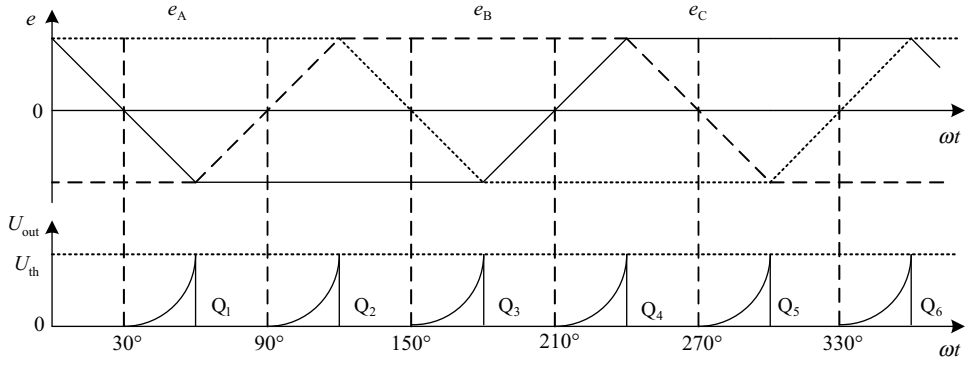


Figure 6.5 Relationship between the back-EMF integration signal and the commutation instant.

where E_0 is the gradient of the sloping-part for back-EMF, U_{out} is the output voltage of the integrator, and K is the gain constant of the integrator.

When the output voltage of the integrator U_{out} is equal to the threshold U_{th}, the integrator stops working, and outputs the commutation signals. The integrator will not restart working until the next back-EMF crosses zero. In the control system, the commutation instant lags the zero-crossing point of the back-EMF with a 30° electrical angle. Thus, at the phase commutation instant, Equation (6.11) can be rewritten as

$$U_{\text{out}} = \left|\frac{1}{2k} \cdot \frac{K_{\text{e}}\omega}{t} \cdot t^2\right| = \left|\frac{1}{2k} K_{\text{e}}\omega t\right| = \left|\frac{1}{2k} \cdot K_{\text{e}} \cdot \frac{\pi}{6}\right| = U_{\text{th}} \tag{6.12}$$

where U_{th} is the threshold, K_{e} is the coefficient of the back-EMF.

To apply the back-EMF integration method, first, U_{th} should be calculated according to Equation (6.12). Then, the control system makes a real-time comparison between U_{out} and U_{th} to determine the commutation instant. The advantages of this method are as follows: rotor speed information is not necessary during the control process; lagging or leading commutation of the motors could be done by regulating the threshold; and also it is insensitive to the switch signal. The disadvantage is that there exist integration accumulated errors and threshold setup problems.

6.1.1.3 The Third-Harmonic Back-EMF Method

The third harmonic of the back-EMF is used in this method to decide the commutation instant of the BLDC motor. Above all, Fourier decomposition is applied to the back-EMF in three-phase windings. Then, multiple harmonics, including the fundamental and a series of odd harmonics, are obtained. So, the back-EMF can be given by

$$\begin{cases} e_{\text{A}} = E_1 \sin\theta + E_3 \sin 3\theta + E_5 \sin 5\theta + \ldots\ldots \\ e_{\text{B}} = E_1 \sin\left(\theta - \dfrac{2\pi}{3}\right) + E_3 \sin 3\left(\theta - \dfrac{2\pi}{3}\right) + E_5 \sin 5\left(\theta - \dfrac{2\pi}{3}\right) + \ldots\ldots \\ e_{\text{C}} = E_1 \sin\left(\theta - \dfrac{4\pi}{3}\right) + E_3 \sin 3\left(\theta - \dfrac{4\pi}{3}\right) + E_5 \sin 5\left(\theta - \dfrac{4\pi}{3}\right) + \ldots\ldots \end{cases} \tag{6.13}$$

where θ is the electrical angle of the rotor.

By adding the three-phase back-EMF in Equation (6.13), we can get

$$e_A + e_B + e_C = 3E_3 \sin 3\theta + 3E_9 \sin 9\theta + E_{15} \sin 15\theta + \ldots\ldots \approx 3E_3 \sin 3\theta \tag{6.14}$$

It is obvious that the phase voltage equations of a BLDC motor can be written as

$$\begin{cases} u_A = Ri_A + (L-M)\dfrac{di_A}{dt} + e_A \\ u_B = Ri_B + (L-M)\dfrac{di_B}{dt} + e_B \\ u_C = Ri_C + (L-M)\dfrac{di_C}{dt} + e_C \end{cases} \tag{6.15}$$

And note that the sum of three phase currents is zero, i.e.

$$i_A + i_B + i_C = 0 \tag{6.16}$$

Hence, by adding the three phase voltages in Equation (6.15), we obtain

$$\begin{aligned} u_{sum} &= u_A + u_B + u_C \\ &= \left(R + (L-M)\frac{d}{dt}\right)(i_A + i_B + i_C) + (e_A + e_B + e_C) \\ &= e_A + e_B + e_C \approx 3E_3 \sin 3\theta \end{aligned} \tag{6.17}$$

After integrating, the third harmonic flux is given by

$$\psi_{3rd} = \int u_{sum} dt \tag{6.18}$$

Accordingly, u_{sum}, the sum of three phase voltages, contains information of the third-harmonic components for the phase back-EMF. The third-harmonic flux linkage can be obtained by integrating the u_{sum}, whose zero-crossing point is exactly the commutation instant. This can be illustrated as Figure 6.6.

To sum up, through software programming, the third-harmonic flux can be obtained from the three phase voltages u_A, u_B and u_C. The zero-crossing point of the third-harmonic flux is exactly the commutation instant. Compared with the terminal voltage detection method, the third harmonic back-EMF method has the following advantages such as wider range of speed, smaller delay of the phase, and so on. However, due to the continuous accumulation of noise signal at low speed, errors will be made during the integration process, which will cause inaccurate commutation.

6.1.1.4 The Freewheeling Diode Method

The freewheeling diode method is also known as the third-phase conducted method, in which the rotor position is determined by detecting the switching condition of the freewheeling diode, which is reversely paralleled with bridge inverter. To illustrate the freewheeling diode method, an example is taken when phases A and B are conducted and phase C is inactive.

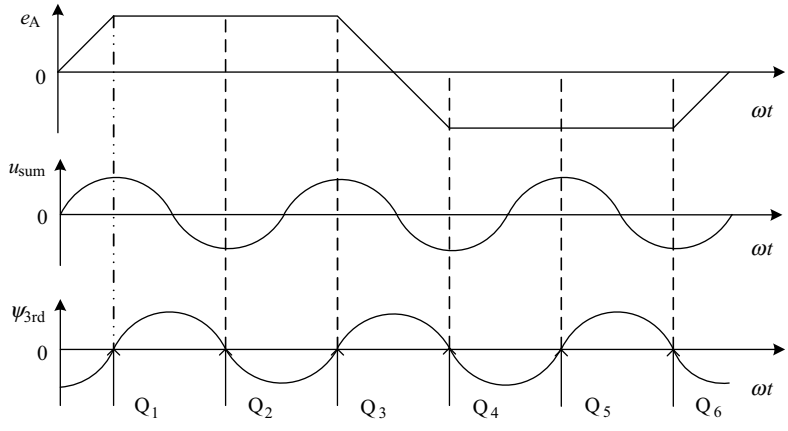


Figure 6.6 Relationship among commutation time, back-EMF harmonic and flux linkage.

The pulsewidth modulation implemented in the inverter is shown in Figure 6.7.

From the modulation shown in Figure 6.7, it is known that the power switch T_1 on the upper half-bridge of phase A is operating at the PWM chopping mode when phases A and B are conducted, with the power switch T_6 on the lower half-bridge of phase B conducted. This is shown as the dark zone in Figure 6.7. During the modulation, when T_1 is off, the freewheeling diode D_4 will be conducted. In such a case, the operating condition of the inverter is shown in Figure 6.8.

From Figure 6.8, it is known that when T_1 is off, current will flow through the freewheeling diode D_4. Then T_6 and diode D_4 compose a conducting circuit. Accordingly, u_{CG}, the terminal voltage of the nonexcited phase, is represented as

$$\begin{aligned} u_{CG} &= e_C + U_N \\ &= e_C + \frac{V_{CE} - V_D}{2} - \frac{e_A + e_B}{2} \end{aligned} \tag{6.19}$$

where V_{CE} is the forward voltage drop of the power switch, V_D is the forward voltage drop of the diode.

To conduct the freewheeling diode D_2, we must have

$$u_{CG} < -V_D \tag{6.20}$$

Substituting Equation (6.19) into Equation (6.20), we obtain

$$e_C - \frac{e_A + e_B}{2} < -\frac{V_{CE} + V_D}{2} \tag{6.21}$$

When the back-EMF e_C in the nonexcited phase approaches zero, the equation $e_A + e_B = 0$ holds, thus

$$e_C < -\frac{V_{CE} + V_D}{2} \tag{6.22}$$

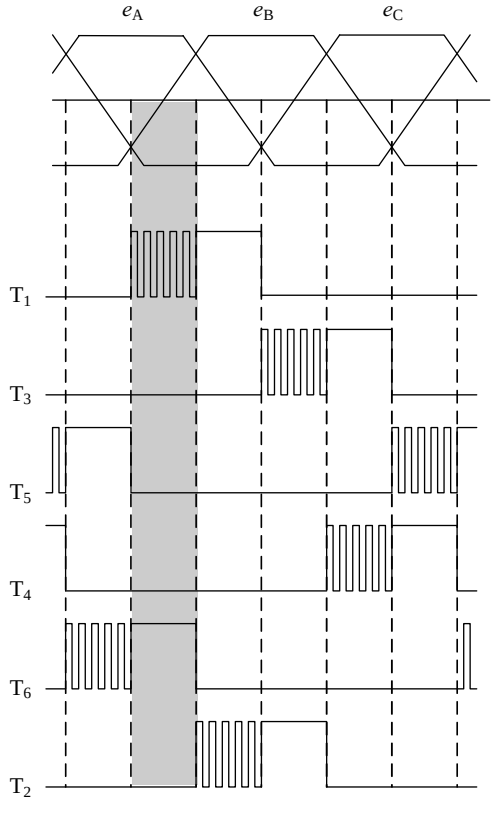


Figure 6.7 PWM waveforms.

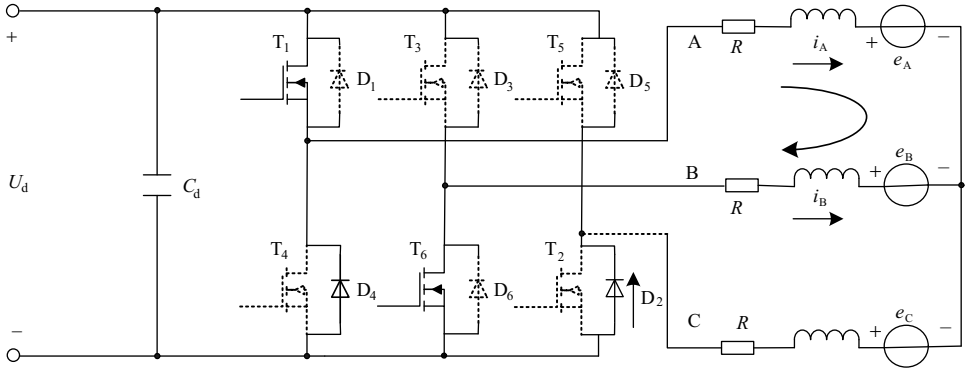


Figure 6.8 Diagram for current flow in freewheeling diode.

In general, V_{CE} and V_D are quite small compared with the back-EMF. When the back-EMF e_C becomes negative, a current will flow through the freewheeling diode D_2 in the nonexcited phase. In this condition, the negative point can be approximately considered as a zero-crossing point of the back-EMF. Therefore, the position of the rotor can be determined by detecting the switch state of the freewheeling diode.

The freewheeling diode method is realized by detecting the zero-crossing point of the back-EMF from currents that flow through the freewheeling diodes. Using this method, high sensibility and wider speed range can be obtained in the sensorless control for BLDC motor drives. Figure 6.9 shows the principle of the detection circuit. The disadvantage of this detection circuit is that six independent sources are needed in the additional detection circuit. Thus, the detection circuit is a little complicated.

6.1.1.5 Line Back-EMF Method

In the phase back-EMF based sensorless control for BLDC motor drives, the commutation instants of the windings are acquired through shifting of 30° for the zero-crossing points of the phase back-EMF in electrical angle. Note that the phase-shifting angle is closely related to the instantaneous speed of the motor. In the variable-speed control of BLDC motor drives, inaccuracy of commutation instants for the windings will occur in the sensorless control with phase back-EMF detection. In contrast with the phase back-EMF detection method, the calculation of phase-shifting angle is not necessary in the line back-EMF method. The commutation instants of the windings are decided directly through the zero-crossing points of the line back-EMF. Hence, this can effectively improve the commutation accuracy in speed control.

Figure 6.10 shows the relationship among the phase back-EMF, line back-EMF and the commutation instants.

Note in Figure 6.10 that the zero-crossing points of line back-EMFs are exactly the commutation instants of the BLDC motor. Thus, it is unnecessary to calculate the delay angle in the sensorless control with line back-EMF. So, by calculating the zero-crossing points of line back-EMFs e_{AB}, e_{BC} and e_{CA}, the six commutation signals can be obtained, which can ensure the reliable sensorless operation of the BLDC motor.

Compared with the phase back-EMF method, the line back-EMF method can be performed at lower speed more easily. Thus, it has a wider speed range of applications. In addition, there is

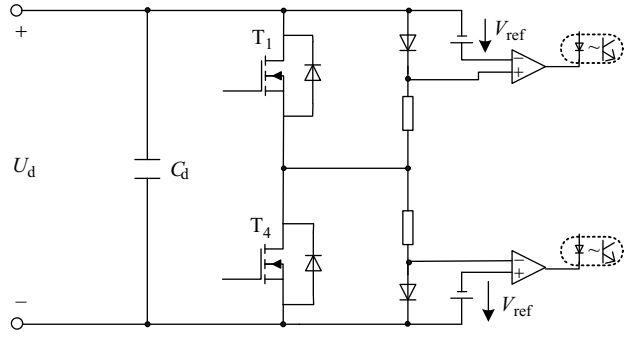


Figure 6.9 Detection circuit with the freewheeling diodes.

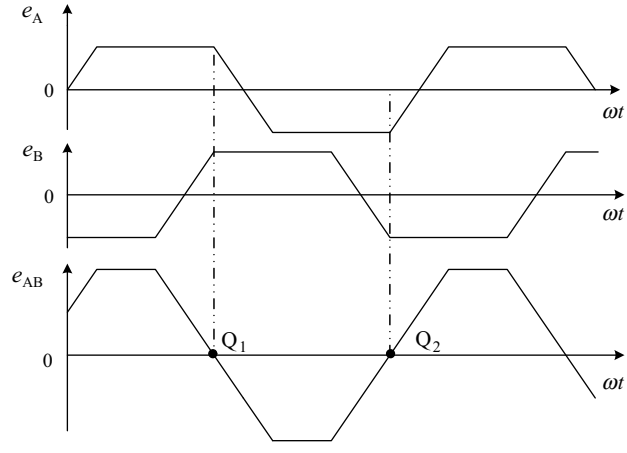


Figure 6.10 Relationship among phase back-EMF, line back-EMF and commutation instant.

no need to use the previous commutation instants for phase shifting in this sensorless control approach. The motor can operate in such a sensorless mode with only the zero-crossing points of line back-EMFs determined.

It can be seen from the above that the purpose of each back-EMF-based method is to achieve correct commutation for the windings by using the signals of rotor position, which can be acquired from the back-EMF signals of the windings. The distinct advantage of the back-EMF-based methods is its easy implementation.

6.1.2 Flux-Linkage-Based Method

The flux-linkage-based method, which is different from the back-EMF-based ones, can obtain the rotor position information by estimating the flux. Note the well-known motor voltage equation is

$$\boldsymbol{U} = \boldsymbol{RI} + \frac{\mathrm{d}\boldsymbol{\psi}}{\mathrm{d}t} \tag{6.23}$$

where $\boldsymbol{U}$ is the phase-voltage matrix, $\boldsymbol{I}$ is the phase current matrix, $\boldsymbol{R}$ is the phase winding resistance matrix, and Ψ is the matrix of flux linkage.

Hence, the flux linkage can be obtained by using the measured voltages and currents as

$$\boldsymbol{\psi} = \int_0^t (\boldsymbol{U} - \boldsymbol{RI})\,\mathrm{d}t \tag{6.24}$$

If the initial rotor position, motor parameters, and the relationship between rotor position and flux linkage are known, the rotor position can be determined by the flux in Equation (6.24). Figure 6.11 shows the principle diagram of the flux-linkage-based method.

When the motor is controlled by the flux-linkage-based method, the initial rotor position should be detected so that we can have the initial flux information required for the integral calculation.

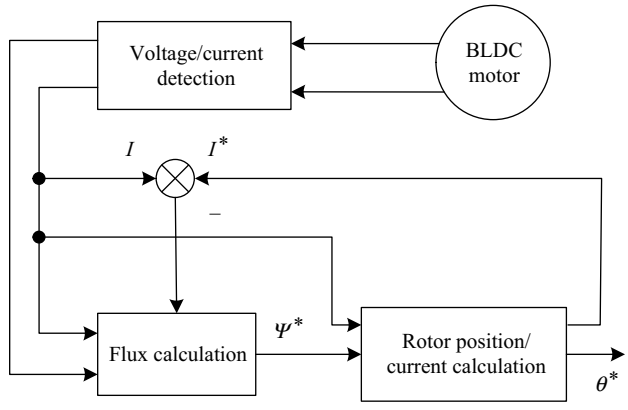


Figure 6.11 Principle of flux-linkage-based method.

Note that due to the large integral calculation of this method, an accumulative error may be produced when the motor is running at low speed. Moreover, this method is easily affected by the motor parameters.

6.1.3 Inductance-Based Method

Both the back-EMF-based method and the flux-linkage-based method determine the rotor position depending on the movement of the rotor magnetic field. As a result, neither of the two methods can provide the initial rotor position for the self-starting of the motor at standstill. In order to solve this problem, an inductance-based method is adopted to determine the rotor position at standstill. The basic principle of the inductance-based method is described as follows. Above all, the amplitude of the current, which is generated by injecting specific square-wave voltage pulse into the winding, is measured. Then, the difference between the inductances is obtained by comparing the amplitude of the currents. Thus, we can determine the rotor position.

The total flux of each phase consists of the flux linkage of the rotor permanent magnet and that generated by the stator winding current, namely

$$\psi_{\text{sum}} = \psi_{\text{rotor}} + L'i \tag{6.25}$$

where ψ_{sum} is the total flux of each phase, ψ_{rotor} denotes the flux of rotor permanent magnet, and $L' = L - M$.

When current pulse i^+ or i^- is injected into the stator winding, different inductances, L'_+ and L'_-, are generated. Note that the direction of i^+ or i^- is the same as or counter to that of the magnetic field. Hence, L'_+ and L'_- can be written as

$$\begin{cases} L'_+ = \dfrac{\psi_{\text{sum}} - \psi_{\text{rotor}}}{i^+} = \dfrac{\Delta\psi^+}{i^+} \\ L'_- = \dfrac{\psi_{\text{sum}} - \psi_{\text{rotor}}}{i^-} = \dfrac{\Delta\psi^-}{i^-} \end{cases} \tag{6.26}$$

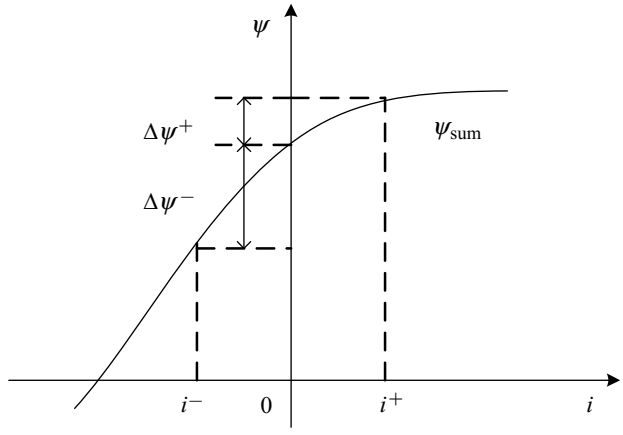


Figure 6.12 Relationship between current and flux.

Since the saturation effect of the stator core is taken into account, the flux will change while injecting current pulses with different directions. Figure 6.12 shows the relationship between the current and the flux linkage.

As shown in Figure 6.12, the flux change $\Delta\psi^+$ produced by i^+ is less than that produced by i^-, that is, $L'_+ < L'_-$. The nonlinear inductance L' is determined both by the magnetic pole's position and the stator winding's current. Therefore, we can get the difference between the inductances by detecting the current pulses, and then determine the rotor position. The current response with different inductances is discussed as follows.

Since the dynamic equation shown in Equation (6.15) can be simplified as

$$u_{\mathrm{x}} = Ri_{\mathrm{x}} + L'\frac{\mathrm{d}i_{\mathrm{x}}}{\mathrm{d}t} + e_{\mathrm{x}} \quad x = \mathrm{A}, \mathrm{B}, \mathrm{C} \tag{6.27}$$

in which, when the rotor stands still, the back-EMF $e_x = 0$.

Consequently, we obtain

$$i_{\mathrm{x}} = \frac{u_{\mathrm{x}}}{R}\left(1 - e^{-\frac{R}{L'}t}\right) \tag{6.28}$$

Hence, the current response, shown in Figure 6.13, will vary with different inductances.

Figure 6.13 shows that the response of the current i^+ is faster due to $L'_+ < L'_-$. Therefore, by detecting the positive and negative phase currents in an appropriate time interval, the differences in inductances can be determined. Thus, the rotor position is determined according to the relationship between the inductance and rotor position.

The inductance-based method is well suited for the rotor initial position detection at standstill. However, because the difference between the inductances is small with different rotor positions, this method relies on high-precision current sensing.

6.1.4 Intelligence-Based Method

It is well known that an artificial intelligence algorithm has strong adaptability and good self-learning ability. Meanwhile, it is very suitable to be applied in sensorless control for a

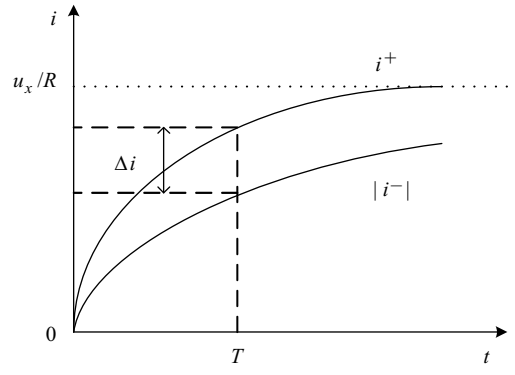


Figure 6.13 Current responses with different inductances.

BLDC motor. The basic principle of rotor-position detection based on an artificial intelligence algorithm is described as follows. Above all, the relationship is established between voltage, current and rotor position of the BLDC motor with the help of such theories as artificial neural networks, fuzzy strategy, genetic algorithms, adaptive artificial immune algorithms, etc. Then, the rotor position or commutation signals for sensorless control are acquired through the measured motor voltage and current signals. In this condition, an accurate mathematic model of BLDC motor is not necessary. Thus, the artificial-intelligence-based method is suitable for a nonlinear electrical machine control system, in which the generalization will be improved. Furthermore, this method has fairly strong robustness to parameter variation and noise measurement. Thus, it is capable of solving some complex problems that conventional and other modern control methods would not be able to deal with. In such cases, the performance of motor control will be enhanced. The advent of high-efficiency MCU and DSP has provided more development opportunity for this method.

The rotor-position-detection methods, including the back-EMF-based method, the flux-linkage-based method, the inductance-based method and the artificial-intelligence-based method, all have their own limitations. So, these control methods should be chosen properly according to different requirements and applications.

6.2 Sensorless Control Strategy

6.2.1 Sensorless Control Based on Disturbance Observer

In modern control theories, the design of controllers can be formulated as an integration design of a state feedback controller and a state observer. This approach offers a solution for the design of a closed-loop system and performance improvement of the entire system. In the design of a state feedback controller, the state variables are needed. In practice, some of these state variables cannot be measured directly. Hence, the state observation or state reconstruction are put forth to solve this problem.

According to the mathematical model of a BLDC motor, the voltage equation will be transformed from nonlinear to linear if the back-EMF is assumed to be a constant disturbance. Thus, the zero-crossing point of back-EMF can be acquired through a disturbance observer, which is designed by using linear observer theory [1–3].

6.2.1.1 Design of Full-State Observer

Obviously, Equation (6.15) can be rewritten in the form of single phase as

$$\frac{\mathrm{d}i_{\mathrm{x}}}{\mathrm{d}t} = a_{11}i_{\mathrm{x}} + a_{12}e_{\mathrm{x}} + b_1u_{\mathrm{x}} \quad x = \mathrm{A},\mathrm{B},\mathrm{C} \tag{6.29}$$

where $a_{11} = -\frac{R}{L-M}$, $a_{12} = -\frac{1}{L-M}$, and $b_1 = \frac{1}{L-M}$.

In order to simplify the design of the observer, the back-EMF in Equation (6.29) is assumed to be a constant disturbance, namely $\dot{e}_x = 0$. Thus, the state variable model of the BLDC motor is

$$\begin{bmatrix} \dot{i}_x \\ \dot{e}_x \end{bmatrix} = \begin{bmatrix} a_{11} & a_{12} \\ 0 & 0 \end{bmatrix} \begin{bmatrix} i_{\mathrm{x}} \\ e_{\mathrm{x}} \end{bmatrix} + \begin{bmatrix} b_1 \\ 0 \end{bmatrix} u_{\mathrm{x}} \tag{6.30}$$

$$y = \begin{bmatrix} 1 & 0 \end{bmatrix} \begin{bmatrix} i_{\mathrm{x}} \\ e_{\mathrm{x}} \end{bmatrix} \tag{6.31}$$

in which, phase voltage u_{x} is the input variable, current i_{x} is the output variable, and back-EMF e_{x} is imposed on the system as a disturbance. The corresponding system diagram is shown in Figure 6.14. It can be verified that the system is completely observable so that an observer can be designed to observe the disturbance e.

Since the system expressed as Equations (6.30) and (6.31) is completely observable, the full-order state observer can be designed as

$$\frac{\mathrm{d}}{\mathrm{d}t} \begin{bmatrix} \hat{i}_x \\ \hat{e}_x \end{bmatrix} = \begin{bmatrix} a_{11} & a_{12} \\ 0 & 0 \end{bmatrix} \begin{bmatrix} \hat{i}_x \\ \hat{e}_x \end{bmatrix} + \begin{bmatrix} b_1 \\ 0 \end{bmatrix} u_{\mathrm{x}} + \begin{bmatrix} g_1 \\ g_2 \end{bmatrix} \left(y - \begin{bmatrix} 1 & 0 \end{bmatrix} \begin{bmatrix} \hat{i}_x \\ \hat{e}_x \end{bmatrix} \right) \tag{6.32}$$

$$\begin{cases} \hat{i}_x(0) = 0 \\ \hat{e}_x(0) = 0 \end{cases} \tag{6.33}$$

where g_1 and g_2 are the feedback gain parameters of the full-state observer.

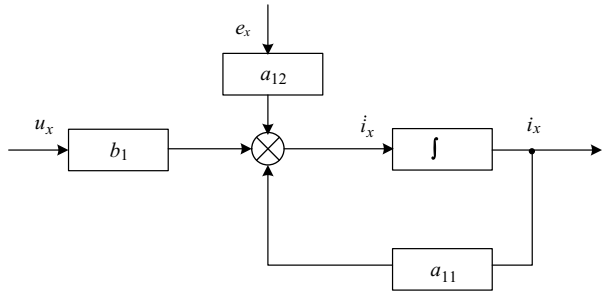


Figure 6.14 The diagram of the BLDC motor.

Equation (6.32) can be rearranged as

$$\frac{\mathrm{d}}{\mathrm{d}t}\begin{bmatrix}\hat{i}_x\\ \hat{e}_x\end{bmatrix}=\begin{bmatrix}a_{11}-g_1 & a_{12}\\ -g_2 & 0\end{bmatrix}\begin{bmatrix}\hat{i}_x\\ \hat{e}_x\end{bmatrix}+\begin{bmatrix}b_1\\ 0\end{bmatrix}u_{\mathrm{x}}+\begin{bmatrix}g_1\\ g_2\end{bmatrix}y \tag{6.34}$$

Solving Equation (6.34), we have

$$\frac{\mathrm{d}\hat{e}_x}{\mathrm{d}t}=g_2(i_{\mathrm{x}}-\hat{i}_x) \tag{6.35}$$

Thus, the error equation of the observer is

$$\frac{\mathrm{d}}{\mathrm{d}t}\begin{bmatrix}\varepsilon_1\\ \varepsilon_2\end{bmatrix}=\begin{bmatrix}a_{11}-g_1 & a_{12}\\ -g_2 & 0\end{bmatrix}\begin{bmatrix}\varepsilon_1\\ \varepsilon_2\end{bmatrix} \tag{6.36}$$

$$\begin{bmatrix}\varepsilon_1\\ \varepsilon_2\end{bmatrix}=\begin{bmatrix}i_{\mathrm{x}}-\hat{i}_x\\ e_{\mathrm{x}}-\hat{e}_x\end{bmatrix} \tag{6.37}$$

From above, the full-state observer can be constructed as shown in Figure 6.15.

6.2.1.2 Pole Placement for the Full-State Observer

The eigenvalue polynomial of the full-state observer is

$$f(s)=\det\begin{bmatrix}s-(a_{11}-g_1) & -a_{12}\\ g_2 & s\end{bmatrix}=s^2-(a_{11}-g_1)s+a_{12}g_2 \tag{6.38}$$

Suppose the expected poles are p_1 and p_2, we obtain the expected eigenvalue polynomial

$$f^*(s)=(s-p_1)(s-p_2)=s^2-(p_1+p_2)s+p_1p_2 \tag{6.39}$$

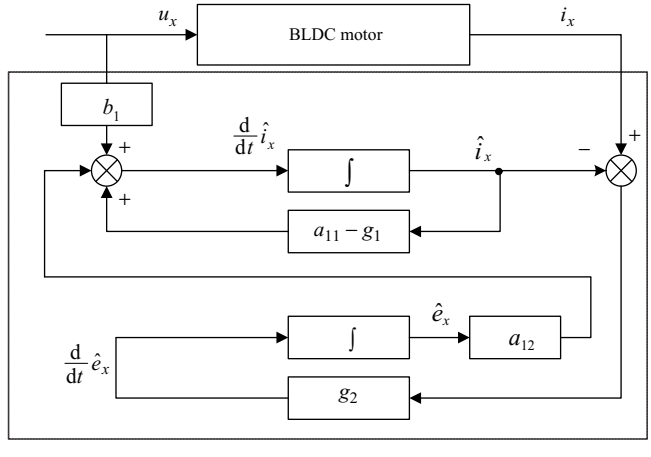


Figure 6.15 Diagram of the full-state observer.

Let the eigenvalue polynomial of the observer equal the expected eigenvalue polynomial, and then the coefficients of like powers of s on both sides are, respectively, equal. Thus, the feedback gains g_1 and g_2 can be acquired by solving the desired characteristic equation.

6.2.1.3 Design of Reduced-Order Observer

Based on the phase voltages and currents, the full-state observer can reconstruct the phase currents and the back-EMF. In practice, the phase currents can be obtained from current sensors directly. Thus, a reduced-order observer can be used to estimate the back-EMF.

The reduced-order observer can be designed in several steps. First, the system state equation should be decomposed according to the observable theory. Then, using a series of equivalent transformations, we obtain the state equation and the output equation, which have to be observed. Finally, the corresponding reduced-order observer is obtained according to the design methods of the full-state observer.

Let

$$z_{\mathrm{x}} = \dot{i}_x - a_{11} i_{\mathrm{x}} - b_1 u_{\mathrm{x}} \tag{6.40}$$

Then, by substituting Equation (6.40) into Equation (6.30), the state equation of a BLDC motor after equivalent transformation can be expressed as

$$\begin{bmatrix} z_{\mathrm{x}} \\ \dot{e}_x \end{bmatrix} = \begin{bmatrix} a_{12} e_{\mathrm{x}} \\ 0 \end{bmatrix} \tag{6.41}$$

Hence, the reduced-order observer can be designed as

$$\dot{e}_x = g(\hat{z}_x - z_{\mathrm{x}}) \tag{6.42}$$

where g is the feedback gain coefficient.

If the phase current (i_{x}) is detected directly, then $\hat{i}_x = i_{\mathrm{x}}$ holds. Hence, from Equation (6.40), we have

$$\hat{z}_x = \dot{\hat{i}}_x - a_{11} \hat{i}_x - b_1 u_{\mathrm{x}} = \dot{\hat{i}}_x - a_{11} i_{\mathrm{x}} - b_1 u_{\mathrm{x}} \tag{6.43}$$

Combining Equation (6.43) with Equations (6.40) and (6.42), we can obtain the state equations of the reduced-order observer as

$$\dot{e}_x = g(\dot{\hat{i}}_x - \dot{i}_x) \tag{6.44}$$

From Equation (6.30), we can get

$$\dot{i}_x = a_{11} i_{\mathrm{x}} + a_{12} e_{\mathrm{x}} + b_1 u_{\mathrm{x}} \tag{6.45}$$

Furthermore,

$$\dot{\hat{i}}_x = a_{11} \hat{i}_x + a_{12} \hat{e}_x + b_1 u_{\mathrm{x}} = a_{11} i_{\mathrm{x}} + a_{12} \hat{e}_x + b_1 u_{\mathrm{x}} \tag{6.46}$$

Thus, according to Equations (6.46) and (6.44), the state equations of the reduced-order observer are rewritten as

$$\dot{\hat{i}}_x = a_{11} i_x + a_{12} \hat{e}_x + b_1 u_x \tag{6.47}$$

$$\dot{e}_x = g(\dot{\hat{i}}_x - \dot{i}_x) \tag{6.48}$$

Equations (6.47) and (6.48) can also be written in vector form as

$$\dot{\hat{\boldsymbol{i}}} = \boldsymbol{A}_{11}\boldsymbol{i} + \boldsymbol{A}_{12}\hat{\boldsymbol{e}} + \boldsymbol{B}_1\boldsymbol{u} \tag{6.49}$$

$$\dot{\hat{\boldsymbol{e}}} = \boldsymbol{G}(\dot{\hat{\boldsymbol{i}}} - \dot{\boldsymbol{i}}) = \boldsymbol{A}_{11}\boldsymbol{G}\boldsymbol{i} + \boldsymbol{A}_{12}\boldsymbol{G}\hat{\boldsymbol{e}} + \boldsymbol{B}_1\boldsymbol{G}\boldsymbol{u} - \boldsymbol{G}\dot{\boldsymbol{i}} \tag{6.50}$$

where $\boldsymbol{A}_{11} = a_{11}\boldsymbol{I}$; $\boldsymbol{A}_{12} = a_{12}\boldsymbol{I}$; $\boldsymbol{B}_1 = b_1\boldsymbol{I}$; $\boldsymbol{G} = g\boldsymbol{I}$, $\boldsymbol{G}$ represents the feedback gain matrix of the observer.

Define the estimated error of the back-EMF as

$$\boldsymbol{\varepsilon} = \boldsymbol{e} - \hat{\boldsymbol{e}} \tag{6.51}$$

Then the estimated error equation of the observer becomes

$$\dot{\boldsymbol{\varepsilon}} = \dot{\boldsymbol{e}} - \dot{\hat{\boldsymbol{e}}} = \boldsymbol{A}_{12}\boldsymbol{G}(\boldsymbol{e} - \hat{\boldsymbol{e}}) = \boldsymbol{A}_{12}\boldsymbol{G}\boldsymbol{\varepsilon} = a_{12}g\boldsymbol{I}\boldsymbol{\varepsilon} \tag{6.52}$$

Let the pole of the observer satisfy

$$\alpha = a_{12}g \quad \alpha < 0 \tag{6.53}$$

To ensure the asymptotic stability of the observer, the feedback gain coefficient g is selected so that the poles of the observer are on the left side of the complex plane. Note that the convergence rate of the estimated error is proportional to the distance between the poles and the imaginary axis. But when the poles are too far from the imaginary axis, the bandwidth of the observer will be broadened. In such a case, the observer cannot suppress the disturbance and the noise effectively. Therefore, these factors should be considered in the procedure of pole placement.

In order to avoid the influence of the current differential item in the state equation, a new variable ξ is defined as

$$\boldsymbol{\xi} = \hat{\boldsymbol{e}} + \boldsymbol{G}\boldsymbol{i} \tag{6.54}$$

Hence,

$$\dot{\boldsymbol{\xi}} = \boldsymbol{A}_{12}\boldsymbol{G}\boldsymbol{\xi} + \boldsymbol{B}_1\boldsymbol{G}\boldsymbol{u} + \boldsymbol{G}(\boldsymbol{A}_{11} - \boldsymbol{A}_{12}\boldsymbol{G})\boldsymbol{i} \tag{6.55}$$

$$\hat{\boldsymbol{e}} = \boldsymbol{\xi} - \boldsymbol{G}\boldsymbol{i} \tag{6.56}$$

Thus, the disturbance observer can be designed successfully, whose scheme diagram is shown in Figure 6.16.

It can be seen from Figure 6.16 that there is a low-pass filter in the disturbance observer. It is used to filter the high-frequency noise that is caused by the phase commutation. The outputs of

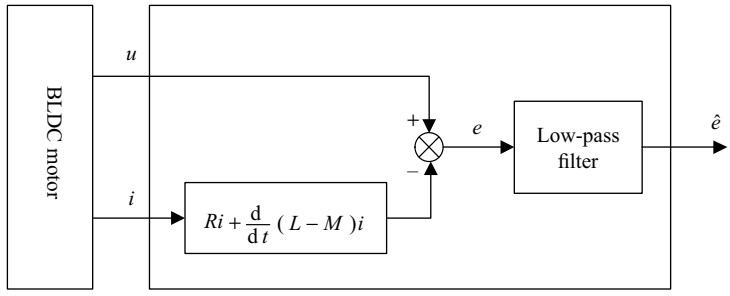


Figure 6.16 Scheme diagram of the disturbance observer.

the observer contain the information about the zero-crossing point of the back-EMF. In addition, the interference pulses, which are caused by the hypothesis that the back-EMF is a constant disturbance, are comprised in the outputs of the observer. Thus, it is necessary to take certain measures to eliminate the disturbances that are caused by these interference pulses.

6.2.1.4 The Elimination of Interference Pulses

1) **The cause of interference pulses**

Through the zero-crossing observation of the back-EMF, we can get the rotor position from the outputs of the comparator circuit. Now, the rotor-position signals are denoted as S_A, S_B and S_C. The waveforms of these signals are the same, while their phases are offset 120° from each other.

Usually, rotor-position signals S_A, S_B and S_C contain interference pulses. The causes of the interference pulses are described as follows. In practice, the waveform of the back-EMF is an irregular trapezoidal wave due to the influence of the slot effect and armature reaction. Moreover, during the design process of the reduced-order observer, the back-EMFs are assumed to be constants. This will result in an estimated error. Thus, the interference pulses are produced.

Therefore, the rotor-position signals not only contain the information about zero crossing of the back-EMF, but also have some interference pulses. The interference pulses should be eliminated from the position signals so that sensorless control is achieved.

2) **Principle of interference pulses elimination**

The basic principle of interference elimination is making logic transformation (i.e. delay, latch, logical operations, etc.) for the rotor-position signals so as to reshape the waveforms of the rotor-position signals. The process of the logic transformation is discussed as follows.

The first step is to obtain the gate signal of S_A by making an XNOR operation between the original S_C and the corresponding signal with appropriate delay on S_C. Afterwards, the width of a low-level pulse in the gate signal is regulated greater than the width of interference by adjusting the delay time of S_C. Thus, we can eliminate the interference pulses by controlling the gate signal of S_A. Note that when the gate signal goes high, S_A is conducted. On the contrary, when the gate signal is low, S_A will be latched. This process of signal logic transformation is illustrated in Figure 6.17.

In Figure 6.17, S_{CC} is the signal with a delay on S_C, $\overline{S_C \oplus S_{CC}}$ is the gate signal, $\overline{S_A}$ represents the rotor-position signal related to phase A after the interference pulses have been eliminated.

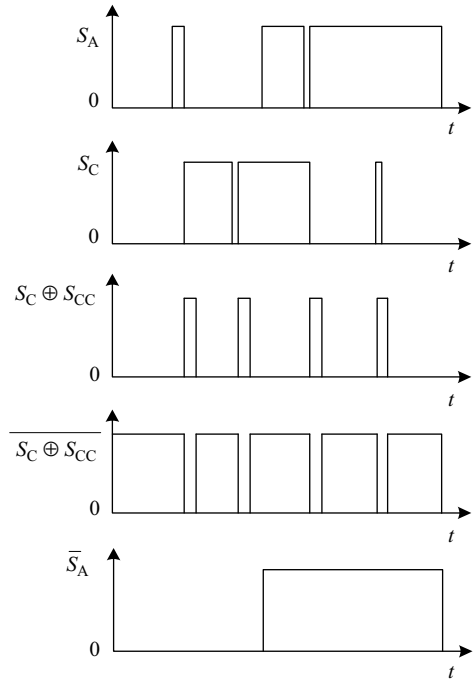


Figure 6.17 Curves for logic transformation signals.

Gate signals can be obtained from the transformation of three rotor-position signals. From above, we can obtain the strobe signal of S_A by logic transformation of S_C. Similarly, the gate signals of S_B and S_C can be, respectively, obtained from S_A and S_B. The two main roles of the gate signals are shown as follows.

(1) Determine the time to generate the interference pulses.

(2) From this moment, produce gate signals whose low-level width is greater than the width of interference pulses.

We can eliminate the interference pulses by certain logic transformations, such as delay, latch, and so on. Then, we will get the accurate zero-crossing information of the back-EMF. Figure 6.18 shows the waveforms of the actual Hall signal H_A and the observed rotor-position signal S_A related to phase A.

6.2.2 Sensorless Control Based on a Kalman Filter

In the dynamic system with random noise, a Kalman filter could achieve the minimum estimation error by optimal estimation. It can be used in both stationary and nonstationary applications. A Kalman filter uses the previous estimate and the latest input data to get new estimate data by using the recursive algorithm. So the filter only needs to store the previous estimate, and can meet the real-time requirement of the system. On the realization of a Kalman filter, it is a recursive algorithm implemented by a computer in essence. Each recursive cycle includes two processes, in which the time and measurements of the estimated value

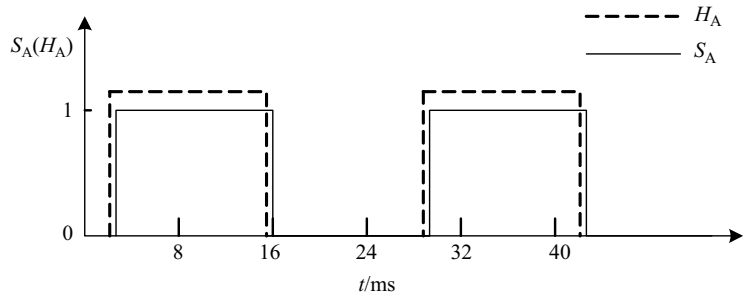


Figure 6.18 Waveform of Hall signal H_A and the rotor-position signal S_A.

are updated. Figure 6.19 shows the state-space model diagram for a linear system with random noise.

In Figure 6.19, $\boldsymbol{U}_k$ is the nonrandomized control input, $\boldsymbol{X}_k$ is the state of the system, $\boldsymbol{w}(k)$ is the random noise input, $\boldsymbol{v}(k)$ is the measurement of the noise, $\boldsymbol{y}(k)$ is the measurement of the system output, Φ_k, $\boldsymbol{R}_k$, $\boldsymbol{G}_k$, $\boldsymbol{H}_k$ are the real matrices. Then, the sensorless control for BLDC motor is achieved by estimating the position of the rotor based on the Kalman filter [4–6].

6.2.2.1 The Control Strategy of a Kalman Filter Based on Line Back-EMF

From Equation (6.1), we can get the terminal voltage model of the BLDC motor as

$$\begin{cases} e_{AB} = u_{AG} - u_{BG} - (L - M)\dfrac{\mathrm{d}(i_A - i_B)}{\mathrm{d}t} - R(i_A - i_B) \\ e_{AC} = u_{AG} - u_{CG} - (L - M)\dfrac{\mathrm{d}(i_A - i_C)}{\mathrm{d}t} - R(i_A - i_C) \\ e_{BC} = u_{BG} - u_{CG} - (L - M)\dfrac{\mathrm{d}(i_B - i_C)}{\mathrm{d}t} - R(i_B - i_C) \end{cases} \tag{6.57}$$

Since the three line back-EMFs have the relationship

$$e_{BC} = e_{AC} - e_{AB} \tag{6.58}$$

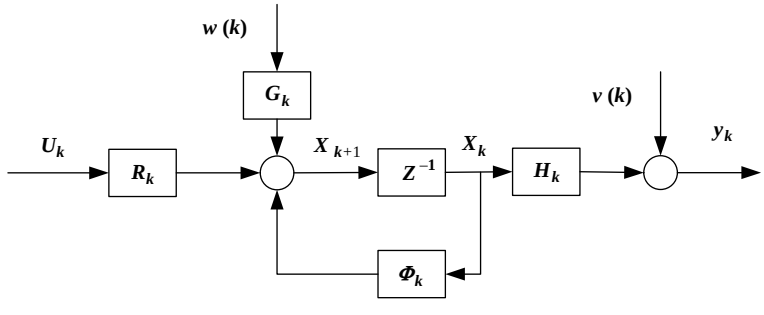


Figure 6.19 State-space model for a linear system with random noise.

then the voltage model of the motor can be simplified as

$$U_{\mathrm{l}} = \begin{bmatrix} 2\left(R + \dfrac{\mathrm{d}}{\mathrm{d}t}(L-M)\right) & 0 \\ R + \dfrac{\mathrm{d}}{\mathrm{d}t}(L-M) & 3\left(R + \dfrac{\mathrm{d}}{\mathrm{d}t}(L-M)\right) \end{bmatrix} I_{\mathrm{l}} + E_{\mathrm{l}} \tag{6.59}$$

where

$$\begin{aligned} E_{\mathrm{l}} &= [\,e_{\mathrm{AB}}\ e_{\mathrm{AC}}]^T; \\ U_{\mathrm{l}} &= [\,u_{\mathrm{AB}}\ u_{\mathrm{AC}}]^T; \\ I_{\mathrm{l}} &= [\,i_{\mathrm{AB}}\ i_{\mathrm{AC}}]^T; \\ i_{\mathrm{AB}} &= \frac{i_{\mathrm{A}} - i_{\mathrm{B}}}{2}; \\ i_{\mathrm{AC}} &= \frac{i_{\mathrm{A}} + i_{\mathrm{B}}}{2}. \end{aligned}$$

Therefore, we can obtain the line back-EMF of the BLDC motor through detecting the terminal voltage and current. Since there is no need for phase delay in the line back-EMF-based sensorless control strategy, an extended speed range for BLDC motor drives is achieved.

In practice, the line back-EMF signal usually includes unmodeled noise, detection noise and burst noise. These noises, especially the burst noise, may lead to a false determination for the zero crossings so that the motor will be uncontrollable. In general, the random noise can be regarded as Gaussian white noise. Therefore, we could use a Kalman filer to eliminate noises and estimate the zero-crossing instants of the line back-EMF.

Based on the line back-EMF, the discrete state model of the BLDC motor is established as

$$\boldsymbol{X}_{k+1} = \Phi_{\mathrm{k}}\boldsymbol{X}_{\mathrm{k}} + \boldsymbol{R}_{\mathrm{k}}\boldsymbol{U}_{\mathrm{k}} + \boldsymbol{G}_{\mathrm{k}}\boldsymbol{w}(k) \tag{6.60}$$

$$\boldsymbol{y}_{\mathrm{k}} = \boldsymbol{H}_{\mathrm{k}}\boldsymbol{X}_{\mathrm{k}} + \boldsymbol{v}(k) \tag{6.61}$$

where

$$\begin{aligned} \boldsymbol{X}_{\mathrm{k}} &= [i_{\mathrm{AB}}(k)\, i_{\mathrm{AC}}(k)\, e_{\mathrm{AB}}(k)\, e_{\mathrm{AC}}(k)\, \omega(k)]^T; \\ R_{\mathrm{k}} &= \begin{bmatrix} \dfrac{T}{2(L-M)} & -\dfrac{T}{6(L-M)} & 0 & 0 & 0 \\ 0 & \dfrac{T}{3(L-M)} & 0 & 0 & 0 \end{bmatrix}^T; \\ \boldsymbol{U}_{\mathrm{k}} &= [u_{\mathrm{AB}}(k)\, u_{\mathrm{AC}}(k)]^T; \\ \boldsymbol{y}_{\mathrm{k}} &= [i_{\mathrm{AB}}(k)\, i_{\mathrm{AC}}(k)]^T; \end{aligned}$$

$$\Phi_{\mathrm{k}} = \begin{bmatrix} 1-\dfrac{RT}{L-M} & 0 & -\dfrac{T}{2(L-M)} & 0 & 0 \\ 0 & 1-\dfrac{RT}{L-M} & \dfrac{T}{6(L-M)} & -\dfrac{T}{3(L-M)} & 0 \\ 0 & 0 & 1 & 0 & 0 \\ 0 & 0 & 0 & 1 & 0 \\ 0 & 0 & 0 & 0 & 1 \end{bmatrix};$$

$$H_{\mathrm{k}} = \begin{bmatrix} 1 & 0 & 0 & 0 & 0 \\ 0 & 1 & 0 & 0 & 0 \end{bmatrix};$$

$\boldsymbol{w}(k)$ — measurement noise vector;
$\boldsymbol{v}(k)$ — system noise vector.

The Kalman filter consists of the predicted equation and the filtering estimation equation. The state equation and estimation error covariance matrices at time t_{k+1} are predicated by the state equation and inputs at time t_k. The state prediction equation is

$$\begin{aligned} \hat{\boldsymbol{X}}_{k+1|k} &= \Phi_{\mathrm{k}}\hat{\boldsymbol{X}}_{k|k-1} + \boldsymbol{K}_{\mathrm{k}}(\boldsymbol{y}_{\mathrm{k}} - \boldsymbol{H}_{\mathrm{k}}\hat{\boldsymbol{X}}_{k|k-1}) \\ &= (\Phi_{\mathrm{k}} - \boldsymbol{K}_{\mathrm{k}}\boldsymbol{H}_{\mathrm{k}})\hat{\boldsymbol{X}}_{k|k-1} + \boldsymbol{K}_{\mathrm{k}}y_{\mathrm{k}} \end{aligned} \tag{6.62}$$

in which

$$\boldsymbol{K}_{\mathrm{k}} = \Phi_{\mathrm{k}}\boldsymbol{P}_{k|k-1}\boldsymbol{H}_k^T(\boldsymbol{H}_{\mathrm{k}}\boldsymbol{P}_{k|k-1}\boldsymbol{H}_k^T + \boldsymbol{R}_{\mathrm{k}})^{-1} \tag{6.63}$$

And the estimation error covariance matrix prediction equation is

$$\boldsymbol{P}_{k+1|k} = \Phi_{\mathrm{k}}[\boldsymbol{P}_{k|k-1} - \boldsymbol{P}_{k|k-1}\boldsymbol{H}_k^{\mathrm{T}}(\boldsymbol{H}_{\mathrm{k}}\boldsymbol{P}_{k|k-1}\boldsymbol{H}_k^{\mathrm{T}} + \boldsymbol{R}_{\mathrm{k}})^{-1}\boldsymbol{H}_{\mathrm{k}}\boldsymbol{P}_{k|k-1}]\Phi_k^{\mathrm{T}} + \boldsymbol{G}_{\mathrm{k}}\boldsymbol{Q}\boldsymbol{G}_k^{\mathrm{T}} \tag{6.64}$$

Finally, by making appropriate replacements in the usual Kalman gain formula, the estimate and the error covariance can be updated by

$$\begin{cases} \hat{\boldsymbol{X}}_{k|k} = \hat{\boldsymbol{X}}_{k|k-1} + \boldsymbol{P}_{k|k-1}\boldsymbol{H}_k^{\mathrm{T}}(\boldsymbol{H}_{\mathrm{k}}\boldsymbol{P}_{k|k-1}\boldsymbol{H}_k^{\mathrm{T}} + \boldsymbol{R}_{\mathrm{k}})^{-1}(y_{\mathrm{k}} - \boldsymbol{H}_{\mathrm{k}}\hat{\boldsymbol{X}}_{k|k-1}) \\ \boldsymbol{P}_{k|k} = \boldsymbol{P}_{k|k-1} - \boldsymbol{P}_{k|k-1}\boldsymbol{H}_k^{\mathrm{T}}(\boldsymbol{H}_{\mathrm{k}}\boldsymbol{P}_{k|k-1}\boldsymbol{H}_k^{\mathrm{T}} + \boldsymbol{R}_{\mathrm{k}})^{-1}\boldsymbol{H}_{\mathrm{k}}\boldsymbol{P}_{k|k-1} \end{cases} \tag{6.65}$$

Thus, based on the line back-EMF estimated by a Kalman filter, a novel commutation strategy is obtained. In such cases, if phases B and C are conducted, then $e_{\mathrm{B}} > 0$, $e_{\mathrm{C}} < 0$, and the value of e_{A} is between e_{B} and e_{C}. Therefore, there exist $e_{\mathrm{AB}} < 0$, $e_{\mathrm{AC}} > 0$ and $e_{\mathrm{BC}} > 0$ in this condition. Similarly, we can derive the signs of back-EMF in other conduction states. The relationship between line back-EMF and the conduction phase winding has been shown in Table 6.1.

6.2.2.2 Simulation Results

Figure 6.20 shows the waveforms of the line back-EMF e_{AB}, which is obtained by solving the state equation directly. Figure 6.21 is the line back-EMF estimated by a Kalman filter. The actual value of the line back-EMF is shown in Figure 6.22.

Table 6.1 The relationship between line back-EMF and conduction phase winding

Line back-EMF			Winding conducting state		
e_{AB}	e_{AC}	e_{BC}	A	B	C
+	+	+	Forward conducting	Non-conducting	Negative conducting
−	+	+	Non-conducting	Forward conducting	Negative conducting
−	−	+	Negative conducting	Forward conducting	Non-conducting
−	−	−	Negative conducting	Non-conducting	Forward conducting
+	−	−	Non-conducting	Negative conducting	Forward conducting
+	+	−	Forward conducting	Negative conducting	Non-conducting

Figure 6.23 shows the waveforms of the line back-EMF and Hall sensor position signals at the motor starting stage.

It can be seen from Figure 6.23 that the speed of the motor will not affect the relationship between the commutation instants and the zero-crossing points of the line back-EMF, while it does influence the waveform of the line back-EMF.

6.2.3 Sensorless Control Based on Sliding-Mode Observer

6.2.3.1 Controller Design

A sliding-mode observer has been successfully used in estimating motor speed by rotor-resistance identification and other applications, because of its good robustness and the antidisturbance ability for system measurement noise. Thus, a sensorless controller of a BLDC motor can be designed based on a sliding-mode observer [7,8]. A BLDC motor sensorless control scheme based on a sliding-mode observer is shown in Figure 6.24.

In Figure 6.24, the current reference signals are obtained from the speed controller based on the error between the rotation speed reference signal ω^* and the estimated signal $\hat{\omega}$. The phase

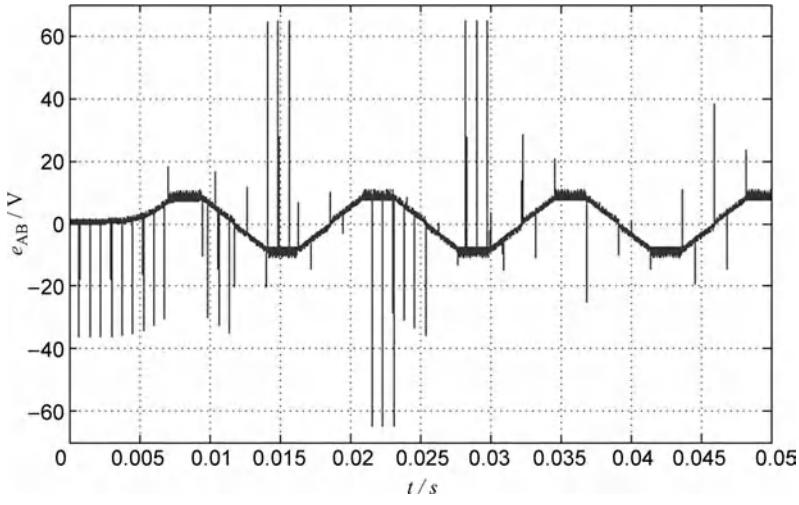


Figure 6.20 Line back-EMF obtained by solving the state equation.

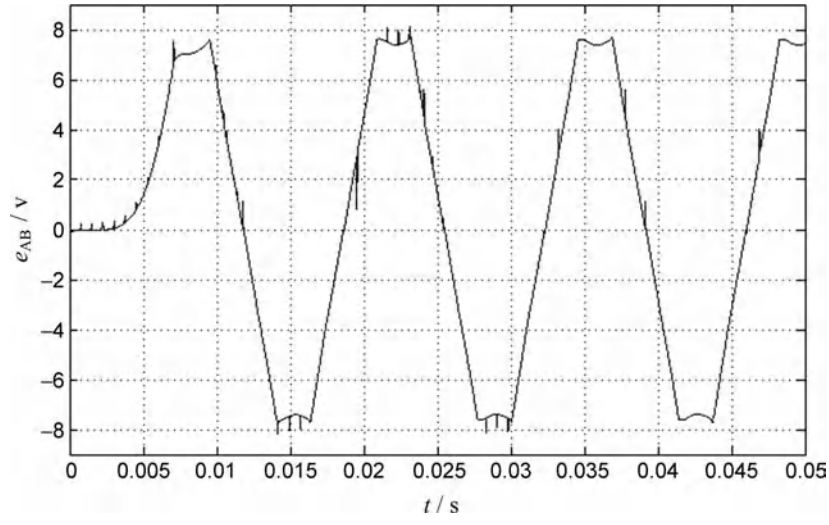


Figure 6.21 Line back-EMF estimated by a Kalman filter.

commutation signals are achieved through the commutation look-up table. Both $\hat{\omega}$ and $\hat{\theta}$ are estimated by the sliding-mode observer. Based on the estimated speed and position signals, the BLDC motor can operate in a sensorless condition.

According to the dynamic mathematic model of a BLDC motor, the sliding-mode control model related to phase A can be written as

$$\frac{\mathrm{d}}{\mathrm{d}t}\hat{i}_{\mathrm{A}} = \frac{1}{L'}u_{\mathrm{A}} - \frac{R}{L'}\hat{i}_{\mathrm{A}} - \frac{1}{L'}\hat{e}_{\mathrm{A}} + K\,\mathrm{sgn}\,(\hat{i}_{\mathrm{A}} - i_{\mathrm{A}}) \tag{6.66}$$

where ^ denotes the estimated value of parameters, K is the sliding gain.

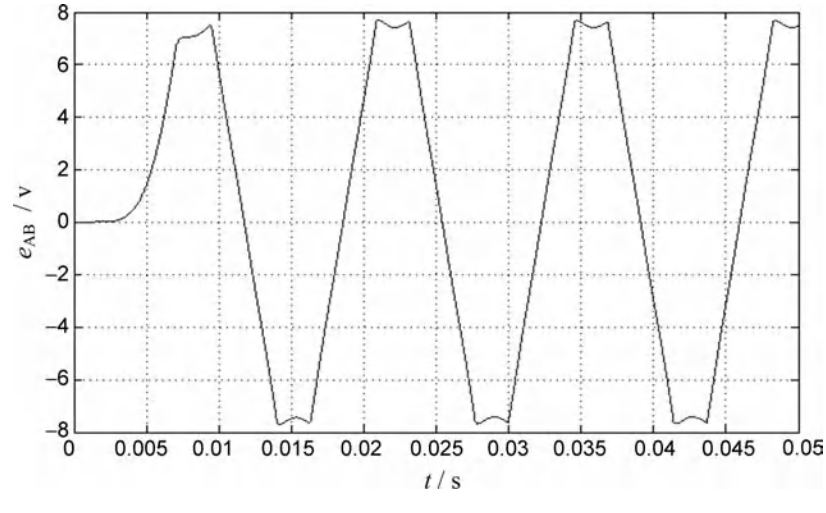


Figure 6.22 Experimental line back-EMF.

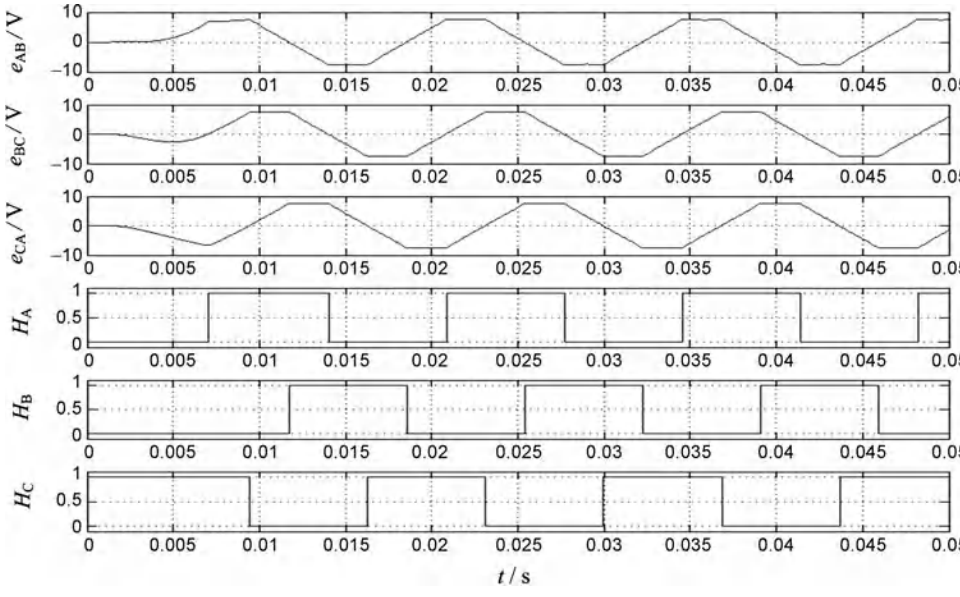


Figure 6.23 Line back-EMF and Hall sensor position waveforms.

From Equation (6.66), we can design the sliding-mode observer model of phase A, which is shown in Figure 6.25.

In Figure 6.25, the phase voltage u_A is the input signal, while the error between the estimated stator current $\hat{i}_A$ and the actual stator current i_A is the feedback signal. However, the error signal is restricted by a symbolic function before being fed back to the input terminal. Sliding surface s can be implemented by stator currents. The switching function and error function are

$$\begin{cases} s = \hat{i}_A - i_A = e_s = 0 \\ \dot{e}_s = -\dfrac{R}{L'} e_s - \dfrac{1}{L'}(\hat{e}_A - e_A) + K\,\mathrm{sgn}(e_s) \end{cases} \tag{6.67}$$

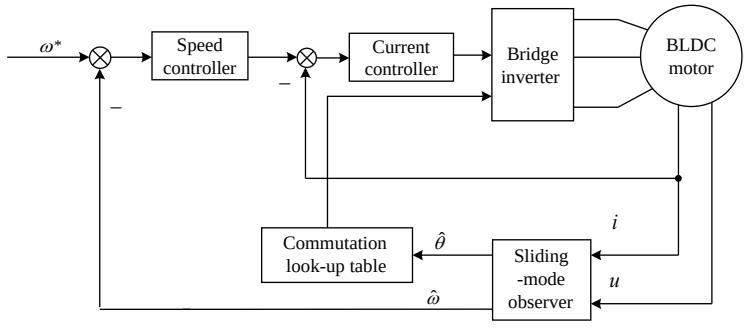


Figure 6.24 BLDC motor sensorless control scheme based on a sliding-mode observer.

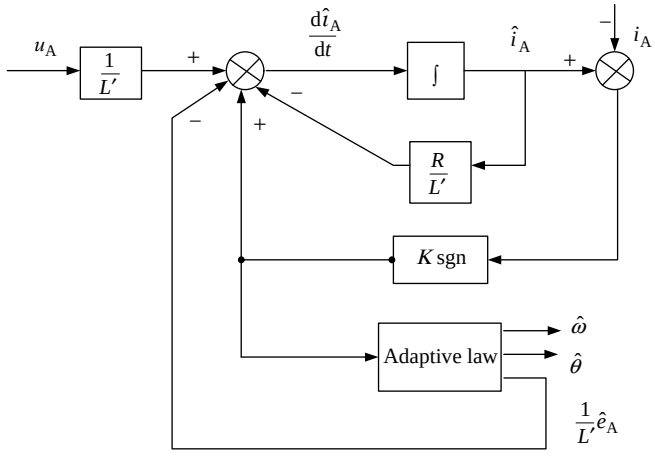


Figure 6.25 Sliding-mode observer.

6.2.3.2 Stability Analysis

Considering $s\dot{s} < 0$, sliding gain K must satisfy

$$\begin{aligned} s\dot{s} &= e_s\dot{e}_s \\ &= (\hat{i}_A - i_A)[-BRe_s - B(\hat{e}_A - e_A) + K\,\mathrm{sgn}(e_s)] < 0 \end{aligned} \tag{6.68}$$

where $B = \frac{1}{L'}$.

Since $\hat{e}_A$ and e_A are time varying, K still needs to satisfy the inequality

$$K < BR|e_s| - B|\hat{e}_A - e_A| \tag{6.69}$$

This means that if K is small enough, the equivalent control works. Then the system will stably run on the sliding surface. At this moment, $e_s = \dot{e}_s = 0$. Thus, Equation (6.67) can be rewritten as

$$z = -K\mathrm{sgn}(e_s) = -B(\hat{e}_A - e_A) \tag{6.70}$$

It can be seen from Equation (6.70) that the back-EMF information of the BLDC motor is included in the signal z. It can be used to estimate the rotor position and speed. According to Equation (6.15), we need to know the phase voltage, the phase current and the derivative of the phase current in order to obtain the back-EMF. The main advantage of sliding-mode observer-based sensorless control is that it is not necessary to calculate the phase current derivative. Besides, this sensorless control method has a good robustness to measurement noise.

According to the characteristics of a BLDC motor, the back-EMF can be written as

$$\begin{cases} e_A = \omega\psi_m f_A(\theta) \\ e_B = \omega\psi_m f_B(\theta) \\ e_C = \omega\psi_m f_C(\theta) \end{cases} \tag{6.71}$$

where ψ_m is the magnetic flux linkage of each phase, $f_A(\theta)$ is the waveform coefficient of back-EMF related to phase A, $f_B(\theta) = f_A(\theta + 2\pi/3)$, and $f_C(\theta) = f_A(\theta - 2\pi/3)$.

Substituting Equation (6.71) into Equation (6.70), we get

$$-K\text{sgn}(e_s) + B\hat{\omega}\psi_m f_A(\hat{\theta}) = B\omega\psi_m f_A(\theta) \tag{6.72}$$

We can see from Equation (6.72) that the rotor position θ on the right side can be calculated by its estimated value on the left side. In this way, the estimated value is renewed. In the current loop of the system, there are lots of switching fluctuations in signal z, which are produced by the sliding movement. Fortunately, low-pass filters can eliminate these fluctuations. In contrast, if the estimated rotor speed $\hat{\omega}$ is gained from the derivation of rotor-position signal $\hat{\theta}$, fluctuations will be enlarged. These fluctuations will deteriorate the performance of speed control for BLDC motors. In such a case, it is very hard for low-pass filters to eliminate the fluctuations. To solve this problem, adaptive methods are usually adopted to estimate the rotation speed. Thus, the estimated value will be less disturbed by switching fluctuations.

If $\hat{\theta}$ is estimated accurately enough, we can let $\hat{\theta} = \theta$. Then, combining Equation (6.67) with Equation (6.71), we get

$$\dot{e}_s = -BRe_s - B\psi_m(\hat{\omega} - \omega)f_A(\theta) + K\text{sgn}(e_s) \tag{6.73}$$

and if the Lyapunov function and adaptive law are defined as

$$\begin{cases} v = \dfrac{1}{2}(\hat{\omega} - \omega)^2 \\ \dot{\hat{\omega}} = -hzf_A(\theta) \end{cases} \tag{6.74}$$

where h is a positive constant.

Further, from Equation (6.73), the equivalent control method can be expressed as

$$z = -K\text{sgn}(e_s) = -B\psi_m(\hat{\omega} - \omega)f_A(\theta) \tag{6.75}$$

Therefore, the estimated rotation speed $\hat{\omega}$ can be calculated from the integral of Equation (6.74). Substituting Equation (6.74) into Equation (6.27), we can renew the estimated rotor position $\hat{\theta}$. If $\hat{\omega}$ is accurate enough, and there exists $\dot{\omega} = 0$, then the sensorless speed control for BLDC motors can be achieved.

Since

$$\begin{aligned} \dot{v} &= (\hat{\omega} - \omega)\dot{\hat{\omega}} = -(\hat{\omega} - \omega)hzf_A(\theta) \\ &= -(\hat{\omega} - \omega)hB\psi_m(\hat{\omega} - \omega)f_A^2(\theta) \\ &= -hB\psi_m(\hat{\omega} - \omega)^2 f_A^2(\theta) \le 0 \end{aligned} \tag{6.76}$$

Thus, the system is Lyapunov stable.

6.2.4 Position-Sensorless Control Using Wavelet Neural Network (WNN)

6.2.4.1 Introduction to WNN

WNN is a feedforward artificial neural network (ANN) based on wavelet decomposition. It combines a wavelet transform with ANN together by replacing a neuron nonlinear excitation function with nonlinear wavelet basis. WNN has many of the merits of a wavelet transform and ANN. It not only realizes wavelet transform by adjusting the wavelet basis function adaptively, but also has good ability of function approximation. The structure diagram of a SISO WNN is shown in Figure 6.26.

In Figure 6.26, the hidden nodes of the network are all wavelet functions, w_i is the weight from the ith hidden node to the output, a_i and t_i are the scale factor and translation factor of the wavelet function for the ith hidden node, respectively. The optimum values of w_i, a_i and t_i are obtained by training so that the network can approximate $f(x)$ well.

6.2.4.2 Sensorless Control Based on WNN

1. Position detection of BLDC motor

Note that the voltage equation of BLDC motor is

$$\begin{bmatrix} u_A \\ u_B \\ u_C \end{bmatrix} = \begin{bmatrix} R & 0 & 0 \\ 0 & R & 0 \\ 0 & 0 & R \end{bmatrix} \begin{bmatrix} i_A \\ i_B \\ i_C \end{bmatrix} + (L-M)\frac{d}{dt}\begin{bmatrix} i_A \\ i_B \\ i_C \end{bmatrix} + \frac{d}{dt}\begin{bmatrix} \psi_m(\theta) \\ \psi_m(\theta - 2\pi/3) \\ \psi_m(\theta - 4\pi/3) \end{bmatrix} \tag{6.77}$$

where ψ_m is a function of θ, ψ_m is related to the stator voltage and current. Therefore, commutation signals can be calculated by stator voltages and currents for the sensorless control [9–13].

2. Structure of WNN

Figure 6.27 shows the topology of a WNN that is used to detect the rotor position. This WNN topology includes six input signals for the input layer, ten nodes in the hidden layer and six switch signals of the output layer.

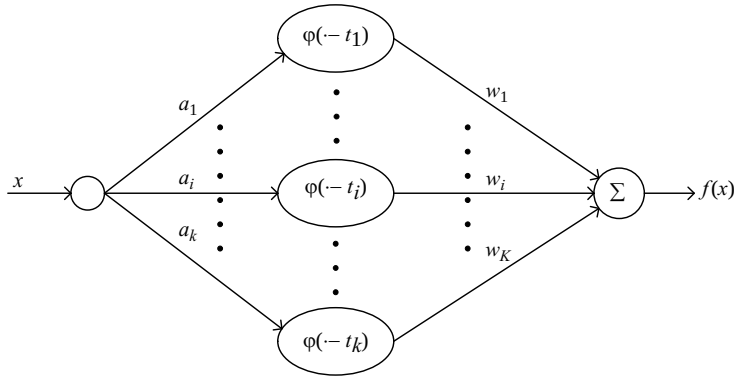


Figure 6.26 Structure diagram of a SISO wavelet neural network.

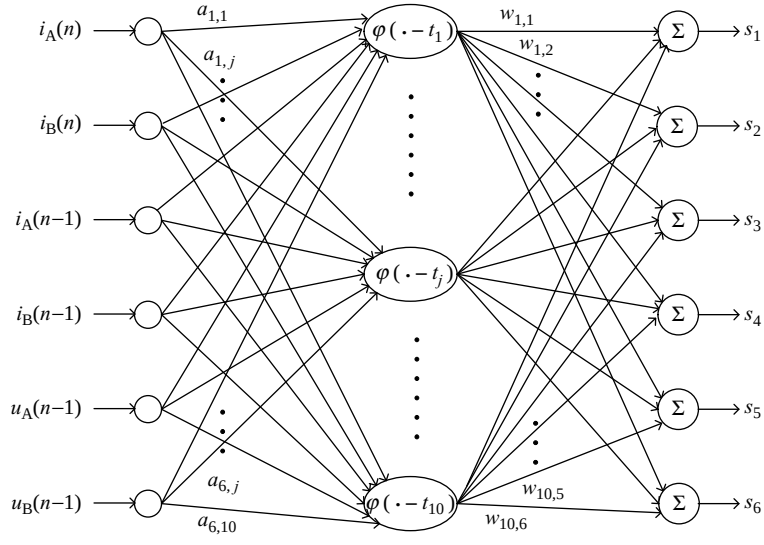


Figure 6.27 Topology of WNN for rotor-position detection.

The Mexican-hat wavelet is chosen for hidden nodes, that is

$$\varphi(x) = (1 - x^2)\, \mathrm{e}^{-x^2/2} \tag{6.78}$$

and the output can be expressed as

$$\boldsymbol{Y} = \boldsymbol{W}^T \varphi(\boldsymbol{A}\boldsymbol{X} - \boldsymbol{T}) \tag{6.79}$$

where

$$\boldsymbol{X} = \begin{bmatrix} i_A(n) & i_B(n) & i_A(n-1) & i_B(n-1) & u_A(n-1) & u_B(n-1) \end{bmatrix}^T;$$

$$\boldsymbol{T} = \begin{bmatrix} t_1 & t_2 & t_3 & \dots & \dots & t_{10} \end{bmatrix}^T;$$

$$\boldsymbol{Y} = \begin{bmatrix} S_1 & S_2 & S_3 & S_4 & S_5 & S_6 \end{bmatrix}^T;$$

$$\boldsymbol{A} = \begin{bmatrix} a_{1,1} & a_{1,2} & \cdots & \cdots & \cdots & a_{1,6} \\ a_{2,1} & \ddots & & & & \vdots \\ \vdots & & \ddots & & & \vdots \\ a_{10,1} & \cdots & \cdots & \cdots & \cdots & a_{10,6} \end{bmatrix};$$

$$\boldsymbol{W} = \begin{bmatrix} w_{1,1} & w_{1,2} & \cdots & \cdots & \cdots & w_{1,6} \\ w_{2,1} & \ddots & & & & \vdots \\ \vdots & & \ddots & & & \vdots \\ w_{10,1} & \cdots & \cdots & \cdots & \cdots & w_{10,6} \end{bmatrix}.$$

3. Offline training

How to obtain the training samples is very important for WNN offline training. Although training samples can be obtained from simulation data, a further training must be done based on the experimental data. This will make the WNN more suitable for the sensorless control of BLDC motors.

Now let the input sample set be $\{i_A(n), i_B(n), i_A(n-1), i_B(n-1), u_A(n-1), u_B(n-1)\}$, and the output sample set is $\{g_1, g_2, g_3, g_4, g_5, g_6\}$. Note that g_i is the switch state related to the ith bridge circuit. g_i is equal to 1 as the corresponding bridge circuit is conducted, while being 0 as the circuit is turned off.

By training $\boldsymbol{A}$, $\boldsymbol{T}$, and $\boldsymbol{W}$ with a gradient descent algorithm, we define the minimize objective function as

$$J = \frac{1}{2}\sum_{n}\sum_{i=1}^{6}(g_i - S_i)^2 \tag{6.80}$$

where n is the number of samples.

The adjusting law for the scale factor of the wavelet function is

$$a_{m,j}(n+1) = a_{m,j}(n) - \alpha\frac{\partial J}{\partial a_{m,j}} \tag{6.81}$$

where

$$\frac{\partial J}{\partial a_{m,j}} = -\sum_{n}\sum_{j=1}^{6} e_i w_{i,j}\left(x_{m,n}\psi'\left(\sum_{m=1}^{6} a_{m,j}\, x_{m,n} - t_j\right)\right) \tag{6.82}$$

where α is the learning rate, $x_{m,n}$ is the mth input of the nth vector of sample data, and e_i is the output error of the ith network, i.e. $e_i = g_i - s_i$.

The adjusting law for the translation factor of the wavelet function is

$$t_j(n+1) = t_j(n) - \alpha\frac{\partial J}{\partial t_j} \tag{6.83}$$

where

$$\frac{\partial J}{\partial t_j} = \sum_{p}\sum_{j=1}^{6} e_i w_{j,i}\psi'\left(\sum_{m=1}^{6} a_{m,j}\, x_{m,p} - t_j\right) \tag{6.84}$$

The weight control law of the wavelet function is

$$w_{j,i}(n+1) = w_{j,i}(n) - \alpha\frac{\partial J}{\partial w_{j,i}} \tag{6.85}$$

where

$$\frac{\partial J}{\partial w_{j,i}} = -\sum_{p} e_i\psi\left(\sum_{m=1}^{6} a_{m,j}\, x_{m,p} - t_j\right) \tag{6.86}$$

Here, offline training method is developed in a PC by using MATLAB. After being trained by 4000 samples, WNN can meet the predetermined precision. Then, the scale factor, the translation factor and the connection weight of the output layer are all determined.

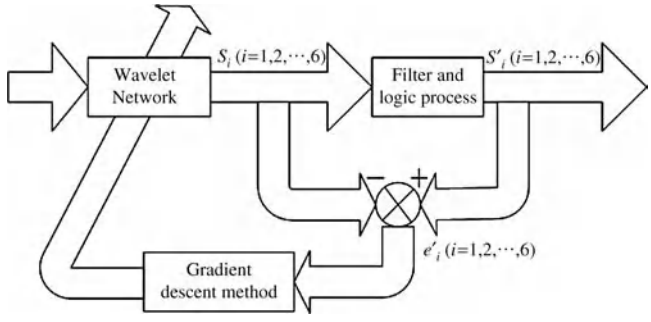


Figure 6.28 Online training scheme of WNN.

4. Online training

Online training is adopted into the WNN to improve its adaptability and robustness. Hence, the connection weights of the output layer can be adjusted by supervised learning. The gradient descent method is employed again, and the external teachers for supervised learning are the output signals coming from the logic process. The training scheme is shown in Figure 6.28.

Actually, the output is not strictly 0 or 1, but fluctuates around them. This indicates that errors exist in output signals. However, the only signals needed by the motor bridge circuit are 0 and 1. So output signals need to be filtered, where the filter is designed as

$$S'_i(n) = \begin{cases} 0 & \mathrm{S_i}(n) \le 0.25 \\ 1 & \mathrm{S_i}(n) \ge 0.75 \\ S'_i(n-1) & 0.25 \le S_{\mathrm{i}}(n) \le 0.75 \end{cases} \tag{6.87}$$

where $S'_i(n-1)$ and $S'_i(n)$ are the $(n-1)$th and the nth sample points of the ith filtered switch signal, respectively.

6.2.4.3 Simulation Results

The simulation is performed in MATLAB. Figure 6.29 shows the waveforms of sample signal g_1, output signal S_1 without filtering, and the error (e_1) between g_1 and S_1.

As shown in Figure 6.29, the output signals can track the sample signals properly, but they are not strictly 0 or 1. This means that the output signal cannot achieve the on-off control of the bridge circuit successfully.

The waveforms of filtered output signal S'_1 and error e'_1 are shown in Figure 6.30.

From Figure 6.30, we can see that the output signal of the WNN can provide a qualified on-off signal to the bridge circuit after being filtered.

Figure 6.31 shows the waveforms of the sample signal, the output signal and the related error, when the load is increased from 0 to 0.5 N m suddenly.

It can be seen from Figure 6.31 that the period of the commutation signal is 20 ms in the beginning, and increases immediately to 24 ms when the load is changed. It can be concluded that the dynamic response of the system is fast.

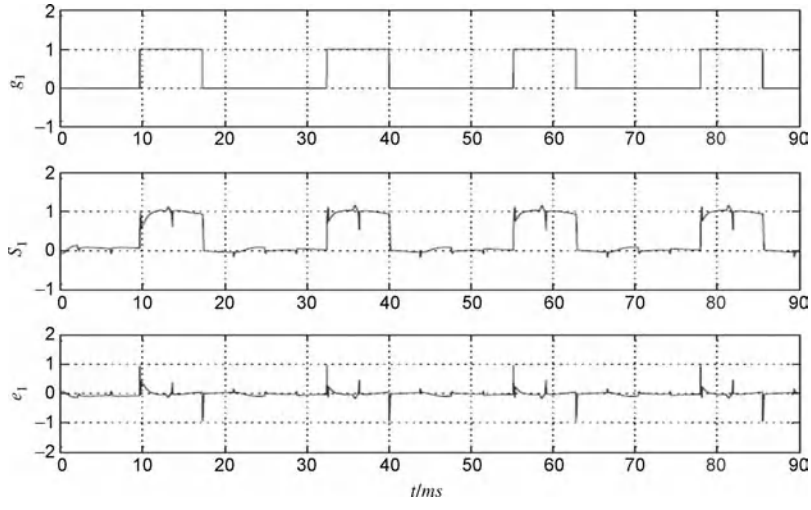


Figure 6.29 Waveform of sample signal g_1, output signal S_1, and error e_1.

6.3 Starting Process for Sensorless Control

6.3.1 Determination of Initial Rotor Position at Standstill

Determination of the initial rotor position is critical for the reliable starting of a BLDC motor. It directly affects the system's maximum starting torque and minimum starting time. At present, the inductance method is the main method for prediction of the initial rotor position. The principle of the inductance method is described as follows. First, a special short time

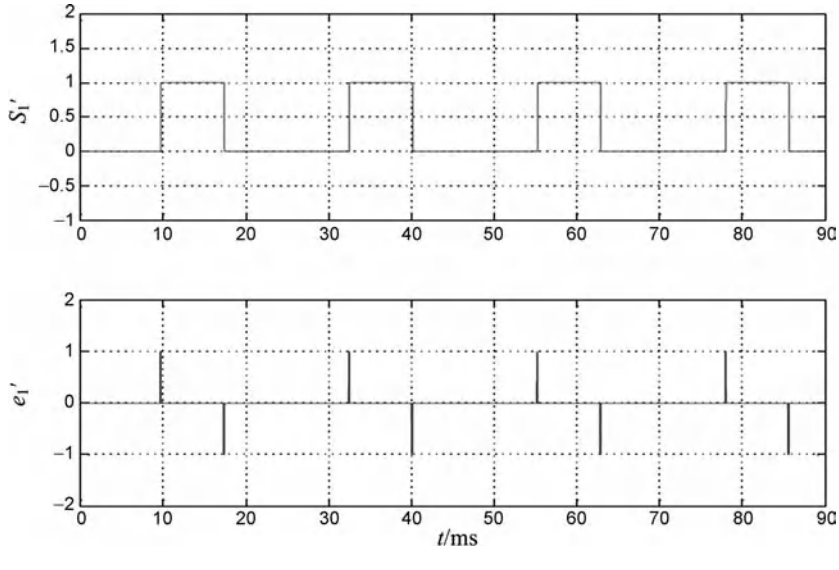


Figure 6.30 Waveforms of filtered signals S_1' and e_1'.

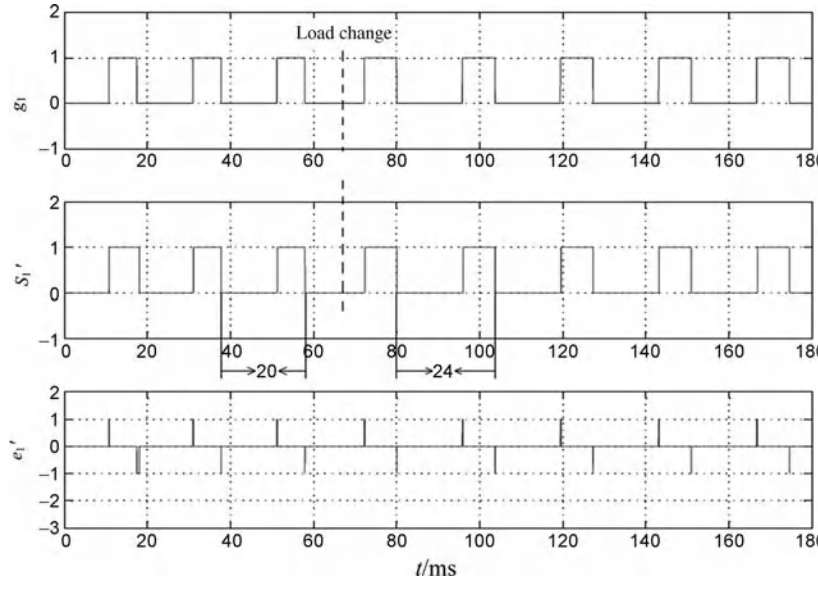


Figure 6.31 Waveforms of sample signal, output signal and their error when load changed suddenly.

impulse voltage is injected into stator winding. Then, the initial rotor position is obtained by differences among each stator winding's inductance, which is determined by the current response at a specific interval. Because the inductance of the windings is small and the reluctance of the PM is large in the BLDC motor, the inductance method requires a large amount of computing time and high-precision current measurement. Another method for determination of initial rotor position is the rotor-locating method. By energizing one specific phase winding, the rotor will be located at the defined location. Thus, the initial rotor position is known. The rotor locating method can be easily implemented. The disadvantages of this method are that the motor might rotate reversely and have a large current during the position location period.

6.3.2 Starting Methods for Sensorless Control

At present, the back-EMF-based method is the most common technique used in sensorless control for BLDC motor drives. It is well known that the back-EMF will become zero or very small, when the motor is at standstill or running at low speed. This makes it difficult for a motor to start by itself. To deal with this problem, many starting methods are presented. The main methods are: the three-step starting method, the prelocation starting method, the raising-frequency and the raising-voltage synchronous starting method, and the voltage interpolation method [14–17].

1) **Three-step starting method**
   The three-step starting method includes three stages: determination of rotor location, speeding up and operation mode switch. In the second stage, the motor is speeded up from

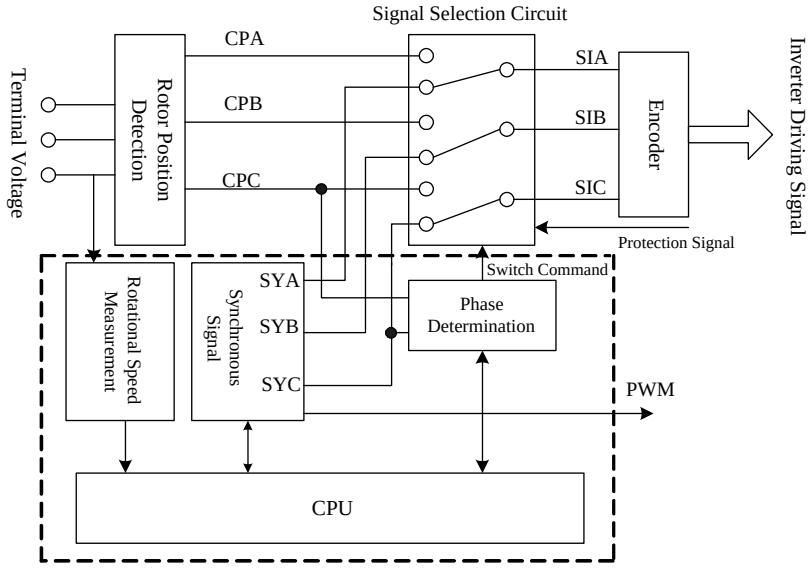


Figure 6.32 Principle diagram of three-step starting method.

stationary by the separate control method used in the synchronous motor. When the speed is high enough, the motor is switched to the common position sensorless running mode to complete the starting procedure. Figure 6.32 shows the corresponding principle diagram of the three-step starting method.

Which power switch should be conducted first depends on the initial rotor position when the BLDC motor is at standstill. Since determination of the initial rotor position is rather complex without position sensor, the rotor-locating method can be used to solve this problem.

After the initial rotor position is determined, the main controller, i.e. the CPU in Figure 6.32, will generate a series of synchronous signals SYA, SYB and SYC (Note that they are corresponding to rotor-position signals CPA, CPB and CPC, respectively), according to the rotation direction. Then the synchronous signals are compiled to generate the trigger signals for the inverter. The frequency of the synchronous signal is increased gradually, while the BLDC motor operates at separate control mode. When the motor runs at a low speed, the back-EMF is small so that the duty cycle of the inverter is also small. Then, the duty cycle of the inverter increases with the speed up. Hence, the normal operation of the BLDC motor is ensured. By speeding up with the separate control method, the BLDC motor may run in an unstable state. Thus, it is necessary to design a proper acceleration curve. Note that the zero-crossing signal of the back-EMF should be strong enough for checking when the motor speeds up to the desired velocity. Meanwhile, the motor shifts to the back-EMF-based sensorless control mode.

The three-step starting method is easily influenced by many factors, such as load torque, applied voltage, acceleration curve, moment of inertia, and so on. Under the condition of small load or low inertia, the three-step starting method can usually be implemented into practice. But it is easy to be unstable in the shifting stage, especially

when the motor has a heavy load. In this condition, the motor may fall out of step and consequently fail in starting. Note that the motor parameters and load have a great influence on the optimal acceleration curve during starting.

2) **Prelocation starting method**

During starting, two desired phase windings of motor are injected into the current and the motor rotates to the corresponding position. Then, commutation is achieved by changing the conduction condition of motor windings in turns. At each commutation procedure, it is necessary to detect the zero-crossing point of the back-EMF for the nonexcited phase, and raise the applied voltage of motor by increasing the PWM duty cycle. When the zero-crossing points of the back-EMF can be reliably detected in N times continuously, the BLDC motor is switched to the back-EMF-based sensorless control mode.

The prelocation starting method has advantages like reliable starting up and easy implementation. It can ensure the motor start at standstill and shift to sensorless control successfully under any initial rotor position. But this method needs an accurate shifting time. When the motor has different moments of inertia or starts up with varied load, it is necessary to modify the prelocation and starting parameters so that the motor runs normally.

3) **Raising-frequency and raising-voltage synchronous starting method**

The raising-frequency and raising-voltage synchronous starting method is usually achieved by hardware circuits. Figure 6.33 shows the basic principle diagram.

As shown in Figure 6.33, after the circuit is connected into the BLDC motor drivers, the capacitor voltage U_C, which is added to the input of the voltage-controlled oscillator, increases slowly. The output of the voltage-controlled oscillator, presented as a clock signal after frequency division, is added to the ring-like distributor, whose outputs are transformed to commutation signals to control the power switches. Meanwhile, U_C is added to the input of PWM circuits to modify the duty cycle of PWM (i.e. to control the windings voltage). So, the voltage and frequency added to the windings all rise with the increasing of

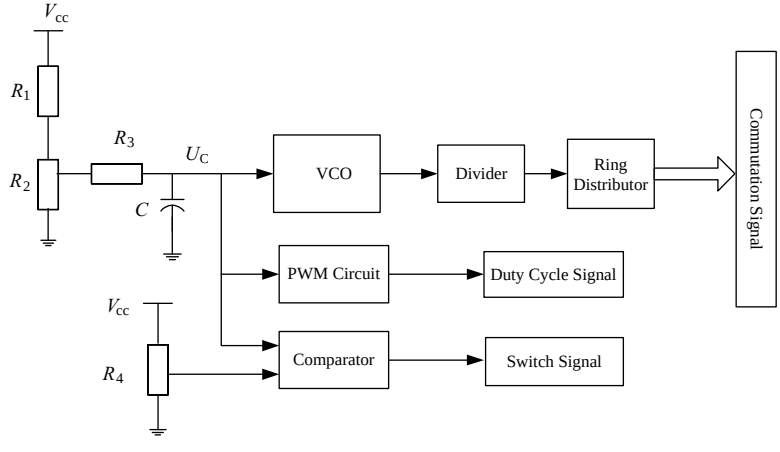


Figure 6.33 Principle diagram of the raising-frequency and raising-voltage synchronous starting method.

U_C, and the motor operates under the raising-voltage and raising-frequency mode. Further, comparing U_C with the designed threshold value, and when U_C is equal to the threshold, the motor should be shifted to the sensorless control mode by a related logic circuit.

At a certain frequency and speed, the BLDC motor can start reliably under no-load, half-load and other desired load conditions by the raising-frequency and raising-voltage synchronous starting method, while the disadvantages of this method are that the design of such a starting circuit must consider motor parameters and the starting current needs to be large.

4) Voltage interpolation starting method

(1) Starting principle

Suppose the acceleration torque is constant, we can obtain the time required for one revolution of the motor as

$$t = 2\sqrt{\frac{J\pi}{\sum_i T_i}} \tag{6.88}$$

where $\sum_i T_i = T_e - B_V\Omega - T_L$.

As shown in Equation (6.88), if the load torque T_L and the damping torque $B_v\Omega$ are assumed to be constant, the motor starting time has a direct relationship with the electromagnetic torque T_e. However, T_e is determined by the bus voltage U. Thus, the DC bus voltage U determines the instant of phase commutation Q. So, by sampling the DC bus voltage as well as the corresponding phase commutation instant, we can use interpolation methods to simulate the relationship between U and Q. Then, the phase commutation instant for BLDC motor drives is determined by the fitting function. Figure 6.34 shows the fitting curve in this condition.

(2) Starting process

Figure 6.35 shows the principle diagram for BLDC motor starting.

As shown in Figure 6.35, the voltage interpolation starting method consists of the following three stages.

Stage 1: Prelocation, i.e. outputting certain two-phase conduction signals to make the motor rotate to the corresponding position, and waiting the starting signals to be determined.

Stage 2: Phase commutation starting, i.e. getting the phase commutation instant of the motor by interpolation calculation and producing corresponding conduction signals for the power switch by using effective values of DC bus voltage (or the PWM duty cycle).

Stage 3: End of starting, i.e. jumping out of the starting program and operating in back-EMF-based sensorless control mode.

Figure 6.36 shows the waveforms of the starting signal (curve 1), actual measured Hall signals H_A (curve 2), H_B (curve 3) and H_C (curve 4), and the speed modulation signal (curve 5) when the BLDC motor starts with the voltage interpolation method at no load.

In contrast with the traditional starting methods, those depending on experiences, the main advantage of the voltage interpolation starting method is that no extra starting circuit is required for the sensorless control of BLDC motors.

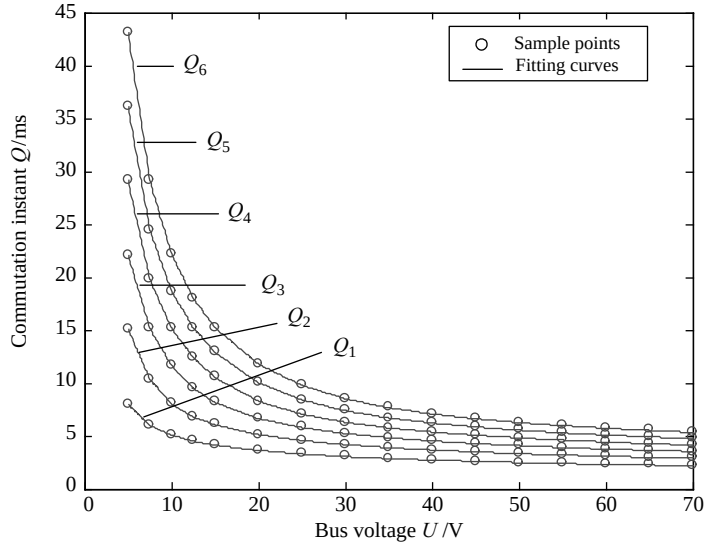


Figure 6.34 Curve for the fitting function between U and Q.

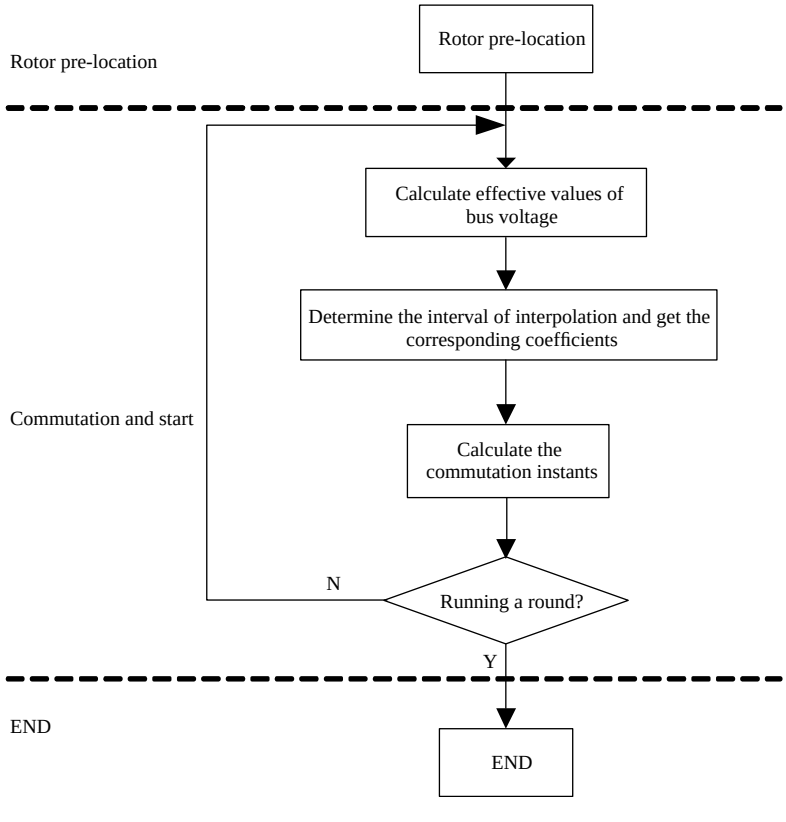


Figure 6.35 Principle diagram for a BLDC motor starting based on voltage interpolation.

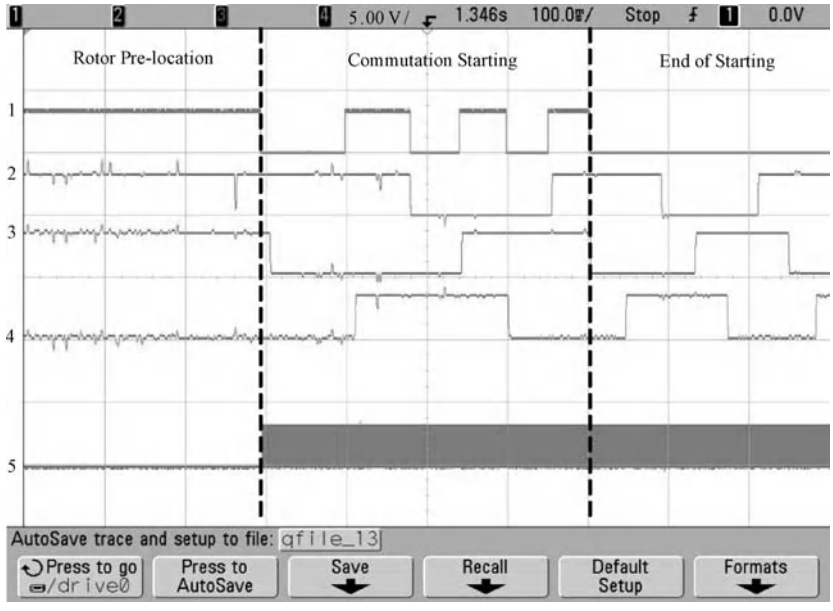


Figure 6.36 Experimental waveforms at starting.

Questions

1. Explain how the BLDC motor runs based on the sensorless control with back-EMF-based method.
2. Try to design an intelligent-based method for sensorless control of BLDC motor with your own knowledge.
3. Give some starting methods for the sensorless control of a BLDC motor.

References

1. Xia, C. L., Yang, X. J., Shi, T. N. (2002) Position sensorless control of brushless DC motor based on the disturbance observer". *Transactions of China Electrotechnical Society*, **17**(6), 25–28 (in Chinese).
2. Tomita, M., Senjyu, T., Doki, S., *et al.* (1998) New sensorless control for brushless DC motors using disturbance observers and adaptive velocity estimations. *IEEE Transactions on Industrial Electronics*, **45**(2), 274–282.
3. Yang, X. J. Sensorless control for brushless DC motor. Tianjin: Tianjin University Master Thesis, 2002 (in Chinese).
4. Chen, W., Xia, C. L. (2006) *Sensorless control of brushless DC motor based on fuzzy logic*. IEEE Proceedings of the World Congress on Intelligent Control and Automation, China, **6**, 6298–6302 (in Chinese).
5. Terzic, B., Jadric, M. (2001) Design and implementation of the extended Kalman filter for the speed and rotor position estimation of brushless DC motor. *IEEE Transactions on Industrial Electronics*, **48**(6), 1065–1073.
6. Chen, Wei. Study on torque ripple suppression technique of permanent magnet brushless DC motor. Tianjin: Tianjin University PhD Thesis, 2006 (in Chinese).
7. Shi, T. N., Lu, N., Zhang, Q., *et al.* (2008) Brushless DC motor sliding mode control with Kalman filter. *IEEE International Conference on Industrial Technology*, **4**, 1–6.
8. Lu, N. Sensorless control for BLDCM using an adaptive sliding mode observer. Tianjin: Tianjin University Master Thesis, 2008 (in Chinese).

9. Tian, Y., Shi, T. N., Xia, C. L. (2007) Position sensorless control using adaptive wavelet neural network for PM BLDCM. *IEEE International Symposium on Industrial Electronics*, 2848–2852.
10. Shi, T. N., Tian, Y., Xia, C. L. (2007) Direct control of voltage based on adaptive wavelet neural network for PM brushless DC motors. *Transactions of China Electrotechnical Society*, **22**(9), 74–79 (in Chinese).
11. Shi, T. N., Tian, Y., Xia, C. L. (2007) Position sensorless control based on wavelet neural network for PM brushless DC motors. *Journal of Tianjin University*, **40**(2), 190–194 (in Chinese).
12. EI-Sharkawei, M. A., EI-Samahy, A. A., EI-Sayed, M. I. (1994) High performance drive of DC brushless motors using neural network. *IEEE Transaction on Energy conversion*, **9**(2), 317–322.
13. Tian, Y. Position sensorless control based on wavelet neural network for PM brushless DC motors. Tianjin: Tianjin University Master Thesis, 2007 (in Chinese).
14. Shen, J. X., Lu, X. C. (1988) Detail analyses of 3-step start for LBLDC motor. *Small & Special Machines*, **26**(5), 8–11 (in Chinese).
15. Liu, M. j., Wang, Q. (1999) The start method by means of rotor pre-setting for the brushless DC motor of electromotive force commutation. *Small & Special Machines*, **27**(2), 8–10 (in Chinese).
16. Zou, J. B., Zhang, Y., Li, Z. Z. (1999) A driving circuit for sensorless brushless DC motor. *Micromotors Servo Technique*, **32**(2), 16–18, 47 (in Chinese).
17. Wu, S. G. Research on sensorless of brushless DC motor starting. Tianjin: Tianjin University Master Thesis, 2008 (in Chinese).

7

Realization of BLDC Motor Drives

Generally, a BLDC motor control system consists of two parts: hardware and software. The hardware part is made up of a main circuit, a driving circuit, a microprocessor control circuit and a protecting circuit. The software part includes the main program, a timing interrupt service subroutine, and so on. This chapter will analyze the above contents, combining with engineering practices and specific design examples, and introduce some antidisturbance methods for hardware and software design of motor control systems.

7.1 Main Circuit

Figure 7.1 shows the hardware system block diagram of a BLDC motor with position sensors. Its main circuit is mainly made up of AC power, a bridge rectifier and a bridge inverter. The input AC current is firstly rectified to DC current, and then transformed by a bridge inverter it is used to drive the BLDC motor.

A single-phase or three-phase AC power supply can be used depending on different system requirements and applications. Regarding a single-phase AC power supply, the commonly used rectifier circuits are showed in Figures 7.2(a)–(c), which are a full-bridge rectifier circuit, a half-bridge rectifier circuit and a voltage-doubling bridge rectifier circuit, respectively. Practically, a boost rectifier circuit shown in Figure 7.2(d) can be used to raise the DC voltage to meet the system's requirements if the above rectified voltages are still too low to drive the BLDC motor.

Besides, a three-phase AC power supply can be used in BLDC motor control systems. Consequently, a three-phase bridge rectifier circuit is applied, which has the advantages of simple connection and good performance, such as the 6RI100G series of Fuji Corporation and the SKD100 series of Semikron Corporation.

Bridge inverters, shown in Figure 7.3, usually have three phases and are formed by six MOSFETs or IGBTs. Diodes D1–D6 noted in the figure are called feedback diodes in that they can work as the passages that feedback the energy from the motor to the DC bus. Meanwhile, they are also called freewheeling diodes for their function of freewheeling the motor current. Beside the freewheeling diode, there is absorber circuit formed by a resistance, a capacitance

Permanent Magnet Brushless DC Motor Drives and Controls, First Edition. Chang-liang Xia.
© 2012 Science Press. Published 2012 by John Wiley & Sons Singapore Pte. Ltd.

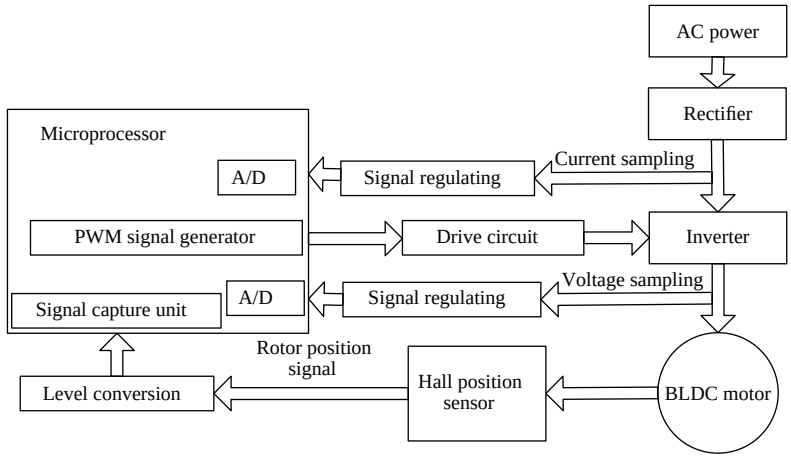
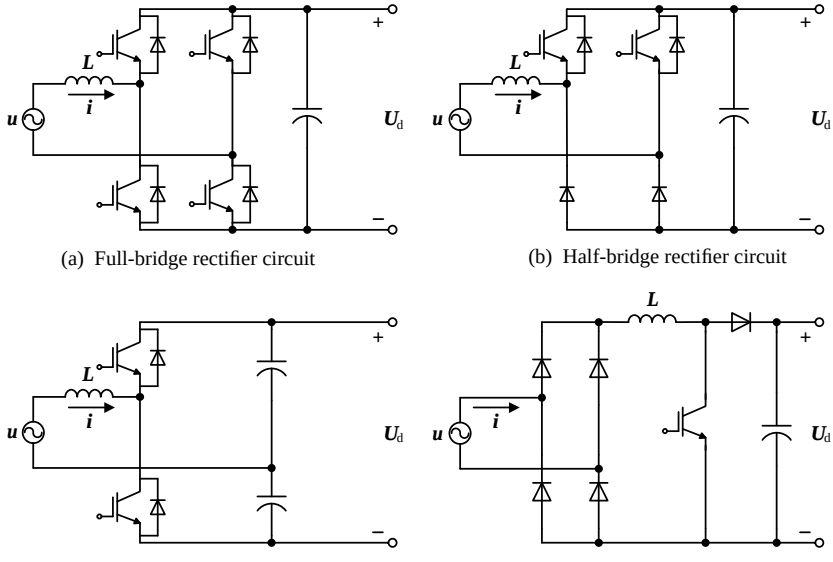


Figure 7.1 Hardware block diagram of a BLDC motor.

and another diode, which performs the function of suppressing the overvoltage and decreasing the turn-off switching losses of the corresponding power switches [1].

Inverter circuits based on four-switch technique shown in Figure 7.4 are proposed in some systems. They have great advantages of fewer power switches, lower costs and smaller switching losses, but a more complex algorithm to generate control signals for power switches and higher-performance requirements for microprocessors are demanded.



(a) Full-bridge rectifier circuit

(b) Half-bridge rectifier circuit

(c) Voltage-doubling rectifier circuit

(d) Boost rectifier circuit

Figure 7.2 Common rectifier circuits.

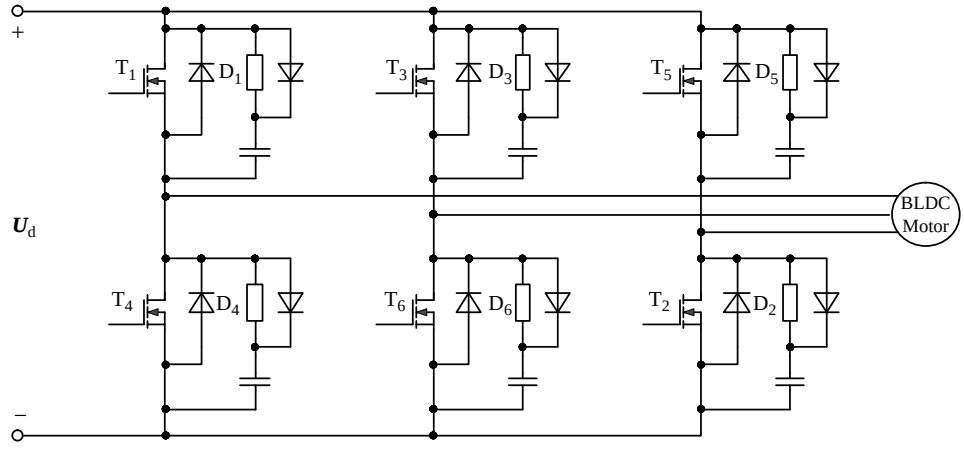


Figure 7.3 Three-phase bridge inverter circuit.

For some low-capacity motor control systems, inverters constructed by MOSFET cannot only meet the requirements of control system but also save costs. IRF530N, the fifth-generation MOSFET product of IR Corporation, is one of the commonly used MOSFET products and has an advanced manufacturing technology. Moreover it can drive a low-capacity motor effectively for its small impedance and fast switching speed. Its drain breakdown voltage is 100 V, the maximum drain current is 17 A under conduction conditions, and its delay time of switching on and off is only tens of nanoseconds.

An IGBT inverter is widely used in high-capacity motor control systems. Its architecture is essentially similar to that of a MOSFET, except that an additional P layer has been added between the drain pole and the drain areas. The naming of its parts is similar to MOSFET. The device, combining the merits of a MOSFET and a GTR, has the advantages of high input impedance, rapid response ability, good thermal stability, simple driving circuit, low conduction voltage drop and good ability to withstand high voltage. So it is applied extensively in some high-capacity motor control systems.

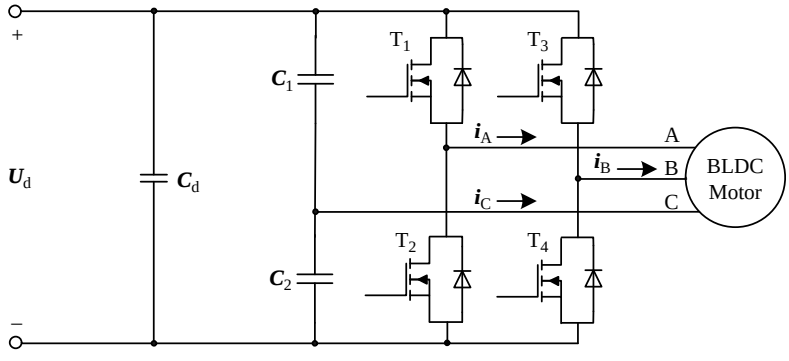


Figure 7.4 Inverter circuit based on four-switching technique.

FGA25N120 produced by Fairchild Corporation is one of the widely used devices of IGBT. Its maximum drain breakdown voltage is 1200 V, the maximum drain current in conducting mode is 25 A, the turn-on delaying time is 50 ns, the turn-off delaying time is 190 ns, and the cost of the device is low. Hence, it can readily meet the requirements of high-capacity motor control systems. As for some higher-capacity motor control systems, the device 1MBI200S-120 of Fuji Corporation can be used since the maximum drain breakdown voltage that the device can withstand is 1200 V, and the maximum drain current in conduction is 200 A.

7.2 Driving Circuit

7.2.1 MOSFET Driving Circuit

The MOSFET driving circuit can be constituted by discrete components as well as the special drivers that have a simple circuit, high reliability and wide application. Among the various drive devices, IR2110 and IR2130 are widely used.

Driver IR2110, manufactured by IR Corporation, uses HVIC and latch-immunity CMOS production techniques and outputs two drive signals. In IR2110, there is an upper-leg suspended bootstrap circuit that can greatly reduce the number of conventional drive power supplies. Moreover, only one drive power supply is enough for three-phase bridge inverter circuit.

IR2110 mainly consists of logical input, voltage translation and output protection. Its operating voltage can be as high as 500 V, the range of grid drive voltage is +10 to +20 V, and the range of logical power voltage is +3.3 to +15 V. The above characteristics make it easy to match the TTL and CMOS voltage level and IR2110 is extensively applied in small- and medium-power driving circuits for its small volume and high speed. Figure 7.5 shows a driving circuit constituted by three IR2110. V_{cc1} and V_{cc2} shown in Figure 7.5 are logical power and drive power, respectively. They are isolated from each other in order to improve the reliability and safety of the circuit.

It is necessary to consider the following problems during the use of IR2110 [2].

(1) Reverse withstand voltage of power supply diodes must be higher than the operating peak voltage of the driven MOSFET since the upper-leg driver supply in IR2110 is obtained by bootstrap techniques. Also, it is necessary to choose a fast recovery diode to prevent the two ends of the bootstrap capacitor from discharging.
(2) The volume of the upper-leg bootstrap capacitor, which is generally 1 μF (disk capacitor), depends on the switching frequency of the driven power switch, the duty cycle and the requirements of the grid drive current.
(3) In three-phase bridge driving circuits for a BLDC motor, the bootstrap capacitor may discharge due to the different voltage of VS pins on IR2110, which makes the upper-leg power switch not work when the control signal is effective and the underleg power switch is still in the operating condition. In order to avoid such a situation, the underleg power switch is conducted in advance to charge the bootstrap capacitor through logic control, or a larger bootstrap capacitor should be chosen.
(4) In three-phase bridge driving circuits for BLDC motors, the insulation between high-voltage bus and logic circuit is ensured by an antibias junction in IR2110. Serious consequences will be caused if any junction in the structure is breakdown. So, optocouplers

or pulse transformers could be applied to isolate the logic circuit from IR2110 to avoid such problems.

(5) Due to the low output impedance of the drive device in IR2110, it will cause fast turn-on and turn-off of the devices and may lead to oscillation between the drain pole and the source pole in the MOSFET if IR2110 is used to drive MOSFET appliances directly. Also, not only will RF interference be caused, but also the device may be in breakdown for high ratio of dv/dt under such conditions. To prevent this happening, a large resistance without inductance whose value is about 100 Ω can be connected between the grid of MOSFET and the output of IR2110.

IR2130, produced by IR Corporation, is a three-phase bridge driver with high performance. It has only one drive power supply which is similar to IR2110. However, it can output six drive signals, which makes system design easier. In addition, IR2130's protective function is better designed to make the circuit more reliable.

IR2130 can be used in circuits with the voltage not higher than 600 V, and its output upper-leg and under-leg drive current peak values are 250 mA and 500 mA, respectively. Integrated in IR2130 are a current comparator, a current amplifier, an under voltage monitor for its own operating power supply, an error-processing unit, a clearing blocked logic unit, three input

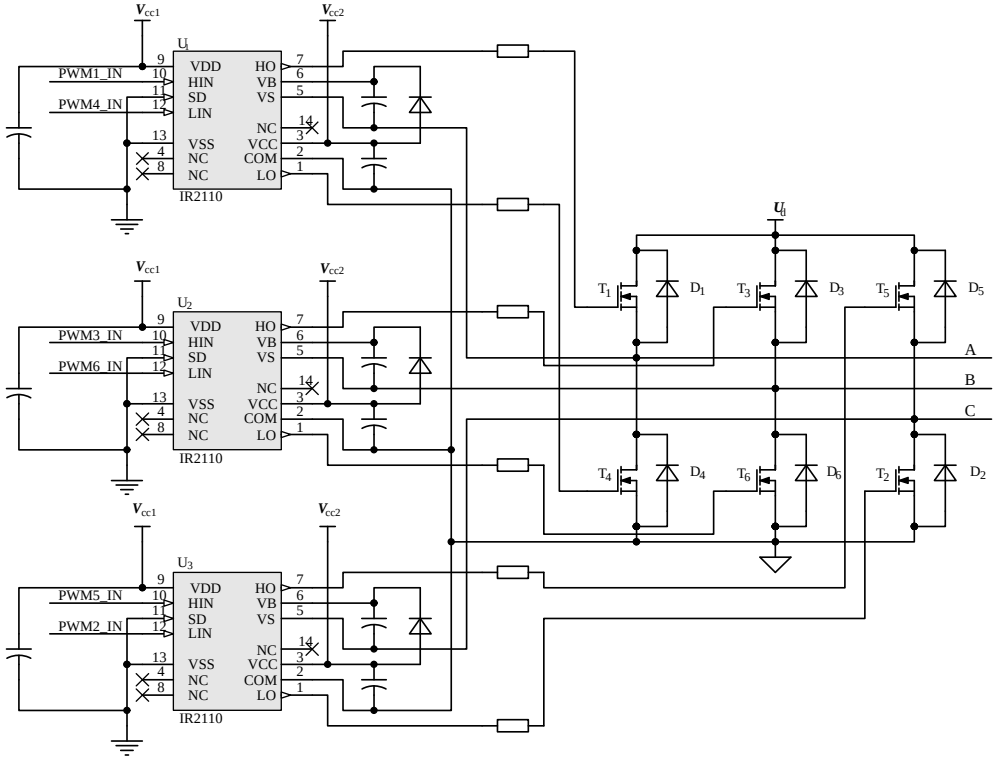


Figure 7.5 IR2110 driving circuit.

signal processors, three pulse-processing and level-shifting devices, three driving signal latches for upper-leg power switches, three undervoltage monitors for upper-leg power switch driving signals, six MOSFET drivers with low output impedance and an OR gate circuit.

In BLDC motor drive systems, six PWM pulse signals produced by a microprocessor serve as six inputs of IR2130, three of them are used to drive the upper-leg and the other three signals are applied to drive the under-leg. The three signals to drive under-leg power switches are injected into control poles after amplification. The other three signals to drive the upper-leg are initially handled by a pulse processor and bootstrap circuit of a level shifter to maintain level displacement and turned into three voltage-suspended drive pulse signals. Then, they are latched through the corresponding three output latch devices and checked by strict driving pulses. Lastly, the three signals are applied to control poles of the driven upper-leg power switches after power amplification.

IR2130 has the functions of overcurrent protection and undervoltage protection. When the output voltage of the current detecting unit is higher than 0.5 V, the phenomenon of overcurrent or direct conduction in the circuit appears. In this condition, the current comparator in IR2130 will reverse quickly, and the logic fault processing unit and $\overline{\text{FAULT}}$ pin output low level voltage and fault indications, respectively. Meanwhile, the six output drive signals are all low level and power switches are all at the off state for protection. The undervoltage detector has a similar operating process. When fault indication is low all the time and the circuit has no output, it is generally in undervoltage protection mode. When fault indication oscillates between high and low levels, and the circuit has output or not from time to time, it is in overcurrent protection mode. It is not until the clearance of the fault and input high-level signals into $\overline{\text{LIN1}}$–$\overline{\text{LIN3}}$ at the same time that the fault latch state could be eliminated and the devices operate in the normal state again. In addition, IR2130 has a logic protective function. When the two input drive signals into one leg are all effective, the corresponding two drive signals output by IR2130 are low level, resulting in latching of this bridge leg [3]. Figure 7.6 shows the driving circuit of IR2130.

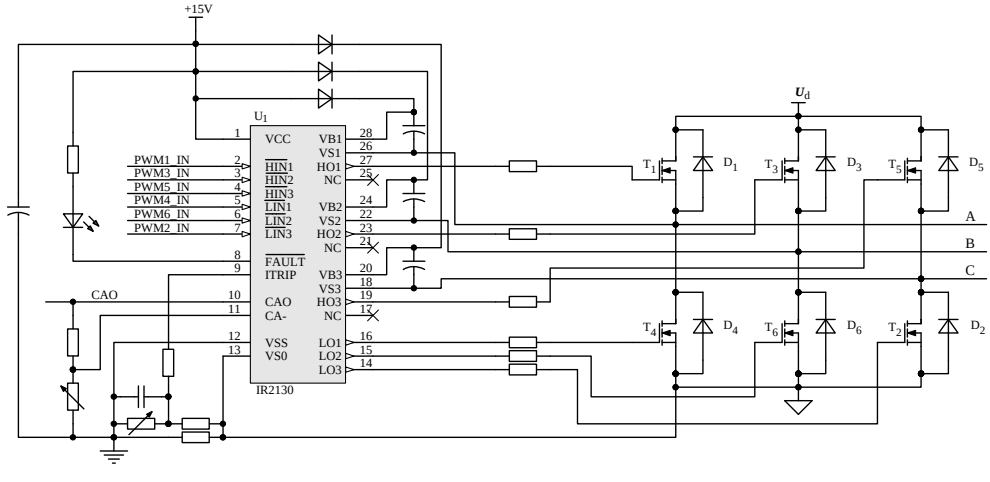


Figure 7.6 IR2130 driving circuit.

7.2.2 IGBT Driving Circuit

Similar to MOSFETs, an IGBT driving circuit can be constructed not only by discrete components but also by integrated IGBT drivers that have better performance, smaller volume and higher reliability. Among various IGBT drivers, EXB series drivers produced by Fuji Corporation are widely used, among which EXB841 is one kind of high-speed driver.

EXB841 can drive an IGBT circuit with the current and voltage level of 400 A, 600 V or 300 A, 1200 V. It can be applied extensively to the 40 kHz switching operation as its delay time of driving circuit signal is less than 1 μs. Figure 7.7 shows a typical application circuit of EXB841, and the following aspects should be remembered when using EXB841 [4].

(1) The driving circuit wire between the grid pole and the source pole of IGBT should be stranded wire and its length should be less than 1 m.
(2) The value of grid series resistance R_G should be increased if a high-voltage peak pulse is engendered in the drain pole of the IGBT.
(3) The function of C_1 and C_2 is to absorb voltage changes aroused by power supply-line impedance, instead of filtering.
(4) The input and output circuits should be far isolated in space under high operating voltage, though they are separated by an optocoupler.

7.2.3 Intelligent Power Module (IPM)

An intelligent power module (IPM) can be used as driving circuit to improve the reliability of a bridge inverter. The IPM, a kind of modularized device, is integrated by the IGBT and circuits that have the functions of signal processing, self-protection and diagnosis. It can perform the functions of inverter circuits, driving circuits and other control circuits for a BLDC motor,

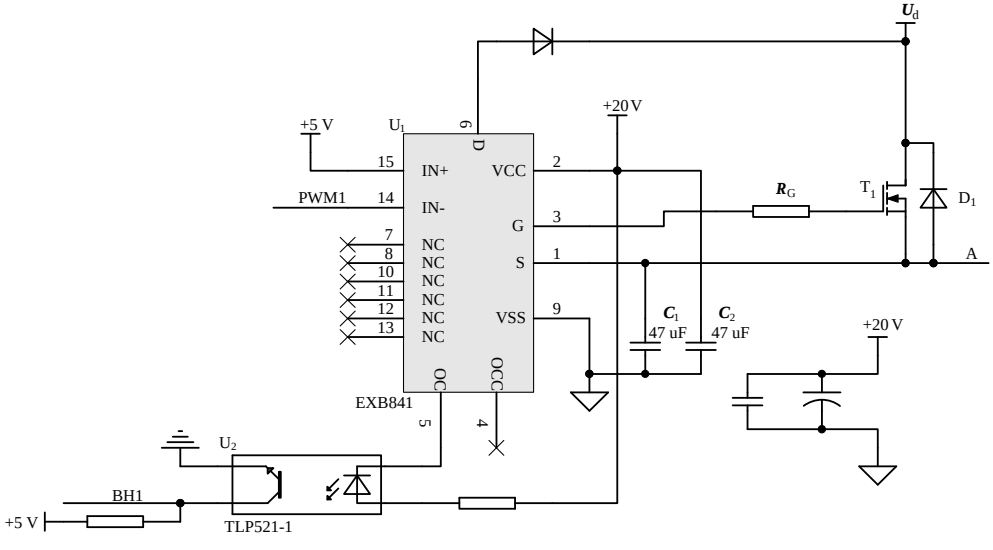


Figure 7.7 EXB841 applied circuit.

which gives the motor controller the advantages of small volume, light weight, simple design and high reliability. Therefore, an IPM is one of the ideal devices for high-performance BLDC motor driving.

Many companies produce IPMs. For example, Fuji Corporation has already manufactured complete IPM series products that have two voltage levels of 600 V and 1200 V and more current specifications from dozens to hundreds of amperes. Among them, 7MBP75RJ120, is a medium-volume IPM, with its withstanding voltage and flowing current as high as 1200 V and 75 A, respectively. Its principle terminal is screw M5. All electrical connections are screws and connectors without soldering, which is easy to assemble and disassemble. Furthermore, overheat protection is designed in the module, which makes it very easy to use. Its typical application circuit is shown in Figure 7.8

7.3 Rotor-Position Sensor Circuit

In the control system of a BLDC motor with position sensors, in order to get the maximum torque, microprocessor controls the BLDC motor to commutate depending on the signals of the position sensors. Torque ripple can be reduced by the proper commutation instants obtained from the position-sensor signals. Therefore, accurate position detection is very important [5,6].

Position sensors in BLDC motors are used to detect the relative position of the rotor magnet and provide the correct commutation information for the logic switching circuit, namely transforming the position signals of rotor magnet to electric signals and then making stator windings commutate properly. The commonly used position sensors mainly fall into electromagnetic, photoelectric and magnetic types. A Hall position sensor, as one kind of magnetic-type sensors, is applied extensively for its simple structure and low cost.

A Hall position sensor, shown in Figure 7.9, is constituted by a Hall integrated circuit fixed on stator and sensor rotor fixed on the main rotor in most BLDC motors. The sensor indicates the main rotor's position since its rotor is rotating with the motor rotor synchronously. Several Hall integrated circuits are fixed on the motor's stator at equal intervals and the sensor will produce a group of jumping signals when the main rotor passes by a pair of magnets. The more pole pairs of the main rotor, the more jumping signals are generated within 360° mechanical angles. In an electrical cycle, a Hall position sensor generates different switching states that have equal electrical angle from one to another. Take the three Hall position sensors with intervals of 120° electrical angles in space for example, each Hall position sensor will generate an output signal with 180° electrical angles pulse width during every electrical cycle. As a result, the three output signals generated by the three Hall position sensors are at 120° electrical angle intervals, which will produce three rising edges and three falling edges, corresponding to six commutation instants. Note that position detection is not only used for commutation but also applied in velocity feedback control.

Rotor position feedback signals, whose electrical level and jumping instants determine the commutation state and instant of the motor, are fed into the corresponding input interface of the microprocessor. As shown in Figure 7.10, the output signals H_A, H_B and H_C of a Hall position sensor are processed through fast optocoupler isolation, then $H'_A H'_B$ and H'_C are obtained after rectifying and capacitor filtering to remove high-frequency interference, after which they are input into the microprocessor for calculation.

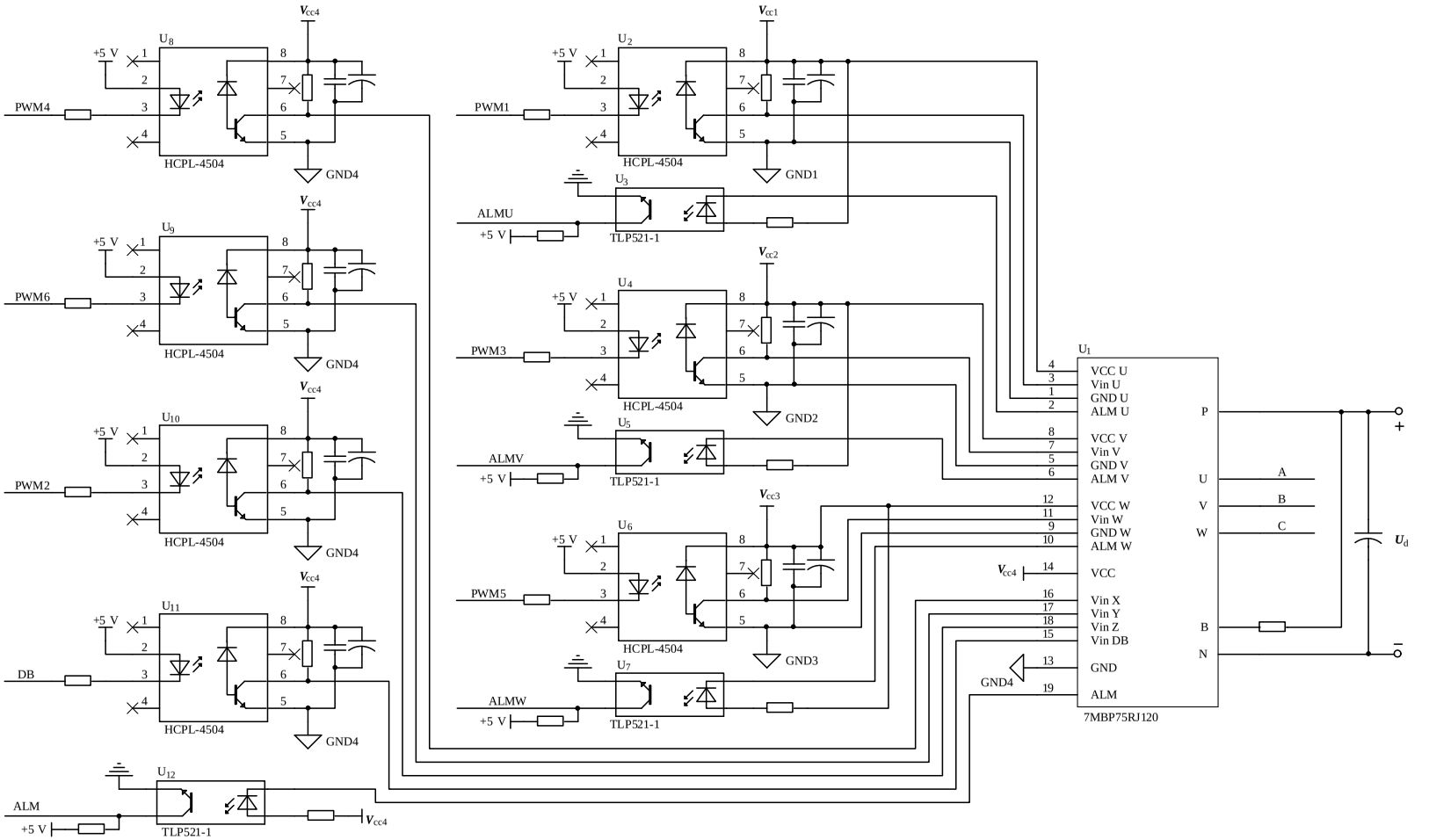


Figure 7.8 7MBP75RJ120 applied circuit.

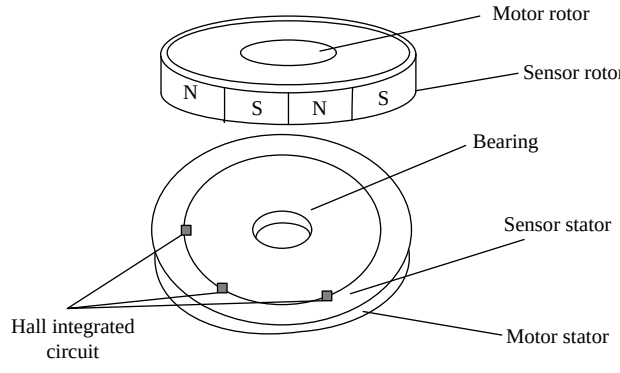


Figure 7.9 The structure of a Hall position sensor.

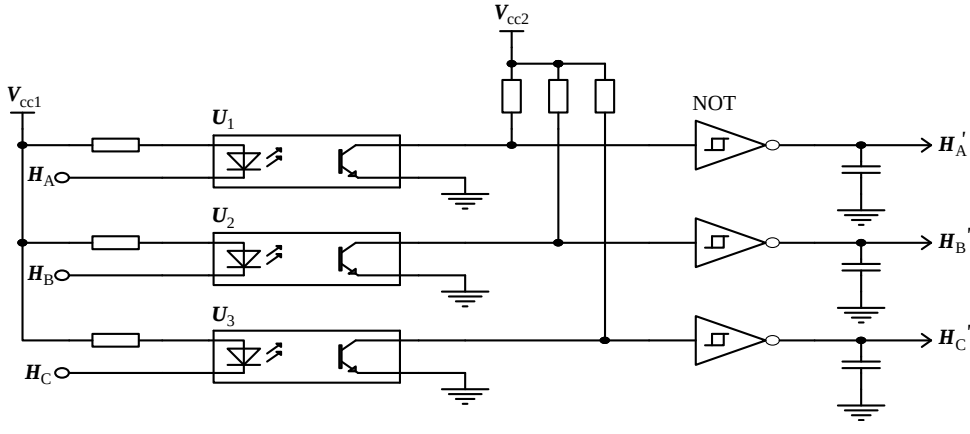


Figure 7.10 Rotor-position detecting circuit.

7.4 Microprocessor Control Circuit

7.4.1 Introduction

A microprocessor control circuit mainly consists of a microprocessor, interface circuits and peripheral components. The microprocessor is the core component of the whole circuit. It can process the input data, complete various complex algorithms, send the control signals to the driving circuit through the output port, send calculated results to peripheral components, accept instruction from peripherals and act accordingly. So, proper selection of the microprocessor is very important for normal operation of the whole circuit and the desired control performance [7].

It is necessary to confirm the technique requirements of a BLDC motor control system at the microprocessor choosing stage. The technique requirements mainly include functions that the system needs and performances that the system would obtain. Specifically, the requirements consist of the control strategy, structure, various control tasks, response time and steady-state accuracy of the control system, etc. Then, it is desired to make a comprehensive consideration of

the microprocessor types. On the one hand, a microprocessor with much too high performance should not be chosen since it would lead to increased complexity, higher cost and performance waste. On the other hand, a microprocessor with much too low a performance should not be chosen, or the technique requirements of the system may not be satisfied. In summary, the following six aspects should be considered when choosing the microprocessor.

(1) Whether the microprocessor instruction set is abundant and whether it is easy enough to achieve the algorithm of the system should be noted. Meanwhile, it shouldn't be difficult to memorize and program, and confusion can be easily avoided.
(2) Whether the rated frequency and the operation speed can satisfy the requirements of the BLDC motor control system.
(3) Whether the on chip source of the microprocessor is sufficient, where the source mainly covers the extensible memory space, the number of I/O ports, electrical level compatible standards, the channels and digits of A/D and D/A circuits.
(4) Whether the power dissipation, volume and working temperature of microprocessor can meet the requirements of the system.
(5) Whether different business grade and industrial grade of the same type of microprocessor can be compatible in packaging.
(6) The time to market, reliability, product volume and price of the microprocessor.

Generally, the performance of the selected microprocessor should be a little higher than the system requirements, consequently hardware performance can be used to compensate part of the software functions to a certain extent, and make the system extensible and updatable in the future.

At present, the microprocessor suitable for a BLDC motor control system falls into mainly microcontroller unit (MCU) and digital signal processor (DSP).

A MCU, which has the characteristics of high integrated level, powerful functions, reasonable structure, rich instructions, large memory capacity, fast speed and strong anti-disturbance ability, is a chip integrated with CPU, ROM, RAM, I/O port and programmable timer/counter, some even include an A/D converter. Now, Inter, Motorola, TI and other corporations have had their own series MCU that are widely used in industrial control systems. For some motor control systems with a relatively simple control algorithm, a MCU is an economical choice.

A DSP chip is a microprocessor that is especially applied to digital signal processing. Its main application is to achieve various kinds of digital signal processing timely and fast. At present, the major DSP chip suppliers are TI, AD and Motorola, etc. Among them, TI Corporation, which accounts for the biggest shares of DSP chip market in the world, has multiple series and a rich variety of DSP chips. According to the requirements of digital signal processing, DSP chips generally have the following characteristics.

(1) Harvard architecture with separated data bus from the program bus is widely used, which has faster instruction execution speed comparing to the traditional Von Neumann architecture.
(2) Assembly-line operation is mostly used to make the fetch, decoding and execution parallel operation and to reduce the execution time of every instruction without increasing the clock frequency.

(3) There are multiple on-chip buses, so that multiple operations can be executed in parallel.
(4) Independent multiplier and adder are equipped in a DSP, which make it easy to finish a multiply and plus calculation within one clock cycle and to achieve filter and matrix operation that need a large number of multiply-accumulate operations at faster speed.
(5) Direct memory access (DMA) controllers are mostly equipped with the on-chip multibus architecture, which makes the transmission speed of the data block greatly improved.
(6) Hardware supports low overhead or zero overhead loop and jump.
(7) Fast interrupt processor and timing controller are integrated in DSP, which makes it convenient to construct a small-scale system.

Compared to universal microprocessor, DSP chip has relatively poor abilities of the controlling and processing multitransactions. However, DSP chips produced in recent years have absorbed some general microprocessor functions. Due to the above characteristics, DSP chips are widely applied in high-speed and high-accuracy motor control systems.

7.4.2 MCU Control Circuit

Among the series of microcontroller units, MSP430F1xx series from TI Corporation is a kind of ultra-low-power mixed-signal controller that can operate in an ultralow-power state under low-voltage conditions. There are multiple kinds of MCU of this series available, which are extensively used in BLDC motor control systems, to be selected to meet the requirements of different users. The MCU of this series has 16-bit RISC structure and it can obtain high code efficiency by using 16 registers and a constant generator in CPU. The power dissipation of the devices can be minimized by selecting proper clock sources to meet the requirements of a given battery power-supply system. When the device operates in low-power dissipation mode, it can be woken rapidly by a digitally controlled oscillator (DCO). The wake-up time is less than 6 μs and then the device is switched to activation mode. The MSP430F149 is introduced to illustrate the BLDC motor control system based on a MCU as follows.

MSP430F149 mainly consists of one basic clock module that is constructed by one DCO and two crystal oscillators, one watchdog timer, two 16-bit comparators with capture/compare register, two 8-bit parallel I/O ports with interrupt function, four general 8-bit parallel I/O ports, one analog comparator, one 12-bit A/D converter, two serial communication ports with asynchronous, synchronous and SPI operation modes and one hardware multiplier.

MSP430F149 has advantages depicted as follows: rich addressing ways with only 27 instructions, which make it easy to remember, large number of inner registers, which can achieve multiple operations, look-up table approach processing methods with high efficiency, many interrupt sources, which can be nested arbitrarily and used flexibly. All these characteristics ensure that a motor control program with high efficiency can be worked out.

Figure 7.11 shows the hardware circuit principle diagram of a BLDC motor sensor control system based on MSP430F149. Port P1 of a MCU contains a capture unit that is used to capture the rotor-position signal output by a Hall position sensor. Port P4 can generate PWM waves to drive the bridge inverter. System fault signals are input into port P2 as interrupt signals. Port P3 is used to communicate with PC. Port P5 is used to accept keyboard instruction that leads the control program to act correspondingly. The function of each part is introduced in detail as follows.

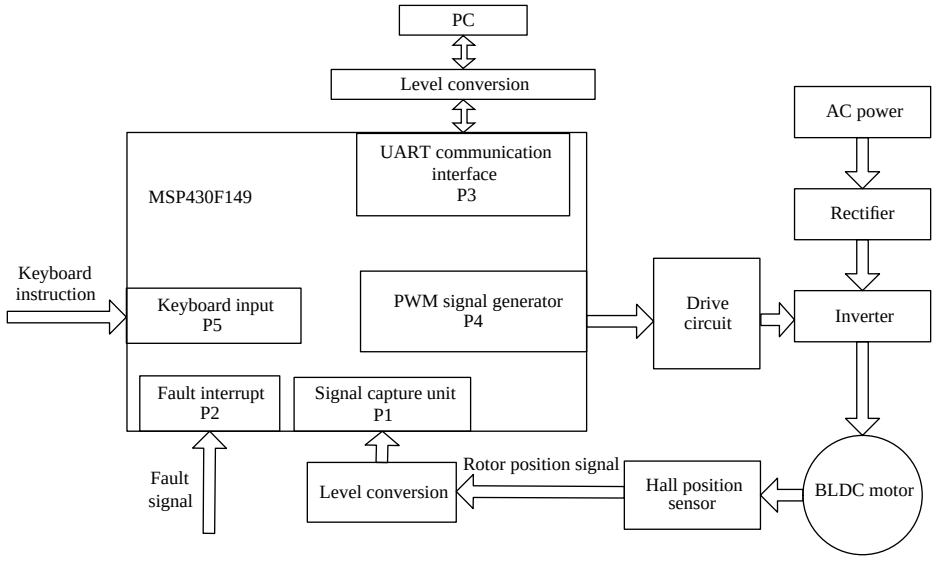


Figure 7.11 The hardware circuit principle diagram of a BLDC motor sensor control system based on MSP430F149 MCU.

7.4.2.1 Commutation Control

The windings of a BLDC motor are usually Y connected and the two-phase conduction mode is generally used. That means each conducting cycle has six conduction states. One state is changed as the rotor rotates 60° electrical angles. A MCU writes continuously the corresponding control words to port P4 based on the output signals of position sensors to complete commutation operation. If MOSFETs in a bridge inverter are arranged as the sequence of Figure 7.3 and the ports P4.1–P4.6 correspond to the grid control signals of T1–T6, the control words under the two-phase conduction mode could be as expressed in Table 7.1. Note that the control words of port P4.0 and P4.7 are always zero.

7.4.2.2 Steering Control

Reverse rotation of a BLDC motor can be achieved by only changing the conducting sequences of MOSFETs according to certain laws. The control words of reverse rotation are shown in Table 7.2.

Table 7.1 Control words under two-phase conduction mode (forward)

Conduction phases	P4.6	P4.5	P4.4	P4.3	P4.2	P4.1	Control words
AC	0	0	0	0	1	1	06H
BC	0	0	0	1	1	0	0CH
BA	0	0	1	1	0	0	18H
CA	0	1	1	0	0	0	30H
CB	1	1	0	0	0	0	60H
AB	1	0	0	0	0	1	42H

Table 7.2 Control words under the two-phase conduction mode (reverse)

Conduction phases	P4.6	P4.5	P4.4	P4.3	P4.2	P4.1	Control words
AC	0	0	0	0	1	1	06H
AB	1	0	0	0	0	1	42H
CB	1	1	0	0	0	0	60H
CA	0	1	1	0	0	0	30H
BA	0	0	1	1	0	0	18H
BC	0	0	0	1	1	0	0CH

7.4.2.3 Capture Unit and PWM Wave Output Control

Capture unit interior to port P1 of MCU is used to detect the jumping edges of the Hall position sensor input signals. The jumping edges can be the rising-edge, falling-edge or bi-edges. Once the corresponding jumping edges are generated, the counting value is recorded and interrupt signals are produced. Then, the rotor magnet position is instantly monitored, which greatly reduces the system overhead.

Port P4 can be designed to run in PWM output mode, which is able to generate three-phase symmetrical PWM waves by programming. Figure 7.12 shows the process of signals when adding counting mode and set/reset output mode are used. Initially, the values of TBCL0 and TBCL1 are set, and then the signal generator begins to operate according to settings and the timer starts to count. When the counting value is equal to TBCL1, the output is set depending on the desired mode. However, when the counting value is equal to TBCL0, the output is reset and the timer counts again and then PWM signals are formed in cycles.

7.4.2.4 Serial Communication Interface Circuit

MSP430F149 has two universal serial communication ports, but it cannot communicate with the PC directly for their voltage levels do not match. Therefore, serial interface level conversion chips are needed, among which MAX3232 produced by Maxim Corporation

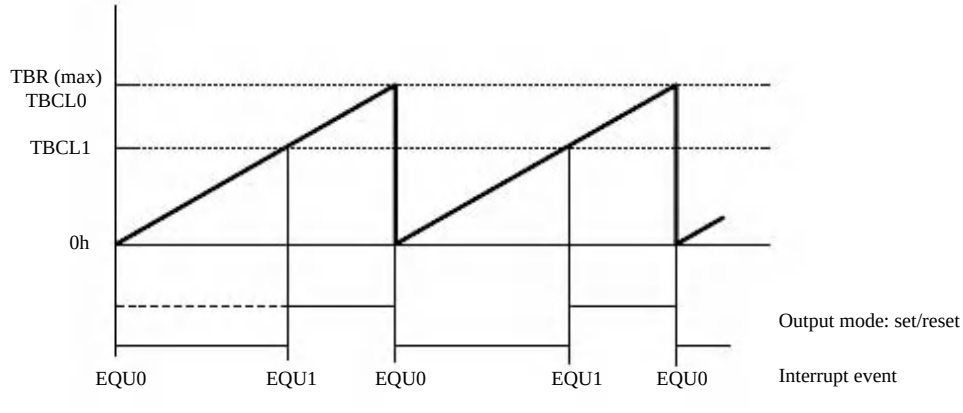


Figure 7.12 Adding counting-mode output example.

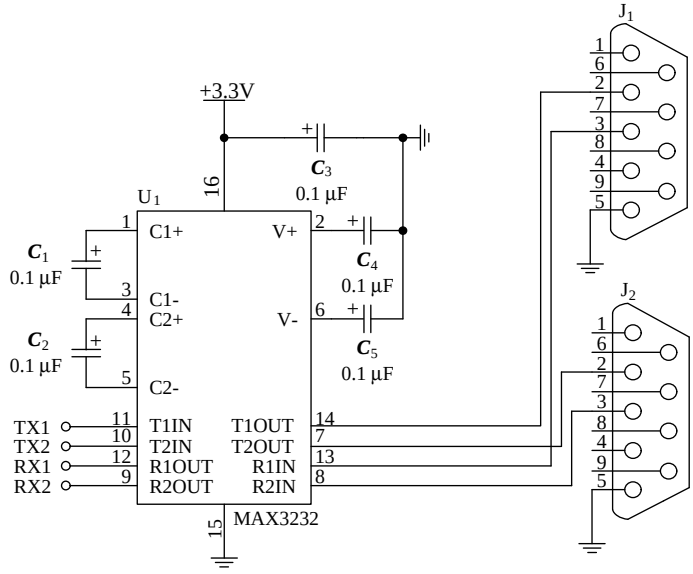


Figure 7.13 MAX3232 serial communication interface circuit.

achieves preferable performance for its simple structure, low power loss, high integrated level, and two receiving and sending channels without extra power supplies. Figure 7.13 is a typical application of the chip.

7.4.3 DSP Control Circuit

Among the numerous DSP products, TI Corporation has the most abundant products. The TMS320F240x and TMS320F281x series are widely applied in BLDC motor control systems. The BLDC motor control circuit based on TMS320F2812 is described as follows [8].

TMS320F2812, which has great signal processing and control functions, is produced by TI Corporation and can supply a motor control system with a good platform. Its code and instructions are completely compatible with those of TMS320F240x series DSP, which ensures the continuity of the project or product design. Compared to TMS320F240x series DSP, TMS320F2812 improves the accuracy of calculation (32 bit) and the processing speed of the system (150 MIPS).

TMS320F2812 mainly consists of one FLASH memory of 128k×16 bit, one ROM of 128k×16 bit, one OTP ROM of 1k×16 bit, two single-cycle access RAM (L0 and L1) of 4k×16 bit, one single-cycle access RAM (H0) of 8k×16 bit, two single-cycle access RAM (M0 and M1) of 1k×16 bit, two event-manager modules, a variety of serial communication interfaces, a high-speed and high-accuracy A/D converter module and a variety of configurable universal I/O pins.

Figure 7.14 shows the hardware circuit block diagram of a BLDC motor sensorless control system based on TMS320F2812. In this system, the rotor-position signal is detected by the back-EMF method, and double closed-loop speed-control system is constructed via TMS320F2812. A DSP control system is similar to the corresponding MCU control system,

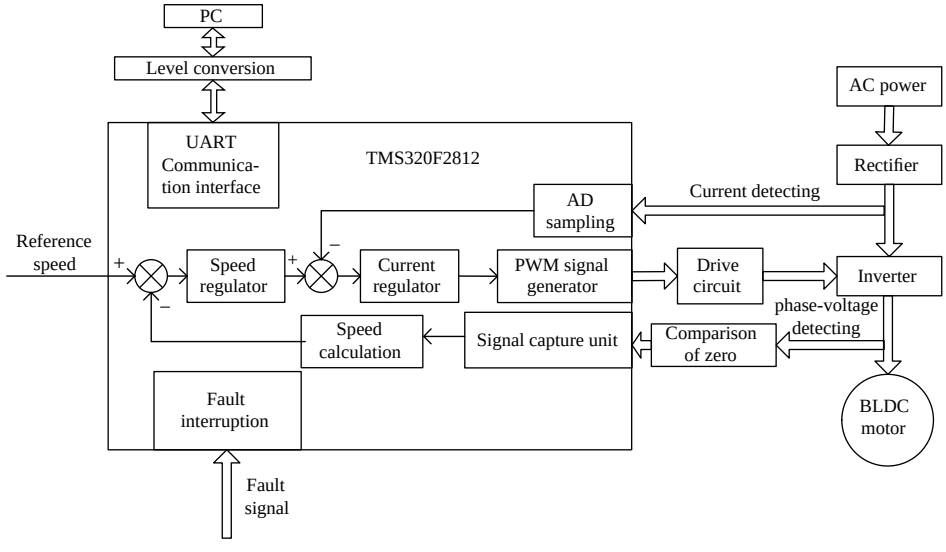


Figure 7.14 Hardware circuit block diagram of BLDC motor control system based on TMS320F2812.

so they can refer to each other when being designed. Meanwhile, their different features should also be noticed.

A BLDC motor control system based on TMS320F2812 DSP needs fewer external components and has a high cost–performance ratio. The high-speed performance of a DSP is the basis of the implementation of real-time intelligent control strategies which largely improves the control accuracy, functions and anti-interference performance of the system. Figure 7.15 shows the application circuit.

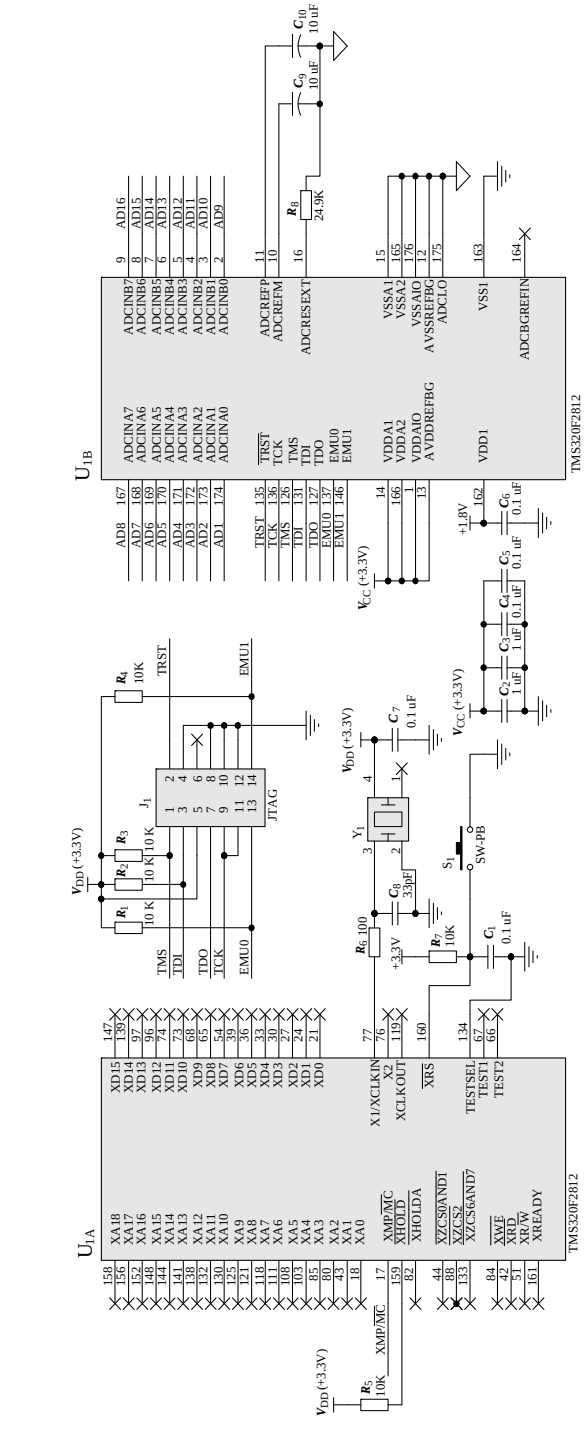
7.5 Protecting Circuit

There are always abnormal conditions during the work of BLDC motor control system, which may cause great damage to the control circuit, driving circuit and the motor. So, proper measures must be taken for protection. The common protection circuits contain an overvoltage protection circuit, an overcurrent protection circuit and a logic protection circuit, etc. These circuits are illustrated as follows.

7.5.1 Overvoltage Protection

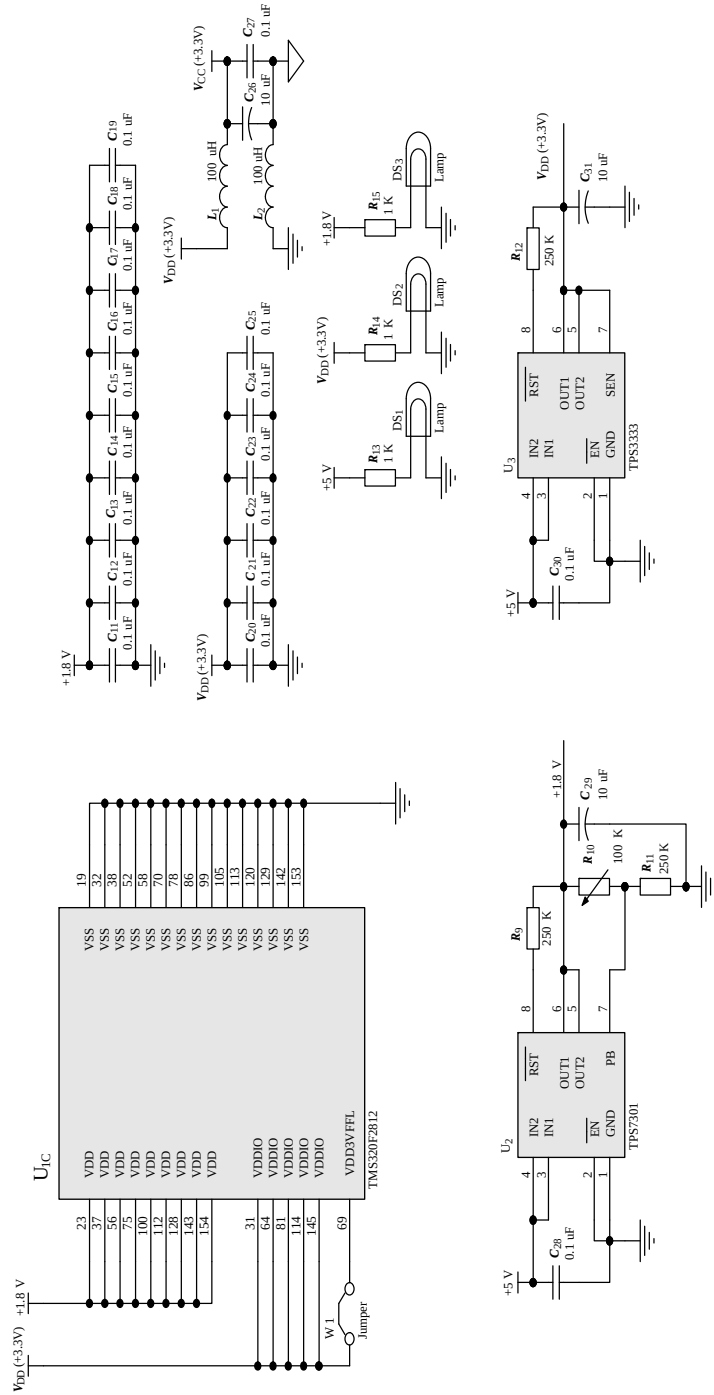
The principle of overvoltage protection circuit can be explained as follows. The DC bus voltage could be obtained by the sampling circuits, which would be compared with the reference voltage. If the sampling value is greater, the comparator will output an overvoltage protection signal to the microprocessor, and then the microprocessor can achieve the overvoltage protection.

The DC bus voltage can be obtained in two ways. The first method is to place a resistance voltage divider on the DC bus, and transfer the measurement into the comparator. The output



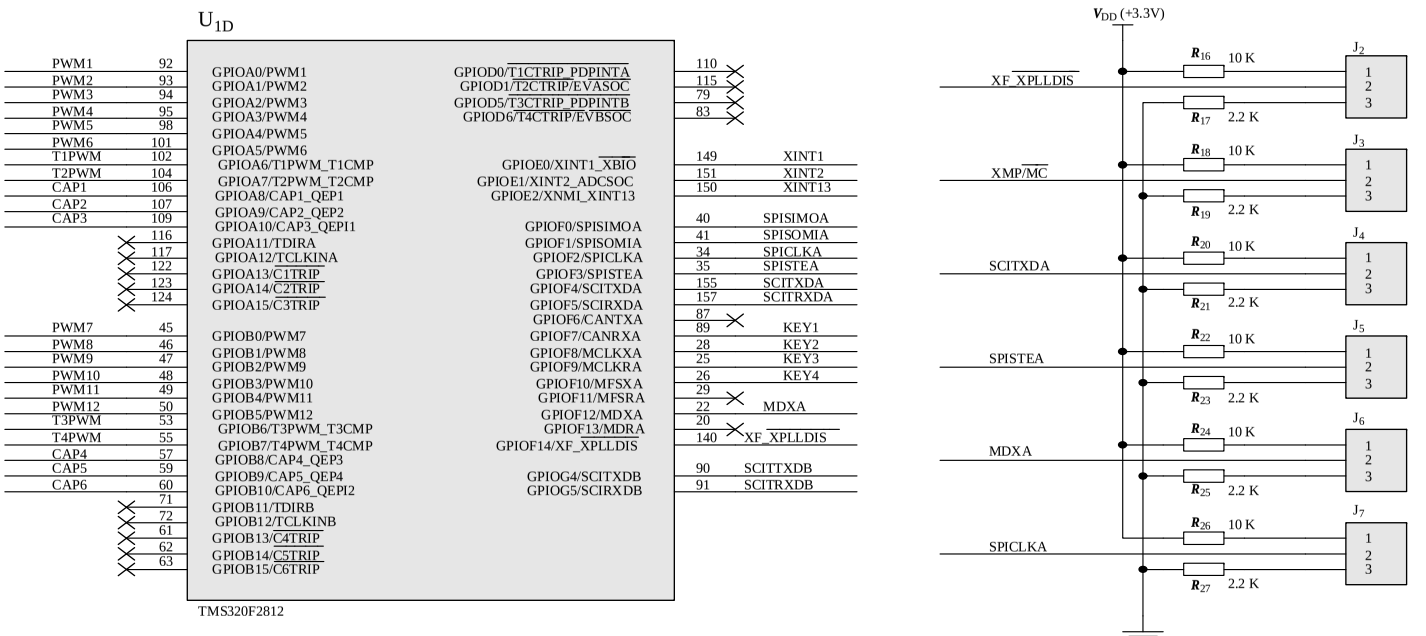
(a) Debugging interface and analog interface

Figure 7.15 TMS320F2812 application circuit.



(b) Power-supply circuits

Figure 7.15 *Continued.*



(c) External circuit interface

Figure 7.15 *Continued.*

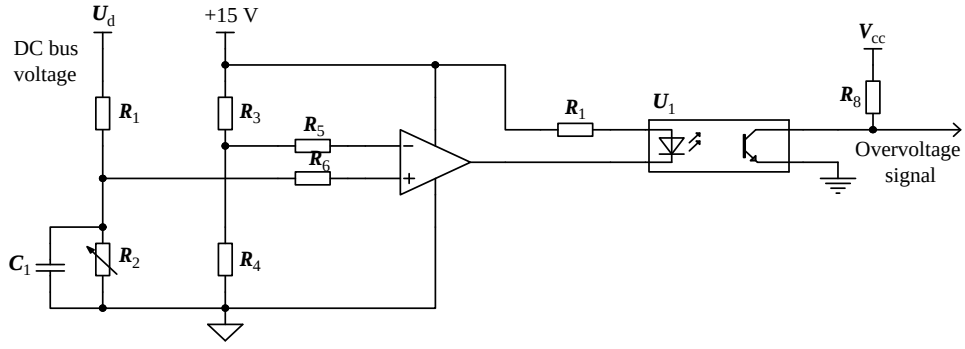


Figure 7.16 Direct detection circuit of the DC bus voltage.

signal of the comparator will be transmitted to the microprocessor by the optocoupler. The optocoupler can ensure the isolation between the control circuit and the main circuit. The diagram of this detection circuit is shown in Figure 7.16.

The second method can be achieved by the voltage sensor with electrical isolation architecture, so there is no need to use the optocoupler. However, the outputs of the voltage sensor not only could be put into the comparator after amplifying, but also can be transmitted into the A/D module of the microprocessor directly, which could obtain a more accurate voltage value of the DC bus. This method has higher flexibility than the first one, but its circuit will be relatively complex. Figure 7.17 shows the diagram of the measurement circuit for the DC bus voltage with a Hall voltage sensor.

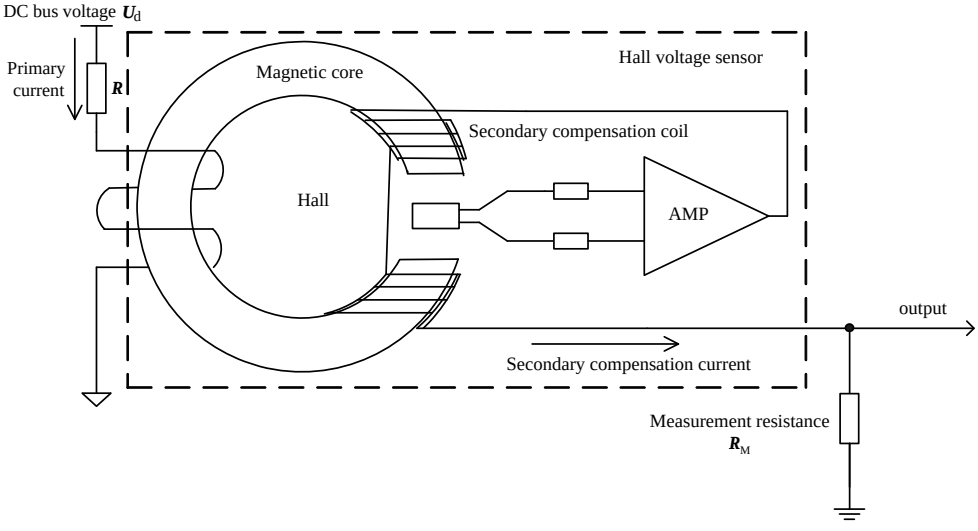


Figure 7.17 Measurement circuit of DC bus voltage with a Hall voltage sensor.

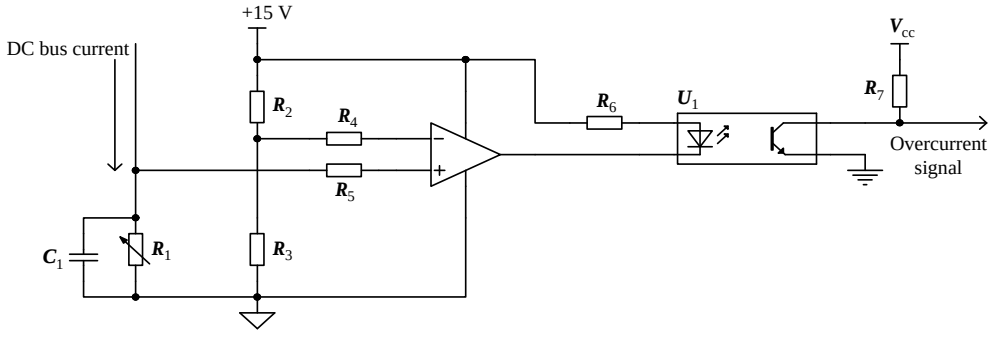


Figure 7.18 Direct detection circuit of a DC bus current.

7.5.2 *Overcurrent Protection*

The overcurrent protection circuit is similar to the overvoltage protection circuit, and it also has two methods. First, we can use the sampling resistance to convert current signals into voltage signals on the basis of a voltage divider, so the operation status of the system can be judged by the voltage signals. The circuit diagram of this method is shown in Figure 7.18. Since the current of the sampling resistance must not be too large, this method is usually applied on low-capacity motor control systems.

Similar to the overvoltage protection circuit, the overcurrent protection circuit uses the current sensor to detect the DC bus current. This method has higher flexibility and better safety, so it has a relatively wider application. In addition, it could make sampling values obtained from the current sensor as the current data in double-closed loop system, so we could simplify the design of the speed-control system through calculating and controlling the sampling data directly.

During the starting process of a motor, the back-EMF is small, but the starting current is large, so the motor might be damaged heavily at this moment. One always needs to add an overcurrent protection circuit which is shown in Figure 7.19, to the motor control system. In the figure, u_0 represents the reference voltage. When the current of the system is large, the voltage drop of the divider R_1 is also very large. Once the feedback voltage u_1 becomes larger than the reference voltage u_0, the comparator will output a low-level voltage to shutdown the power transistors T_2, T_4 and T_6 in order to reduce the current of the main circuit. On the contrary, if the feedback voltage u_1 is smaller than the reference voltage, the comparator would output a high-level voltage, T_2, T_4 and T_6 will work normally. The protection system has a great advantage as it doesn't need a microprocessor to judge whether the system works in an overcurrent status or not. So, the protection system could take an action rapidly according to the value of output of the comparator even if the program of the system goes wrong. A current-detection circuit shown in Figure 7.19 is usually used in the low-capacity motor system. As for high-capacity motor systems, it is better to use the current sensor to detect the current of the system.

7.5.3 *Logic Protection*

The motor control system involves many complex logic circuits, and the circuit for the generation of PWM driving signals is the most important one. As for the circuit shown in

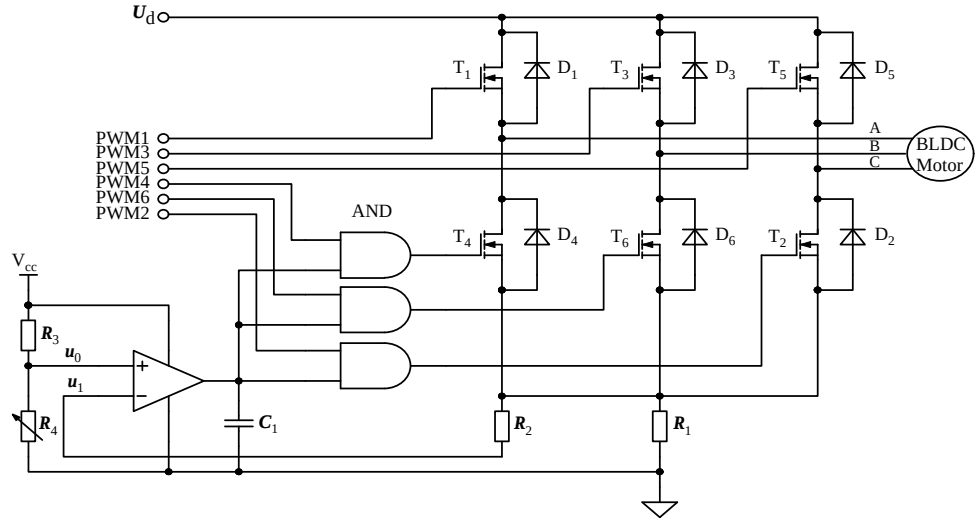


Figure 7.19 Overcurrent protection circuit in the starting process.

Figure 7.19, if the two power switches in the same leg (such as T_1 and T_4) conduct at the same time, it will cause a short circuit. The short current would be very significant. Therefore, many microprocessors nowadays always set the dead time for the PWM generation unit in order to avoid being shorted. In addition, when the motor starts or the program goes wrong, the logic protection circuit shown in Figure 7.20 is usually used for protection too. It can be seen from the figure that if the power switches in the same leg work at the same time, the XOR gate will output a low-level voltage. After two AND gates, all of the control signals in this leg would become low-level voltages. Thus, this logic protection circuit can protect the PWM unit from being shorted effectively, and its realization is simple.

7.5.4 Other Protection Circuits

7.5.4.1 Optocoupler Isolation Circuit

To avoid the high voltage or current signals in the main circuit disturbing the low voltage or current signals in the control system, it usually applies the optocoupler isolation circuit to isolate them from each other, which would also improve the security of the system.

The use of optocoupler isolation is relatively simple. However, two points should be noted. The first is whether the optocoupler can satisfy the requirements of system. It is better to use a

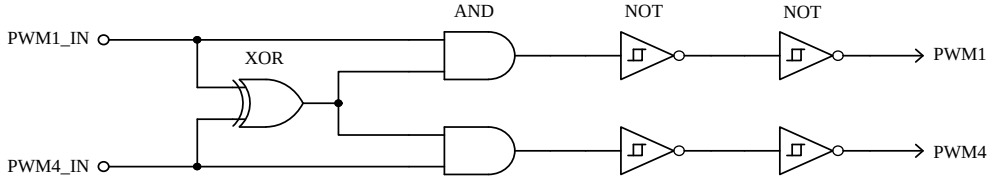
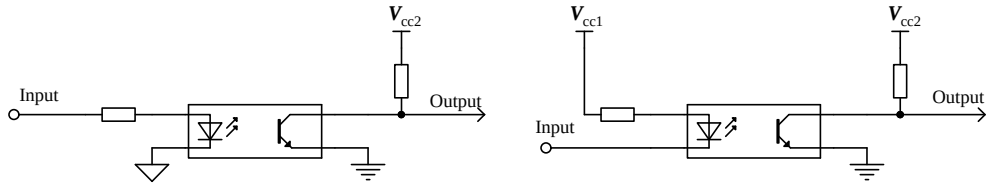


Figure 7.20 Logic protection circuit.



(a) High-level drive mode (b) Low-level drive mode

Figure 7.21 Optocoupler application circuit.

high-speed optocoupler especially in some situations that need high switching speed. The second is that the drive type for the input signals of the optocoupler must be determined. Since the optocoupler is a current-driven device, the connection mode shown in Figure 7.21(a) should be used when the input signals are high-level effective. On the contrary, the connection shown in Figure 7.21(b) should be used. Note that if the input signal has both high-level and low-level driving ability, then either mode could be used. But what should be paid attention to is the logical relationships between the input and output signals.

7.5.4.2 Capacitor Charging Protection Circuit

The relationship between capacitor current i_c and voltage u_c is

$$i_c = C\frac{du_c}{dt} \tag{7.1}$$

In the high-capacity system, the voltage of the DC bus is quite large, so the voltage change rate of the capacitor is large at the instant of power-on. In this condition, the filter capacitance value is also large. Thus, it can be obtained from Equation (7.1) that the instantaneous current of the capacitor is also very large. Consequently, it may cause damage to the devices, so a capacitor charging protection circuit is demanded with regard to the filter capacitor, which is shown in Figure 7.22. In Figure 7.22, K_1 represents the double-contact relay. At the instant of power-on,

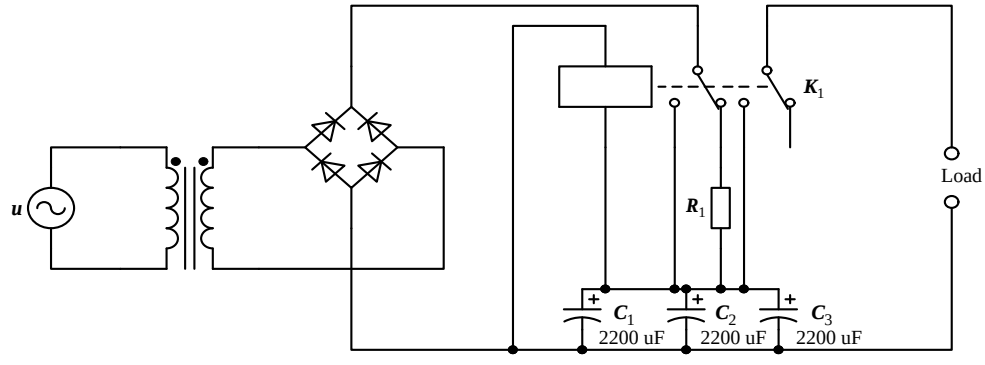


Figure 7.22 Capacitor charging protection circuit.

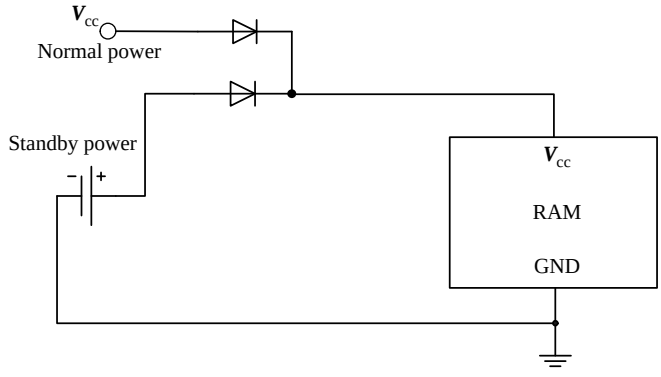


Figure 7.23 Power-off protection circuit.

the capacitor was charged by the bridge rectifier through the resistance R_1 and the normally closed (NC) contact of the relay, thus the current of the capacitor is limited. When the current of the capacitor gets higher than the action value of the relay, the relay will switch the NC contact to the normally open (NO) contact rapidly, so that R_1 will be disconnected, and the capacitors that are paralleled cross the power source directly play the role of filtering.

7.5.4.3 Power-off Protection Circuit

In motor control systems, it is necessary to store some important data or intermediate results of calculations in the memory chip independent of the microprocessor sometimes. Hence, in order to avoid the read and write errors of important data in the memory because of voltage instability, or the data loss due to power off, a power-off protection circuit of the memory should be set. The corresponding circuit diagram is shown in Figure 7.23, where standby power is needed besides the normal power. The standby power is applied in the event of normal power failure, which makes sure the system works normally. Note that the voltage of the standby power should be a little lower than that of the normal power supply.

7.6 Sensorless Control Circuits

7.6.1 Voltage Detection

The types of position sensors commonly used in BLDC motors are electromagnetic, photoelectric, magnetic, etc. The BLDC motor adopting the electromagnetic position sensor needs to install the opening transformer, a ferroresonance circuit, proximity switches and other sensor components on the stator. Considering the large volume and its poor anti-interference ability, it is rarely used nowadays. Similarly, the large volume of the photoelectric position sensor limits its application, especially the sinusoidal position sensor of which the high price and poor reliability cannot be ignored. In contrast, a Hall magnetic position sensor is small in size and convenient to use, but it usually has certain nonsensitive magnetic areas that may cause detection errors of rotor position. All in all, the position sensor will cause several problems to a motor, such as more difficulty in system maintenance, increase of motor size,

and more complex motor design. In addition, the position sensor could hardly be embedded in the small-scale motor systems, and it is difficult for a position sensor to adapt to the harsh working environment. So position-sensorless control strategies are demanded in many applications for BLDC motor systems [9–11].

It is necessary to detect certain variables related to the rotor position to obtain the rotor position in the sensorless control of a BLDC motor. The back-EMF-based strategy is the most commonly used, and it can detect the position of the rotor through the waveform of the back-EMF. However, the back-EMF cannot be detected directly in practice. Hence, indirect methods for detecting and calculating the waveforms of back-EMF are required. The work in this section is all based on the assumptions that the motor has a three-phase Y-connected winding, and a two-phase conduction mode is used to drive the motor.

7.6.1.1 Back-EMF Detection Circuit Based on Terminal Voltage

The waveforms and commutation points of BLDC motor are shown in Figure 6.1. It can be seen from the figure that the commutation points lag 30° electrical angles behind the zero-crossing points of the back-EMF. Hence, the accurate detection of the zero-crossing points is very important.

The back-EMF detection circuit based on the terminal voltages is shown in Figure 7.24. The zero-crossing detection equations of the back-EMF are obtained as

$$\begin{cases} e_{\mathrm{A}} = u_{\mathrm{AG}} - \dfrac{1}{2}(u_{\mathrm{BG}} + u_{\mathrm{CG}}) \\ e_{\mathrm{B}} = u_{\mathrm{BG}} - \dfrac{1}{2}(u_{\mathrm{AG}} + u_{\mathrm{CG}}) \\ e_{\mathrm{C}} = u_{\mathrm{CG}} - \dfrac{1}{2}(u_{\mathrm{AG}} + u_{\mathrm{BG}}) \end{cases} \tag{7.2}$$

where u_{AG}, u_{BG} and u_{CG} represent the terminal voltages of the motor.

From Equation (7.2), it is known that only u_{AG}, u_{BG} and u_{CG} are needed in order to get the zero-crossing points of the back-EMF. In practice, u'_{AG}, u'_{BG} and u'_{CG} are obtained after the terminal voltage dividing and filtering, and then the subtraction circuit is built according to Equation (7.2), through which the zero-crossing points of the back-EMF is obtained. Note that the point G in the circuit is connected with the negative pole of U_{d}.

7.6.1.2 Back-EMF Detection Circuit Based on Phase Voltage

Further, in order to reduce disturbances, we can break the connection between point G and the negative pole of U_{d}, and then the back-EMF detection circuit based on phase voltage is formed. Assume that u_{N} is the neutral point voltage of the motor windings. Then, according to the symmetry principle, the voltage of point G has relationship as $u_{\mathrm{G}} \approx u_{\mathrm{N}}$ when the back-EMF crosses zero. Thus, we can obtain

$$\begin{cases} e_{\mathrm{A}} = u_{\mathrm{A}} \\ e_{\mathrm{B}} = u_{\mathrm{B}} \\ e_{\mathrm{C}} = u_{\mathrm{C}} \end{cases} \tag{7.3}$$

where u_{A}, u_{B} and u_{C} represent the phase voltages of the motor.

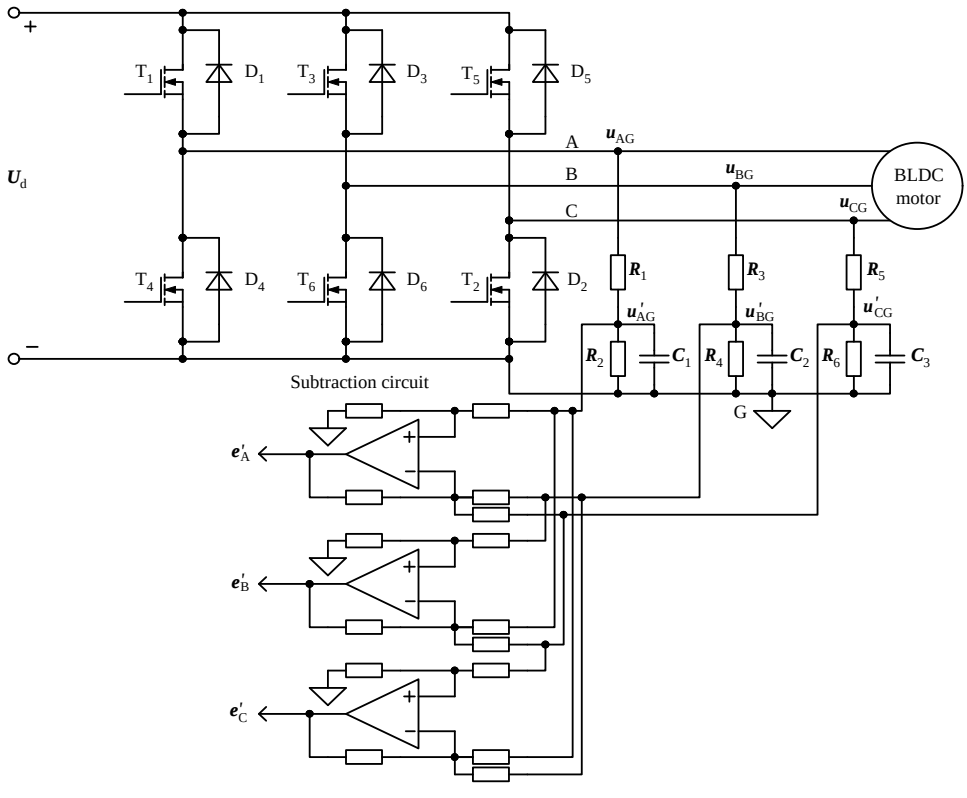


Figure 7.24 Back-EMF detection circuit based on terminal voltage.

The corresponding circuit is shown in Figure 7.25, where the detection signals u'_A, u'_B and u'_C are, respectively, proportional to the phase voltages u_A, u_B and u_C after voltage dividing. Then we can obtain the zero-crossing points of the back-EMF with Equation (7.3).

7.6.2 Filtering and Phase Shifting

7.6.2.1 Calculation of Phase-Angle Delay

In order to improve the signal quality, high-frequency electromagnetic interferences are removed by filtering, resulting in the phase shifting of the signals at the same time, which should be corrected appropriately.

According to the circuits shown in Figures 7.24 and 7.25, it is easy to calculate the phase-shift angle of the detected signals. Take phase A in Figure 7.25 as an example, the relationship between the original signal and processed signal, which is calculated according to the fundamental frequency of the back-EMF can be expressed as

$$\frac{u'_A}{u_A} = \frac{R_2}{R_1 + R_2 + j2\pi f R_1 R_2 C_1} \tag{7.4}$$

where f represents the frequency of the back-EMF.

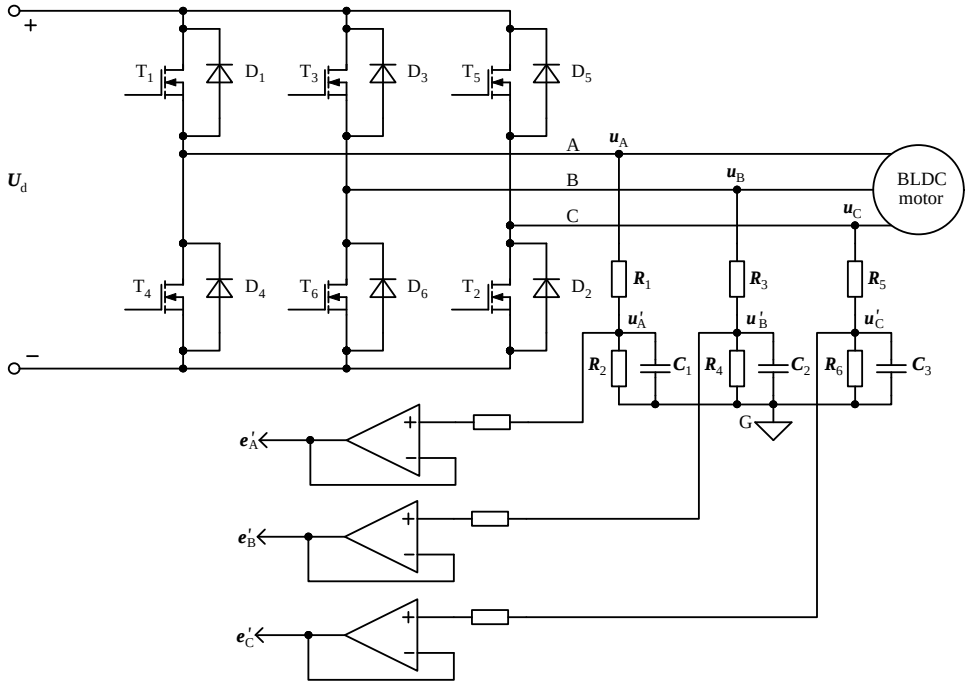


Figure 7.25 Back-EMF detection circuit based on phase voltage.

Thus, the corresponding phase delay is

$$\alpha = \arctan\frac{2\pi R_1 R_2 C_1 f}{R_1 + R_2} \tag{7.5}$$

Further, in the complex high-order system, approximation is adopted sometimes to get relatively accurate results. After the phase delay angle is determined, the correction of the zero-crossing points of the back-EMF can be achieved through software algorithms according to practical conditions.

7.6.2.2 Active Filter

In some situations requiring better waveform quality, an active filter is usually used to reshape the detected signals. The functions of the active filter fall into two aspects. First, it can weaken or eliminate the PWM chopper pulses in the terminal voltage signals, so as to guarantee that those pulses contained in the filtered terminal voltages will not affect the follow-up treatment of the back-EMF. Secondly, it extracts the back-EMF signal from the terminal voltage, and limits its amplitudes within an appropriate range to avoid damaging the devices.

There are a number of classification methods for active filters. According to the amplitude–frequency or the phase–frequency characteristics near the cut-off frequency, the active

filters can be divided as the Butterworth filter, the Chebyshev filter and the Bessel filter, etc. To reduce the complexity of the system, the Butterworth filter is commonly used due to its relatively flat pass band.

The order of the active filter must be determined with comprehensive consideration and calculation. If the order is too high, it would not only increase the complexity and instability of the circuit, but also increase the system error so that the final results would be influenced. On the contrary, if the order is too low, it will not achieve a good filtering effect. Usually, the second- or third-order filter is appropriate. Furthermore, the active filter should suppress the high-frequency interferences and retain the back-EMF signals effectively.

7.6.2.3 Phase-Shift Filter Circuit

It can be seen from Figure 6.1 that the commutation points of the BLDC motor always lag 30° electrical angles than the corresponding zero-crossing points of the back-EMF. However, phase shifting of 30° electrical angles is commonly hard to achieve in practice. In order to input the output signals of the circuit into the microprocessor directly, a novel method is proposed, which is to introduce a phase-shift filter after the detected signals, thus the output signals, lagging 90° electrical angles behind the corresponding zero-crossing points, can be regarded as commutation signals.

During the design of the phase-shift filter circuit, it is necessary to consider both the amplitude–frequency characteristics and the phase–frequency characteristics since the frequency of the terminal voltage and phase voltage are changing with the speed of the motor. In order to achieve the most satisfactory control performance, the filter should be able to eliminate the disturbances, retain the detected signals at the maximum extent, and keep the phase delay as close to 90° electrical angle at the same time.

7.6.3 Current Detection

Generally, phase currents are required to be sampled in the position-sensorless control of a BLDC motor, and the sampling resistor or the current sensor are commonly used in current detection. However, both methods have their own limitations. So certain specific current-detection chips are used in some moderate-capacity motor systems, where the system doesn't need electrical isolation between the main circuit and the control circuit.

MAX472, an ideal current detection chip produced by Maxim Company, can achieve bidirectional current sensing. Its internal structure and typical application circuits are shown in Figures 7.26 and 7.27, respectively.

Assume that phase current i_{load} flows to point B from point A, the comparator A_1 in MAX472 will output a high-level voltage, then T_1 will be excited, and A_2 outputs a low-level signal to block T_2. Consequently, the pin 5 of MAX472 will output a high-level voltage. As the positive terminal voltage of A_1 is approximately equal to its negative terminal voltage, and the current flowing from pin 8 is also approximately equal to the current flowing past R_G and T_1, so the relationship between i_{load} and i_{out} becomes

$$i_{\text{load}} \times R_{\text{sense}} = i_{\text{out}} \times R_{\text{G}} \tag{7.6}$$

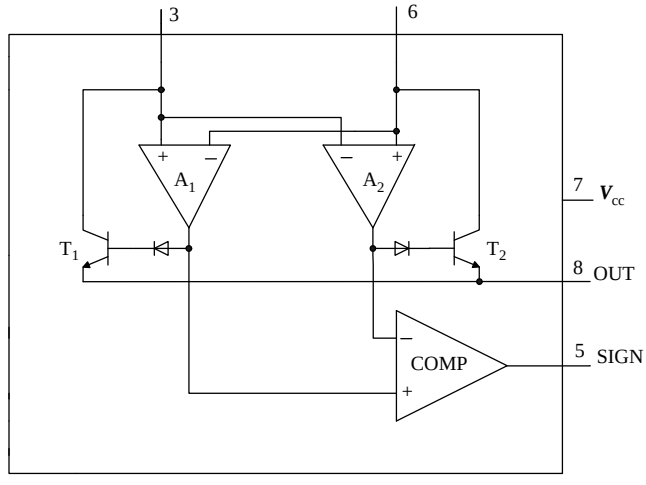


Figure 7.26 Structure diagram of MAX472.

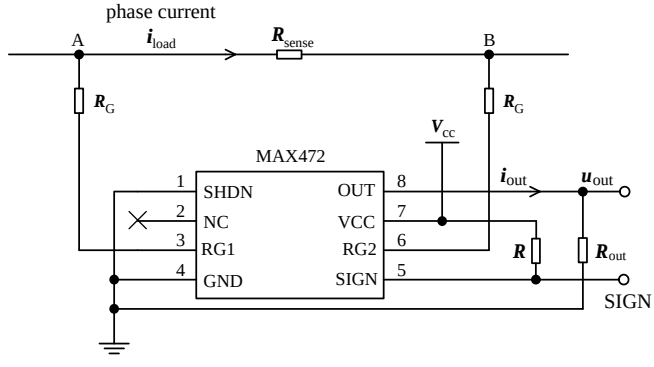


Figure 7.27 Typical application of MAX472.

Hence, the relationship between u_{out} and i_{load} can be expressed as

$$i_{\text{load}} = \frac{u_{\text{out}} R_{\text{G}}}{R_{\text{out}} R_{\text{sense}}} \tag{7.7}$$

As the phase current flows from point B to point A, the relationship between the output voltage u_{out} and phase current i_{load} remains unchanged. The only difference is that the pin 5 of MAX472 outputs a low-level voltage, thus the value and direction of the phase current can be judged by the sampling value of u_{out} and the obtained output signal of pin 5. Furthermore, a voltage regulator is needed on the end of the output to avoid an overvoltage. The selection of the sampling resistance R_{sense} should make sure that the output voltage u_{out} corresponding to the maximum sampling current doesn't surpass the maximum permissible input value of the A/D chip.

7.7 ASIC for BLDC Motor Drives

With the wide application of BLDC motors, more attention has been paid to this motor control technology. Renowned semiconductor companies of several countries have produced ASICs for BLDC motors. These highly integrated circuits have complex structure, most of which are medium or large-scale integrated circuits. Generally, it contains linear and nonlinear devices. It can be used in low- and some high-power control circuits, and be applied in simple open-loop control or high-precision closed-loop control systems. ASICs have many protection circuits, such as overcurrent protection, overheat protection and overvoltage protection, etc. This improves the reliability of the control circuit. However, an ASIC for a BLDC motor always has a fixed control scheme, instead of user-programmable features, that makes it hard to update. Therefore, an ASIC is usually applied in certain BLDC motor control systems which require relatively fixed features and real-time high-quality control [12]. Here, MC33033 and TB6537P are introduced to illustrate the applications of ASIC for BLDC motor drives.

7.7.1 MC33033

MC33033 is a high-performance IC chip for BLDC motor control produced by the Motorola Company. Because of its bipolar analog technology, it can be used in harsh industrial environments. The IC contains all the features that can achieve open-loop control of three- or four-phase motors. MC33033 has units for undervoltage lockout, cycle-by-cycle current limiting and internal thermal shutdown. In addition, it has functions of open-loop speed control, forward/reverse control, operation enable and other typical motor control functions. And it has a $60^\circ/\overline{120^\circ}$ selection pin, which can be matched to sensors with 60° or 120° electrical phasing.

MC33033 mainly contains a rotor position decoder used for determining the correct commutation, a reference power supply source with temperature compensation used for the Hall sensor, a sawtooth oscillator with adjustable frequency, an error amplifier, a PWM comparator, three upper-arm drivers with open collector and three high-current lower-arm drivers for high-power MOSFET. The working principle of the IC is introduced as follows.

The rotor-position decoder built in the MC33033 can not only monitor signals from three input pins (pins 4–6), but also output the correct commutation signals for the bridge inverter. The input pins of the sensors can be connected to the Hall position sensor or the optocoupler directly, and they all have embedded pull-up resistances internally, which greatly simplifies the design of the peripheral circuits. In addition, they are compatible to the TTL level, and the typical threshold voltage is 2.2 V.

The $60^\circ/\overline{120^\circ}$ selection pin allows connection of the MC33033 to the sensor with 60°, 120°, 240° and 300° electrical phasing conveniently. Theoretically, there are eight possible input codes for the three input ports of the sensor, but only six of them are effective, and the other two invalid codes are usually caused by a line failure of the connection to the sensor. Base on the six effective codes, the position decoder could locate the rotor position within the range of 60° electrical angle.

The forward/reverse input interface (pin 3) changes the rotation direction of the motor by changing the power turn-on sequence of the stator windings. When the state of this pin is changed, the output drive for the upper and lower arms of the same phase will be swapped. And then the commutation sequence will be reversed, so that the rotation direction of the motor is changed.

The start/stop control of the motor can be achieved by the output enabling pin (pin 19). When this pin is floated, it will be connected to the positive power supply through the internal pull-up resistance. Then, the driving signals for the upper and lower arms of the bridge can work normally. On the contrary, if this pin is grounded, the output driving signals for the upper arm of the bridge will be closed, and signals for the lower arm of the bridge will be forced low too so that the motor is braked until it stops.

MC33033 contains a fully accessible error amplifier for closed-loop speed control of BLDC motors. The DC voltage gain of the error amplifier is 80 dB with a 0.6 MHz gain bandwidth. The input voltage range is changing from 0 to V_{ref}. Note that in most open-loop control systems, the amplifier is configured as a voltage follower with its input connected to the reference voltage source for setting the speed.

The frequency of the internal oscillator in MC33033 is programmed by selecting the appropriate external resistor R_T and capacitor C_T parameters. The capacitor C_T is charged from the pin 7 through resistor R_T in MC33033, and discharged by the internal discharge transistor. The peak and valley voltages of oscillator are typically 4.1 V and 1.5 V, respectively. In order to reduce noise and improve the efficiency of the switch, the oscillator frequency is recommended to be 20–30 kHz.

The main task of PWM units is to achieve the effective control of motor speed by varying the average voltage applied to each stator winding. When C_T discharges, the oscillator will set both latches, allowing the corresponding top and bottom drive signals output. However, when the voltage of the C_T is higher than the output of the error amplifier, the PWM comparator will reset the upper latch and shutdown the bottom drive output.

Continuous operation might cause the motor overload. This would make the windings overheat or become damaged, which can be overcome by cycle-by-cycle current limiting. The cycle-by-cycle current limiting regards each cycle as an independent unit, and monitors the real-time stator current. Once overcurrent occurs, the driving signals for the bridge inverter are shut down at once, which will be kept blocked within the remaining period. The voltage developed across the sense resistor R_s is monitored by the current sense input (pin 12), then it is compared to the internal 100 mV reference voltage. If the current sense threshold is exceeded, the comparator will reset the lower latch, and terminate the drive output. The value of the corresponding sampling resistor can be calculated by

$$R_s = \frac{0.1}{I_{stator(max)}} \tag{7.8}$$

The capacitor C_T can be charged by the on-chip 6.25 V reference voltage regulator (pin 7) in MC33033. This source can also provide a reference voltage to the error amplifier, and can supply 20 mA of current suitable for direct powering sensors in low-voltage applications. In higher-voltage applications, it is necessary to add a suitable transistor so as to provide a larger current up to 1 A, which meets the requirements for power supply of the external Hall sensor.

MC33033 contains a dual undervoltage lockout to prevent damage to the IC and the external power switches. In low-power supply conditions, it can make sure that the IC and sensors are fully functional. The threshold voltage of the IC is 8.9 V. This ensures that the IC, which is connected to a MOSFET, could output a sufficient gate driving voltage. When directly powering the Hall sensors from the reference voltage, improper sensor operation can result if the reference output voltage falls below 4.5 V. Hence, when the comparator detects power

supply or reference voltage is too low, the top drives will be turned off and the bottom drive outputs are kept at low level. Thus, the chip will be protected.

The open-loop control system of a BLDC motor with MC33033 is shown in Figure 7.28. In the figure, the power switch is a MOSFET. At any given rotor position, MOSFETs on the upper and lower arms of the same bridge can not work at the same time, and the two excited MOSFETs belong to different Totem poles. This switch structure ensures that the current can flow bidirectionally as the stator windings are connected to the DC bus and the ground. However, it may cause leading-edge peaks on the current waveform, so RC filter is added on the current sense input (pin 12).

In order to achieve closed-loop control for a BLDC motor, it is necessary to build a feedback voltage, which is proportional to the motor speed. The three-phase closed-loop control system for the BLDC motor based on MC33033 is shown in Figure 7.29, where the feedback voltage is generated by MC33039.

MC33039 is powered by the 6.25 V reference voltage (pin 7) of MC33033. The same Hall sensor signals used by MC33033 for rotor-position decoding are utilized for MC33039. Based on these signals, a pulse with defined amplitude and time interval is generated by MC33039 from its pin 5. Then, a DC voltage that is proportional to the motor speed is produced with the internal integrator of MC33033. This voltage will establish the PWM reference level at pin 11 of MC33033, so as to achieve the closed-loop control. If the jumper at pin 18 is conducted, the control system will be suitable for the motors having 120°/240° electrical phasing. The system can be easily be modified to accommodate 60°/300° Hall sensor electrical phasing by removing the jumper.

7.7.2 TB6537P

TB6537P, produced by the TOSHIBA Company, is used for the position-sensorless control of a BLDC motor. Because this chip can allow users design their own external driving circuits, it can be used for driving various capacity motors. TB6537P is packaged by DIP18, and contains overcurrent protection, forward/reverse rotation control and lap turn-on functions. In addition, the IC has two types of PWM output (upper PWM and upper/lower alternate PWM). The principle of the IC will be introduced in detail as follows.

Once the IC receives a PWM start instruction signal, a turn-in signal for forcible commutation is output and the motor starts to rotate. The motor rotation will produce EMF on each phase winding. The generated voltage signals are converted to signals of rotor position through the detection circuit. Then the position signals are transferred to pin 18. Thus, the forcible commutation is automatically switched to turn-on signal for position signal. The forcible commutation frequency during the start of the motor is determined by

$$f_{st} = \frac{f_{xt}}{6 \times 2^{bit+3}} \tag{7.9}$$

where

f_{st} — starting commutation frequency;
f_{xt} — resonator frequency;
bit — 14.

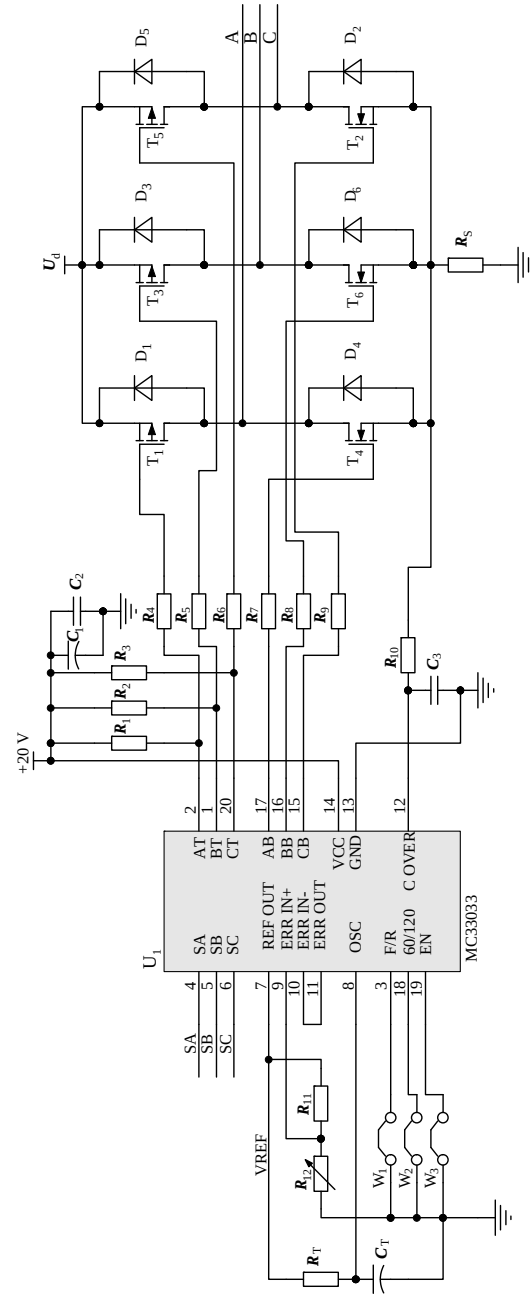


Figure 7.28 Open-loop control circuit for a BLDC motor based on MC33033.

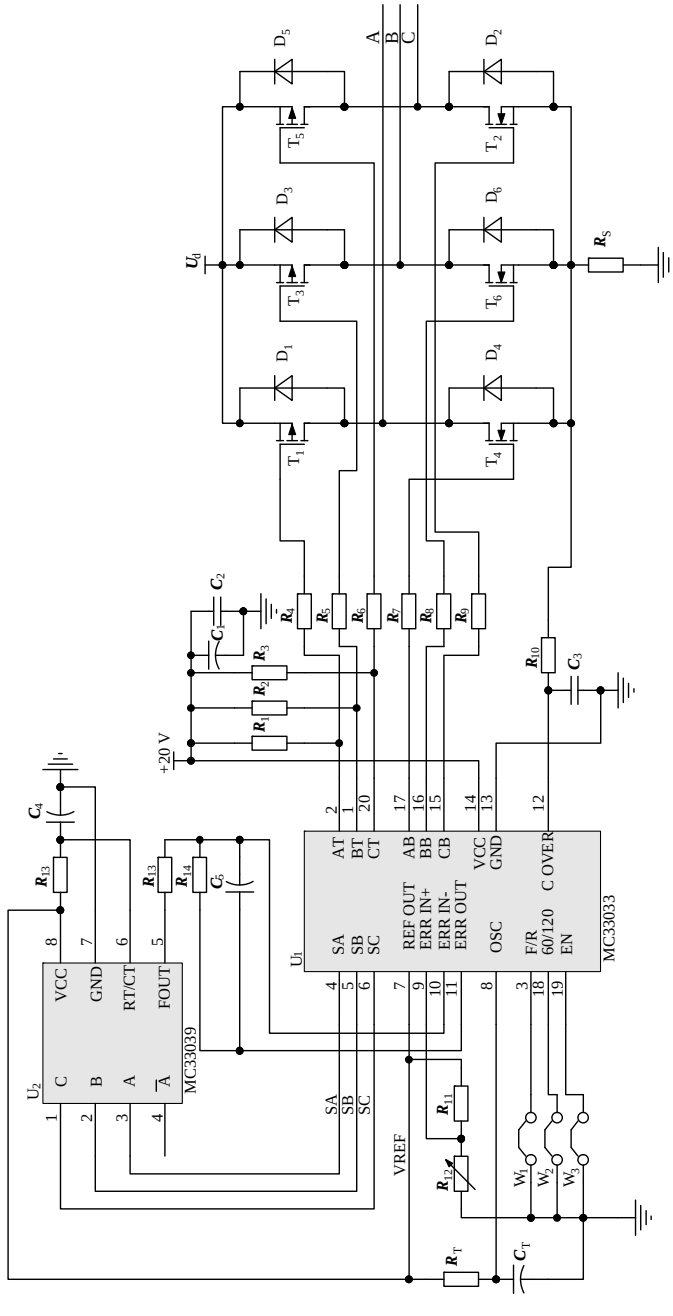
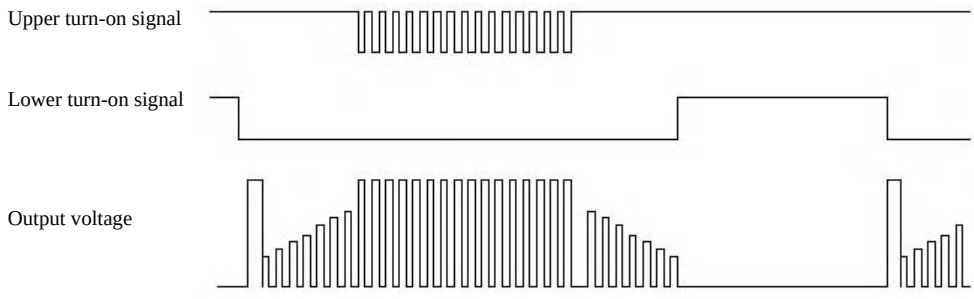
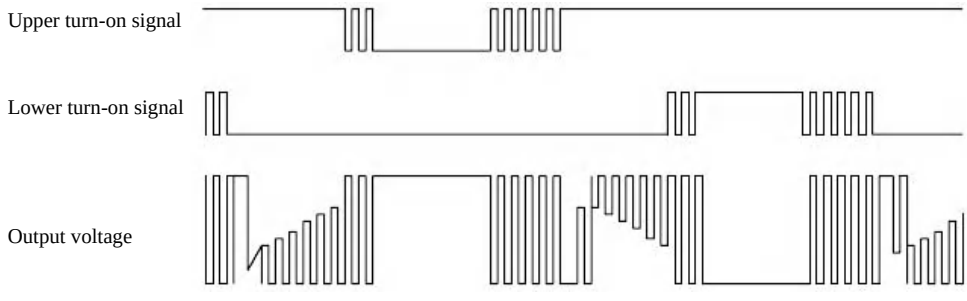


Figure 7.29 Closed-loop control circuit of a BLDC motor based on MC33033.



(a) SEL_OUT is low-level



(b) SEL_OUT is high-level

Figure 7.30 Two PWM output forms of TB6537P.

Note that the frequency of forcible commutation during the start can be adjusted according to the inertia of the motor and load. The frequency should be set higher as the number of motor poles increases. And it should be set lower as the inertia of the load increases.

The external input PWM signals are output after transformation. The output PWM signals should have proper frequency, so as to satisfy the requirements for electrical frequency and the switching characteristics of the driving circuit. Since the position detection depends on the rising edge of the PWM signals, position detection cannot be performed with 0% or 100% duty. Note that even if the reference duty cycle is 99%, the practical duty cycle may already be 100% because of the existence of delay time. So the narrow pulse width should be larger than 250 ns at the maximum and minimum duty cycle in practice.

The PWM output form is determined by the pin SEL_OUT of TB6537P as shown in Figure 7.30. The system runs in upper PWM and upper/lower alternate PWM modes, respectively, when the SEL_OUT is low and high.

As the position detection and the PWM signals are implemented synchronously, the moment of the position detection is related to the frequency of PWM signal. When the IC is used to control a high-speed motor, position signals are changing rapidly. Thus, if the frequency of PWM signals is very low in this condition, it might cause detection errors. In order to avoid such problems, a proper PWM signal frequency should be selected. The rotor-position variation is calculated depending on two consecutive rising edges of PWM signals, as shown in Figure 7.31. Assume that f_p is the frequency of PWM signal, then detection time is between $1/f_p$and $2/f_P$.

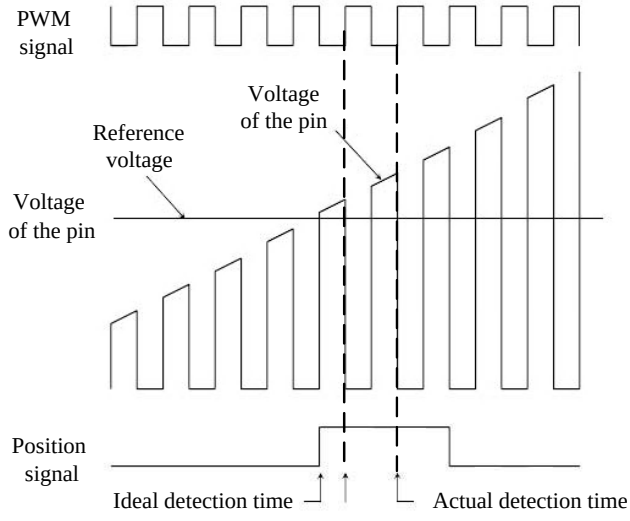


Figure 7.31 Relationship between position signal and PWM signal.

During the start of forcible commutation, the advanced conduction angle is zero, and when normal commutation is started, the advanced conduction angle will be automatically set with LA0 and LA1. However, if both pins of LA0 and LA1 are set for high, then the advanced conduction angles of forcible commutation and normal commutation are all 30°. The set of advanced conduction angle is shown in Table 7.3.

When SEL_LAP is at high-level, each phase winding conducts 120° electrical angle, while when SEL_LAP is at low-level, the IC works at overlapping conduction mode, in which the conduction time of each phase winding is longer, and the conduction durations of different phases overlap. The overlapping time is related to the set of advanced conduction angle.

Start/stop of motor is achieved by controlling the input pin of PWM signal. When the duty cycle is zero, the motor stops. If the PWM signals work normally, and its average low-level duration is longer than two resonator signal periods, the motor starts. In addition, the external noise interferences of the input pin should be minimized.

The typical TB6537P application circuit, whose peripheral circuit is designed by using discrete components, is shown in Figure 7.32. Note that the RC parameters and the power switches in the figure should be selected properly for different applications.

Table 7.3 Set of advanced conduction angles

LA0	LA1	Advanced conduction angle
L	L	0°
H	L	7.5°
L	H	15°
H	H	30°

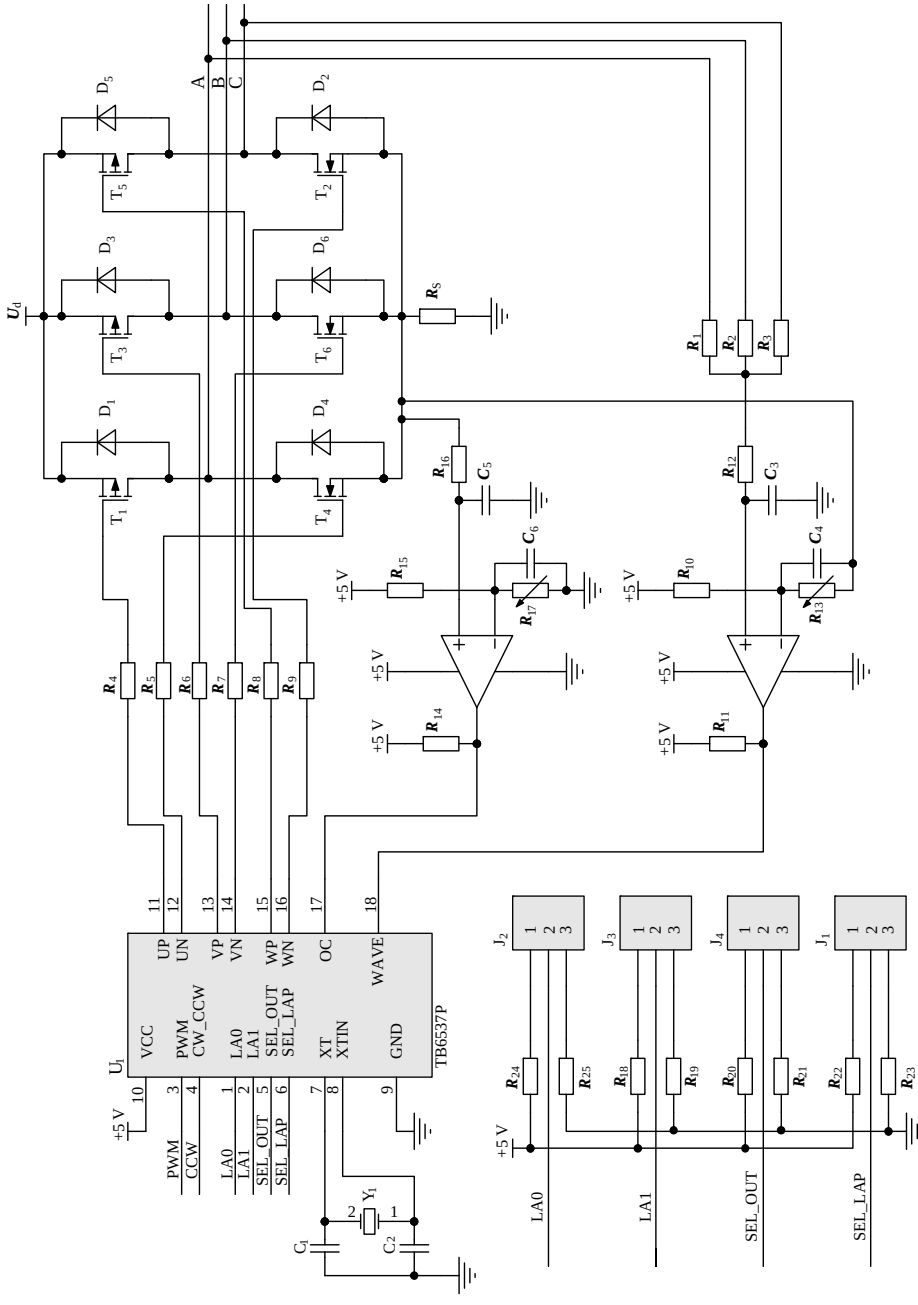


Figure 7.32 Application circuit of TP6537P.

7.8 Software Design

7.8.1 BLDC Motor Driving with Position Sensor

7.8.1.1 Main Program

The flowchart of the main program of a BLDC motor control system with a position sensor is shown in Figure 7.33(a). For an initialization module, it contains not only the initialization of the system clock, the watchdog, the I/O port status, system interruption and other hardware systems, but also includes the initialization of the corresponding variables. During the initialization, in order to prevent accidental interrupt request, system interruption should be disabled at the start of program, which will be enabled after initialization has been performed.

In addition, the general timer should be set to provide the sampling period after the initialization. Then the system will go into the cyclic-waiting state. Once the interrupt signal is received, the program will run into the timer interrupt service routine.

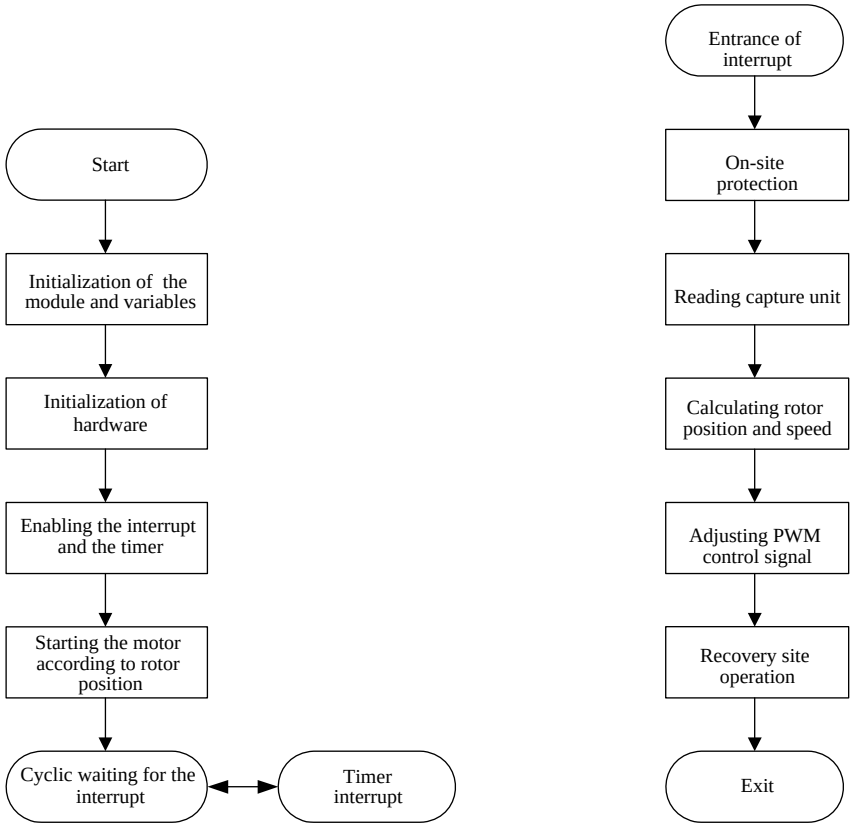


Figure 7.33 Flowcharts of a BLDC motor control system with position sensors.

7.8.1.2 Timer Interrupt Subroutine

The flowchart of the timer interrupt service routine is shown in Figure 7.33(b). After entering the interrupt, the program first executes the onsite protection, and then the Hall sensor position signals will be detected by the capture unit, so as to calculate the rotor position and the speed of the motor. Thus, we could determine the commutation time and adjust PWM control signal. Furthermore, the conduction sequence of the power switches can be obtained. After all the tasks have been performed, the program will execute site-recovery operations, and jump out of the interrupt service routine.

Note that Figure 7.33 only shows a basic program process. The corresponding current detection and fault protection programs are included in practical applications.

7.8.2 BLDC Motor Driving Without Position Sensor

The flowcharts of a BLDC motor control system without position sensors based on TMS320F2812 are shown in Figure 7.34. Usually, the back-EMF-based method is used to

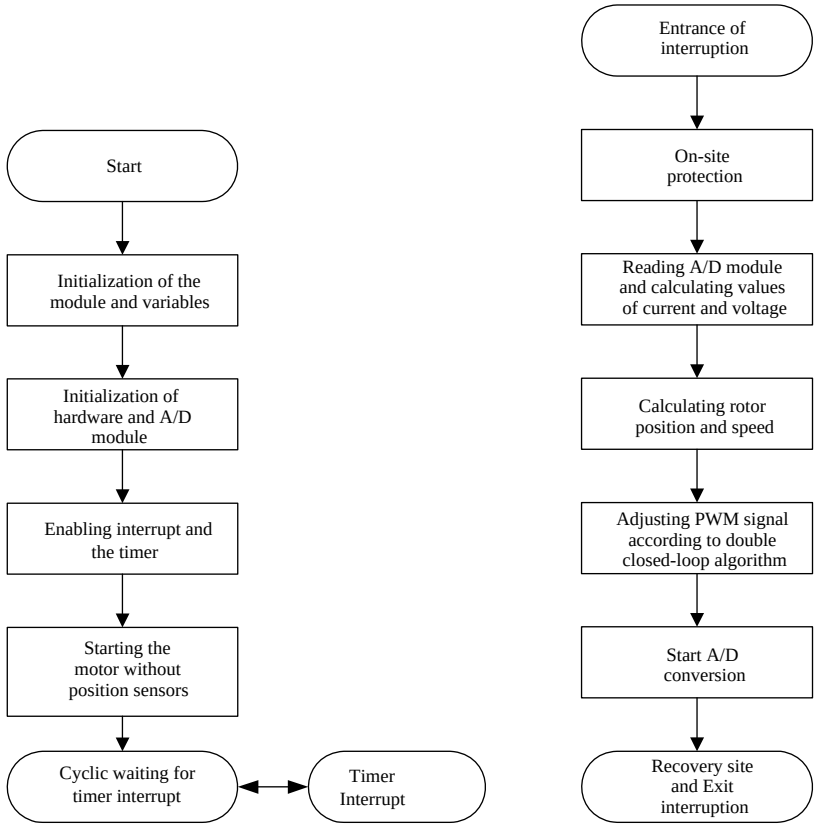

Start
Initialization of the module and variables
Initialization of hardware and A/D module
Enabling interrupt and the timer
Starting the motor without position sensors
Cyclic waiting for timer interrupt
Timer Interrupt
(a) Main program
Entrance of interruption
On-site protection
Reading A/D module and calculating values of current and voltage
Calculating rotor position and speed
Adjusting PWM signal according to double closed-loop algorithm
Start A/D conversion
Recovery site and Exit interruption
(b) Interrupt service routine

Figure 7.34 Flowcharts of a BLDC motor control system with position sensors.

calculate the rotor position. The program is similar to that of the system with position sensors. However, there are three different points, as follows.

(1) Since the stator phase current and the DC bus current need to be sampled, the initialization should include the parameters of the A/D module in DSP as shown in Figure 7.34(a).
(2) Programs for reading the A/D conversion result and starting the A/D conversion should be added to interrupt the service routine. Since the position sensors are removed, the capture unit could be discarded as shown in Figure 7.34(b).
(3) Since the initial rotor position is unknown, the rotor start program is different.

7.8.3 Reliability

With larger scale BLDC motor control systems and more complex algorithms, the requirement for reliability of the software have been given more attention, so it is necessary to add an anti-interference program to improve the reliability [13]. There are a variety of factors that have an influence on the motor. Some common measures, which can improve the reliability of software, are discussed as follows.

7.8.3.1 Anti-Interference Approaches for Switching Signals of Inputs and Outputs

Acquisition for switching signals is a common problem in motor control. In the control system, higher requirements for the accuracy of signal acquisition and real-time control of the system are necessary. However, in certain conditions, the requirements for accuracy and real-time control may contradict each other. If more attention is paid on the accuracy, it might take a longer time for the program to meet the requirement of the system control resolution. On the contrary, if only the real-time control requirement is considered, the accuracy of signal acquisition may be reduced, which may cause frequent changes of switching signals, so that the control system would not work normally. Note that the interference signals are usually narrow pulses, and the effective duration of switching signals are relatively long. According to this feature, we can sample the same switching signal repeatedly at short intervals, and the interval is determined according to the width of the effective signals and the speed of the motor. When the results of two or more than two consecutive samplings are the same, the sampled signals are regarded as valid.

When the system outputs switching control signals, related interference may be conveyed to the output interface as feedback through the shared line, then the output register might be changed, so errors or malfunction may occur. The most effective software solution for this problem is to output the same data repeatedly. If possible, the repetition period should be as short as possible, which would make sure that the control system isn't able to respond to the interferences before correct signals are sent, consequently the malfunction is avoided.

7.8.3.2 Anti-Interference Approaches for Analog Inputs

If the interference affects the input channels of analog signals, the results of the A/D module will have a deviation from the true value, especially when the analog signals are weak. Usually, the reliability of A/D conversion results cannot be guaranteed by only one sampling. Consequently, multiple sampling with digital filtering technology is applied. There are a

variety of digital filtering methods, such as arithmetic mean filtering, weighted mean filtering, sliding mean filtering and inertia filtering. In the control system of a BLDC motor, the arithmetic mean filtering, which is used to sample the same analog signal for certain times, can be adopted. By taking the average of these signals as its sampling value, the influence of systematic random interference on the sampling results can be reduced.

7.8.3.3 Anti-Interference Approaches During Operation of Program

If the interference affects the microprocessor, the microprocessor might not work normally, which leads the program to run away. In this condition, the program may take some operands as operation codes, thus it would cause confusion in the whole program. In addition, if the interferences affect the process of the data transmission, the error of data could also cause system confusion. In summary, five typical approaches can be taken to suppress the interferences during the operation of a program.

(1) **Instruction redundancy**
Single-byte NOP instructions are inserted into the program. In this condition, when the program runs away to certain NOP instruction, the confusion about operands and operation codes can be avoided. Thus, the instruction can be executed correctly, so that the program runs normally.

(2) **Software trap**
The software trap is a bootstrap used to capture the run-away program and force the program to go to certain error procession segment. Software traps are usually placed where normal program cannot reach, so these traps would not affect the efficiency of the program.

(3) **Watchdog**
If the run-away program falls into an accidental endless loop, then the above two strategies are less effective. In this condition, nothing but a reset can force the program to run again so that the system runs normally. The most commonly used autoreset method is to use the watchdog function of the microprocessor.

(4) **Data-transmission verification**
The data transmission is easily disturbed between the host computer and the MCU. In order to solve this problem, the following two approaches can be adopted. The first is to send the critical data multiple times. This means only when the receiver receives the same data in certain times, can the data be regarded as valid, so that the command can be executed. Secondly, insert a check program in the communication protocol, and the communication protocol should be coded according to certain rules. So, even if there are certain bits of data being disturbed during communication, the receiver can also correct these errors. However, this approach makes the bit of communication data longer so that the real-time control performance will be reduced.

(5) **Data protection**
During the operation of the program, if the program itself isn't allowed to be changed, ROM can be configured in the system. This can avoid system malfunction and improve system reliability. In addition, in order to avoid losing the critical data caused by sudden power off, a nonvolatile memory such as FLASH can be adopted, by which the critical data of the system can be protected effectively.

7.9 EMC Design

EMC of an electronic device refers to the ability to work in the designed level within the required security range for electrical or electronic systems, equipment and devices in a given electromagnetic environment without causing damage or unacceptable performance degradation due to electromagnetic interference. A BLDC motor control system is composed of the high-voltage part, like power electronic devices, and the low-voltage part, such as the microprocessor, digital logic gates and A/D converters. Since the low-voltage part has features such as low power, low voltage and high frequency, it is vulnerable to the high-voltage part. Hence, the EMC design of a BLDC motor control system falls into two aspects: one is to reduce the electromagnetic interference caused by the high-voltage part, and the other is to enhance the antidisturbance ability of the low-voltage part.

7.9.1 EMC Design of High-Voltage Part

The high-voltage part chiefly contains the main circuit of a BLDC motor control system. In order to reduce the electromagnetic radiation emitted by the high-voltage part, a shielding box can be installed outside the main circuit. The shielding box can be made from electrolytic copper foil material and connected with the ground reliably. In addition, the cooling fins for power switches in the main circuit should be connected with the shielding box for reliable heat dissipation.

If the DC bus between the bridge rectifier and the inverter is too long, the distributed inductance of the DC bus will be great, which may cause a large impulse voltage during the switching instants of the power switches. Sometimes, the impulse voltage is more than 30% of the DC bus voltage, which would lead to interferences in the low-voltage part. In order to reduce this impulse voltage, three measures can be applied. First, the length of the DC bus should be shortened as much as possible. Hence, its distributed inductance can be reduced. Secondly, according to the length of the DC bus, a proper parallel capacitor filter should be installed at the side of the bridge inverter, so as to absorb the distributed inductance on the bus. Finally, absorbing circuits should be paralleled at both ends of the power switches, so as to absorb the impulse voltage. The commonly used absorbing circuits are shown in Figure 7.35.

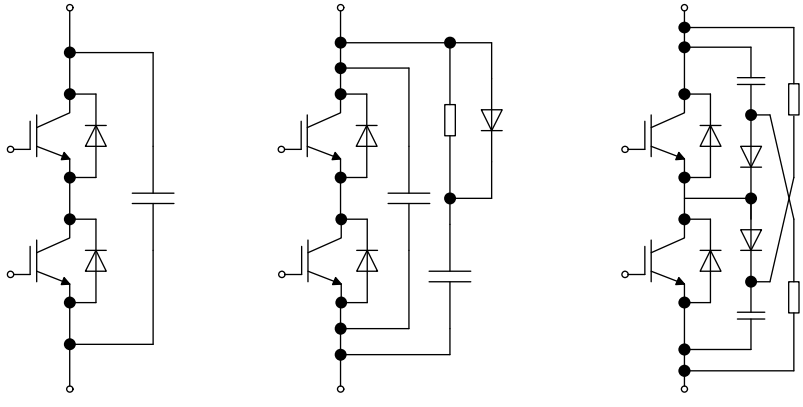


Figure 7.35 Commonly used power-absorbing circuits.

Since driving signals for the power switches are relatively low, the shielding wire should be used between the control part and the power switches. In addition, it must make sure that the metal skin of shielding wires is connected to the shielding box reliably.

7.9.2 EMC Design of Low-Voltage Part

7.9.2.1 Power-Supply Design

This not only needs to supply the power for the main circuit in BLDC control system, but also to supply the power for the microprocessor and the related peripheral driving circuit. According to different devices, the power supply may include +2.5 V, +3.3 V, ±5 V and ±15 V, etc. Therefore, the problem of matching and interference among them should be considered.

At the design of the main power source, a switch-mode regulated AC–DC power supply is usually employed for its simple structure. Moreover, it cannot be easily influenced by the voltage and frequency of the power grid and can isolate the disturbance from the wire of power supply. The switch-mode power supply should install a filter to eliminate the high-frequency interferences from the grid. Also, the input power cable is better to be the shielding wire. Moreover, it should connect a parallel capacitor filter at the DC output of the switch-mode power supply in order to reduce the power ripple. The linear power supply could be used for the microprocessor in order to reduce interferences, which is usually isolated from other power sources. Note that the rating capacity of the power supply must be larger than the system required, so that the system works normally.

7.9.2.2 PCB Design of Control System

The EMC design of a BLDC motor control system can be considered from the following three aspects, i.e. ground protection, PCB placement and routing, and configuration of a decoupling capacitor [14].

(1) **Ground protection**

There are various ground wires in the motor control system, such as system ground, chassis ground (shielding ground), digital ground and analog ground, etc. In the real-time control system, the commonly used anti-interference measure is grounding. Proper combination of grounding and shielding can solve most of the interference problems.

In the low-frequency circuits, when the working frequency is lower than 1 MHz, the distributed inductance of the circuit board routing and the components are very low, while the circulation formed by a grounded circuit is very large, which will cause great interference to the system. Hence, one-point grounding is applied for the circuit board in this condition. When the working frequency is larger than 10 MHz, the ground impedance becomes very large, so multipoint grounding is adopted in the circuit board to reduce the ground impedance. When the working frequency ranges between 1 and 10 MHz, the length of the ground wire should not exceed 1/20 of that of the minimum wavelength if one-point grounding is used. Otherwise, the multipoint grounding is more appropriate.

The digital circuits, isolated from the analog circuits, are always grounded at one point with the latter. Usually, in the circuit board there are not only the high-speed digital circuits, but also analog circuits, which should be separated in the layout. In addition, their ground wires mustn't be confounded. Both ground wires of digital circuits and analog circuits should be connected to the power source ground at the input of the power supply. Moreover, the ground area of linear circuits should be expanded as much as possible.

The ground wire should be as thick as possible. If the ground wire is too thin, the grounding resistance will be great. Hence, the variation of current will cause a great change in the voltage of ground, which will deteriorate the anti-interference performance of the circuit board. So, the ground wire should be thick enough so that a current as large as three times the rated current could flow through it.

(2) **PCB layout**

The circuit board of a BLDC motor control system always contains digital circuits and analog circuits, and some control circuits even have power circuits. During the design of these circuits, it is better to achieve a reasonable partition to reduce the mutual interference of each partition, and try to limit the current circulation in their own regions. For example, the power circuit should be placed near the entrance of the power source, so as to avoid interference caused by large power changes. The crystal and the shell of the crystal oscillator should be grounded. Moreover, there should be enough copper covering the area of the clock region in order to suppress the interference of high-frequency clock signals. Note that digital circuits should be far from analog circuits without interaction, and it is necessary to place a protective ground for analog signals that are vulnerable to interference.

In practice, the number of vias on a circuit board should be minimized and 135° lines rather than the 90° lines should be used. In the places where the system is easy to disturb, the arc lines are better. Common lines should not be too thick, generally 10–15 mil is fine. For a group of high-speed parallel signal lines, such as the data bus and the address bus, the length of them should be approximately equal. In particular, the serpentine line method can be used to keep them isometric. As for some long lines, matching resistors are necessary in order to ensure the integrity of signal. Furthermore, the power lines and ground wires should be as thick as possible at different current ratings. In addition, the direction of power lines and ground wires should be in accordance with that of data transmission, which will be helpful to enhance the antinoise ability of the system.

It is also worth noting that the unused digital gate circuit and input ports of operational amplifier should not be idle. Free microprocessor I/O ports should be set as output ports at the initialization of software.

(3) **Decoupling capacitor configuration**

Decoupling capacitors should be configured on key parts of the circuit board to improve the system anti-interference ability. A 10–470 μF electrolytic capacitor should be connected at the input of the power supply. And usually a 0.1 μF ceramic capacitor, which has a low high-frequency impedance (lower than 10 Ω within 500 kHz to 20 MHz) and small leakage current, is placed at the power input pin of each IC chip.

For devices having poor anti-interference ability and large current variation during switching or memory devices such as ROMs/RAMs, a decoupling capacitor should be

directly inserted between their power line and the ground. Since the presence of an impulse voltage at the reset pin of the microprocessor may change the state of a register, a decoupling capacitor is needed at the reset pin too.

Further, decoupling capacitors should be placed as close as possible to devices, so as to reduce the distributed inductance. In particular, with regard to some high-frequency signals, if the line is a little longer, the distributed inductance will be very great. In this condition, the equivalent decoupling capacitor may be inductive and nonfunctional. Hence, the value of a decoupling capacitor should be selected according to the frequency of major interferences, and capacitors with good high-frequency characteristic and small parasitic inductance will be better.

Questions

1. What does the BLDC motor control system consist of?
2. Compare the advantages and disadvantages of MOSFET drive circuits and IGBT drive circuits, respectively.
3. What should be considered when choosing a microprocessor?
4. Please briefly introduce the principle of the DSP control circuits.
5. List some typical protection circuits in the BLDC motor control system, and try to describe their functions.
6. How to determine the rotor position in sensorless control of BLDC motors, and what are the relationships between the rotor position and back-EMF?
7. Establish your own BLDC motor sensorless control system based on MC33033 and TB6537P.
8. Try to draw the flowchart of software for sensorless control of a BLDC motor.
9. What should be paid attention to during the software design of a BLDC motor control?

References

1. Wang, Z. A., Huang, J. (2006) *Technology of Power Electronics*. Machinery Industry Press, Beijing (in Chinese).
2. Li, Z. Q. (2005) *Single neuron adaptive PID control for BLDC motor based on online identification of RBF neural network*. Tianjin University, Tianjin Master thesis, (in Chinese).
3. Liu, D. (2007) *BLDC motor speed control based on immune feedback*. Tianjin University, Tianjin Master thesis, (in Chinese).
4. Hu, C. Y. (1998) *Modern Speed Control for AC Motor*. Machinery Industry Press, Beijing (in Chinese).
5. Xia, C. L., Yu, W., Li, Z. Q. (2006) Disturbance rejection control for torque ripple of BLDC motor. *Proceedings of the CSEE*, **26**(24), 137–142 (in Chinese).
6. Xia, C. L., Li, Z. J. (2005) BLDC motor control based on ADRC. *Proceedings of the CSEE*, **25**(2), 82–86 (in Chinese).
7. Li, Y. D. (2002) *Digital Control System for AC Motor*. Machinery Industry Press, Beijing (in Chinese).
8. Xia, C. L., Liu, D., Wang, Y. F. (2007) BLDC motor immune PID control based on fuzzy rules. *Transactions of China Electrotechnical Society*, **22**(9), 68–73 (in Chinese).
9. Xia, C. L., Wen, D., Fan, J. (2002) Position sensorless control for BLDC motor based on RBF neural network. *Transactions of China Electrotechnical Society*, **17**(3), 26–29, 76 (in Chinese).
10. Shi, T. N., Tian, Y., Xia, C. L. (2007) Position sensorless control based on wavelet neural network for PM brushless DC motors. *Journal of Tianjin University*, **40**(2), 190–194 (in Chinese).

11. Zhang, X. J. (2001) *Position sensorless control for BLDC motor.* Shanghai University, Shanghai PhD thesis, (in Chinese).
12. Tan, J. C. (2006) *Application of ASIC for Motor Control*. Machinery Industry Press, Beijing (in Chinese).
13. Li, Z. J. (2004) *BLDC motor control based on ADRC*. Tianjin University, Tianjin Master thesis, (in Chinese).
14. T Y. (2007) *Position sensorless control for BLDC motor based on wavelet network*. Tianjin University, Tianjin Master thesis, (in Chinese).

8

Applications of BLDC Motor Drives

BLDC motor is widely applied in industrial products, office automation, household, vehicles, medical equipment and other fields due to its excellent performance. In this chapter, the applications of BLDC motors in the elevator-door system, driving lift system, inverter air conditioner and the related technologies will be presented.

8.1 Elevator-Door Control System

8.1.1 Introduction

An elevator is indispensable in high-rise commercial and residential building, multistory factories and other buildings. Nowadays, 70% of elevator faults occur in elevator doors, so the elevator-door system is critical to the entire elevator system. There are two major types of elevator-door-motor systems: DC motor drive systems and AC motor drive systems. Both of these door-motor systems have their own defects. The presence of electric brushes and commutators in DC motors will result in high noise, poor maintenance and EMC performance. The structure of an AC motor is simpler, but it has the disadvantages such as large volume, low efficiency, large vibration and shock, and so on. Thus, these two types of motor control system cannot meet the requirements for architectural modernization and the development of the elevator industry. Therefore, the research on intelligence, small size, high efficiency, reliable operation and easy maintenance for elevator doors, will be one of the developing directions of the elevator industry.

According to the control signals sent by the host computer, elevator-door-motor system drives the elevator-door motor to control the opening and closing of the car door and the landing door in an elevator. The elevator door runs frequently, so fast and reliable operation of elevator doors for ensuring the normal working of an elevator is quite important. A high-performance elevator-door system should have advantages of smoothness, low noise, high efficiency and security, so as to shorten the waiting time, improve the transport capacity of the elevator, and ensure the safety of passengers.

The experimental system of an elevator door is shown in Figure 8.1.

Permanent Magnet Brushless DC Motor Drives and Controls, First Edition. Chang-liang Xia.
© 2012 Science Press. Published 2012 by John Wiley & Sons Singapore Pte. Ltd.

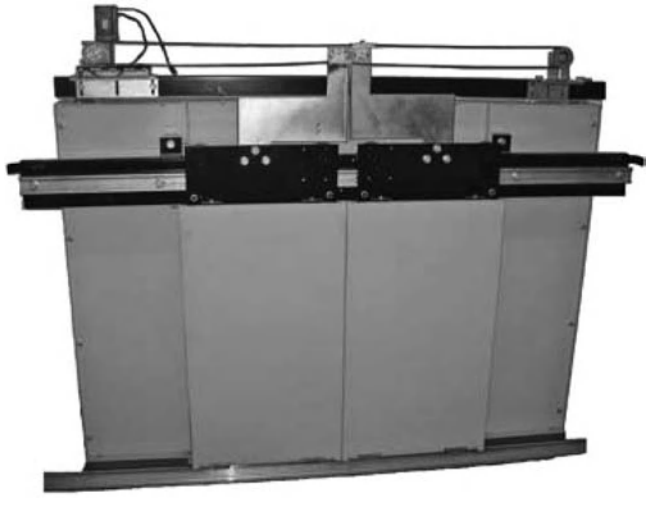


Figure 8.1 The experimental system of an elevator door.

The elevator-door system consists of the door motor, the controller of door motor, the driving device of door motor, the mechanical parts of door system, the security detection system, and so on, as shown in Figure 8.2.

8.1.1.1 Elevator-Door Controller

The elevator-door controller is primarily used to control the door motor installed at the top of the elevator car, and drive the landing doors by a mechanical linkage to open and close the landing doors and the car doors along the given curve quickly and accurately.

8.1.1.2 Structure of Elevator Door

The mechanical part of the elevator door mainly consists of car doors, landing doors, door locks, door-protection devices, and so on. Among them, the car door and landing door play an

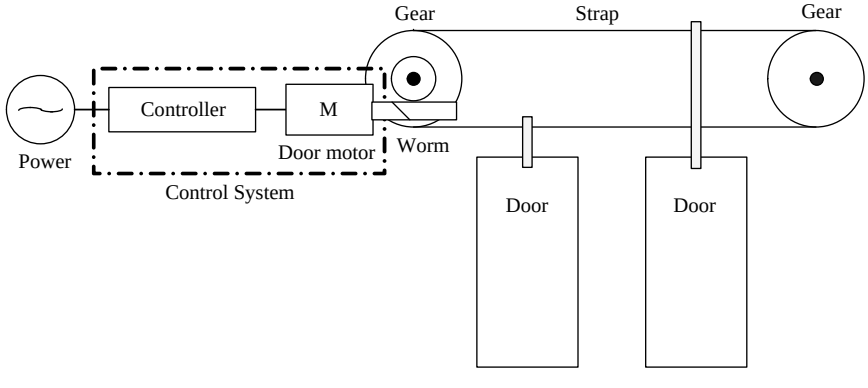


Figure 8.2 Block diagram of elevator-door control system.

important role in protecting passengers in the car from colliding with the elevator hoistway and preventing the waiting passengers from falling into the elevator hoistway. The car door, set near the landing door, is the channel for passengers to go into and out of the car. The landing door or floor door, which is the opening and closing device set at the entrance to the elevator hoistway of each floor, is used to ensure the safety of passengers. Further, the landing doors must be locked in time when the door reaches the closing point to ensure the safety of passengers, too. Currently, there are two structures of the car door and landing door: the single door and the double door opening from the middle. To improve the rapidity of the door system, the double-door structure is mostly adopted in high-performance elevator-door systems.

8.1.1.3 Safety Detection Subsystem

In order to prevent the passengers from being injured when they are going into or out of the elevator, the safety detection subsystem is set in the elevator control system to detect whether there are passengers going through the elevator door when the door is closing. If there are passengers going into or out of the elevator car (including situations where passengers are somewhere in front of the car door or the door being prevented from closing by passengers), the car door should stop closing immediately and reopen, to make sure that passengers go into and out of the elevator safely. Currently, there are two common types of safety detection subsystem: a contact detection device and a noncontact detection device. A contact detection device is mainly based on the safety edge, while the noncontact detection device includes a photoelectric detection device (photosensor), ultrasound monitoring device, electromagnetic induction detector and infrared light curtain detector and other forms.

8.1.1.4 Technology Requirements of Elevator-Door Motor System

The elevator-door control system drives a gear box and mechanical transmission through the door motor to complete the process of opening and closing for the car door and the landing door. The opening and closing for the elevator car is a speed-changing process including start, stop, acceleration and deceleration. In order to guarantee the opening and closing for elevator door smoothly and rapidly, and avoid the collision at the beginning and the end, speed-regulating control of the elevator-door motor is essential. The common curve of opening and closing for elevator door is shown in Figure 8.3.

As shown in Figure 8.3, the door motor runs at low speed to ensure a smooth opening in the initial opening stage, then the elevator door accelerates to high-speed operation. When the elevator is going to open completely, the door motor should also run at low speed to avoid the collision. Similarly, the elevator door starts slowly in the initial closing stage, and then accelerates to high-speed operation. When elevator is going to be completely closed, the elevator door slows down to low-speed operation, and closes slowly too. Considering the safety of passengers, the average speed of closing should be lower than the average speed of opening so as to avoid clipping. During the closing process, in order to prevent the elevator doors from hurting human bodies, a limited speed of elevator is set. Similarly, during the opening process, the speed should not be too high. So the maximum speed of opening and closing for the door is set in advance.

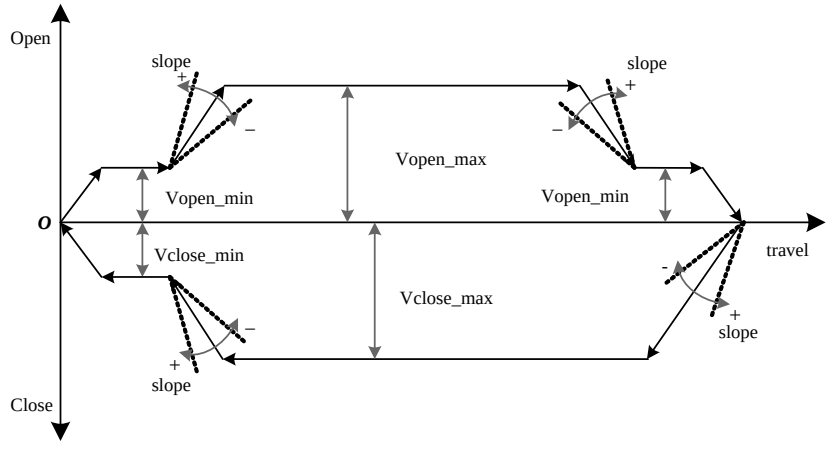


Figure 8.3 Elevator-door operation curve.

The elevator-door system is closely related with the safety and comfort of passengers. On the elevator-door control, a number of technical requirements have been introduced. Currently, European Standard CEN-EN81-1, the most common criterion of elevator manufacturing and installation, prescribes that the maximum kinetic energy of an elevator door in the direction of closing should not exceed 10 J. For example, if the total mass of the elevator door is 80 kg, the corresponding maximum velocity of closing is 0.5 m/s. The corresponding limited speed curve of elevator door is shown in Figure 8.4.

In the closing process, if the elevator door is stopped by impediment and the stopping torque reaches the set value, the elevator-door system should terminate the closing process and open the elevator door, then shut down again after a short waiting time. If the elevator door still cannot be closed after repeating three times, the waiting time of closing the door should be gradually extended to prevent the motor temperature from being too high.

In the early elevator-door control systems, travel switches and tachometer generators were used to complete the control of opening and closing for the elevator door. Because of the single

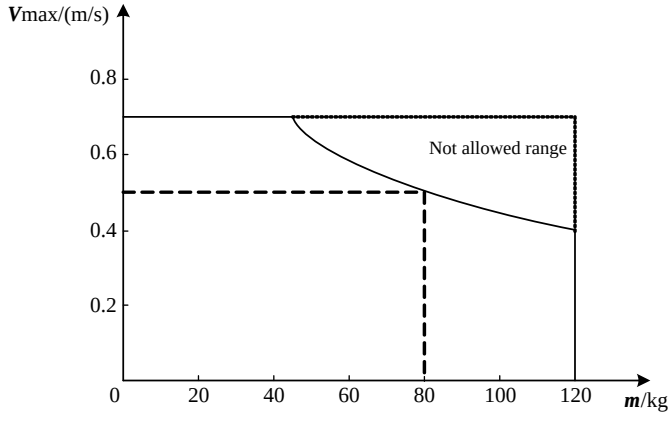


Figure 8.4 Limited speed curve of elevator door.

operating parameter and low reliability, this method was unable to meet the requirements of the modern elevator control technology. Therefore, in order to avoid installing position sensors, door systems should study the width of the elevator door by itself at the time of initial installation, namely detecting the required distance that the elevator door runs from fully closed to fully open and storing these parameters for future use. The closed position of elevator doors can be confirmed by way of opening slightly, then shutting down three times with large torque. When the width of the door or environmental condition is changed, the controller is manually made to run again under the self-learning operation mode.

For the elevator-door control system, the technical requirements are as follows:

(1) The elevator-door motor installed in the elevator car controls the opening and closing process of door. When the elevator car reaches the stop points of any levels, the door knives and other mechanisms ensure that the current level landing door and elevator car door are linked to achieve the car door and landing door opening and closing synchronously.
(2) The elevator door can run smoothly, and there is no severe vibration and noise. According to national standards, the noise of opening and closing of door should not be more than 65 dB.
(3) When the elevator door is fully open or closed, a certain capability of locking the rotor is required.
(4) To be safe, when the car door and the landing door are closed, electrical and mechanical confirming and displaying equipments are needed to guarantee that the door is completely closed.

8.1.2 Hardware Design

The elevator-door system driven by a BLDC motor based on sensorless control consists of a BLDC motor, a main power circuit, a driving circuit, voltage and current sampling circuits, a DSP control circuit, and protection circuits for overvoltage, undervoltage and overcurrent, as shown in Figure 8.5.

In the elevator-door-control system, TI's DSP TMS320F2812 is used for the controller. This processor has high signal processing and control capability. It has integrated many kinds of advanced peripherals, and provides a good platform for the realization of motion control.

The single-phase 220 V, 50 Hz AC current is transformed into 22 V, 50 Hz AC current by the transformer in the main power circuit of the system, and then rectified by the full-bridge

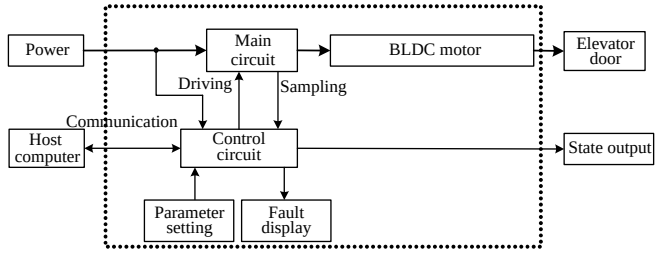


Figure 8.5 Elevator-door system driven by a BLDC motor based on sensorless control.

rectifier module, after which the voltage U_d on the DC side of the inverter circuit is obtained through a voltage-stabilizing capacitor, and then the BLDC motor is driven through a bridge inverter with MOSFETs.

In addition, the system has the function of communicating between the host computer and the slave MCU. Then, the operation parameters of the elevator-door system can be controlled and set through the monitor program in the host computer directly.

8.1.2.1 Inverter Circuit

To ensure the safe operation of power devices, the bridge-inverter circuit has a turn-off snubber circuit, namely the damping snubber circuit. Besides, MOSFET switches are very sensitive to overvoltage between the gate and source, so some appropriate protective methods must be taken. The bridge inverter with damping snubber circuit is shown in Figure 8.6.

In Figure 8.6, the internal freewheeling diodes provide freewheel paths for winding currents. When the motor is working in the stage of electromagnetic brake, the motor's regenerative energy can be fed back to the DC bus through the freewheeling circuit, so that the MOSFET power switches are protected.

At the moment of turning off or turning on the MOSFET, due to the larger rate of change of the winding current, the induced EMF is large. Then, if the induced EMF is not limited, the power switches will be damaged. Therefore, the buffer circuit should be put next to each power switch, as shown in Figure 8.6, to slow down the rate of changes of voltage and current, in which $C_1 - C_6$ are used to restrain the growth rate of voltage of $T_1 - T_6$ when they are turned off, and resistors $R_1 - R_6$ can restrain the growth rate of the discharge current flowing from $C_1 - C_6$ to $T_1 - T_6$ when they are turned on.

Besides the above-mentioned protective methods, normal operation of the MOSFET also needs an appropriate driving voltage and power. While discrete components are used to achieve these functions, the circuit design is relatively cumbersome. It is also difficult to determine the parameters of the devices, and to guarantee the reliability of the circuit. At present, specific integrated circuits are widely used to drive the power devices in

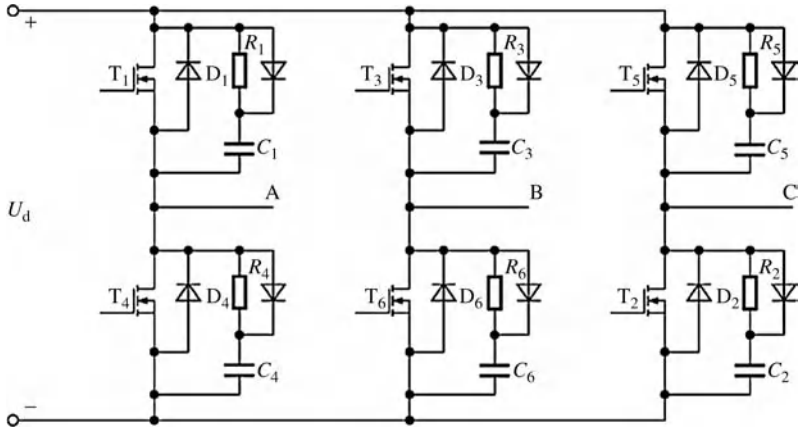


Figure 8.6 Three-phase bridge-inverter circuit.

industrial applications. This can overcome the shortcomings of discrete components and improve the reliability of the control circuit effectively. In the design, a specific gate drive IC for power MOSFET IR2110 manufactured by IR is used. The IC can simultaneously drive two output signals, thus it is usually used to drive the upper and lower arms of the same bridge.

The driving circuit is related to normal operation of the whole control system. So the following design principles should be followed in the design process of driven circuit:

(1) provide sufficient power for power switches of a bridge inverter;
(2) having essential protective functions;
(3) strive to reduce the self-loss of driving circuit;
(4) achieve electrical isolation from the control circuit;
(5) be able to transfer driving signals quickly.

8.1.2.2 Overcurrent Protection

The DC bus current is converted to a voltage signal through sampling resistance, then sent to the voltage comparator after amplification and filtering, and compared with the predefined reference value. If the current exceeds the set value, the comparator output toggles, then the interrupt response of DSP takes place. Thus, the overcurrent protection is achieved.

8.1.2.3 Voltage Protection

The bus voltage differential sampling circuit is used to implement the voltage-protection circuit. At the same time, overvoltage and undervoltage protection are achieved by setting the upper and lower limits of the main circuit.

8.1.2.4 LED Display Circuit

In order to achieve a real-time display for speed and other status information of the motor during operation, an LED display circuit is added to the control system. A designed LED display circuit is shown in Figure 8.7.

In Figure 8.7, CD4511 is the seven-segment decoder driver chip produced by TI. The chip converts binary data into decimal data, and then produces corresponding signals to drive the seven-segment LED for displaying decimal numbers. Since CD4511 has strong load capacity, the circuit does not need an additional drive circuit. During the operation process, only the chip-selecting signal and the binary data, which will be displayed on the CD4511, are coming from the DSP. Then, the data display is achieved.

8.1.3 Software Design

The elevator-door-control system usually adopts a modular programming method to achieve the related functions, such as sensorless control of the BLDC motor, self-learning on door width, automatic opening and closing of the door, and block torque detection [1].

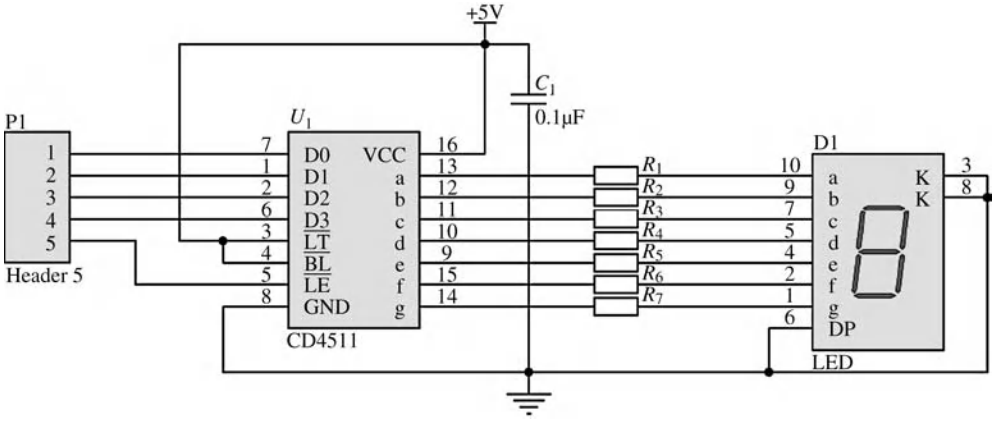


Figure 8.7 LED display circuit.

8.1.3.1 Sensorless Control

First, the terminal voltage and phase current are sampled by hardware detection circuits, then the line back-EMF of the BLDC motor is calculated based on a Kalman filter algorithm. When the zero-crossing point is detected, the controller changes the drive signal to implement the commutation of BLDC motor, ensuring the normal operation of the BLDC motor.

Meanwhile, according to the average time interval between the two commutation points, the motor speed can be calculated approximately. Speed deviation is obtained by comparing the motor speed with the speed reference. Then it is controlled by a PI regulator, so that the current reference signal is obtained. After that, the reference current with the feedback current are compared. Finally, the control of the motor achieves the double-loop speed control by adjusting the duty cycle of the PWM signal. During the operation of the motor, the rotor position of the motor and the moving distance of the elevator door can be calculated by the times of phase commutation. Speed reference values on corresponding points are determined by the given operation curve of the elevator door, so as to achieve the speed-operation curve of the elevator door in the process of opening and closing the door.

The flowchart of sensorless control for BLDC motor is shown in Figure 8.8.

8.1.3.2 Self-Learning of Door Width

For first installation, the self-learning subroutine of the door width should be run to measure the width of the elevator doors, which is the moving distance from the elevator door opening completely to closing completely. In addition, parameters of the door width about operation curves of the door motor also include the low-speed operation point, the accelerating operation point, the high-speed operation point and the decelerating operation point. Then the parameters are saved, and the maximum speed, minimum speed, acceleration and deceleration values are set in the control system according to the requirement. Hence, it is ensured that these settings are suitable for different working conditions. The flowchart of a door-width self-learning subroutine is shown in Figure 8.9.

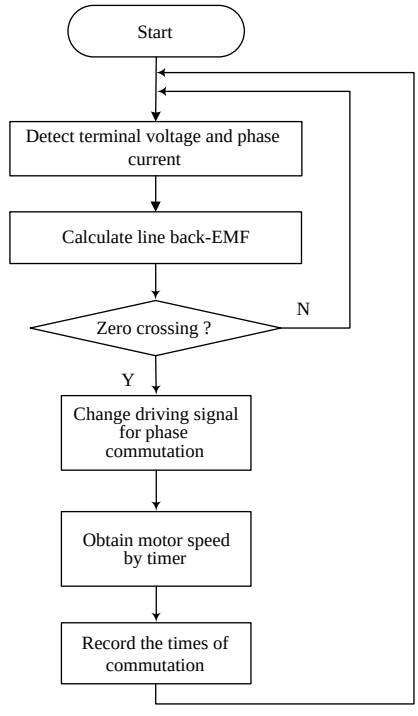


Figure 8.8 Flowchart of sensorless control for BLDC motor.

At the end of the self-learning subroutine of the door width, the control system will record the measured width of the elevator door and the initial location of the elevator. By using the initial position and the moving distance, the location of the elevator door can be confirmed to determine whether the elevator door is completely open or completely closed. Hence, a dead-space switch in a traditional door device is not needed. Then, the complexity of installation is reduced and the operation reliability of the device is improved. After determining the location of the elevator door, the real-time speed command signal is given according to the operation curve of the elevator door, and the elevator door operation is controlled in accordance with the curve. In the actual program, a smooth curve is usually used for the speed operation of the elevator door to ensure its opening and closing quickly and smoothly.

The parameters of the operation curve, such as the minimum speed and the maximum speed of the door's opening, the minimum speed and the maximum speed of the door's closing, slope, accelerating distance and decelerating distance of door's closing, decelerating distance of door's opening are set by a potentiometer. Then, they are converted to a speed commands table for controlling the elevator door, and the commands table is stored in FLASH or EEPROM to ensure that these parameters are not lost after being restarted and make to sure that the elevator door works normally.

In addition, after the control device of elevator door has run a certain time, the system should automatically reconfirm the required running distance from fully closed to fully open, thus eliminating the accumulated error generated in the operation process.

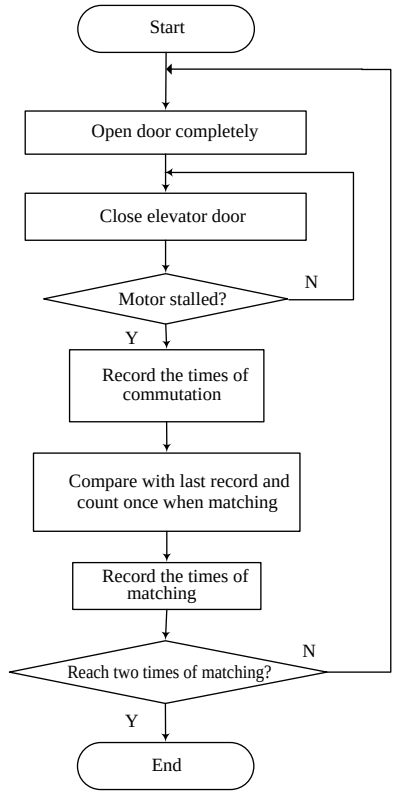


Figure 8.9 Flowchart of self-learning subroutine of door width.

8.1.3.3 Opening and Closing of Door

The subroutine for opening and closing of elevator door is mainly responsible for controlling the operation status of the motor and achieving the operation curve of the elevator door as show in Figure 8.3. When the elevator door receives commands to open or close door from the host computer, the elevator car doors driven by the door motor run forward or reverse smoothly in accordance with the given curves. When the elevator door reaches the fully open or fully closed position, the controller sends corresponding signals to the host computer, then the current status of the elevator door is confirmed.

8.1.3.4 Detecting Stalling Torque

In the opening and closing process of the elevator door, the stalling torque is calculated according to the motion equation of the motor. When the calculated stalling torque is greater than the setting value of the stalling torque, it is considered that there are some obstacles, so the elevator doors stop closing, or open again. If the door cannot be closed after three times of trial, the waiting time for the door's closing should be prolonged gradually to prevent overheating of the motor. Meanwhile, the obstacle should be pushed away in a slow way by the elevator door so that the door can close.

8.2 Elevator Traction Machine System

8.2.1 Introduction

With the accelerated process of urban modernization and sustainable development of the construction industry, the elevator market is also developing rapidly. An elevator is a more complex mechatronic piece of equipment providing transport services for high-rise buildings. In recent years, new requirements for high-performance drive system are being proposed. More comfortable, small size, energy saving, reliable and accurate speed control are becoming the developing directions of elevator drive systems.

An elevator is mainly composed of a traction machine, a guide system, a door system, a car door, a counterweight balancing system, an electric drive system, a power control system and a security system [2,3]. Among them, the traction machine is composed of a motor, a traction wheel and an electromagnetic braking device. According to whether there is a gear box between the motor and traction wheel, it is divided into gear and gearless traction machines. The gearless elevator traction machine is shown in Figure 8.10.

An elevator traction machine and its drive system are the major components of the elevator drive system. As the power source for driving the elevator, their performances directly affect the performance index of the elevator such as start up, braking, acceleration, deceleration, landing accuracy and comfort. Currently, a gear traction machine is the main method used in elevator traction drive systems. Gear transmission systems adopt a mechanical decelerator, worm gears or a planetary gear, resulting in many shortcomings such as complex system structure, hard maintenance work and high noise. The low efficiency of gear transmission also results in increasing the energy consumption and running costs of the whole system. In addition, the large

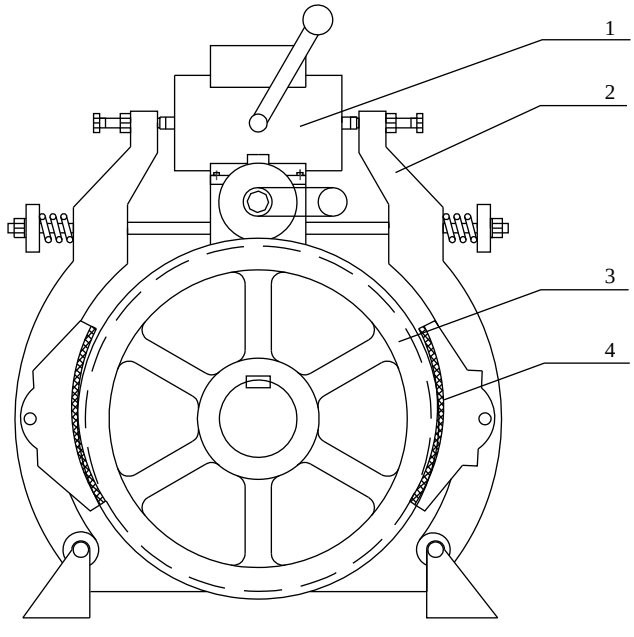


Figure 8.10 Schematic diagram of gearless elevator traction machine (1: Electromagnetic braking device, 2: Brake arm, 3: Traction wheel, 4: Brake disk).

size of the gear box and traction machine makes the volume of the on-top machine room larger and the architecture cost increases, influencing the overall beauty of the building. The gearless elevator traction machine of a BLDC motor has the advantages of compact mechanical structure, energy saving, low noise, and high transmission efficiency. Therefore, the further research of gearless elevator traction machines has far-reaching significance of improving the technical content of the elevator and competitiveness in international markets. A physical photo of a BLDC motor elevator traction machine is shown in Figure 8.11.

The designed BLDC motor gearless elevator traction device includes a BLDC motor, a traction wheel, an electromagnetic braking device, a brake disk, and the controller. The brake disk and traction wheel are mounted on the rotor shaft of the BLDC motor. The BLDC motor is used to drive the traction wheel and provide the torque needed to drag the car. Its stator adopts concentrated winding, and radially magnetized permanent magnets are mounted on the surface of the rotor. The traction wheel drags the elevator car moving up and down through the wire rope. The brake arm controlled by the electromagnetic brake is used to lock the traction wheel under power failure and other fault conditions. The controller is used to control the BLDC motor in four-quadrant operation. This kind of gearless elevator traction machine device has advantages of high efficiency, low cost, small size, large torque, wide speed regulating range, and higher safety and reliability.

8.2.2 Characteristics of a BLDC Motor Gearless Elevator Traction Machine

A BLDC motor gearless elevator traction machine is a gearless elevator traction machine driven by a BLDC motor. This kind of motor doesn't need an excitation current and has high

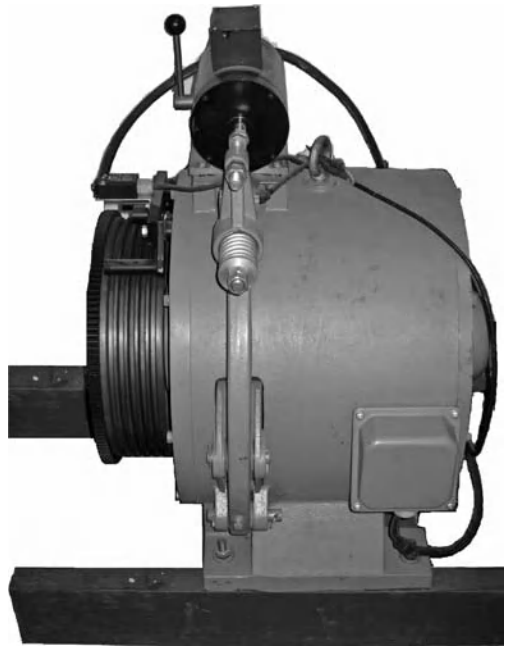


Figure 8.11 Physical photo of the BLDC motor elevator traction machine.

efficiency, low noise, and it can work in strict accordance with the speed required by the elevator, resulting in better comfort for passengers. Thus, it is favored by the elevator manufacturing industry. Its main characteristics are given as follows:

(1) Environmental protection and energy saving. High magnetic flux-density permanent magnetic material is used in the BLDC motor, no excitation coil is required. Hence, miniaturization and high efficiency of the motor system is achieved. Also, by adopting the way of gearless traction, the previous gear box is no longer needed.
(2) Lower vibration and noise. A BLDC motor gearless elevator traction machine without gears eliminates the noise and vibration generated by gearing mesh of a gear traction machine. Meanwhile, the motor speed is significantly reduced, so the noise caused by high-speed rotation of the motor is avoided.
(3) Safe and reliable. A permanent-magnet motor can constrain or lock the operation of system by a proper control mode. In addition, the electromagnetic brake is mounted directly on the rotor. When the brake works, the braking force acting directly on the rotor stops the operation of the traction machine, effectively preventing the elevator from slipping.
(4) Excellent and stable performance. As a result of the frequency control and nongear system, a traction machine does not produce torque fluctuations and effectively improves the running stability of the system.

8.2.3 The Technical Requirements of the Elevator Traction Machine

The movement characteristics of the elevator traction machine include repetitive work, variable speed, frequent starting, forward and reverse rotating. Compared with taking the transport in the horizontal direction, the human body is more sensitive to speed changing of vertical movement of the elevator. Therefore, the speed curve of the elevator, which can improve not only the efficiency of the elevator but also the comfort of passengers, needs to be designed to obtain higher operating performance of the elevator.

The ideal speed curve of an elevator should meet the following two requirements.

(1) Acceleration is an important parameter to the operation curve of the elevator. The maximum acceleration a_{max} must not exceed 1.5 m/s^2. If the acceleration is too large, people will be severely uncomfortable or feel dizzy. The average acceleration a_{av} must not be less than 0.5–0.7 m/s^2. If the acceleration is too small, it will not only extend the process of acceleration, lowering operating efficiency, but also make humans feel fluctuations in the change of the speed, and they may become uncomfortable.
(2) The rate of acceleration change in elevator technology is known as the physiological factor. The rate of acceleration change cannot exceed 1.3 m/s^3. The speed curve of the elevator should be a smooth transition in the corner, because it is decided by the body's physiological characteristics. A human is not only sensitive to the acceleration but also more sensitive to the rate of acceleration change. If the rate of acceleration change is larger, humans will feel dizziness or pain.

It can be seen from the analysis above that when the speed curve of the elevator is designed, it is necessary to choose the right acceleration and rate of acceleration change, so as to meet the requirement of ride comfort and improve the operation efficiency. Therefore, when the

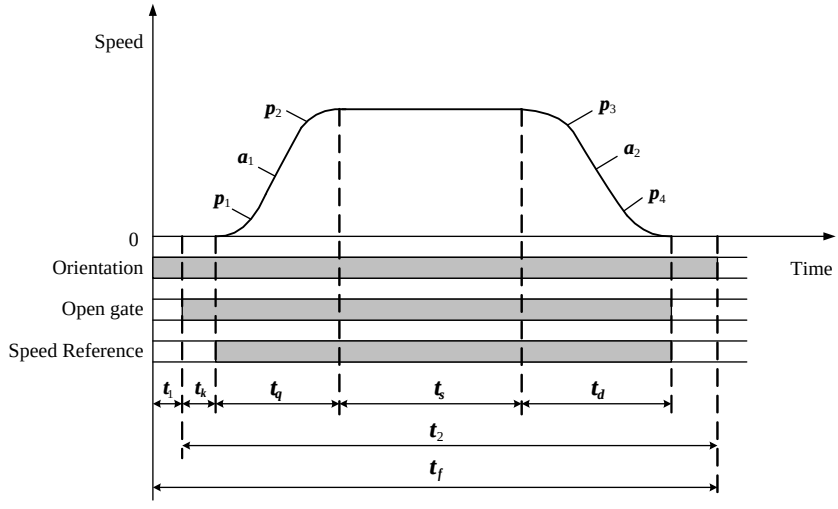


Figure 8.12 Operation curve of elevator traction machine.

elevator starts, it should speed up slowly, and have a smooth transition to the steady-state operation. The ideal speed curve of the elevator should be designed as a parabolic shape, as shown in Figure 8.12.

In Figure 8.12, the elevator starts accelerating slowly from the stationary state, passing slowly from the stationary state to the operation of acceleration at the rate of acceleration change p_1, and continues to accelerate at acceleration a_1, going to the highest speed through a smooth transition to the uniform state at rate of acceleration change p_2, then enters the stage of deceleration at the rate of acceleration change p_3 after running for a certain time. Finally, it decelerates at acceleration a_2, and transits to the stop state at rate of acceleration change p_4.

During the operation, the elevator traction machine starts and brakes frequently, and the loads are changed markedly. Usually, there are the following technical requirements to be met.

(1) The elevator traction machine should have characteristics such as intermittent and repeating operation, variable speed, frequent starting, forward and reverse operation.
(2) When it starts with a full load, the starting current should be as little as possible to avoid influence on the motor windings from a large current.
(3) It should have large enough starting torque so that the car is capable of starting up and accelerating at full load.
(4) It requires hard mechanical characteristics, i.e. when the load of the elevator changes, the speed of the elevator will not change drastically.
(5) In order to make sure that the passengers feel comfortable, it should have low vibration and noise, as well as high transmission efficiency.

8.2.4 Hardware Design

The BLDC motor gearless traction system consists mainly of a BLDC motor, a rectifier/inverter circuit, a drive circuit, a sampling circuit, the position detection circuit, a control

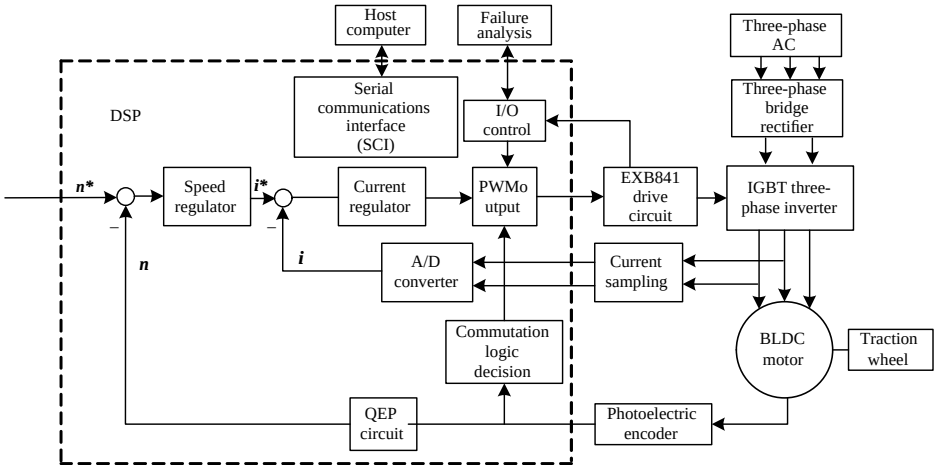


Figure 8.13 The BLDC motor gearless traction control system.

circuit and an interface circuit. The whole structure diagram of the system is shown in Figure 8.13.

8.2.5 Software Design

When an elevator traction machine works, it is required that the elevator can automatically gain the operation direction according to the status of the elevator and elevator-calling signal, and achieve the given speed curve. When the elevator descends, it responds sequentially to the down elevator-calling signals from lower layers than the one that the elevator is currently on. When the elevator ascends, it responds sequentially to the up elevator-calling signals from higher layers than the one that the elevator is currently on. It should make sure to take all the requests of going downstairs before the ones of going upstairs, or in the inverse sequence. Therefore, when the elevator runs in the automatic operation mode, the following functions should be implemented.

(1) According to the current running state of the elevator and elevator-calling signal, the direction of the operation is determined automatically, and the system responds sequentially to the requests. When the elevator reaches the top floor or the bottom floor, the direction is changed automatically. In addition, the elevator runs according to the designed speed curve of the elevator.
(2) Open door automatically according to the leveling signal, and count the layers automatically. When the elevator is running, the operation status of the elevator and the number of the layer are displayed inside and outside the building simultaneously.
(3) The elevator-calling signals are stored and recorded in a real-time way. When the elevator-calling layer is reached, the corresponding elevator-calling signal should be canceled in time.
(4) When the frequency converter of the traction machine or the elevator-door system has broken down, it should stop running immediately and produce related alarm signals. Then, the elevator goes to the nearest floor slowly and remains in waiting mode.

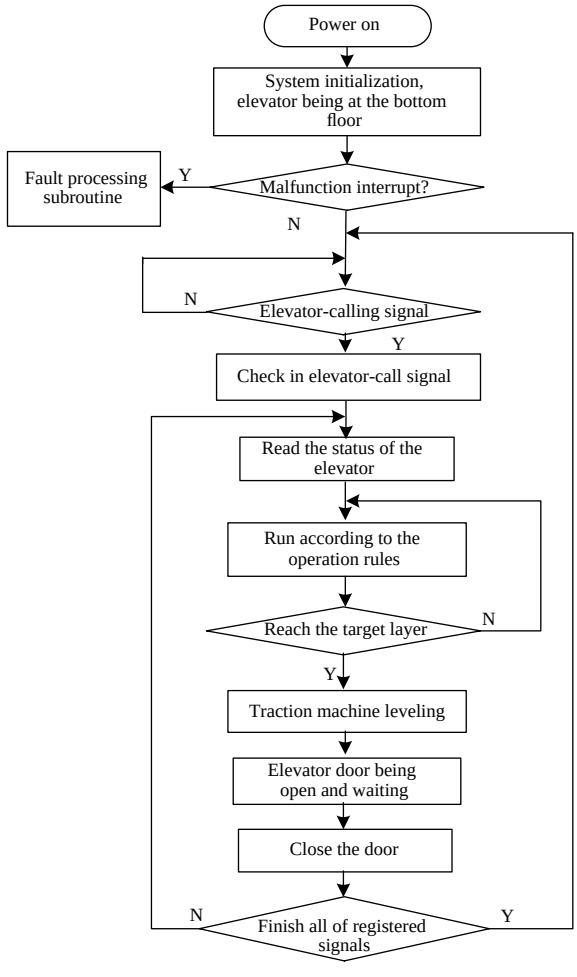


Figure 8.14 Flowchart of the elevator traction machine control system.

According to the above requirements, general functions of the elevator traction machine control system are achieved. The flowchart of the designed elevator traction machine control system is shown in Figure 8.14.

8.3 Inverter Air Conditioner

A variable-frequency air conditioner is a new kind of high-efficiency equipment that can automatically regulate the speed of the compressor motor according to the indoor load. Compared to the traditional fixed-frequency air conditioner, a variable-frequency air conditioner has the advantages of high efficiency, fast temperature regulating, small temperature fluctuation, and adapting to a wide range of environment temperatures.

Among most of the current domestic variable-frequency air conditioners, the compressors are driven by induction motors with high noise, low efficiency and power factor. The application

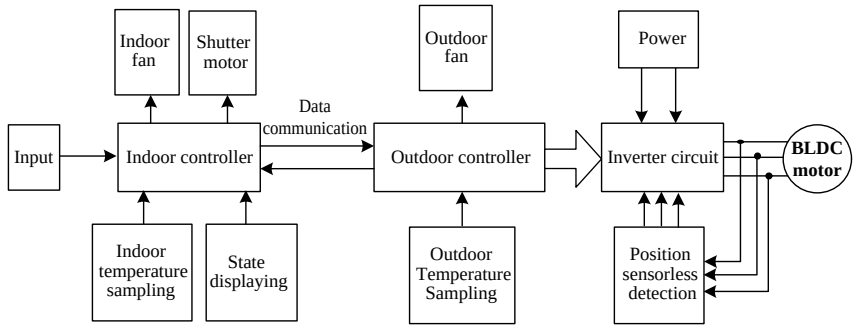


Figure 8.15 Structure diagram of variable-frequency air-conditioner control system.

of a BLDC motor for driving the compressor can effectively overcome these shortcomings, and significantly reduce the overall size of the compressor system. Currently, Hitachi, Sanyo, Toshiba and other companies have used a BLDC motor as the driving motor of the air-conditioner compressor.

Through a microprocessor chip, the variable-frequency air conditioner controls the speed of the compressor and the fan. The structure diagram of a variable-frequency air-conditioner control system is shown in Figure 8.15.

8.3.1 Control Function of Indoor Controller

Generally, the following functions should be achieved for the indoor controller [4].

(1) Receive input signal to control the switching of the air conditioner.
(2) According to different working environments, five operating modes: cooling, heating, dehumidification, auto, and defrosting, are achieved.
(3) The indoor temperature is detected in real time by using a sensor. According to the difference between the given temperature and the actual indoor temperature, and the temperature changing rate, the speed of the compressor is controlled. Then, temperature detection of the indoor heat exchanger and protection function are achieved.
(4) According to different modes selected by the user, the indoor fan runs at four modes: high speed, medium speed, low speed and auto.
(5) When the air conditioner works, the current operating status is displayed.
(6) After the air conditioner starts to work, the air deflector is open, and the swing of air deflector can be controlled by the shutter motor.

8.3.2 Control Function of Outdoor Controller

For the outdoor controller, it should have the following common functions.

(1) All of the outdoor temperatures are detected in real-time mode by sensors, and signals of the outdoor environment temperature, coil temperature, and discharge temperature of the compressor are sent to the indoor controller.

(2) According to the outdoor environment temperature and the compressor speed, the speed of the outdoor fan is controlled.
(3) It is controlled coordinately with indoor unit.

In addition, the position sensors installed in the BLDC motor increase the system cost, while they affect the structure compactness of the compressor. Therefore, position-sensorless control of the BLDC motor is mostly adopted in the compressor. The schematic diagram of sensorless control for a BLDC motor is shown in Figure 8.16.

In Figure 8.16, the whole control system consists of the current loop and speed loop. In the speed loop, the voltage signal is processed through the program of a position-sensorless control algorithm to obtain the speed n. The deviation between the reference speed n^* and the calculated speed n is processed through the speed regulator to obtain the reference current i^*. In the current loop, the reference current i^* and the detected armature current i are calculated by the current regulator to generate a PWM signal with variable duty cycle. Thus, the BLDC motor is driven through the inverter circuit to drag the compressor.

8.4 Electric Vehicles

Fuel vehicles consume a large amount of oil resources, and discharge a lot of exhaust gas, which seriously pollute the environment, bring noise and other inevitable negative impacts. The Chinese Environmental Protection Center has demonstrated that the emission of vehicle exhaust gas pollution is the main pollution source, and EPA also estimates that vehicle emissions account for as much as half of all the cases of cancer attributed to outdoor air pollution. Faced with such a grim situation, research and development of electric vehicles have drawn worldwide attention.

8.4.1 Pure Electric Vehicles

Electric vehicles have advantages of less pollution, saving oil consumption, simple structure, easy maintenance, and long service life. Thus, in the fields of energy, environmental protection and energy saving, it shows excellent development potential. In addition, electric vehicles have advantages of rapid torque response, short process of acceleration, direct control of the wheel speed, easy implementation four-wheel independent drive and four-wheel steering, high safety and reliability of braking. These make electric vehicles show significant merits and

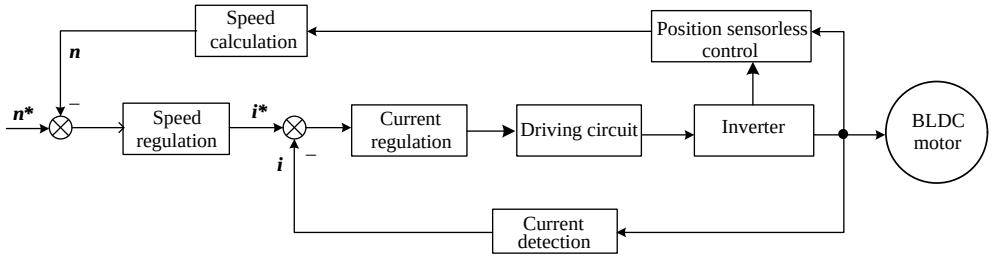


Figure 8.16 Schematic diagram of sensorless control of a BLDC motor.

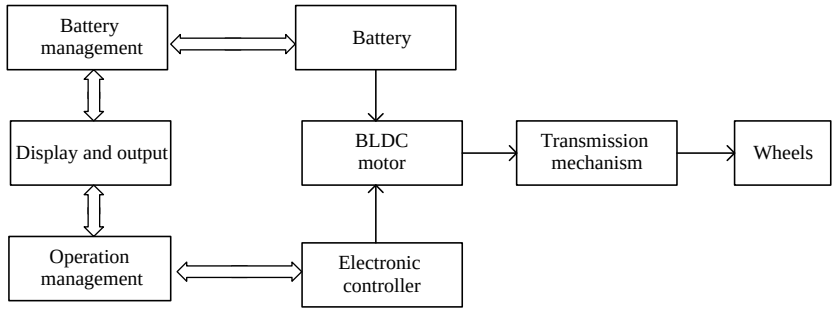


Figure 8.17 Structure diagram of the electric vehicle.

strong market competitiveness. A structure diagram of an electric vehicle derived by a BLDC motor is shown in Figure 8.17.

The motor and control technology are the keys to electric vehicles. They should have characteristics of wide adjustable speed range, high speed and starting torque, small size, light weight, high efficiency, and regenerative braking to ensure good operating performance of electric vehicles. With the improvement of motor drive systems and its digital intelligent control methods, the application of variable structure control, fuzzy control, neural-network control, expert system, genetic algorithm and other nonlinear intelligent control technologies will enhance the performance of electric vehicle control system and its antidisturbance capability, and improve the responding ability. Then, the overall performance can be significantly improved.

Currently, electric vehicles mostly adopt a DC motor, an induction motor, a switched reluctance motor, the BLDC motor, and so on. Among them, the BLDC motor used as the drive motor retains good characteristics of speed regulation, control and operating. It overcomes the shortcomings of the mechanical commutation, and has many advantages such as high efficiency, high power density, maintenance-free operation, high-speed operation, and so on. So it perfectly meets the basic requirements of drive motors used in electric vehicles [5].

The electromagnetic design of a BLDC motor used to drive electric vehicle should mainly aim at increasing the rotation speed of the motor. Then, motors with characteristics of small size, light weight, high power and torque density are provided to meet its operating requirements. Meanwhile, BLDC motors can also be applied to other parts of the car. For example, they can be used as the driving motor of the auto air conditioner [6,7].

8.4.2 Hybrid Electric Vehicles

A hybrid electrical vehicle (HEV) is a vehicle that combines a conventional internal combustion engine (ICE) propulsion system with an electric propulsion system. The hybrid vehicles can benefit from the best features of both conventional ICE vehicles and electric vehicles. The hybrid vehicle offers a long drive range and rapid refueling as for conventional vehicles. Also, it can provide high efficiency with low loads, and deliver better acceleration at low speeds. Since HEV is an emerging technology in the automotive market, the manufacturers are designing and producing hybrid systems for passenger cars, light-duty vehicles, and even heavy-duty vehicles. In general, the internal combustion engine provides the main power

during the long-distance drive, while the electrical motor can either complement the ICE or power the vehicle in electric-only mode during the urban service, where the ICE is less efficient. Improving battery capacity and technology may enable longer electric drive range and reduce the need for the ICE contribution. At present, only hybrids combining a petrol or diesel combustion engine with an electric motor are commercially available, the costs and technical bottlenecks still restrain the deployment of the hybrid vehicles.

There are basically three kinds of hybrid electric vehicles. One kind is using the engine as the main driving power, and the electric motor is used as a secondary power unit. This kind of operation of a hybrid electric vehicle as shown in Figure 8.18(a) is called the parallel mode. In this mode, engines are used as the main power to drive the vehicle. The electric motor can produce a strong driving force in the course of restarting, while the starting and accelerating of the vehicle engine will consume a large amount of fuel. The electric motor is used as an auxiliary driving way to reduce the consumption of fuel. The structure of this mode is simple, which only needs to add an electric motor, a battery, and a related controller to the system. The second kind of hybrid electric vehicle is that at low speed, the vehicle is driven only by electric motor. When the velocity increases, the vehicle is driven by the engine and the electric motor. This kind is called the series-parallel mode, which is shown in Figure 8.18(b). Note that in this mode, power-sharing devices, generator and other devices are needed, so the structure is complicated. Another kind of hybrid electric vehicle is where the electric motor is the only driving power, which is called the series mode as shown in Figure 8.18(c). In this mode, the engine is used as the power source of the generator, and the vehicle is driven only by the electric motor. At the same time, the engine is required to charge the battery.

8.5 Electric Bicycles

With the improvement of people's living standards, environmental protection has drawn increasing attention. So the green nonpolluting electric bicycle has become a current major

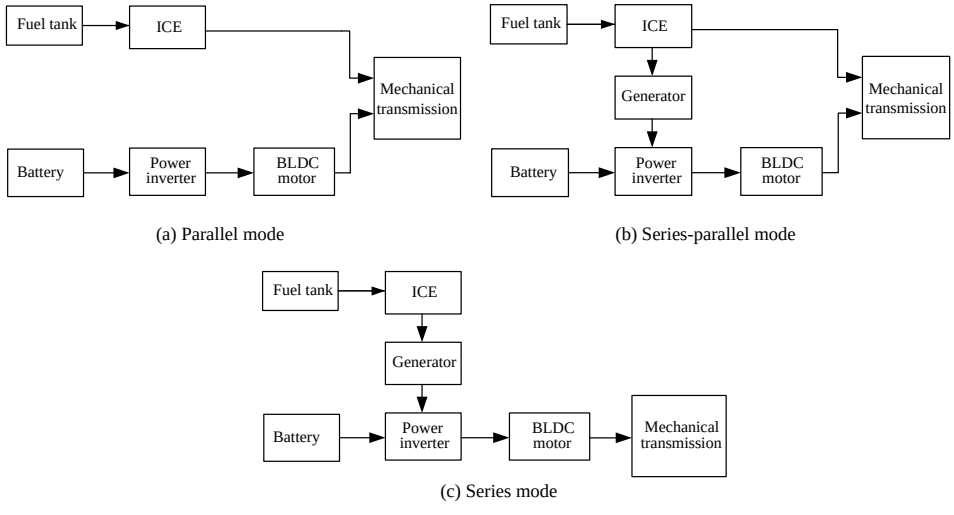


Figure 8.18 Structure diagram of HEVs.

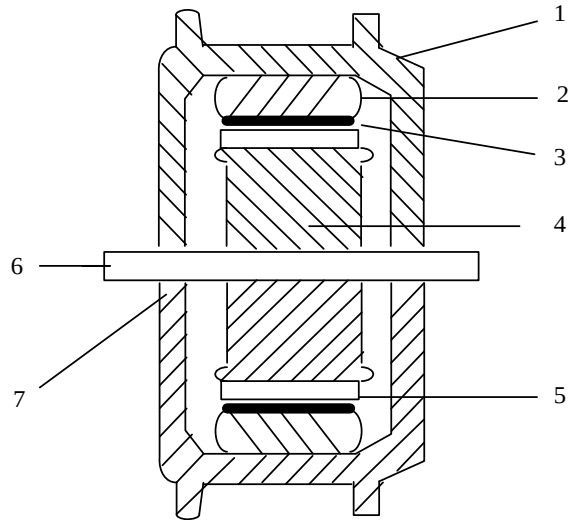


Figure 8.19 The structure diagram of a wheel BLDC motor (1: Wheel hub, 2: Rotor core, 3: Magnet steel, 4: Stator core, 5: Stator winding, 6: Shaft, 7: Bearing).

development trend. Applying the BLDC motor to electric bicycles instead of the traditional DC motor fully utilizes the significant advantage of electronic noncontact commutation of the BLDC motor, which effectively extends the service life of electric bicycles, with convenient speed regulation, ease of control, and smooth operation [8].

At present, the control mode of an electric bicycle is mostly to drive electric bicycle directly by an in-wheel motor. The in-wheel motor is mounted on the bicycle wheel to directly drive the bicycle, which can significantly reduce noise of transmission and improve system efficiency. Figures 8.19 and 8.20 are, respectively, the structure diagram and the actual product picture of a wheel BLDC motor.

Since high-efficiency rare-earth permanent magnet material is adopted in the rotor to replace exciting windings, electric bicycles driven by a BLDC motor thus have higher operation efficiency.

8.6 Others

8.6.1 The Applications in the Fan and Pump

With the rapid economic development, energy conservation has become an important issue. In China, power consumption of fans and pumps accounts for more than 60% of the total power consumption of motors. Therefore, the development and application of related energy-saving technology in the fields of fans and pumps play an important role in the practical implementation of our country's energy-reduction strategy.

Fan equipment is mainly used for drying and cooling systems, where power consumption accounts for about 20% or more of the national power output. In the traditional control method, the output power is mainly wasted in the closure process of the baffle and valve. Note that the shaft power of the fan and pump is proportional to the cube of the rotational speed. When the



Figure 8.20 The wheel BLDC motor.

rotational speed decreases, the shaft power will also decline rapidly. Thus, the use of variable-speed regulation in flow control can improve mechanical efficiency and achieve significant energy saving.

Currently, the BLDC motor has been successfully used to drive axial fans, cross-flow fans, electric fans, scavenger fans and other small fans of household air conditioners. Due to the improvement of motor efficiency, the power consumption of small fans is decreased significantly, and the related performance and quality of system have been greatly improved.

8.6.2 The Application in the Washing Machine

With the continuous improvement of consumption level and the quality of life, the demand of environmental protective and intelligent washing machines is increasing. Washing quality, drying quality, noise and vibration of the washing machine depend largely on the performance of the motor. Therefore, the motor used in washing machines should be developed towards high-power density, energy saving, environmental protection (low noise) and intellectualization, which require the motor of washing machines to provide proper speed and torque according to the different washing modes, namely achieving variable-speed operation. In traditional washing machines, the single-phase induction motor is used to drive the washing machine via a belt drive and gear reducing. Although the motor has a simple structure and low cost, the efficiency of this drive system is low, and it is difficult to achieve speed regulation.

The pulsator washing machine driven directly by a BLDC motor does not need the belt and reduction gear. So the wide speed range of a BLDC motor can change the water flow in the washing machine, and a variety of washing modes are achieved with less noise.

8.6.3 The Application in Medical Instrumentation

Because of the need for surgery, the power system of orthopedic medical devices should achieve continuous speed regulation in a wide range to meet the requirements of different occasions, such as drilling, milling gap, reciprocating saw, swing saw and grinding. In the existing orthopaedic hospitals of our country, motors used to drive medical instrumentation are mostly single-phase DC series motors, of which the motor commutator and brush are prone to produce sliding friction between the mechanical wear, sparks and noise. This seriously affects not only the operative level of the medical staff, but also the psychological emotion of patients. Along with the development of the medical treatment level and the improvement of people's living standard, a new generation of low-noise, wide range of speed, small volume, and light weight of BLDC motor drive systems is urgently needed. Therefore, the BLDC motor is expected to be widely used in medical devices.

Questions

1. In what fields can the BLDC motor be applied?
2. What are the main hardware components of the elevator-door-control system?
3. What are the main characteristics of the elevator traction machine driven by the BLDC motor?
4. Give more than 5 other applications of BLDC motor that are not included in this book.

References

1. Chen, W. *Study on torque ripple suppression technique of permanent magnet brushless DC motor.* Tianjin: Tianjin University, PhD Thesis, 2006 (in Chinese).
2. Yang, L. C. (2000) The Design, Installation, *Maintenance of Elevator Traction Machine*. Machinery Industry Press, Beijing (in Chinese).
3. Xu, J. Q., Yu, S. B., Xu, Y. L., *et al.* (2002) Present state and perspectives of driving system for elevator. *Small & Special Machines*, **30**(3), 5–7 (in Chinese).
4. Song, H. L. *Study on air conditioner control system of BLDC motor.* Harbin: Harbin Institute of Technology, PhD Thesis, 2003 (in Chinese).
5. Chen, Q. Q., Zhan, Y. J. (2001) *The 21st Century Green Transport-Electric Automobile*. Tsinghua University Press, Beijin (in Chinese).
6. Xia, C. L., Xue, X. D., Shi, T. N. (1999) Design of the brushless DC motor for the air conditioner in the automobile. *Micromotors Servo Technique*, **32**(3), 7–8 (in Chinese).
7. Xia, C. L., Shi, T. N., Wen, D. (2001) Simulation of non-bridge brushless DC motor for the air conditioner in the automobile. *Micromotors Servo Technique*, **34**(3), 7–9 (in Chinese).
8. Xia, C. L., Xue, X. D., Shi, T. N. (1997) Optimum design of brushless DC motor for electromotive bicycle. *Small & Special Machines*, **25**(3), 13–15 (in Chinese).

Index

AC asynchronous motor 8
acceleration torque 56, 204
AC–DC–AC converter 79
active disturbance rejection control 3, 11, 127, 146, 150
adaptive control 3, 20, 155–157
advanced conduction 76, 78–82, 144, 145, 244
air gap 18, 20, 27, 28, 33, 34, 37, 38, 48, 59, 72, 78–80, 89, 127–130, 158–161, 163
angular position 46
angular velocity 39, 41, 54, 132, 138
antiwindup 86, 87
application-specific integrated circuit (ASIC) 12
armature reaction 11, 33, 46, 51, 89, 147, 186
armature winding 17, 25, 26, 47, 54, 127
asynchronous motor 8
automotive 1, 4, 5, 273
auxiliary rotor winding 10

back-EMF 6, 9–11, 13, 27, 35, 37, 38, 40, 47–49, 52, 54, 56, 58, 59, 60, 62, 65, 67, 69, 76, 78–80, 89, 90, 99, 119, 127, 128, 130, 132–136, 138, 140, 143–148, 152, 157–161, 164, 165, 168–170, 172–175, 177–182, 184–195, 201–204, 206, 223, 233–236, 247, 253, 262, 263
back-EMF-based method 6, 9, 10, 168, 178, 179, 181, 201, 206, 247
basic structure 25
bipolar power transistor (BPT) 17
brake 260, 265–267
brush 20, 26, 277
brushless DC motors (BLDC motor, BLDCM) 1–21, 25–33, 38–45, 47, 48, 50–52, 54, 56–59, 62–67, 72–74, 76, 78–82, 83, 84, 86–92, 94, 95, 97, 99–101, 103, 104, 106–109, 111–117, 119–121, 123, 124, 127–133, 136, 140, 145–147, 149, 150, 152, 155, 157, 158, 161, 163, 165, 167–169, 173, 174, 177, 179, 181–184, 186, 188, 189, 191–194, 196, 200–206, 209–212, 214–216, 218–221, 223, 224, 230, 232–236, 238, 240, 241, 246–253, 255, 259–263, 266–269, 271–277

centrifugal 2, 5
centrifugal pump 5
ceramic capacitor 252
chopper pulses 235
coercivity 17, 18, 27
cogging effect 10, 33
cogging torque 10, 11, 127–130, 160, 165
coil winding 27
commutating current 120
commutation 1–3, 6, 10–13, 19, 25, 28, 31, 39, 51, 52, 58–62, 64, 73, 79–81, 97, 107, 127, 131–146, 152, 154–157, 161, 163, 165, 167, 168, 170, 172–175, 177, 178, 181, 185, 190–193, 196, 199, 203–205, 216, 221, 233, 236, 238, 240, 243, 244, 247, 262–264, 269, 273, 275
commutation torque 10, 11, 19, 31, 58, 62, 127, 132, 133, 135, 140, 143, 144, 146, 152, 155–157, 161, 163, 165, 167
commutator 2, 25, 277

Permanent Magnet Brushless DC Motor Drives and Controls, First Edition. Chang-liang Xia.
© 2012 Science Press. Published 2012 by John Wiley & Sons Singapore Pte. Ltd.

comparator 14, 186, 203, 213, 214, 220, 224, 228, 229, 236, 238, 239, 261
complex programmable logic device (CPLD) 3
computation capability 15
computer peripheral equipment 7
concentrated full-pitch winding 27, 33
conductor 158
copper material 27
core loss 18, 49
coreless BLDC motor 6, 19
current control 94, 95, 97
current sensing 180, 236

DC machine 20
DC motor 1–4, 6, 8, 15, 25, 26, 40, 48, 51, 76, 79, 255, 273, 275
differential equation 25, 33, 39, 45, 62
digital control 8, 14, 20, 44, 45, 85, 124, 273
digital signal processor (DSP) 219
diode 2, 9, 52, 61, 65, 67, 68, 123, 169, 174–177, 209, 210, 212
distributed function 94
distributed inductance 250, 251, 253
distributed winding 27
double-stator type 6
doubly salient PM motor 20
driving circuit 25, 28, 30–33, 48, 52, 109, 123, 209, 211–215, 218, 224, 243, 251, 259, 261, 272
dynamic characteristics 25, 45, 52
dynamic response 5, 48, 85, 99, 117, 119, 120, 124, 199

eccentric wheel 6
efficiency 1, 2, 4, 6, 16–20, 26, 44, 48–50, 56, 57, 62, 120, 121, 123, 147, 157, 161–165, 181, 220, 239, 249, 255, 265–268, 270, 273, 275, 276
electrical angle 16, 29, 30, 33, 73, 132, 144–146, 157, 159, 167, 168, 170, 173, 174, 177, 216, 236, 238, 244
electric bicycle 274, 275
electrical vehicle 273
elevator door 57, 255–264, 269, 270, 277
elevator traction machine 265–270, 277
EMC 250, 251
EMF 2, 9, 10, 34, 240, 260
energy conversion 1, 79
energy loss 7
energy product 17, 18, 128
energy saving 4, 6, 26, 265–267, 272, 275, 276
equivalent circuit 3, 38, 40, 41, 133
estimation 9, 11, 46, 88, 94, 95, 102, 107, 112, 116, 155, 156, 168, 187, 190
extended state observers (ESO) 11
external load 117

fan and pump 275
Faraday 2
feedback controller 181
feedback gain coefficient 184, 185
ferrite magnetic materials 17
field-circuit method (FCM) 28
field programmable gate array (FPGA) 3
floppy disc drives 7
flux 9, 20, 27, 34, 35, 37, 46, 72, 79, 83, 86, 89, 90, 130, 132, 158, 159, 161, 163, 164, 168, 174, 175, 178–180, 195, 267
flux linkage 9, 34, 37, 46, 168, 174, 175, 178–180, 195
flux-linkage-based method 168, 178, 179
four-quadrant 31, 266
frequency conversion 5, 6
frequency response 40
friction loss 49, 80
frictional force 69
full-bridge 16, 30–32, 40, 59, 131, 132, 209, 210, 259
full-pitch windings 27, 158, 159
fuzzy control 3, 10, 20, 88, 90–92, 94, 103, 104, 106–108, 117, 145, 157, 162, 163, 273

gain 44, 57, 84, 89, 104, 173, 182, 184, 185, 190, 192, 194, 239, 269
gate circuit 214, 252
gate signal 65, 73, 186
gate terminal 49
gearless 8, 265–269
genetic algorithm optimization 102, 103, 105, 109
grey control 113, 115, 117, 124

half-bridge 16, 28–31, 133, 175, 209, 210
Hall element 2
Hall sensor 28, 191, 193, 238–240, 247
hardware design 9, 259, 268
heating 26, 52, 79, 271
high efficiency 1, 2, 4, 6, 16, 17, 19, 20, 57, 181, 220, 255, 266, 267, 270, 273, 275
hysteresis losses 33

impedance 124, 211, 213–215, 251–252
induced electromotive force (induced EMF) 2, 34, 260
induction motor 1, 4, 26, 86, 115, 273, 276
inertia 19, 39, 43, 52, 56, 65, 83, 117, 119, 122, 154, 202, 203, 243, 249
initial rotor position 178, 179, 200–203, 248
insulated gate bipolar transistor (IGBT) 3
intelligent power module (IPM) 215
insulation 212
inverter 3, 6, 9, 11, 15, 16, 25, 32, 47, 52, 65–67, 72, 73, 80, 86, 95, 97, 100, 101, 117, 136, 148–150, 152, 174, 175, 193, 202, 209–212, 215, 220, 221, 224, 238, 239, 250, 255, 260, 261, 268–272, 274
inverter air conditioner 255, 270

Kalman filter 9, 112–114, 187, 188, 190, 192, 262

laminations 129
Laplace transformation 41
laser printer 8
linear DC motor 6
linear motion system 6
load matching 56, 58, 62
loss 5–7, 17–19, 32, 38–39, 49–51, 80, 123, 129, 233, 232, 261

magnetic field 18, 25, 27–30, 33, 34, 48, 49, 59, 76, 78–80, 128, 160, 179
magnetic pole 18
maximum efficiency 50, 62
maximum speed 52, 120, 121, 257, 262, 263
mechanical characteristic 1, 2, 51, 56, 81
mechanical loss 39
mechanical time constant 43, 44, 56
medical instrumentation 277
microprocessor 85, 123, 124, 209, 210, 214, 216, 218–220, 224, 228, 229, 232, 236, 249–253, 271
microcontroller 3, 219, 220
microcontroller unit (MCU) 219
micromotor 18
minimizing torque ripple 157
moment of inertia 39, 52, 56, 65, 83, 117, 119, 122, 202
multiple-input multiple-output (MIMO) 46

NEMA 1
neural-network control 3, 94, 100, 102, 118, 273
neutral point 26, 32, 38, 67, 68, 169, 172, 233
niche algorithms 18
no-load condition 52
no-load loss 49
no-load torque 49
nominal flux 90
nominal inductance 90
nominal resistor 90
nominal transfer function 89
nonlinear states error feedback (NLSEF) 11

observer 9, 107, 109, 112, 146, 148, 149, 181–186, 191–194
operating conditions 11, 47, 89, 119
operating frequency 17, 85
operating parameters 106
optical disc drives 7
overload 239

pancake-shaped rotors and stators 20
parallel operation 219
permanent magnet 1–4, 15, 17, 18, 20, 25–28, 86, 94, 127, 128, 179, 267, 275
permanent-magnet synchronous motor PMSM 86
permeability 35, 130
permeance 35
phase shifting 117, 118, 234, 236
PI controller 44, 74, 76, 85, 87, 100, 116
PID 16, 20, 83–86, 91–93, 106–109, 112, 113, 117, 119, 146
pitch 27, 33, 129, 158–160
platform width 27, 157–161, 164, 165
pole placement 183, 185
position control 94, 129
position-sensorless control 5, 6, 8–10, 12, 16, 17, 99, 167, 196, 233, 236, 240, 272
power density 4, 19, 54, 273, 276
power electronic switch 49, 51
power factor 2, 6, 163, 270
power switch 16, 17, 31, 32, 48, 51, 95, 123, 175, 202, 204, 212, 214, 240, 260
power transistor 17
principle 9, 10, 25, 30–32, 44, 78, 80, 82, 83, 84, 91, 107, 124, 127, 133, 157, 165, 167, 169, 177–179, 181, 186, 200, 202–205, 216, 220, 221, 224, 233, 238, 240, 253
protection 6, 123, 124, 202, 212, 214–216, 224, 229–232, 238, 240, 246, 247, 249, 251, 253, 256, 259, 261, 267, 271, 272, 274, 276

PWM generator 74
PWM modulation 16, 17, 51, 62, 86

quadrant 31, 123, 266

rare-earth permanent magnetic materials 8, 27
ratings 252
rectifier circuit 123, 124, 209, 210
regenerative braking 123, 273
reluctance motor 2, 4, 20, 273
reluctance torque 128
rotating magnetic field 28, 30
rotation speed 25, 191, 195, 273
rotor 1–3, 7–10, 13, 15, 20, 25–30, 33–40, 46, 47, 49, 65, 69, 70, 72–78, 80, 89, 97, 99, 100, 102, 122, 123, 127–129, 131, 132, 135, 138, 140, 144, 150, 163, 167–169, 173, 174, 177–181, 186–188, 194–197, 200–203, 205, 210, 216, 218, 220–223, 232, 233, 238, 240, 246–248, 253, 259, 262, 266, 267, 275

salient pole 35, 36
saturation 33, 51, 86, 89, 180
series excitation DC motor 1
short circuit 230
short-pitch winding 27
single-phase induction motor 276
skewed slot 160
sliding-mode variable structure control 3, 107, 113, 114
slot-type motor 10
slotless-type BLDCM 18
software design 209, 246, 253, 261, 269
speed control 16, 44, 51, 72, 74, 80, 82,
speed regulation 83, 85, 86, 90, 94, 95, 97, 100–102, 107, 109, 115–117, 119, 120, 122–124, 129, 149, 177, 195, 223, 229, 238, 239, 262, 265
stabilization 89, 127
starting circuit 204
starting methods for sensorless control 201
starting torque 2, 56, 163, 164, 200, 268, 273
state-space equation 45, 62
static characteristics 104
static stability 85
stator 6, 7, 9, 10, 11, 15, 18, 20, 25–30, 33, 34, 36, 38, 52, 65, 89, 90, 97, 119, 120, 122, 127–130, 159, 163, 164, 179, 180, 193, 196, 201, 216, 218, 232, 239, 240, 248, 266, 275
switch 16, 17, 25, 28, 30–33, 48, 49, 51, 86, 91, 92, 95, 97, 123, 140, 168, 173, 175, 177, 196, 198, 199, 201–204, 210, 212, 214, 232, 239, 240, 251, 260, 263
synchronous motor 1, 3, 26, 72, 73, 76, 86, 115, 202

three-phase conduction mode 31
three-phase two-pole BLDC motor 33
three-phase winding 26, 45, 65, 67, 97, 99
thyristor 2, 3, 123
time constant 43, 44, 52, 56, 84, 89, 90, 119, 120
time-sharing commutation strategy 131, 140, 144, 145
tooth flux 163, 164
torque constant 59
torque ripple 3, 10, 11, 12, 17–19, 27, 54, 56, 62, 79, 81, 100, 102, 121, 127–133, 135–147, 149–153, 155–157, 159–161, 163, 165, 216
tracking differentiator (TD) 11, 146
transfer function 25, 40, 41, 43–45, 47, 89
transformer 232, 259
transient process 40, 52, 58, 68, 133, 136–141, 143, 144, 156, 157
two-phase conduction mode 16, 30, 31, 40, 131, 132, 221, 222, 233

ultrasonic motor 94
uncertainty 88–90, 115

variable-voltage variable-frequency (VVVF) 7
variable 3, 5, 7, 9, 10, 20, 50, 51, 59, 65, 66, 68, 69, 83, 85, 87, 91, 104, 107, 109, 110, 112–115, 129, 150, 161, 163, 177, 182, 185, 267, 268, 270–273
viscous friction coefficient 39, 52, 65
voltage comparator 261
voltage regulation 156
voltage source inverter 11
voltage-controlled oscillator 203

washing machine 276, 277
wavelet neural network 196
winding current 52, 97, 164, 179, ,260
winding inductance 10, 17, 35, 36, 157
winding voltage 157

Y-connection 172
Y-type 26

zero-crossing point 135, 144, 145, 168, 170, 172–174, 177, 181, 186, 203, 262